ISSN 2518-7198 (Print)
ISSN 2663-5089 (Online)

BULLETIN
OF THE KARAGANDA UNIVERSITY

PHYSICS
Series

№ 3(107)/2022

ISSN 2663-5089 (Online)
ISSN-L 2518-7198 (Print)
Индексі 74616
Индекс 74616

ҚАРАҒАНДЫ УНИВЕРСИТЕТІНІҢ ХАБАРШЫСЫ

ВЕСТНИК КАРАГАНДИНСКОГО УНИВЕРСИТЕТА

BULLETIN OF THE KARAGANDA UNIVERSITY

ФИЗИКА сериясы

Серия ФИЗИКА

PHYSICS Series

№ 3(107)/2022

Шілде–тамыз–қыркүйек
30 қыркүйек 2022 ж.
Июль–август–сентябрь
30 сентября 2022 г.
July–August–September
September 30th, 2022

1996 жылдан бастап шығады
Издается с 1996 года
Founded in 1996

Жылына 4 рет шығады
Выходит 4 раза в год
Published 4 times a year

Қарағанды, 2022
Караганда, 2022
Karaganda, 2022

Редакцияның мекенжайы: 100024, Қазақстан, Қарағанды қ., Университет к-сі, 28
Тел.: +7 701 531 4758; факс: (7212) 35-63-98.
E-mail: vestnikku@gmail.com; karabekova71@mail.ru
Сайты: physics-vestnik.ksu.kz

Редакторлары

Ж.Т. Нурмуханова, С.С. Балкеева, З.Е. Рамазанова

Компьютерде беттеген

Г.Қ. Жанбосова

Қарағанды университетінің хабаршысы. «Физика» сериясы.

ISSN-L 2518-7198 (Print). ISSN 2663-5089 (Online).

Меншік иесі: «Академик Е.А. Бөкетов атындағы Қарағанды университеті» КЕАҚ.

Қазақстан Республикасы Ақпарат және қоғамдық даму министрлігімен тіркелген. 30.09.2020 ж. № KZ38VPY00027378 қайта есепке қою туралы куәлігі.

Басуға 29.09.2022 ж. қол қойылды. Пішімі 60×84 1/8. Қағазы офсеттік. Көлемі 14,62 б.т. Таралымы 200 дана. Бағасы келісім бойынша. Тапсырыс № 97.

«Акад. Е.А. Бөкетов ат. Қарағанды ун-ті» КЕАҚ баспасының баспаханасында басылып шықты.
100024, Қазақстан, Қарағанды қ., Университет к-сі, 28. Тел. (7212) 35-63-16. E-mail: izd_kargu@mail.ru

Адрес редакции: 100024, Казахстан, г. Караганда, ул. Университетская, 28
Тел.: +7 701 531 4758. Факс: (7212) 35–63–98.
E-mail: vestnikku@gmail.com; karabekova71@mail.ru
Сайт: physics-vestnik.ksu.kz

Редакторы
Ж.Т. Нурмуханова, С.С. Балкеева, З.Е. Рамазанова

Компьютерная верстка
Г.Қ. Жанбосова

Вестник Карагандинского университета. Серия «Физика».
ISSN-L 2518-7198 (Print). ISSN 2663-5089 (Online).
Собственник: НАО «Карагандинский университет имени академика Е.А. Букетова».
Зарегистрирован Министерством информации и общественного развития Республики Казахстан. Свидетельство о постановке на переучет № KZ38VPY00027378 от 30.09.2020 г.

Подписано в печать 29.09.2022 г. Формат 60×84 1/8. Бумага офсетная. Объем 14,62 п.л. Тираж 200 экз. Цена договорная. Заказ № 97.
Отпечатано в типографии издательства НАО «Карагандинский университет им. акад. Е.А. Букетова». 100024, Казахстан, г. Караганда, ул. Университетская, 28. Тел. (7212) 35-63-16. E-mail: izd_kargu@mail.ru

Postal address: 28, University Str., 100024, Karaganda, Kazakhstan
Tel.: +7 701 531 4758; Fax: (7212) 35-63-98.
E-mail: vestnikku@gmail.com; karabekova71@mail.ru
Web-site: physics-vestnik.ksu.kz

Bulletin of the Karaganda University. "Physics" Series.
ISSN-L 2518-7198 (Print). ISSN 2663-5089 (Online).
Proprietary: NLC "Karagandy University of the name of academician E.A. Buketov".
Registered by the Ministry of Information and Social Development of the Republic of Kazakhstan. Rediscount certificate No. KZ38VPY00027378 dated 30.09.2020.

Signed in print 29.09.2022. Format 60×84 1/8. Offset paper. Volume 14,62 p.sh. Circulation 200 copies. Price upon request. Order № 97.

Printed in the Publishing house of NLC "Karagandy University of the name of acad. E.A. Buketov".
28, University Str., Karaganda, 100024, Kazakhstan. Tel. (7212) 35-63-16. E-mail: izd_kargu@mail.ru

МАЗМҰНЫ — СОДЕРЖАНИЕ — CONTENT

КОНДЕНСАЦИЯЛАНҒАН КҮЙДІҢ ФИЗИКАСЫ
ФИЗИКА КОНДЕНСИРОВАННОГО СОСТОЯНИЯ
PHYSICS OF THE CONDENSED MATTER

Kulbachinskii V.A., Kytin V.G., Korsakov I.E., Kupriyanov E.E., Ismailov Zh.T. Effect of synthesis duration on heat and charge transport in polycrystalline $CuCr_{1-x}Mg_xO_2$ 6

Mussabekova A.K., Tussupbekova A.K., Aimukhanov A.K. Optical and Electrical Transport Properties of the ZnO:CdO Composite Film..... 12

Maulet M., Sagdoldina Zh.B., Rakhadilov B.K., Kakimzhanov D.N., MagazovN.M. Influence of the content of aluminum on the structure of gradient detonation coatings based on NiCr-Al 18

ТЕХНИКАЛЫҚ ФИЗИКА
ТЕХНИЧЕСКАЯ ФИЗИКА
TECHNICAL PHYSICS

Brim T., Abdeyev B., Muslimanova G., Baigereyev S., Baizakova G. On the issue of a new solution of the materials resistance contact problem on compression of elastic cylinders in contact with parallel generators 25

Markhabayeva A.A., Baidilda M.B., Nurbolat Sh.T., Kalkozova Zh.K., Nemkayeva R.R., Abdullin Kh.A. Comparison of electrochemical characteristics of $NiCo_2O_4$ and $NiCo_2S_4$ nanostructures for supercapacitors..... 36

Sagdoldina Zh.B., Baizhan D.R., Kambarov Y.Y., Torebek K. Obtaining functional-gradient Ti-HA coatings by detonation spraying 43

Berdinazarov Q.N., Khakberdiev E.O., Normurodov N.F., Ashurov N.R. Mechanical and thermal degradation properties of Isotactic Polypropylene Composites with Cloisite15A and Cloisite20A 52

Sagdoldina Zh.B., Rakhadilov B.K., Buitkenov D.B., Zhurerova L.G., Kenesbekov A.B. Improvement of tribological properties of detonation carbosilicide coatings with subsequent pulsed-plasma treatment..... 61

Ispulov N.A., Abdul Qadir, Zhumabekov A.Zh., Kurmanov A.A., Dosumbekov K.R. On nonclassical boundary conditions for the contact of thin interlayers with different physical and mechanical properties on wave propagation in anisotropic media 68

Kengesbekov A.B., Sagdoldina Zh.B., Buitkenov D.B., Ocheredko I.A., Abdulina S.A., Torebek K. Investigation of the characteristics of an indirect plasma torch..... 80

ЖЫЛУФИЗИКАСЫ ЖӘНЕ ТЕОРИЯЛЫҚ ЖЫЛУТЕХНИКАСЫ
ТЕПЛОФИЗИКА И ТЕОРЕТИЧЕСКАЯ ТЕПЛОТЕХНИКА
THERMOPHYSICS AND THEORETICAL THERMOENGINEERING

Shvidia V.O., Stepanenko S.P., Kotov B.I., Spirin A.V., Kucheruk V.Yu. Influence of vacuum on diffusion of moisture inside seeds of cereals 90

Kazhikenova A.Sh., Alibiyev D.B., Tentekbayeva Zh.M., Smailova A.S., Orazbekova R.A., Kauymbek I.S. The use of a cluster-associate pattern for calculation of melt viscosity 99

Bakhtybekova A.R., Tanasheva N.K., Shuyushbayeva N.N., Minkov L.L., Botpaev N.K. Analysis of velocity and pressure vector distribution fields in a three-dimensional plane around a wind power plant.. 108

АВТОРЛАР ТУРАЛЫ МӘЛІМЕТТЕР — СВЕДЕНИЯ ОБ АВТОРАХ — INFORMATION ABOUT AUTHORS 115

ТЕХНИКАЛЫҚ ФИЗИКА
ТЕХНИЧЕСКАЯ ФИЗИКА
TECHNICAL PHYSICS

DOI 10.31489/2022PH3/6-11

UDC: 538.93

V.A. Kulbachinskii[1*], V.G. Kytin[1,2], I.E. Korsakov[1], E.E. Kupriyanov[1], Zh.T. Ismailov[3]

[1]M.V. Lomonosov Moscow State University, Moscow, Russia;
[2]VNIIFTRI, Mendeleevo, Moscow region, Russia;
[3]Karaganda University of the name of academician E.A. Buketov, Karagandy, Kazakhstan
*(*E-mail: kulb@mig.phys.msu.ru)*

Effect of synthesis duration on heat and charge transport in polycrystalline $CuCr_{1-x}Mg_xO_2$

Magnesium-doped polycrystalline ceramic samples of cooper chromite (I) have been prepared by solid phase synthesis. Phase composition and crystal structure of synthesis have been investigated by X-ray diffraction. Microstructure of samples has been investigated by scanning electron microscopy. Thermal conductivity and electrical conductivity have been measured in the temperature range 78<T<320 K. Significant reduction of thermal conductivity with an increase of synthesis duration have been observed. This effect was explained by formation of small amount of $MgCr_2O_4$ and Cr_2O_3 and CuO crystallites operating as effective phonon scatters. Formation of the $MgCr_2O_4$ phase is observed in X-ray diffraction patterns and SEM images of the samples with Mg content higher than 3 at. %. Formation of a small amount of Cr_2O_3 or CuO phase could be due to deviation of precursor's content from stoichiometry. Obtained results open a perspective of thermoelectric figure of merit enhancement for copper chromite-based material.

Keywords: p-type semiconductors, thermal conductivity, electrical conductivity, copper chromite (I).

Introduction

Copper chromite (I) is an attractive material due to the unusual composition of its properties. It is known as quasi two dimensional frustrated magnetic and multiferroic [1, 2]. Simultaneously it is a p-type semiconductor partially transparent for visible light [3]. It makes it perspective material for optoelectronic devices [4, 5]. One of the key issues is its low conductivity compared to the best-known n-type transparent semiconductors such as zinc oxide or indium tin oxide [6, 7]. It has been shown however that conductivity of copper chromite (I) can be increased several orders of magnitude by doping with group II elements [8–11]. The mechanism of electron transport and conductivity enhancement by doping is still a subject of research. The variety of different factors that could affect electron transport makes its investigation relatively difficult. In particular observations of features in the temperature dependence of conductivity near magnetic (ferroelectric) transition points to the influence of the ordering of magnetic ions on hole transport [8–11]. Most often copper chromite (I) is synthesized in the form of polycrystalline ceramic or thin films. Polycrystalline ceramic of magnesium doped copper chromite (I) is usually obtained by heating the mixture of copper, chromium and magnesium oxides in an oxygen-poor atmosphere for a few tens of hours [9–11]. Such material exhibits up to several hundred microvolts per kelvin Seebeck coefficient together with relatively large conductivity at room temperature [9, 10]. Therefore its conductivity and Seebeck coefficient are investigated for understanding electron transport and for possible application as thermoelectric material at elevated temperatures [9, 10]. Ceramic material consists of connected crystallites. Electron transport in polycrystalline ceramic of magnesium-doped copper chromite (I) is affected by point defects such as oxygen vacancies, do-

pant atoms, contacts between crystallites, fraction of empty space, incorporation of crystallites of other phases. Thermal conductivity of such material is more determined by contacts between crystallites, presence of other phases and fraction of other phases and is less affected by point defects. Therefore measurement and analysis of both heat and electric conductivity could help to separate factors determining electron and heat transport. There is a lack of thermal conductivity measurements in the available literature dedicated to polycrystalline copper chromite (I) doped with magnesium.

In the present work, we report the results of the investigation of temperature dependencies of thermal and electrical conductivity of polycrystalline copper chromite doped with magnesium synthesized during a different time. Longer synthesis led to an increase in the density of the material. The main objective is to study the effect of synthesis duration on a microstructure, the phase composition, thermal and electron transport.

Experimental

Polycrystalline Mg doped copper chromite samples have been synthesized by solid phase method from a mixture of CuO, Cr_2O_3, and MgO. This mixture has been obtained by thermolysis of nitrates in a liquid phase solution in NH_4NO_3. Reaction and details of nitrate thermolysis are presented in [12]. According to X-ray diffraction data, obtained mixtures were amorphous. The mixtures were annealed at 500–600 ^oC to dissolve the rest of the nitrates. Small traces of CuO have been detected by X-ray diffraction after this annealing. Then mixtures have been pressed in tablets and annealed for 24 hours or 48 hours at 1080 ^oC in argon flow for the final formation of Mg-doped copper chromite (I) and cooled to room temperature. Table 1 presents the composition and density of obtained samples.

Table 1

Mg content, duration of annealing and density ρ of some samples, ρ_0 is the density of $CuCrO_2$ single crystal

Mg content, at. %	Duration of annealing, hours	ρ, g/cm^3	ρ/ρ_0
0,3	24	2,73(3)	49
	48	2,97(2)	53
0,6	24	2,85(5)	51
	48	3,12(3)	56
1,3	24	3,60(3)	64
	48	4,05(3)	72
4,0	24	3,84(5)	69
	48	4,11(4)	73

Crystal structure and phase composition of obtained tablets have been characterized by X-ray diffraction. Only the delafossite phase has been detected in the samples with Mg content below 3 at. %. For larger Mg content small fraction of the spinel phase of $MgCr_2O_4$ has been detected. Lattice parameters of delafossite phase vary monotonously with Mg content as shown in Figure 1.

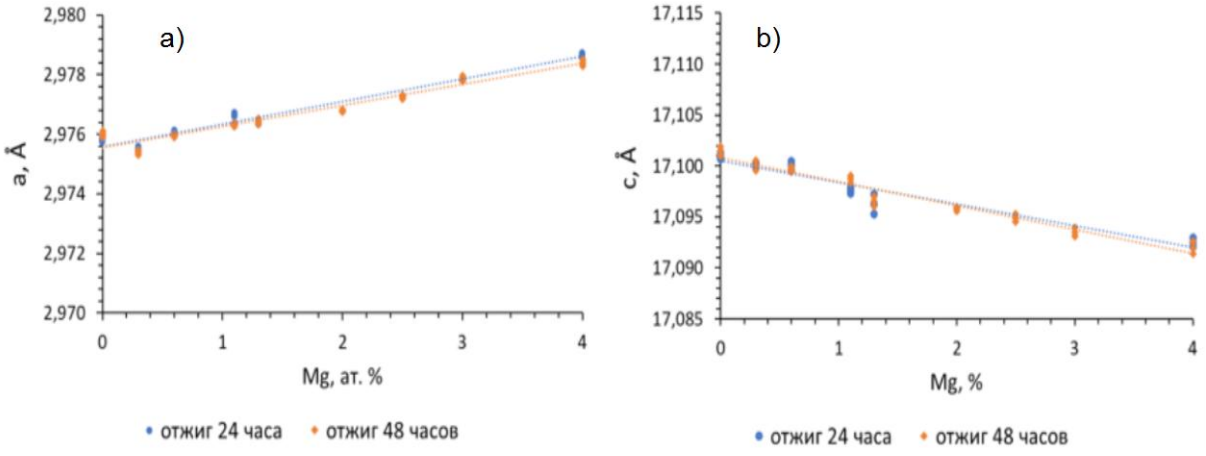

Figure 1. Dependence of lattice parameters on Mg content: a) parameter *a*; b) parameter *c*

Dependence of lattice parameters on Mg content confirms incorporation of Mg in delafossite crystalline lattice. No significant dependence of lattice parameters on the duration of synthesis has been observed. Density of all samples increases with an increase in Mg content and duration of annealing.

Microstructure of synthesized samples was studied by electron microscopy. Figures 2 and 3 illustrate some characteristic SEM images.

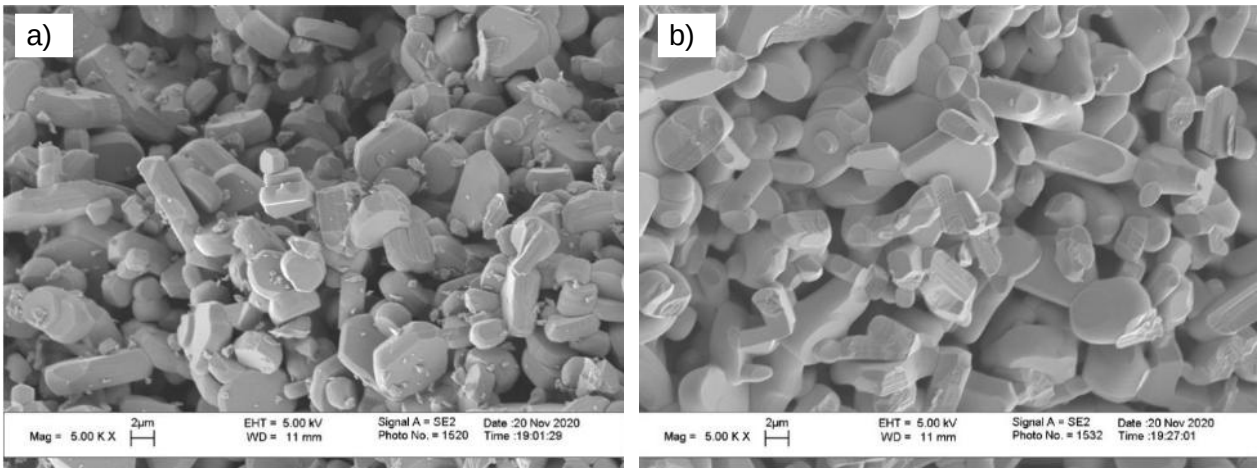

Figure 2. SEM images of the samples annealed 24 hours with different magnesium content: a) 0.6 at. %; b) 1.3 at %.

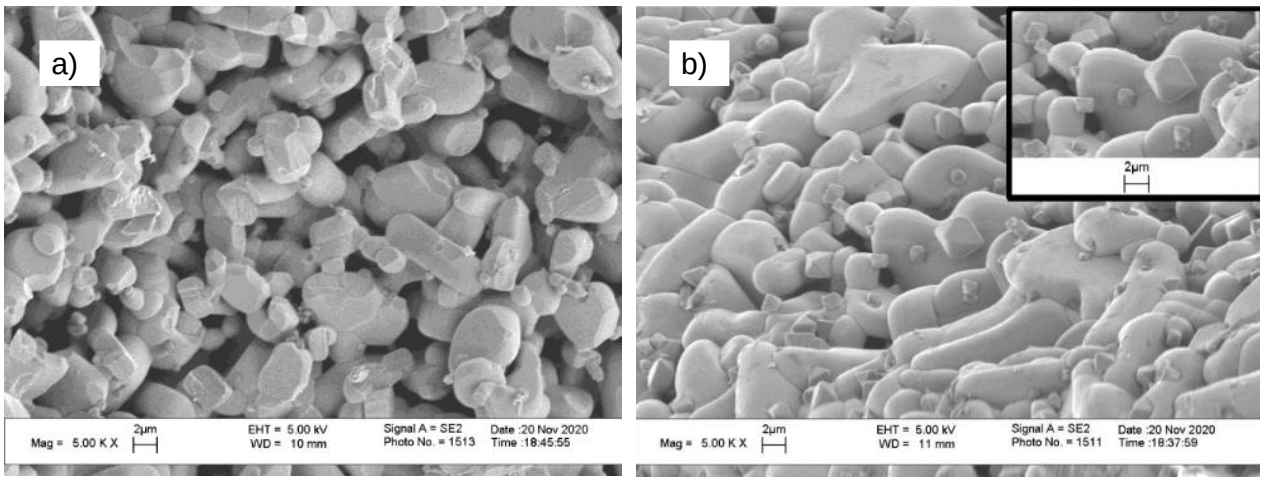

Figure 3. SEM images of the samples with 4 at. % Mg content and different duration of syntesis a) 24 hours; b) 48 hours.

Crystallites in the samples with larger Mg content look better connected. Fraction of empty space decreases with an increase in Mg content under an observed increase in density. A similar tendency was observed with an increase of annealing duration. Fraction of empty space in the samples annealed at 48 hours is smaller than in the samples annealed at 24 hours. Connection of crystallites looks better in the samples annealed at 48 hours. For the samples with 4 at. % Mg formation of micrometer size $MgCr_2O_4$ crystallites is seen in the SEM image (insert in Figure 3b).

For the measurement of thermal conductivity and Seebeck coefficient samples with a rectangular shape and typical dimensions of 2x2x5 mm have been prepared. Conductivity was measured by the 4-probe method at constant current. For the measurement of thermal conductivity, one end sample was connected in series with the copper wire with known thermal conductivity and dimensions. Another end of the sample was brought into thermal contact with the heater while the other end of the copper wire was brought into thermal contact with the heat drain. Temperature differences have been measured by thermocouples between 2 points at the sample and 2 points at the copper wire separated by known distance in steady-state conditions. Then thermal conductivity was calculated from the ratio of temperature differences.

Results and Discussion

Figure 4 demonstrates examples of temperature dependencies of thermal conductivity. For the samples with Mg content below 1.3 at % an enhancement of thermal conductivity was observed with an increase in Mg content. However, thermal conductivity of the sample with 4 at. % Mg is smaller than heat conductivity of the sample with 1.3 at. %. An increase of annealing duration from 24 to 48 hours leads to thermal conductivity reduction for the samples with Mg content from 0.6 to 1.3 at. %.

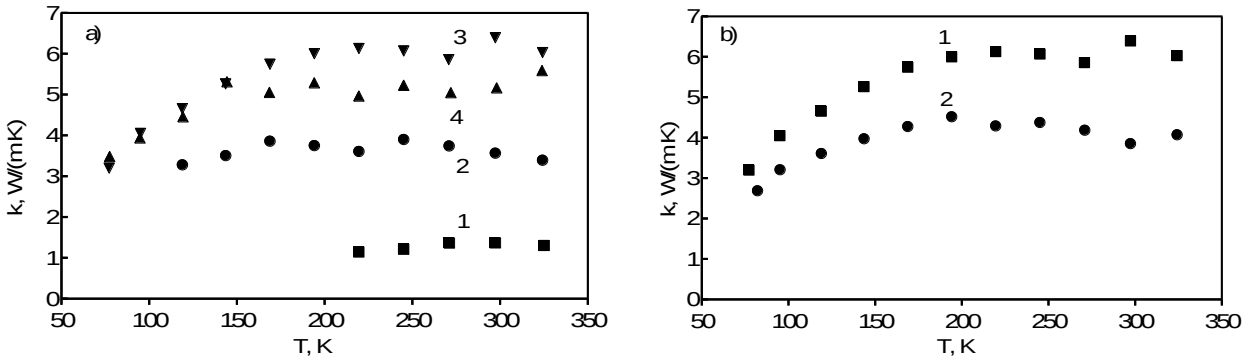

Figure 4. Temperature dependencies of thermal conductivity: a) for samples annealed 24 hours with different Mg content: 1 – 0.3 at. %; 2 – 0.6 at. %; 3 – 1.3 at. %; 4 – 4 at. %; b) for samples with 1.3 at. % Mg content with different duration of annealing: 1- 24 hours; 2 – 48 hours

Temperature dependencies of conductivity of investigated samples are shown in Figure 5.

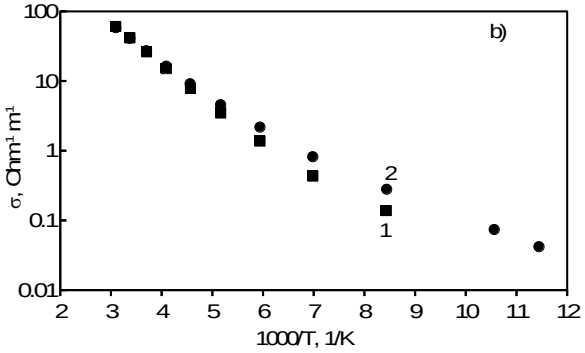

Figure 5. Temperature dependencies of conductivity: a) for samples annealed 24 hours with different Mg content: 1 – 0.3 at. %; 2 – 0.6 at. %; 3 – 1.3 at. %; b) for samples with 0.6 at. % Mg content with different duration of annealing: 1- 24 hours; 2 – 48 hours

Several orders of magnitude conductivity enhancement have been observed for an increase of Mg content from 0.3 ar % to 4 at. %. Activation energy of conductivity decreases several times with the same increase of magnesium content. Enhancement of annealing duration from 24 hours to 48 hours leads to a small decrease of conductivity at room temperature and higher temperatures. At lower temperatures conductivity of the samples annealed at 48 hours is larger than the conductivity of the samples annealed at 24 hours.

Enhancement of conductivity on Mg content could be one origin of observed variation of the density and microstructure of the polycrystalline ceramic copper chromite (I). Enhancement of conductivity with Mg content could lead to an enhancement of the mobility of ions. This, in turn, could lead to a reduction of the fraction of empty space and improvement of the connection between crystallites.

Enhancement of thermal conductivity with an increase of Mg content from 0.3 to 1.3 at. % can be explained by improvement of connection between crystallites. Smaller thermal conductivity of the sample with 4 at. % Mg content compared to thermal conductivity of the sample with 1.3 at. % Mg can be explained by formation of $MgCr_2O_4$ crystallites operating as effective scatterers of phonons. This suggests the stronger effect of phonon scattering by these crystallites compared to the improvement of connection between crystallites. Reduction of thermal conductivity with an increase in synthesis duration is in contradiction with an ob-

served improvement of connection between crystallites. This points to the formation of effective phonon scatterers, These scatterers could be small crystallites of copper and chromium oxides formed due to deviation of stoichiometry in the mixture of precursors. Other possible phonon scatters are oxygen vacancies formed during annealing in oxygen deficit atmosphere.

The most probable mechanism of electron transport in polycrystalline copper chromite (I) is the thermally activated hopping of holes [13]. The value of hopping conductivity is essentially determined by energy dependence of the density of localized states and the value of the density of states near Fermi energy. Density of localized states depends in particular on the energy disorder originating from randomly distributed charged defects and their complexes. Variation of conductivity during annealing from 24 hours to 48 hours can be explained by formation of oxygen vacancies. Obtained results also show relatively small contribution of contacts between crystallites to resistivity of material. Relatively small variation of conductivity with an increase of annealing time together with noticeable reduction of thermal conductivity can be useful for improvement of thermoelectric properties of polycrystalline copper chromite (I) and other materials synthesized in similar way.

Conclusions

The effect of synthesis duration thermal conductivity and conductivity have been studied for Mg-doped polycrystalline copper chromite (I). Electron microscopy shows that longer synthesis leads to the improvement of connection between crystallites and increase of the density of material. Effect of synthesis duration from 24 to 48 hours on conductivity is relatively small. This shows that conductivity is not essentially limited by contacts between crystallites. Significant reduction of thermal conductivity has been observed for enhancement of synthesis duration from 24 to 48 hours for material with Mg content from 0.6 to 4 at. %. This points to the formation of effective phonon scatter and can be used for improvement of thermoelectric properties of Mg-doped copper chromite (I) and polycrystalline materials synthesized in similar way.

Acknowledgments

The authors are grateful to I.O. Angelovskii for his essential contribution to the synthesis and characterization of investigated samples.

The work was supported by the Ministry of Education and Science of the Russian Federation, grant № 075-15-2021-1353.

References

1 Hemmida, M., Krug von Nidda, H.-A., & Loidl, A. (2011). Traces of Z_2-Vortices in $CuCrO_2$, $AgCrO_2$, and $PdCrO_2$. *Journal of Physical Society of Japan*, 80, 053707. https://doi.org/10.1143/JPSJ.80.053707

2 Hemmida, M., Krug von Nidda, H.-A., Büttgen, M., Loidl, A., Alexander, L.K., Nath, R., Mahajan, A.V., Berger, R.F., Cava, R.J., Singh Yogesh, & Johnston, D.C. (2009). Vortex dynamics and frustration in two-dimensional triangular chromium lattices. *Physical Review*, 80, 054406. https://doi.org/10.1103/PhysRevB.80.054406

3 Zhang, K.H.L., Xi, K., Blamire, M.G., & Edgell, R.G. (2016). P-type transparent conducting oxides. *Journal of Physics Condensed Matter*, 28, 383002. https://doi.org/0.1088/0953-8984/28/38/383002

4 Xiong, D., Xu, Z., Zeng, X., Zhang, W., Chen, W., Xu, X., Wang, M., & Cheng, Y.-B. (2012). Hydrothermal synthesis of ultrasmall CuCrO2 nanocrystal alternatives to NiO nanoparticles in efficient p-type dye-sensitized solar cells. *Journal of Material Chemistry*, 22, 24760. https://doi.org/10.1039/C2JM35101C

5 Xiong, D., Zhang, W., Zeng, X., Xu, Z., Chen, W., Cui, J., Wang, M., Sun, L., & Cheng, Y.-B. (2013). Enhanced performance of p-type dye-sensitized solar cells based on ultrasmall Mg-doped $CuCrO_2$ nanocrystals. *ChemSusChem*, 6, 1432–1437. https://doi.org/10.1002/cssc.201300265

6 Batzill, M., & Diebold, U. (2005). The surface and materials science of tin oxide. *Progress in Surface Science*, 79, 47–154. https://doi.org/10.1016/J.PROGSURF.2005.09.002

7 Özgür, Ü., Alivov, Ya.I., Liu, C., Teke, A., Reshchikov, M.A., Doğan, S., Avrutin, V., Cho, S.-J., & Morkoç, H. (2005). A Comprehensive Review of ZnO Materials and Devices. Journal of Applied Physics, 98(4), 041301. https://doi.org/10.1063/1.1992666

8 Sinnarasa, I., Thimont, Y., Presmanes, L., Barnabé, A., & Tailhades, Ph. (2017). Thermoelectric and Transport Properties of Delafossite $CuCrO_2$:Mg Thin Films Prepared by RF Magnetron Sputtering. *Nanomaterials*, 7, 157, https://doi.org/10.3390/nano7070157

9 Moreira M., Afonso, J., Crepelliere, J., Lenoble, D., & Lunca-Popa, P. (2022). A review on the p-type transparent Cu–Cr–O delafossite materials. *Journal of Materials Science*, 57, 3114–3142. https://doi.org/10.1007/s10853-021-06815-z

10 Guilmeau, E., Poienar, M., Kremer, S., Marinel, S., Hébert, S., Frésard, R., & Maignan, A. (2011). Mg substitution in $CuCrO_2$ delafossite compounds. *Solid State Communications*, 151, 1798–1801. https://doi.org/10.1016/j.ssc.2011.08.023

11 Okuda, T., Jufuku, N., Hidaka, S., & Terada, N. (2005). Magnetic, transport, and thermoelectric properties of the delafossite oxides $CuCr_{1-x}Mg_xO_2$ (0<x<0.04). *Physical Review B.*, 72, 144403. https://doi.org/10.1103/PhysRevB.72.144403

12 Kulbachinskii, V.A., Kondratieva, D.Yu., Konstantinova, E.A., Pavlikov, A.V., Grigoriev, A.N., Mankevich, A.S., & Korsakov, I.E. (2019). Electrical conductivity, thermoelectrical properties, and EPR spectroscopy of copper chromite ceramic samples doped with magnesium. *Low Temperature Physics*, 45, 194–200. https://doi.org/10.1063/1.5086413

13 Kulbachinskii, V.A., Kytin, V.G., Duvakina, A.V., Zinoviev, D.A., Kupriyanov, E.E., Korsakov, I.E., Ovchenkov, E.A., & Kondratieva, D.Yu. (2021). Effect of magnesium doping on thermoelectric and magnetic properties of copper chromite ceramic samples. *Materials Today: Proceedings*, 44(14), 3511–3515. https://doi.org/10.1016/j.matpr.2020.09.163

В.А. Кульбачинский, В.Г. Кутин, И.Е. Корсаков,
Е.Е. Куприянов, Ж.Т. Исмаилов

Синтез ұзақтығының $CuCr_{1-x}Mg_xO_2$ поликристалындағы жылу және заряд алмасу үдерісіне әсері

Магний қосылған мыс (I) хромитінің поликристалды керамикалық үлгілері қатты фазалық синтез арқылы алынды. Синтездің фазалық құрамы мен кристалдық құрылымы рентгендік дифракциялық талдау арқылы зерттелді. Сканерлеуші электронды микроскоп арқылы үлгілердің микроқұрылымы анықталды. Жылуөткізгіштік пен электрөткізгіштік 78<T<320 К температура диапазонында өлшенді. Синтез ұзақтығының ұлғаюымен жылу өткізгіштіктің айтарлықтай төмендеуі байқалған. Бұл әсер $MgCr_2O_4$, Cr_2O_3 және CuO кристаллиттерінің аз мөлшерде түзілуімен түсіндіріледі және олар тиімді фонондық шашыратқыш ретінде әрекет жасаушы болып табылады. $MgCr_2O_4$ фазасының түзілуі Mg мөлшері 3 ат-%. жоғары үлгілердің рентгенограммалары мен СЭМ кескіндерінде байқалады. Cr_2O_3 немесе CuO фазасының аз мөлшерінің түзілуі прекурсорлар құрамының стехиометриядан ауытқуымен байланысты болуы мүмкін. Алынған нәтижелер мыс хромит негізіндегі материалдың термоэлектрлік қасиетін арттыру перспективасын ашады.

Кілт сөздер: термоэлектрлік тиімділік, мыс хромиті, синтез ұзақтығы, жылуөткізгіштің төмендеуі.

В.А. Кульбачинский, В.Г. Кутин, И.Е. Корсаков,
Е.Е. Куприянов, Ж.Т. Исмаилов

Влияние продолжительности синтеза на перенос тепла и заряда в поликристаллических $CuCr_{1-x}Mg_xO_2$

Методом твердофазного синтеза получены поликристаллические керамические образцы хромита меди (I), легированные магнием. Методом рентгеноструктурного анализа исследованы фазовый состав и кристаллическая структура синтеза. Микроструктура образцов исследована методом сканирующей электронной микроскопии. Теплопроводность и электропроводность измерялись в интервале температур 78<T<320 K. Наблюдалось значительное снижение теплопроводности с увеличением продолжительности синтеза. Этот эффект был объяснен образованием небольшого количества кристаллитов $MgCr_2O_4$ и Cr_2O_3 и CuO, действующих как эффективные рассеиватели фононов. Образование фазы $MgCr_2O_4$ наблюдается на рентгенограммах и СЭМ-изображениях образцов с содержанием Mg более 3 ат. %. Образование небольшого количества фазы Cr_2O_3 или CuO может быть связано с отклонением содержания прекурсора от стехиометрии. Полученные результаты открывают перспективу повышения термоэлектрической эффективности материала на основе хромита меди.

Ключевые слова: термоэлектрическая эффективность, хромит меди, продолжительность синтеза, снижение теплопроводности.

DOI 10.31489/2022PH3/12-17

UDC 535.215; 535.3

A.K. Mussabekova*, A.K. Tussupbekova, A.K. Aimukhanov

Buketov University, Scientific Center for Nanotechnology and nanomaterials, Karaganda, Kazakhstan
*(*E-mail: assel50193@gmail.com)*

Optical and Electrical Transport Properties of the ZnO:CdO Composite Film

In this work, zinc oxide films and composite ZnO:CdO films with cadmium oxide concentrations of 3 μl, 5 μl, 7 μl, 10 μl, and 12 μl were obtained by spin-coating on FTO. The films were annealed in the atmosphere under the same temperature conditions of 450°C. The morphology of ZnO:CdO composite films was studied by the SEM method and an electron-dispersion analysis of the concentration of the studied substance was carried out. The influence of the surface morphology of the composite film with an increase in the CdO concentration from 3 μl to 12 μl on the optical and electrotransport properties of the ZnO:CdO composite film was studied. The optical absorption spectra of composite films of zinc oxide and cadmium were measured. A Tauc plot is presented to determine the band gap of a ZnO:CdO composite film. It has been established that an increase in the CdO concentration on the ZnO surface leads to a decrease in the optical band gap. The observed decrease in the optical band gap of the film with increasing CdO is due to the small band gap of CdO. The method of impedance spectroscopy was used to study the main electrophysical characteristics, in particular, the dynamics of charge carrier transfer in nanocomposite films based on ZnO:CdO. It has been established that the CdO layer on the ZnO surface contributes to a decrease in the resistance value of the composite film R_w, an increase in the charge recombination resistance parameter R_{rec} at the interface, and an increase in the efficiency of electron injection.

Keywords: ZnO, CdO, composite, morphology, electron transport layer, absorption, structural layer, impedance spectroscopy.

Introduction

The transformation of the demand for electricity is one of the possible cases, which in the short term may take place in the case of a rapidly growing value on true energy. Among the various photovoltaic converters that currently exist, organic solar cells are of great interest among various international scientific groups. The efficiency level of organic solar cells (OSC) already exceeds 14% due to the search for new materials, the improvement of existing materials and the optimization of the active layer morphology [1–6]. The inverted structure is widely used in organic photoconverters due to its good stability and efficient phase separation [7–9]. The electron transport layer (ETL) in the inverted structure plays an important role in the performance of organic solar cells. The ETL layer can not only enhance electron extraction and reduce charge recombination, but also affect the morphology of the photoactive layer.

ETL layers based on metal oxides have attracted great attention because of their high transparency in the visible region of the spectrum, as well as their ability to change energy levels and electrical properties by doping or chemical modification [10]. Among the known metal oxides used in OSC is ZnO [11–14] and TiO_2 [15]. However, ETL layers based on ZnO and TiO_2 have relatively low charge carrier mobility and photoactivity in the visible spectral range. One way to increase the photoactivity of oxide semiconductors is to dope them with another semiconductor with a narrow band gap. This will increase the sensitivity of the composite system in the visible range of the spectrum and reduce the efficiency of charge recombination. As such a semiconductor, CdO, which is an n-type oxide semiconductor with a narrow band gap, can be used (2.16-2.6 eV). The purpose of this work is to increase the photoactivity of oxide semiconductors.

In this regard, in this work, ZnO:CdO composite structures are obtained and the optical and electrical transport properties of composite films are studied.

Experimental

To obtain composite films, initial research solutions were preliminarily prepared. For this purpose, $Zn_5(OH)_8Cl_2$ (pure 99.9%, Sigma Aldrich) powder with m=48.9 mg was dissolved in V=0.5 ml of isopropanol. After 20 min, monoethanolamine was added to the resulting solution in an amount of V=36 μl. After the solution was stirred at a temperature of T=60°C for 2 hours, and then kept for 24 hours at room temperature. To obtain CdO films, $Cd(CH_3COO)_2$ (pure 99.9%, Borun New Material Technology Co., Ltd) crystallites weighed m=34.5 mg were dissolved in V=0.5 ml of isopropanol. After the solution was kept for 20 minutes,

then V = 0.5 μl of monoethanolamine was added to the resulting mixture. After the solution was stirred at a temperature of T=80°C for 2 hours.

Preparation of substrates for composite films was carried out according to the procedure [16]. The preparation of composite films was carried out as follows: the initial solution for ZnO films (V=30 μl) was applied to FTO surfaces by centrifugation (model SPIN150i, Semiconductor Production System) at a rotation speed of 4000 rpm/min. After the films were annealed in an air atmosphere at a temperature of 200°C for 10 min, then a solution for CdO films (V = 3 μl, 5 μl, 7 μl, 10 μl, and 12 μl) was applied to the surface of the resulting film at a rotation speed of 4000 rpm/min, after which the resulting films were annealed at a temperature of 450°C for 50 min [17].

To carry out electrophysical measurements, the surface of the ZnO and ZnO:CdO films were deposited on an aluminum electrode 120 nm thick by thermal deposition on a CY-1700X-SPC-2 (Zhengzhou CY Scientific Instruments Co., Ltd) setup.

The film morphology was studied on a MIRA 3 LMU (TESCAN) scanning electron microscope. Elemental analysis (EDX analysis) of the samples was carried out using an INCAPentaFET-x3 (Oxford Instruments, England) energy dispersive analyzer. A Co (9905-17, Micro-Analysis Consultants Ltd Unit 19, Edison Road, St Ives Cambridgeshire PE27 3LF U.K) sample was used as a standard. The absorption spectra of the studied samples were measured on an AvaSpec-ULS2048CL-EVO spectrometer (Avantes). The impedance spectra were measured using a P45X potentiostat-galvanostat (Elins) in the impedance mode.

Results and Discussion

Figure 1 shows SEM images of ZnO and ZnO:CdO films. The surface of the ZnO film has a granular structure with an average grain size of d~12 nm. For the ZnO:CdO composite film, the film surface does not change.

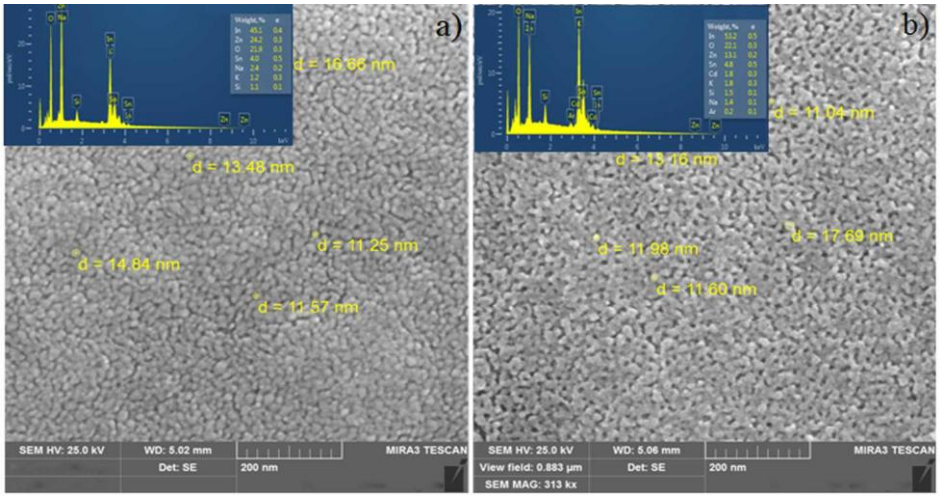

Figure 1. SEM images and EDX spectra of the films
a) morphology of the ZnO film, b) morphology of the ZnO:CdO composite film

The inset in Fig. 1 shows the EDX spectra of the studied composite films. When a CdO layer is deposited on a ZnO layer, a change in the redistribution of elements in the quantitative ratio at the surface layer is observed. According to Table 1, the initial film is enriched with zinc and oxygen; after the deposition of the CdO layer, an increase in the proportion of cadmium is observed, the amount of oxygen does not change.

Table 1

Elemental composition of ZnO and ZnO:CdO films

No.	Films	Zn, weight %	Cd, weight %	O, weight %	Zn/Cd ratio
1	ZnO	14.1	-	22.6	-
2	CdO (3 μl)	19.7	1	22.9	19.7
3	CdO (5 μl)	14.1	1.2	22.6	11.7
4	CdO (7 μl)	13.7	1.4	21.9	9.7
5	CdO (10 μl)	13.1	1.5	22.2	8.7
6	CdO (12 μl)	13.1	1.8	22.1	7.2

Figure 2 represents the absorption spectra of the films. The absorption spectrum is typical of the absorption spectrum of wide-gap semiconductors. The edge of the fundamental absorption band falls in the near ultraviolet region, which corresponds to the optical transition of the band gap of oxide semiconductors. It can be seen from the figure that an increase in the CdO concentration on the surface of the ZnO layer leads to a threefold increase in the absorption of the composite film.

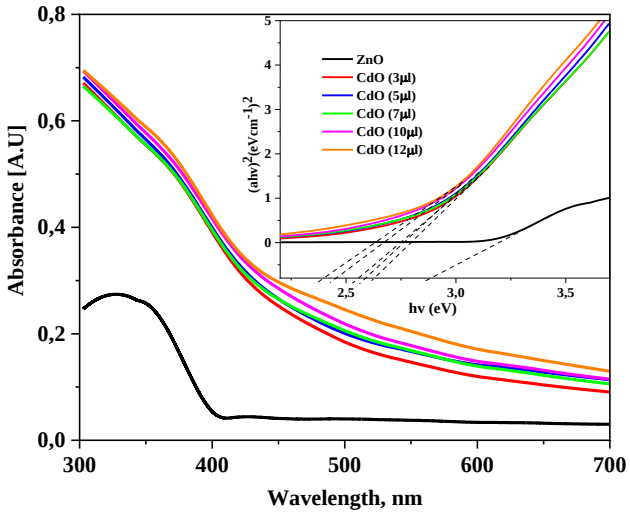

Figure 2. Absorption spectra of ZnO and ZnO:CdO films

The inset in Figure 2 shows the Tauc plot for determining the band gap (Eg) of the composite films. Table 2 lists the values of the film band gap depending on the CdO concentration. It can be seen that an increase in the CdO concentration on the surface leads to a decrease in the optical band gap (Eg) from 2.9 eV to 2.37 eV. The decrease in the optical band gap of the composite film is due to the fact that CdO is a semiconductor with a small band gap.

Table 2

Maximum absorption value of ZnO and ZnO:CdO films

No.	Films	D, (λ= 360 nm)	Optical band gap (eV)
1	ZnO	0.25	2.9
2	CdO (3 μl)	0.51	2.62
3	CdO (5 μl)	0.52	2.58
4	CdO (7 μl)	0.54	2.54
5	CdO (10 μl)	0.57	2.4
6	CdO (12 μl)	0.59	2.37

Figures 3b and 3c demonstrate the structural layer of a ZnO film and a ZnO:CdO composite, respectively. To determine the mechanisms of transport and recombination of charge carriers, the impedance spectra of composite films consisting of several layers were measured: a glass substrate coated with a transparent conducting FTO electrode (anode); ZnO:CdO layer; aluminum electrode in Figure 3c. Figure 3d shows the equivalent electrical circuit that was used to interpret the impedance spectra. The fitting of the impedance spectra was calculated using the EIS-analyzer software package.

Figure 3a designates the following parameters for obtaining the film hodograph: R_1 and R_2 – R_h and R_{ext} – resistances corresponding; where R_w is the resistance of the ZnO:CdO nanocomposite layer, R_{rec} is the charge carrier recombination resistance at the ZnO:CdO/electrode interface associated with the extraction of charge carriers from ZnO:CdO, CPE_1 is the constant phase element, which is the equivalent component of the electrical circuit that models the behavior double layer but is an imperfect capacitor.

After fitting, the values of the hodograph parameters were determined, characterizing the kinetics of transport and recombination of charge carriers based on ZnO and ZnO:CdO films. These parameters are giv-

en in Table 3, where τ_{eff} is the effective lifetime of charge carriers, k_{eff} is the recombination index characterizing the recombination rate.

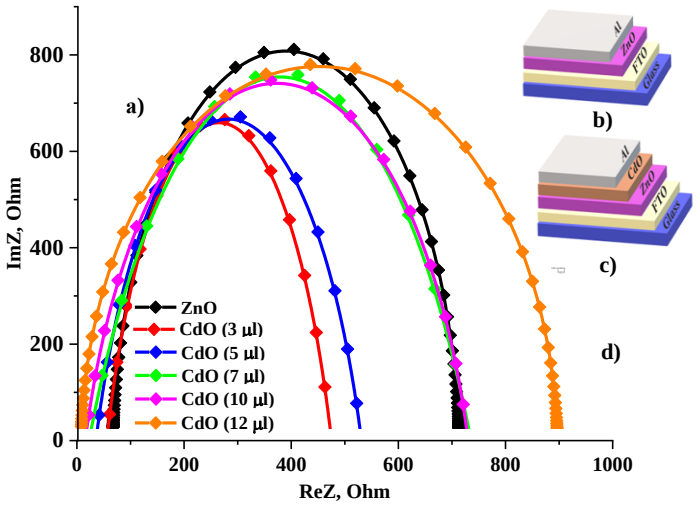

Figure 3. a) impedance spectra of ZnO and ZnO:CdO, b) structural layer of ZnO, c) structural layer of ZnO:CdO, d) equivalent electrical circuit

Table 3

The value of the electrophysical parameters of the films

No.	Films	R_w, (Ohm)	R_{rec}, (Ohm)	R_{rec}/R_w	τ_{eff}, (msec)	k_{eff}, (sec^{-1})
1	ZnO	73.6	642.4	8.7	0.13	7309
2	CdO (3 μl)	60.2	412	6.8	0.12	8176
3	CdO (5 μl)	38.9	489.4	12.9	0.11	9054
4	CdO (7 μl)	27.3	702.4	25.7	0.08	12882
5	CdO (10 μl)	21.4	706.3	33	0.08	12589
6	CdO (12 μl)	11.9	880.1	73.9	0.06	15848

Table 3 presents the obtained values of R_w, R_{rec}, etc. It can be seen that the R_w value has the highest value for the ZnO film. With an increase in the concentration of CdO in ZnO, the resistance R_w of the film decreases, which should improve the transport of injected electrons to FTO. R_{rec}, the resistance characterizing the recombination of electrons at the ZnO:CdO/electrode interface, varies depending on the CdO concentration. A slight decrease in the film recombination resistance is compensated by a decrease in the resistance R_w. The effective lifetime of charge carriers τ_{eff} decreases, which indicates an increase in the rate of charge injection onto the current-collecting electrode. Also, an increase in k_{eff} is observed, which characterizes the rate of charge recombination after a complete cycle in the circuit; this indicates a decrease in electron recombination at the ZnO:CdO/electrode interface. Thus, the conducted studies show that the CdO layer on the ZnO surface contributes to a decrease in the resistance of the composite film, an increase in the resistance of charge recombination at the interface, and an increase in the efficiency of electron injection.

Conclusions

In this work, ZnO films and a ZnO:CdO composite were obtained by spin-coating on the FTO surface. The concentration of cadmium in the solution to obtain a layer on the surface of zinc oxide ranged from 3 to 12 µl. The influence of the CdO layer on the ZnO surface on the morphology, optical and electrical properties of composite films has been studied. Analysis of SEM images showed a change in the redistribution of elements in a quantitative ratio with the surface layer of the composite film. According to the absorption spectrum of ZnO:CdO composite films, an increase in the CdO concentration leads to an increase in the optical absorption of the composite film and a decrease in the optical band gap. The study of impedance spectroscopy showed that the CdO layer on the ZnO surface contributes to a decrease in the resistance of the

composite film, an increase in the resistance of charge recombination at the interface, and an increase in the efficiency of electron injection.

References

1 Che, X., Li, Y., Qu, Y., & Forrest, S.R. (2018). High fabrication yield organic tandem photovoltaics combining vacuum- and solution-processed subcells with 15% efficiency, *Nature Energy*, 3, 422–427. https://doi.org/10.1038/s41560-018-0134-z1

2 Zhang, S., Qin, Y., Zhu, J., & Hou, J. (2018). Over 14% Efficiency in Polymer Solar Cells Enabled by a Chlorinated Polymer Donor, *Advanced Materials*, 30, 1800868. https://doi.org/10.1002/adma.201800868

3 Li, S., Ye, L., Zhao, W., Yan, H., Yang, B., Liu, D., Li, W., Ade, H., & Hou, J. (2018). A Wide Band Gap Polymer with a Deep Highest Occupied Molecular Orbital Level Enables 14.2% Efficiency in Polymer Solar Cells, *Journal of the American Chemical Society*, 140(23), 7159–7167. https://doi.org/10.1021/jacs.8b02695

4 Fei, Z., Eisner, F. D., Jiao, X., Azzouzi, M., Röhr, J. A., Han, Y., Shahid, M., Chesman, A. S. R., Easton, C. D., McNeill, C. R., Anthopoulos, T. D., Nelson, J., & Heeney, M. (2018). An Alkylated Indacenodithieno [3,2-b] thiophene-Based Nonfullerene Acceptor with High Crystallinity Exhibiting Single Junction Solar Cell Efficiencies Greater than 13% with Low Voltage Losses, *Advanced Materials*, 30, 1705209. https://doi.org/10.1002/adma.201705209

5 Sun, C., Pan, F., Bin, H., Zhang, J., Xue, L., Qiu, B., Wei, Z., Zhang, Z. G., & Li, Y. (2018). A low cost and high performance polymer donor material for polymer solar cells, *Nature Communications*, 9, 743. https://doi.org/10.1038/s41467-018-03207-x

6 Lin, Y., Zhao, F., Prasad, S. K. K., Chen, J. D., Cai, W., Zhang, Q., Chen, K., Wu, Y., Ma, W., Gao, F., Tang, J. X., Wang, C., You, W., Hodgkiss, J. M., & Zhan, X. (2018). Balanced Partnership between Donor and Acceptor Components in Nonfullerene Organic Solar Cells with >12% Efficiency, *Advanced Materials*, 30, 1706363. https://doi.org/10.1002/adma.201706363

7 Li, G., Chu, C. W., Shrotriya, V., Huang, J., & Yang, Y. (2006). Efficient inverted polymer solar cells, *Applied Physics Letters*, 88, 253503. https://doi.org/10.1063/1.2212270

8 Chen, L. M., Hong, Z., Li, G., & Yang, Y. (2009). Recent Progress in Polymer Solar Cells: Manipulation of Polymer Fullerene Morphology and the Formation of Efficient Inverted Polymer Solar Cells, *Advanced Materials*, 21, 1434-1449. https://doi.org/10.1002/adma.200802854

9 Huang, W., Gann, E., Cheng, Y. B., & McNeill, C. R. (2015). In-Depth Understanding of the Morphology–Performance Relationship in Polymer Solar Cells, *ACS Applied Materials & Interfaces*, 7 (25), 14026-14034. https://doi.org/10.1021/acsami.5b03095

10 Yang, G., Tao, H., Qin, P., Ke, W., & Fang, G. (2016). Recent progress in electron transport layers for efficient perovskite solar cells, *Journal of Materials Chemistry*, 4, 3970-3990. https://doi.org/10.1039/C5TA09011C

11 Sun, Y., Seo, J. H., Takacs, C. J., Seifter, J., & Heeger, A. (2011). Inverted Polymer Solar Cells Integrated with a Low-Temperature-Annealed Sol-Gel-Derived ZnO Film as an Electron Transport Layer, *Advanced Materials*, 23, 1679-1683. https://doi.org/10.1002/adma.201004301

12 Liang, Z., Zhang, Q., Jiang, L., & Cao, G. (2015). ZnO cathode buffer layers for inverted polymer solar cells, *Energy & Environmental Science*, 8, 3442-3476. https://doi.org/10.1039/C5EE02510A

13 Liu, X., Li, X., Li, Y., Song, C., Zhu, L., Zhang, W., Wang, H. Q., & Fang, J. (2016). High-Performance Polymer Solar Cells with PCE of 10.42% via Al-Doped ZnO Cathode Interlayer, *Advanced Materials*, 28, 7405-7412. https://doi.org/10.1002/adma.201601814

14 Chen, J. D., Li, Y. Q., Zhu, J., Zhang, Q., Xu, R. P., Li, C., Yu, X., Zhang, J., Huang, Sh., Zhan, X., You, W., & Tang, J. X. (2018). Polymer Solar Cells with 90% External Quantum Efficiency Featuring an Ideal Light- and Charge-Manipulation Layer, *Advanced Materials*, 30, 1706083. https://doi.org/10.1002/adma.201706083

15 Park, S. H., Roy, A., Beaupré, S., Cho, S., Coates, N., Moon, J. S., Moses, D., Leclerc, M., Lee, K., & Heeger, A. J. (2020). Bulk heterojunction solar cells with internal quantum efficiency approaching 100%, *Nature Photonics*, 3, 297-303. https://doi.org/10.1038/nphoton.2009.69

16 Aimukhanov, A. K., Zeinidenov, A. K., & Zavgorodniy, A.V. (2020). The influence of system dimension on the generation and charge carrier transfer in copper phthalocyanine nanostructures, *Journal of Photonics for Energy*, 1(10), 015501. https://doi.org/10.1117/1.JPE.10.015501

Ә.Қ. Мұсабекова, А.К. Тусупбекова, А.К. Аймуханов

ZnO:CdO композитті қабықшаның оптикалық және электротасымалдау қасиеттері

Мақалада мырыш оксидінің қабықшалары мен кадмий оксидінің концентрациясы 3 мл, 5 мл, 7 мл, 10 мл және 12 мл композиттік ZnO:CdO қабықшалары FTO-да spin-coating әдісі арқылы алынды. Қабықшалар атмосферада бірдей температура жағдайында 450°C қыздырылды. SEM әдісімен ZnO:CdO композиттік қабықшаларының морфологиясы зерттеліп, зерттелетін заттың концентрациясына электронды-дисперстік талдау жүргізілді. CdO концентрациясы 3 мл-ден 12 мл-ге дейін артқан кезде ZnO:CdO композиттік қабықшаларында оптикалық және электротасымалдау қасиеттерінің композиттік қабықшасының беткі морфологиясына әсері зерттелді. Мырыш және кадмий оксидінің композит қабықшаларының оптикалық жұтылу спектрлері өлшенді. ZnO:CdO композиттік қабықшасының тыйым салынған аймағын анықтау үшін Тауқ графигі (Tauc plot) көрсетілген. ZnO бетіндегі CdO концентрациясының артуы тыйым салынған аймақтың оптикалық

енінің төмендеуіне әкелетіні анықталды. CdO артқан сайын қабықшаларда бақыланып отырған тыйым салынған аймақтық оптикалық енінің төмендеуі CdO-ның шағын тыйым салынған аймағымен байланысты. Импеданс спектроскопия әдісі арқылы негізгі электрофизикалық сипаттамаларды, атап айтқанда ZnO:CdO негізіндегі нанокомпозиттік қабықшалардағы заряд тасушының динамикасын зерттеу үшін қолданылды. ZnO бетіндегі CdO қабаты композиттік қабықшаның Rw кедергісінің төмендеуіне, бөлу шекарасындағы зарядтардың Rw рекомбинация кедергісінің жоғарылауына және электронды инжекция тиімділігінің артуына ықпал етеді.

Кілт сөздер: ZnO, CdO, композит, морфология, электрондық тасымалдау қабаты, жұтылу, құрылымдық қабат, импеданс спектроскопия.

А.К. Мусабекова, А.К. Тусупбекова, А.К. Аймуханов

Оптические и электротранспортные свойства композитной пленки ZnO:CdO

В статье методом *spin-coating* на FTO были получены пленки оксида цинка и композитные пленки ZnO:CdO с концентрацией оксида кадмия 3 мл, 5, 7, 10 и 12 мл. Пленки отжигались на атмосфере при одинаковых температурных условиях 450°C. Методом СЭМ исследована морфология композитных пленок ZnO:CdO, и проведен электронно-дисперсионный анализ концентрации исследуемого вещества. Изучено влияние морфологии поверхности композитной пленки при увеличении концентрации CdO с 3 мл до 12 мл на оптические и электротранспортные свойства композитной пленки ZnO:CdO. Проведены измерения спектров оптического поглощения композитных пленок оксида цинка и кадмия. Приведен график Таука (*Tauc plot*) для определения ширины запрещенной зоны композитной пленки ZnO:CdO. Установлено, что увеличение концентрации CdO на поверхности ZnO приводит к уменьшению оптической ширины запрещенной зоны. Наблюдаемое уменьшение оптической ширины запрещенной зоны пленки с увеличением CdO связано с малой запрещенной зоной CdO. Методом импедансной спектроскопии исследованы основные электрофизические характеристики, в частности, динамика переноса носителей заряда в нанокомпозитных пленках на основе ZnO:CdO. Доказано, что слой CdO на поверхности ZnO способствует уменьшению значения сопротивления композитной пленки Rw, увеличению параметра сопротивления рекомбинации зарядов *Rrec* на границе раздела и возрастанию эффективности инжекции электронов.

Ключевые слова: ZnO, CdO, композит, морфология, электронный транспортный слой, поглощение, структурный слой, импеданс-спектроскопия.

DOI 10.31489/2022PH3/18-24

UDC 621.793

M. Maulet[1*], Zh.B. Sagdoldina[1], B.K. Rakhadilov[1,2],
D.N. Kakimzhanov[1], N.M. Magazov[1]

[1]*S. Amanzholov East Kazakhstan University, Ust-Kamenogorsk, Kazakhstan,*
[2]*PlasmaScience LLP, Ust-Kamenogorsk, Kazakhstan*
(E-mail:maulet_meruert@mail.ru)

Influence of the content of aluminum on the structure of gradient detonation coatings based on NiCr-Al

This paper studies the effects of aluminium content in the composite powder on the structure of detonation gradient coatings based on NiCr-Al. Gradient coatings were obtained by detonation spraying with a gradual stepwise decrease in the barrel filling volume with an acetylene-oxygen gas mixture from 50% to 25%. The elemental and phase composition, microstructure and surface roughness of coatings based on NiCr-Al with different aluminium content of 15%, 20%, and 30% were investigated. By varying the aluminium content in the powder composition, coatings with a gradient structure were obtained. The study results showed that the phase composition of the gradient coating strongly depends on the mass fraction of Al. In the case of an aluminium content of 30% in the composition of the composite powder, the formation of aluminium oxide was detected. It is established that under the same detonation deposition modes, the formation of the gradient structure of coatings will strongly depend on the aluminium content in the NiCr-Al composition. The study results showed that the optimal composition of the powder is NiCr – 80% and Al – 20% to obtain NiCr-Al coatings with a gradient structure.

Keywords: NiCr-Al coatings, gradient coatings, MCrAlX coating, detonation spraying, thermal spraying, structure, SEM.

Introduction

Currently, the components of power plants are under the influence of high temperatures suffer from corrosion, oxidation, hot corrosion, etc. This is because the heat-resistant superalloys from which the components are made cannot provide simultaneous heat resistance and erosion-corrosion resistance. Therefore, protective coatings with heat resistance and wear resistance are obtained on the surface of superalloys. Among the heat-resistant protective coatings, the most common is obtaining coatings in the system MCrAlX (M = Ni, Co or NiCo; X = Y, Ce, Si, Ta) [1]. This is because the coating is heat-resistant when M and Cr provide wear and heat resistance, and Al resists oxidation of the coating, forming Al_2O_3 on the coating surface. Elements such as Y increase the adhesion of the coatings. However, the coatings of this system still require further improvement. Many Al and Cr elements in the coating composition lead to cracking of the coating. A small amount of Al causes the insufficient formation of an Al_2O_3 film on the coating surface, which prevents oxidation. Therefore, more research is being conducted to improve the exploitation properties and extend the service life of the MCrAlX coating.

In recent years, research on improving the corrosion resistance of MCrAlY coatings has mainly focused on modifying MCrAlX coatings using reactive elements by laser treatment and the production of multilayer and gradient coatings. Reactive elements or their oxides can increase the resistance of MCrAlX coatings to high-temperature corrosion and oxidation. However, there are conflicting opinions about the effect of the inclusion of reactive element oxide in the oxidising properties of MCrAlY coatings [2]. Therefore, more attention has recently been paid to multilayer and gradient coatings based on MCrAlY. The structure and chemical composition of multilayer/functional gradient materials are gradually changing to improve their properties (for example, mechanical, thermal, physical, etc.) [3–5]. Functionally graded coatings have recently been developed and successfully applied to work at high temperatures and difficult thermal conditions [4, 6, 7].

Typically, MCrAlX coatings are obtained using the following methods: electron beam physical vapour deposition (EB-PVD), thermal spraying methods [1,8]. After application, both EB-PVD and thermal spraying coatings have a relatively thin microstructure. However, a high level of Al is oxidised during thermal spraying, and, after spraying, Al_2O_3 at the coating boundaries is formed, which protects from the

oxidation process. Recently, modern heat-resistant gradient coatings have been obtained by thermal spraying. According to studies by Kim et al. [9] and Choi et al. [10], functional gradient heat-resistant coatings were obtained using detonation and plasma spraying methods. They were sprayed in the form of multilayer gradient coatings in thickness. The structural characteristics of the obtained coatings based on the formation of microcracks during high-temperature operation are investigated and, accordingly, compared with homogeneous coatings. In another study, a gradient coating of MCrAlX was obtained based on three main layers: an outer layer, an Al-rich, Cr-rich middle layer, and a standard MCrAlX layer [11]. The functional gradient coating MCrAlY to hot corrosion has significantly increased compared to the homogeneous coating MCrAlY.

Our previous work [12] proposed a method for obtaining a gradient coating based on NiCr-Al by detonation spraying. The peculiarity of this method is to obtain the necessary gradient structure by changing the barrel filling volume with gas during the coating process, by managing the distribution of NiCr-Al composite powder from the substrate to the coating surface. That is, forming heat-resistant and wear-resistant in most particles Ni and Cr on the surface of substrate, and Al gradually increasing on the coating surface from the substrate to the surface, forming a large number of Al on the surface. This makes it possible to form a sufficient amount of Al_2O_3 on the coating surface. In addition, our work [13] compared the structure and properties with homogeneous and gradient coatings based on NiCr-Al obtained by detonation spraying.

The main purpose of this work is to study the effect of the mass proportion of alumina composite powder on the structure and properties of gradient coatings based on NiCr-Al.

Experimental

Heat-resistant steel 12Kh1MF was chosen as the substrate. The chemical composition of steel: 0,15% C; 0,37% Si; 0,7% Mn, 0,3% P, 1,2% Cr; 0,35% Mo, 0,3% V, 0,2% Cu. To obtain coatings, steel was cut with a diameter of 50 mm and a thickness of 3 mm and ground with P100 to P1000 SiC grinding paper. Before obtaining coating, the sample's surface was sandblasted. NiCr and Al powders (99.99%) were mixed in various ratios (Table 1) in a PULVERISETTE 23 planetary ball with a frequency of 30 Hz for 2 hours, and composite powders were prepared.

The coating was obtained on the CCDS 2000 detonation unit [14-15]. Oxygen-acetylene mixtures of O_2/C_2H_2 = 1.856 were used as explosive gas and nitrogen as a carrier gas. Gradient coatings were obtained by reducing barrel filling volume with gas from 50% to 25%. Our previous work explained the method of obtaining a gradient coating in detail [12]. Table 1 demonstrates the technological parameters for obtaining coatings.

Table 1

Technological parameters for obtaining NiCr–Al gradient coatings

№	Composition, Powder, wt %	O_2/C_2H_2	Barrel Filling Volume,%	Spray Distance, mm	Number of Shots
1	NiCr70Al30	1,856	50-25	250	40
2	NiCr80Al20	1,856	50-25	250	40
3	NiCr85Al15	1,856	50-25	250	40

We determined the phase composition of the sprayed coatings via the X-ray diffraction technique (XRD) using an X'PertPRO diffractometer with Cu-Kα radiation (λ = 2.2897 Å) at a voltage of 40 kV and a current of 30 mA. The diffractograms were decoded using the HighScore program with measurements performed in the range of 2Ɵ equal to 200–900 with 0.02 step size and 0.5 s/step counting time. The surface roughness of the coatings was estimated according to GOST 2789-73 using the Ra parameter by profilometer model 130. We photographed the surface of the coatings at 5× optical magnification using a metallographic microscope (Altami MET 5S model). We employed scanning electron microscopy (SEM) using backscattered electrons (BSE) at accelerated voltages of a JSM-6390LV (Jeol, Tokyo, Japan) scanning electron microscope to study the morphology of sample cross-section [16].

Results and Discussion

Gradient coatings of NiCr-Al of the various mass proportion of aluminium have been successfully obtained using the CCDS2000 single-dossier detonation unit. The cross-sectional view of the obtained coatings and coating surface roughness is shown in Figure 1. The cross-sectional surface was pickled to see

the microstructure of the coating and substrate. According to the microstructure, it can be seen the ferrite-pearlite structure of the substrate and the wave-like obtained coating on the substrate. The thickness of the obtained coatings is in the range of 70–116μm. The thickest coating (116μm) was obtained in the mass proportion of Al 15%. And the coating with the smallest thickness (70 μm) Al was obtained with a mass proportion of 30%. Probably, during detonation spraying, an important content of a soft element in the composition of the powder, in our case, Al, is melted and fixed on the surface of the processed material. Particles of relatively solid elements are driven into the plastic matrix [17, 18]. The surface roughness of the obtained coating was represented in the average surface roughness according to the parameter Ra. The values of the average roughness of the coating surfaces are similar. The highest value was obtained in the Al mass proportion of 30% (Ra=6.06 μm).

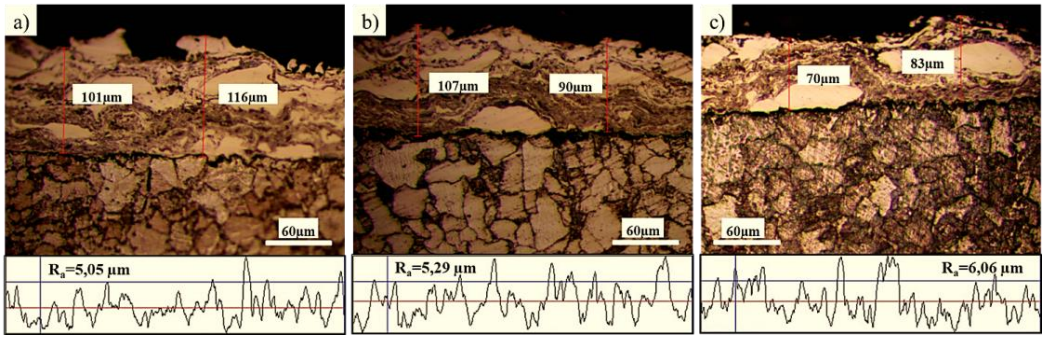

Figure 1. The microstructure results of the cross-section of the gradient coating NiCr-Al and the average surface roughness obtained with a different content of Al: a) NiCr85Al15, b) NiCr80Al20, c) NiCr70Al30

The X-ray diffraction phase analysis of the obtained gradient coatings NiCr-Al at a different mass proportion of aluminium (15%, 20%, 30%) is shown in Figure 2. Figure 2 shows that changing the mass proportion of Al leads to phase changes in the gradient NiCr-Al coatings. When the mass proportion of Al in the coating was 15% and 20%, the coating consisted of $CrNi_3$ and Al phases, and with a mass fraction of Al of 30%, it could be seen that a new phase of γ-Al_2O_3 appeared.

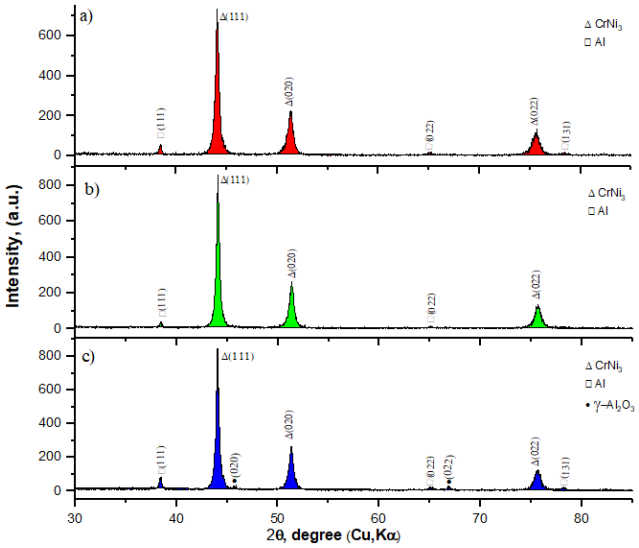

Figure 2. The result of the analysis of the X-ray phase structure of the NiCr-Al gradient coatings at various Al mass proportions: a) NiCr85Al15, b) NiCr80Al20, c) NiCr70Al30

Figure 3 represents an SEM image of the cross-section of the NiCr-Al gradient coating with a mass proportion of Al 15%, maps of the distribution of elements, EDS analysis and the results of the distribution of elements. The SEM figure of the coating cross-section (a) shows that aluminium spreads from the substrate to the coating surface, and it can be seen an increase in the amount of aluminium on the coating surface. Also, it can be sighted in the mapping of aluminium by element distribution maps (b, c) and the

results of element distribution (e). However, the aluminium mapping (c) shows the uneven distribution of aluminium. Also noticed is an insufficient distribution of aluminium on the coating surface. Based on these results, the mass proportion of aluminium in 15% may not be enough to form the required amount of aluminium on the coating surface.

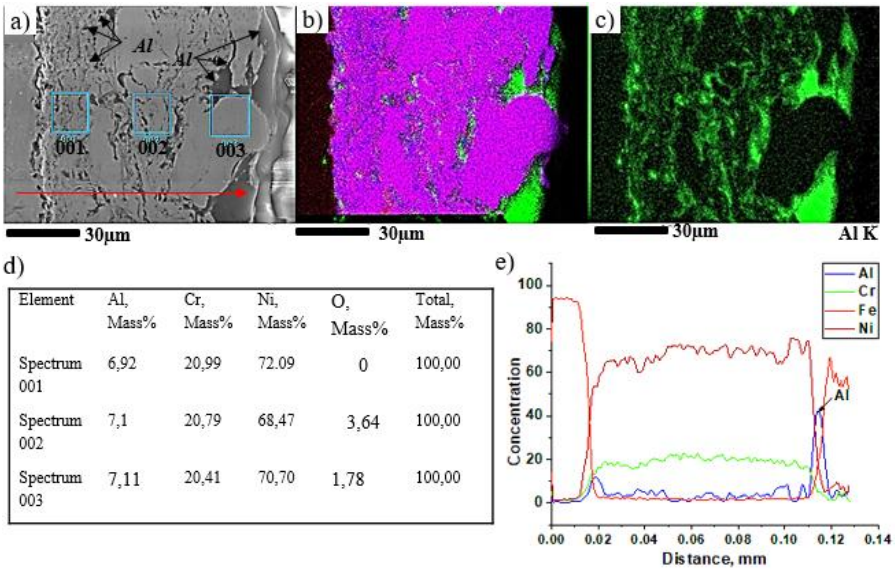

Element	Al, Mass%	Cr, Mass%	Ni, Mass%	O, Mass%	Total, Mass%
Spectrum 001	6,92	20,99	72.09	0	100,00
Spectrum 002	7,1	20,79	68,47	3,64	100,00
Spectrum 003	7,11	20,41	70,70	1,78	100,00

Figure 3. Gradient coating NiCr-Al with a mass fraction of NiCr85Al15: cross-sectional picture of the SEM (a), maps of the distribution of elements (b,c), the results of the analysis of EDS (d) and the distribution of elements (e)

Figure 4 illustrates the SEM image, element distribution maps, EDS analysis and element distribution results of a cross-section of the NiCr-Al gradient coating obtained at a mass proportion of Al 20%. The SEM image of the cross-section of the coating (a) shows that aluminium is gradually distributed from the substrate to the coating surface, and a large amount of aluminium is uniformly formed on the coating surface. The element distribution map (b) and the aluminium distribution map (c) also see aluminium, which increases from the substrate to the coating. The analysis of EDS (d) and the distribution of elements (e) results also confirm this. Based on these results, it can be seen that in the NiCr-Al gradient coating obtained with a 20% mass proportion of aluminium, the elements were successfully distributed over the structure. The Ni and Cr elements formed on the substrate surface ensure the wear resistance of the coating, aluminium formed in large quantities on the coating surface can form a sufficient amount of Al_2O_3 film, which resists oxidation.

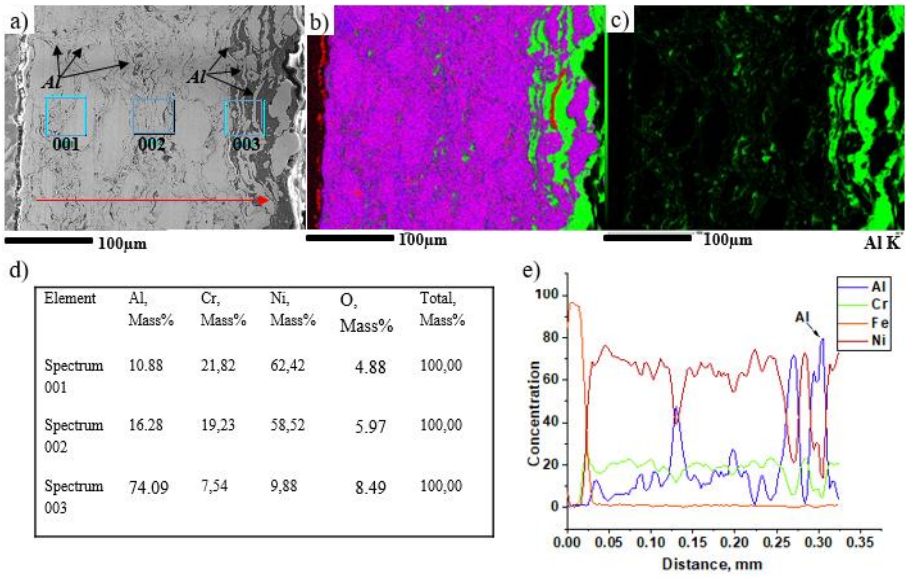

Element	Al, Mass%	Cr, Mass%	Ni, Mass%	O, Mass%	Total, Mass%
Spectrum 001	10.88	21,82	62,42	4.88	100,00
Spectrum 002	16.28	19,23	58,52	5.97	100,00
Spectrum 003	74.09	7,54	9,88	8.49	100,00

Figure 4. Gradient coating NiCr-Al with a mass fraction of NiCr80Al20: cross-sectional picture of the SEM (a), maps of the distribution of elements (b,c), the results of the analysis of EDS (d) and the distribution of elements (e)

Figure 5 shows an SEM image of a cross-section of the NiCr-Al gradient coating with a mass proportion of Al30%, maps of the distribution of elements, EDS analysis and the results of the distribution of elements. The SEM figure of the cross-section of the coating (a) shows that aluminium in large quantities and uneven spreads from the substrate to the coating surface. It can be seen in the mapping of aluminium by element distribution maps (c) and in the results of element distribution (e).

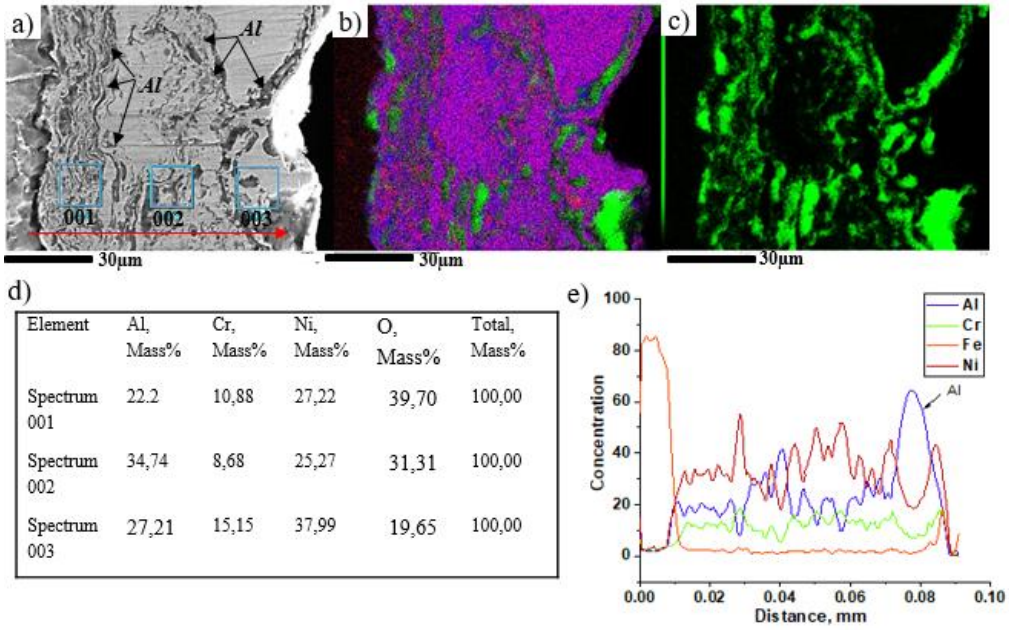

Element	Al, Mass%	Cr, Mass%	Ni, Mass%	O, Mass%	Total, Mass%
Spectrum 001	22.2	10,88	27,22	39,70	100,00
Spectrum 002	34,74	8,68	25,27	31,31	100,00
Spectrum 003	27,21	15,15	37,99	19,65	100,00

Figure 5. Gradient coating NiCr-Al with a mass fraction of NiCr70Al30: cross-sectional picture of the SEM (a), maps of the distribution of elements (b,c), the results of the analysis of EDS (d) and the distribution of elements (e)

Conclusions

Analyzing the experimental results obtained in the work, we can make the following conclusions:

– NiCr-Al coatings with a different aluminium content of 15%, 20%, and 30% were obtained by detonation spraying. The process of forming the coating structure depending on the composition of the powder was investigated. The technological mode of detonation spraying was chosen to obtain a gradient structure by gradually varying the barrel filling volume with an acetylene-oxygen gas mixture from 50% to 25% during the NiCr-Al coating process. The obtained results showed that the composite composition of NiCr – 80% and Al- 20% powder is optimal for the formation of a gradient structure of coatings with a high Al content in the surface layers of coatings;

– It was found that at 30% Al content in the coatings, aluminium oxides γ-Al_2O_3 are formed. The study results of the elemental composition of coatings by EDS analysis showed a high oxygen content in the composition of coatings obtained with the composite composition NiCr70Al30 and are consistent with the results of X-ray phase analysis.

– The study of the characteristics of coatings showed the dependence of the thickness of coatings on the composition of the composite powder. With NiCr70Al30, coatings are formed with a relatively minor thickness than NiCr85Al15 and NiCr80Al20. Probably, during detonation spraying, an important content of a soft element in the composition of the powder, in our case, Al, is melted and fixed on the surface of the processed material. Particles of relatively solid elements are driven into the plastic matrix. The study results of the microstructure of the cross-section of NiCr70Al30 coatings confirm this assumption.

Acknowledgements

This research was funded by the Science Committee of the Ministry of Education and Science of the Republic of Kazakhstan (Grant No. AP08857579).

References

1 Darolia, R. (2013). Thermal barrier coatings technology: critical review, progress update, remaining challenges and prospects. *International Materials Reviews*, 58(6), 315–348.

2 Shuting, Z., Kaiping, D., Xianjing, R., & Ji, S. (2017). Effect of Si on hot corrosion resistance of CoCrAlY coating. *Rare Metal Materials and Engineering*, 46(10), 2807-2811.

3 Bolelli, G., Cannillo, V., Lusvarghi, L., Rosa, R., Valarezo, A., Choi, W.B., Dey, R., Bolelli, G., Weyant, C., & Sampath, S. (2012). Functionally graded WC-Co/NiAl HVOF coatings for damage tolerance, wear and corrosion protection. *Surface Coatings Technology*, 206(8), 2585–2601.

4 Naebe, M., & Shirvanimoghaddam, K. (2016). Functionally graded materials: a review of fabrication and properties. *Applied Materials Today*, 5, 223–245.

5 Song, Y., Murakami, H., & Zhou, C. (2011). Cyclic-oxidation behavior of multilayered Pt/Pu modified aluminide coating. *Journal of Materials Science & Technology*, 27(3), 280–288.

6 Lee, W.Y., Stinton, D.P., Berndt, C.C., Erdogan, F., Lee, Y.D., & Mutasim, Z. (1996). Concept of functionally graded materials for advanced thermal barrier coating applications. *Journal of the American Ceramic Society*, 79(12), 3003–3012.

7 Movchan, B.A., & Yakovchuk, K.Y. (2012). Graded thermal barrier coatings, deposited by EB-PVD. *Surface Coatings Technology*, 188, 85–92.

8 Meghwal, A., Anupam, A., Murty, B.S., Berndt, C.C., Kottada, R.S., & Ang, A.S.M. (2020). Thermal spray high-entropy alloy coatings: a review. *Journal of Thermal Technology*, 29(5), 857–893.

9 Kim, J.H., Kim, M.C., & Park, C.G. (2003). Evaluation of functionally graded thermal barrier coatings fabricated by detonation gun spray technique. *Surface Coatings Technology*, 168(2), 275–280.

10 Choi, K.H., Kim, H.-S., Park, C.H., Kim, G.-H., Baik, K.H., Lee, S.H., Kim, T., & Kim, H.S. (2016). High-temperature thermo-mechanical behavior of functionally graded materials produced by plasma sprayed coating: experimental and modeling results. *Metals and Materials International*, 22(5), 817–824.

11 Wang, H., Zuo, D., Chen, G., Sun, G., Li, X., & Cheng, X. (2010). Hot corrosion behaviour of low Al NiCoCrAlY cladded coatings reinforced by nano-particles on a Ni-base super alloy, *Corrosion Science*, 52(10), 3561–3567.

12 Rakhadilov, B., Maulet, M., Abilev, M., Sagdoldina, Zh., & Kozhanova, R. (2021). Structure and tribological properties of Ni-Cr-Al based gradient coating prepared by detonation spraying. *Coatings*, 11(2), 218.

13 Rakhadilov, B.K., Maulet, M., Kakimzhanov, D.N., Stepanova, O.A., & Botabaeva, G.B. (2022). Comparative study of the structure and properties of homogeneous and gradient Ni-Cr-Al coatings. *Eurasian Journal of Physics and Functional Materials*, 6(1), 47–55.

14 Buitkenov, D.B., Rakhadilov, B.K., Sagdoldina, Zh.B., & Maulet, M. (2020). Obtained of powder coatings by detonation spraying. *Eurasian Journal of Physics and Functional Materials*, 4(3), 242–248.

15 Rakhadilov, B.K., Sagdoldina, Zh.B., Buitkenov, D.B., & Maulet, M. (2020). Phase composition and structure of composite Ti/HA coatings synthesized by detonation spraying. *AIP Conference Proceedings*, 2297.

16 Mamaeva, A., Kenzhegulov, A., Panichkin, A., Alibekov, Z., & Wieleba, W. (2022). Effect of Magnetron Sputtering Deposition Conditions on the Mechanical and Tribological Properties of Wear-Resistant Titanium Carbonitride Coatings. *Coatings*, 12.

17 Sagdoldina, Z., Rakhadilov, B., Skakov, M., & Stepanova, O. (2019). Structural evolution of ceramic coatings by mechanical alloying. *Materials testing*, 61, 304–308.

18 Rakhadilov, B.K., Buitkenov, D.B., Sagdoldina, Z.B., Zhurerova, L.G., & Wieleba, W. (2020). Preparation of powder coatings on the surface of steel balls by mechanochemical synthesis. *Bulletin of the university of Karaganda-Physics*, 4, 8–13.

М. Маулет, Ж.Б. Сагдолдина, Б.К. Рахадилов, Д.Н. Какимжанов, Н.М. Магазов

Алюминий құрамының NiCr-Al негізіндегі градиентті детонациялық жабындардың құрылымына әсері

Мақалада композиттік ұнтақ құрамындағы алюминийдің массалық үлесінің NiCr-Al негізіндегі детоанациялық градиент жабындарының құрылымына әсері зерттелді. Градиенттік жабындар оқпанды ацетилен-оттегі газ қоспасымен толтыру көлемін 50%-дан 25%-ға дейін біртіндеп азайта отырып, детонациялық бүрку арқылы алынды. NiCr-Al негізіндегі жабындардың элементтік және фазалық құрамы, микрокұрылымы және бетінің кедір-бұдырлығы 15 %, 20 % және 30 % алюминийдің әртүрлі құрамымен зерттелді. Ұнтақтың композиттік құрамындағы алюминий құрамын өзгерту әдісімен градиент құрылымы бар жабындар алынды. Зерттеу нәтижелері градиент жабынының фазалық құрамы Al массалық үлесіне қатты тәуелді екенін көрсетті. Композиттік құрамдағы алюминийдің 30% жағдайында алюминий оксидінің түзілуі анықталды. Детонациялық тозаңдандырудың бірдей режимдерінде жабындардың градиенттік құрылымын қалыптастыру NiCr-Al құрамындағы алюминий құрамынан қатты әсер ететіні анықталған. Зерттеу нәтижелері градиент құрылымы бар NiCr-Al жабындарын алу үшін NiCr 80% және Al 20% ұнтағының композиттік құрамы оңтайлы екенін көрсетті.

Кілт сөздер: NiCr-Al жабыны, градиентті жабындар, детонациялық бүрку, құрылымы, ұнтақтың композиттік құрамы.

М. Маулет, Ж.Б. Сагдолдина, Б.К. Рахадилов, Д.Н. Какимжанов, Н.М. Магазов

Влияние содержания алюминия на структуру градиентных детонационных покрытий на основе NiC–Al

В статье было изучено влияние массовой доли алюминия в составе композиционного порошка на структуру детоанционных градиентных покрытий на основе NiCr–Al. Градиентные покрытия были получены детонационным напылением с постепенным ступенчатым уменьшениием объема заполнения ствола газовой смесью ацетилен–кислород от 50 % до 25 %. Были исследованы элементный и фазовый составы, микроструктура и шероховатость поверхности покрытий на основе NiCr–Al с разным содержанием алюминия 15 %, 20 и 30 %. Методом варьирования содержания алюминия в композиционном составе порошка были получены покрытия с градиентной структурой. Результаты исследования показали, что фазовый состав градиентного покрытия сильно зависит от массовой доли Al. В случае содержания алюминия в составе композиционного пророшка 30 % обнаружено образование оксида алюминия. Установлено, что при одинаковых режимах детонационного напыления формирование градиентной структуры покрытий сильно зависит от содержания алюминия в составе NiCr–Al. Результаты иследования показали, что для получения NiCr–Al покрытий с градиентной структурой оптимальным является композиционный состав порошка NiCr 80 % и Al 20 %.

Ключевые слова: покрытия NiCr–Al, градиентные покрытия, детонационное напыление, структура, композитный состав порошка.

DOI 10.31489/2022PH3/25-35

UDC 517.958:539.3(2)

T. Brim*, B. Abdeyev, G. Muslimanova, S. Baigereyev, G. Baizakova

D. Serikbayev East Kazakhstan Technical University, Ust-Kamenogorsk, Kazakhstan
*(*E-mail: tbrim@mail.ru)*

On the issue of a new solution of the materials resistance contact problem on compression of elastic cylinders in contact with parallel generators

As a result of logarithmic singularity in the plane classical problem of elastically deformable material mechanics, it is proved that the reference formula for determining the convergence of two statically compressed parallel cylinders made of a homogeneous, isotropic, and physically linear material is not applicable. In the special case of elastic interaction of a cylinder with a half-plane, it is established that the convergence becomes equal to infinity. This paradoxical result confirms the inadequacy of Flaman's model of a simple radial stress state in determining displacements. Based on this model, it is possible to determine only the stresses in parallel contacting cylinders, while the calculation of displacements, in this case, is not possible. Based on a previously developed and mathematically approximated by the authors flat design scheme of Flaman the algorithm exception of conflicts has been proposed. The algorithm is based on the integral Fredholm equation solution and can be seen as a new fundamental and applied elasticity theory problem, which is of great importance when assessing the contact of refined strength and stiffness of the cylindrical parts of the supporting structures subject to the general and local deformations (cylindrical rollers, gears, pavements with their seal steel rollers, etc.).

Keywords: displacement, convergence, cylinder, stress, force, load, compression, contact pressure, half-plane, uniformity, isotropy, elasticity.

In various branches of modern mechanical engineering and construction, supporting structural elements in the form of cylindrical caps that interact in contact over a surface of finite dimensions are widely used. Typical examples of such parts are plain and rolling bearings; supporting parts of bridges, overpasses and sluice gates; wheels of railway rolling stock, etc. [1–5].

The well-known structurally nonlinear [6–9] theory of small elastic contact deformations of two physically linear, isotropic, and homogeneous circular cylinders is based on the following assumptions (Figure 1) [1–3, 10, 11]:

1) the radii R_1, R_2 of cylindrical bodies are large in comparison with the size $2a$ of the contact area, i.e.,

$$R_1 \gg 2a\,, \quad R_2 \gg 2a, \tag{1}$$

where a is half the width of the pressure band;

2) the cylinders have strictly parallel longitudinal axes O_1, O_2 and length $l \gg 2a$ and their initial contact occurs along a straight line which is called the generatrix when the distance between arbitrary points A_1, A_2 before deformation is expressed by the formulas given in Figure 2 [1, 3, 10–12];
3) within the limits of assumption (1), the contact area can be considered as part of the plane tangent to the guide (circle) of non-deformable cylinders;

4) there is no friction between touching surfaces that are supposed to be absolutely smooth.
5) the contacting elements are pressed against each other by two equal in magnitude and oppositely directed external forces-resultant Q, distributed over a given length l of the cylinders in the form of a constant static load

$$P = \frac{Q}{l} = const \tag{2}$$

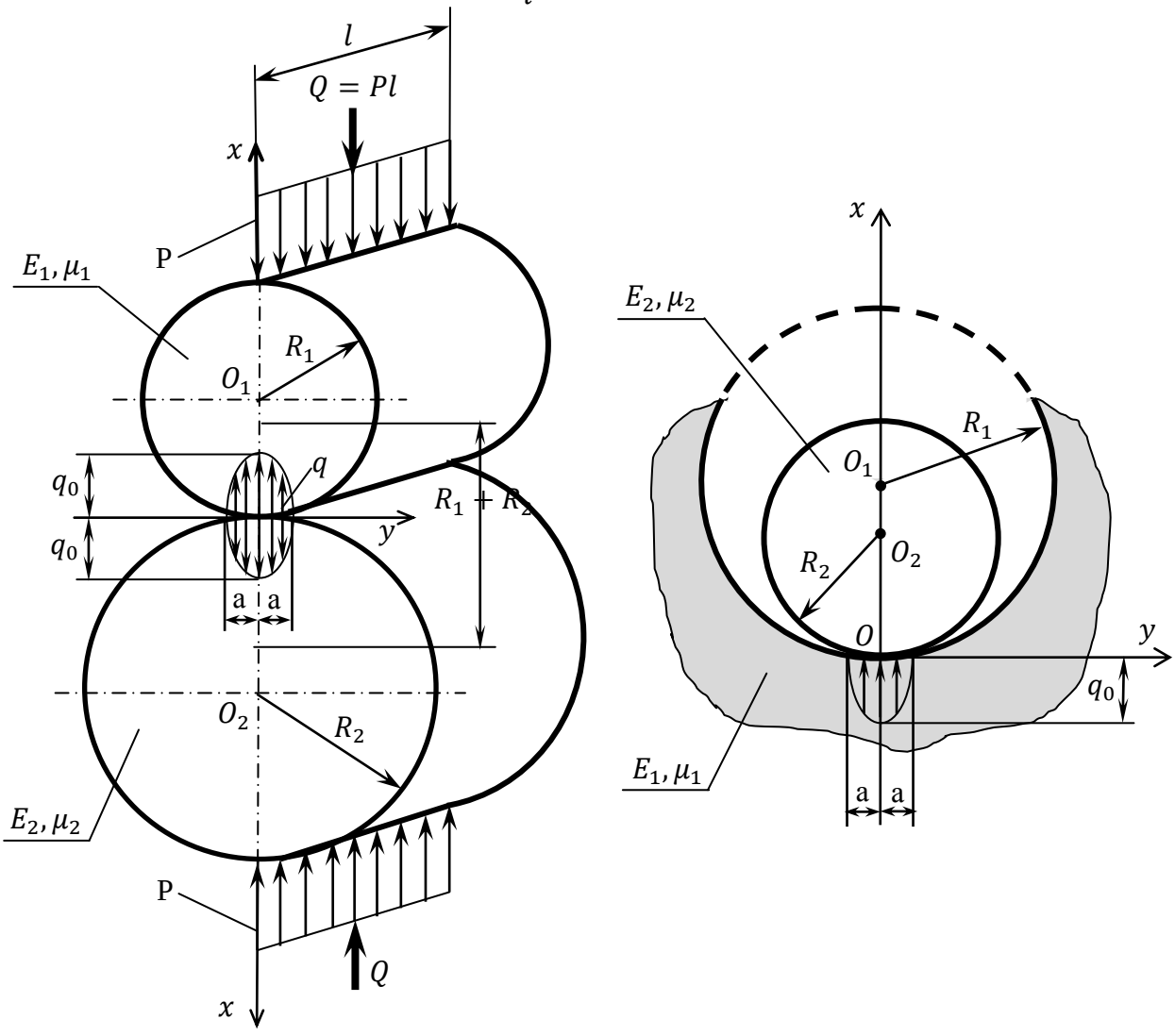

Figure 1. Design schemes of contacting elstic cylinders with radii R_1 and R_2:
a) the basic model of length *l*, where: $R_1 < R_2$;
b) For roller cylindrical rolling bearings at $R_1 \gg R_2$ [1, 18]

if the equilibrium condition is met [11, 13–21]

$$l \cdot \int_{-a}^{a} q(y)dy = P \cdot l = Q, \tag{3}$$

where $q = q(y)$ is the reactive boundary voltage approximated by the Hertz elliptic function [11, 12, 14–17, 20–24]

$$q(y) = q_o \sqrt{1 - \frac{y^2}{a^2}}\,, \qquad -a \ll y \ll a\,, \tag{4}$$

having an extreme value [1, 11–16, 20–22, 23, 25]

$$q_o = \frac{2}{\pi} \cdot \frac{Q}{a \cdot l} = max. \tag{5}$$

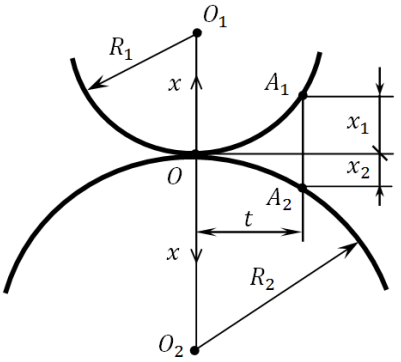

$$x_1 + x_2 = \frac{t^2}{2} \cdot \left(\frac{1}{R_1} + \frac{1}{R_2}\right) = \frac{t^2 \cdot (R_1 + R_2)}{2 \cdot R_1 \cdot R_2}$$

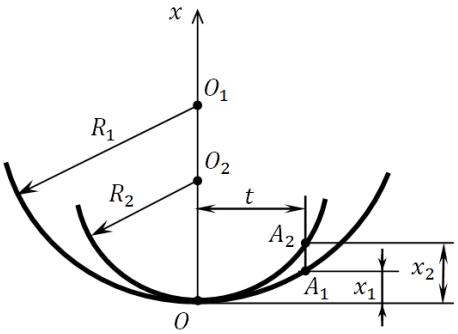

$$x_2 - x_1 = \frac{t^2}{2} \cdot \left(\frac{1}{R_2} - \frac{1}{R_1}\right) = \frac{t^2 \cdot (R_1 - R_2)}{2 \cdot R_1 \cdot R_2}$$

Figure 2. Geometry of the contact of two elasticall desormable bodies-cylinders:
a) to modeling the external interaction according to Fig. 1a ($R_1 < R_2$);
b) for contacting a cylinder of radius R_2 with a cylindrical cavity having a radial size $R_1 \gg R_2$
Figure 1b

If the cylinders are made of materials that have elastic modulus $E_1,\ E_2$, Poisson's ratios $\mu_1,\ \mu_2$, then the formulas for $a,\ q_o$ and the total kinematic displacement δ (convergence of the axes O_1, O_2) have the following form [1, 2, 11, 25]:

$$a = 2\sqrt{\frac{Q}{\pi \cdot l} \cdot \frac{R_1 \cdot R_2}{(R_1 \pm R_2)} \cdot \left(\frac{1-\mu_1^2}{E_1} + \frac{1-\mu_2^2}{E_2}\right)}, \tag{6}$$

$$q_o = \sqrt{\frac{Q}{\pi \cdot l} \cdot \frac{(R_1 \pm R_2)}{R_1 \cdot R_2} \cdot \left(\frac{1-\mu_1^2}{E_1} + \frac{1-\mu_2^2}{E_2}\right)^{-1}}, \tag{7}$$

$$\delta = \frac{2 \cdot Q}{\pi \cdot l} \cdot \left[\frac{1-\mu_1^2}{E_1} \cdot \left(ln\frac{2 \cdot R_1}{a} + 0{,}407\right) + \frac{1-\mu_2^2}{E_2} \cdot \left(ln\frac{2 \cdot R_2}{a} + 0{,}407\right)\right]; \tag{8}$$

where the "+" sign refers to the main calculation scheme shown in Figures 1, 2, and "-" corresponds to the model of Figure 1b.

Relations (6)–(8) are used to quantify the load-bearing capacity of cylindrical systems in Figure 1. From a practical point of view, these are design calculations for the contact strength and stiffness of friction and gear gears, roller parts of bridge supports, and other critical elements of engineering structures.

At the same time, it should be noted that the definition of the displacement δ at Eq.(8) has significant mechanical-mathematical incorrectness [2, 10], as in the classic problem of Flaman [1, 10, 12–17, 22, 27, 28] on the effects of concentrated and distributed force $P = const$ (Figure 1) on an elastic isotropic half-plane lying in the basis of the Eq. (8). In Eq. (8) the displacement is calculated relative to a fairly remote from the contact point. Its position is unknown arbitrary. In Eq. (8) as of such points taken the centers of curvature of O_1 and O_2 (Figures 1, 2) in the hypothetical assumption that the parameter δ is determined only by the total deformations of cylinders [2], excluding contact components, which according to [29], can represent a significant percentage (30 to 90%) in the overall balance of the elastic displacements of the contacting parts.

The indicated uncertainty (multivariance) in choosing the coordinate of a fixed point when determining displacements directed perpendicular to the boundary of the half-plane is a consequence of the general logarithmic feature of Flaman's physical and mathematical model [10, 12, 20, 22]. In this relation, Galin [10] states that, based on the Flaman solution, it is possible to determine only the stresses in parallel-located contacting cylinders, and the calculation of displacements, in this case, is not possible. Thus, it can be stated that the estimation of contact stiffness by formula (8) will not adequately characterize the deformed state of the cylinders. Another negative consequence of the presence of the logarithm ln in Eq. (8) is manifested in its special case when one of the radii, for example

$$R_2 = \infty. \tag{9}$$

In this case, we will have a common engineering problem in design calculations about the contact of a compressible cylinder with an elastically deformable half-plane (Figure 3) [1–5].

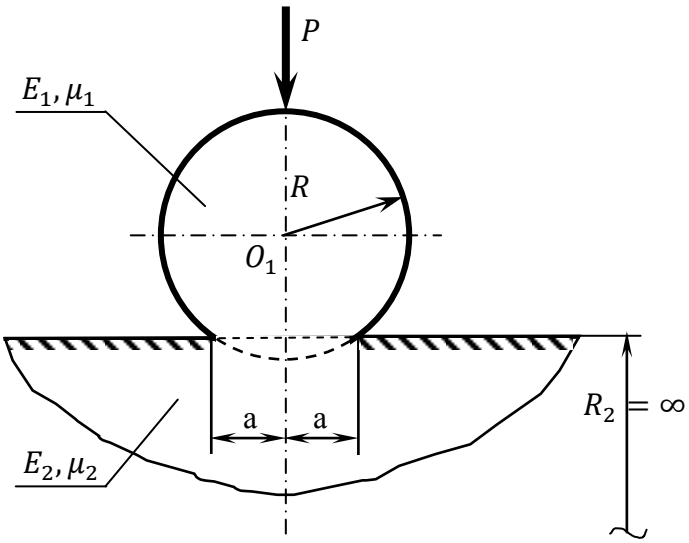

Figure 3. Model of pressure of a cylinder of radius R and length 1 on a linearly elastic half-plane

Considering the condition (9) and the equality $R_1 = R$, we obtain the final value for linear size *a* under Eq. (6):

$$a = 2\sqrt{\frac{Q \cdot R}{\pi \cdot l} \cdot \left(\frac{1-\mu_1^2}{E_1} + \frac{1-\mu_2^2}{E_2}\right)}. \tag{10}$$

Substituting Eq. (10) in Eq. (8) for $R_2 = \infty$, according to Eq. (9), leads to the paradoxical answer

$$\delta = \infty, \tag{11}$$

which contradicts the physical meaning of the contact problem under consideration and confirms the unacceptability of the Flaman mathematical model in determining the displacements δ [10, 21].

The incorrect result (11) also does not correspond to the basic fundamental axisymmetric problem of Boussinesca [18, 20–22, 23, 24, 28] on a concentrated force directed perpendicular to an elastic half-space, in which there are no contradictions mentioned above.

Based on the classical interpretation of plane linear-elastic deformation [2, 11–15, 19, 21–23] and the refined innovative solution of the Flaman problem [30], which includes three stresses (compared to one radial component [12, 13]) and parameter a, in the work [30] a fundamentally new formula for calculation of displacement

$$v_g = v_g(y) = \frac{2 \cdot P \cdot (1-\mu^2)}{3 \cdot \pi \cdot E} \cdot \left(\frac{a}{y}\right)^2 \tag{12}$$

of a boundary of the half-plane in the unlimited range

$$-\infty \le y \le \infty. \tag{13}$$

of variable change has been obtained.

In contrast to the incorrect logarithmic dependence [11–14, 21, 22, 24]

$$v_{gf} = v_{gf}(y) = \frac{2 \cdot P \cdot (1-\mu^2)}{\pi \cdot E} \cdot ln\frac{l_k}{|y|}\ , \tag{14}$$

containing the distance to an arbitrary point *K* (Figure 3) and approximating only the relative value of displacements v_{gf} over a closed interval

$$-l_k \le y \le l_k, \tag{15}$$

in the formula (12) derived in [30] allows us to determine the absolute precipitation of the boundary $x = 0$ of the half-plane without reference to the parameter l_k over a theoretically infinite interval (13).

The behavior of functions (12) and (14) is illustrated in dimensionless forms

$$v_g^*(y) = v_g(y) \cdot \frac{\pi \cdot E}{P \cdot (1-\mu^2)} = \frac{2}{3} \cdot \left(\frac{a}{y}\right)^2, \tag{16}$$

$$v_{gf}^*(y) = v_{gf}(y) \cdot \frac{\pi \cdot E}{P \cdot (1-\mu^2)} = 2 \cdot ln\frac{l_k}{|y|} \tag{17}$$

in Figure 4, using data of Table.

Table

Values of functional relations (16), (17), when $l_k = 6a$.

y	0	$\pm a$	$\pm 2a$	$\pm 4a$	$\pm 6a$	$\pm 8a$	$\pm 10a$	$\pm\infty$
v_g^*	∞	0,6667	0,1667	0,0416	0,0186	0,0104	0,0066	0
v_{gf}^*	∞	3,5836	2,1972	0,8110	0	−0,5751	−1,0216	$-\infty$

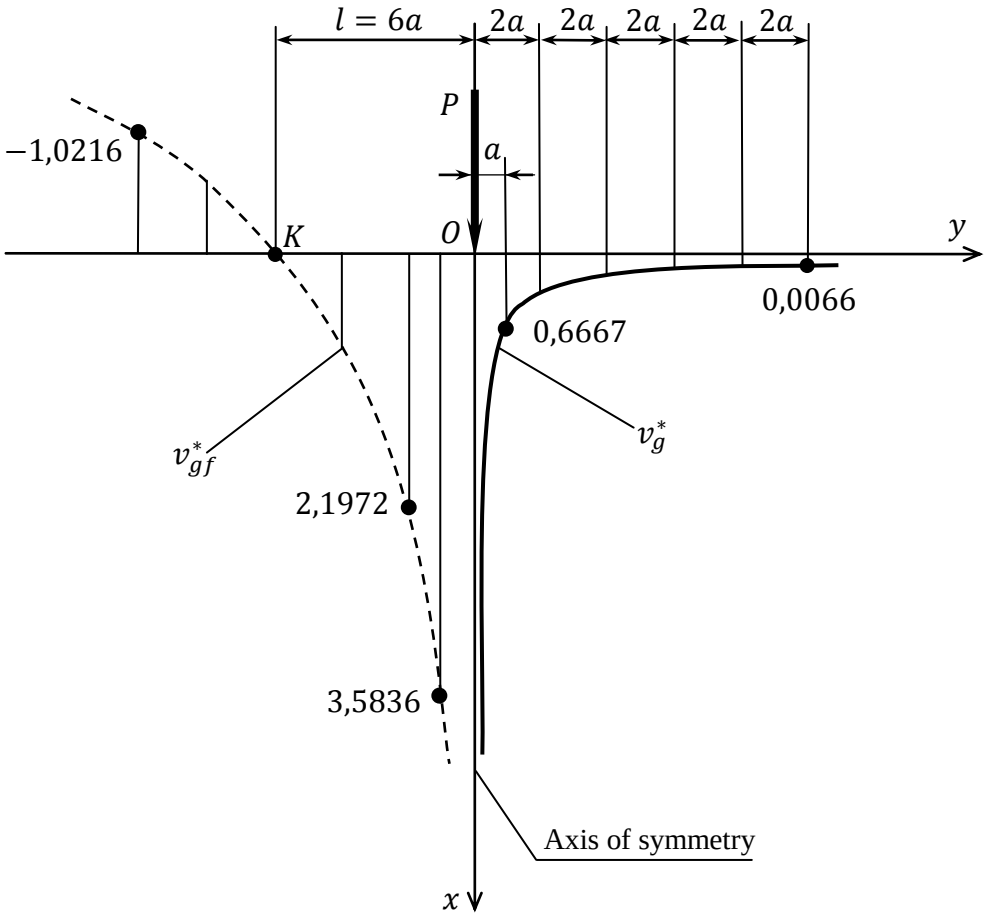

Figure 4. General view of changes in functional dependencies v_g^*, v_{gf}^*:
$v_g^*(y)$ is a solid curve according to the new formula (16) [30];
$v_{gf}^*(y)$ is a dashed line according to Flaman's solution (17) [12–14, 21, 22, 24]

A mechanical system in which a local uniformly distributed stationary force *P* acts on an elastic isotropic medium (Figures 1, 3) should be considered as an abstract system that does not reflect the actual possible conditions. However, using the formally idealized mathematical solution (12), we proceed to a real simulation of the reactive load $q = q(y)$ that occurs between contacting elastically deformable bodies Figure 1). Therefore, by analogy with the developed theory of calculating the sediment of a belt foundation [30] and guided by [11, 15–17, 21–24, 31–33], to answer this question, we present the following Fredholm equation of the first kind [13, 16, 20-22, 31, 32] with an unknown function $q(y)$ under the sign of a certain integral:

$$-\frac{2\cdot a^2}{3\cdot\pi}\cdot\left(\frac{1-\mu_1^2}{E_1}+\frac{1-\mu_2^2}{E_2}\right)\cdot\int_{-a}^{a}\frac{q(y)\cdot dy}{(t-y)^2}=\delta-\frac{1}{2}\cdot\left(\frac{1}{R_2}\pm\frac{1}{R_1}\right)\cdot t^2\,, \tag{18}$$

where $q = q(y), q_o, a, \delta$ are the desired physical and geometric characteristics of the interaction pro cess of two round cylindrical elements, while meeting the obvious requirements

$$-a \le y \le a, \qquad q(\pm a) = 0, \quad q(0) = q_o = max \tag{19}$$

and condition (3) is met;

t is an auxiliary variable that varies within $-a \le t \le a$ and represents the horizontal coordinate of arbitrary points A_1, A_2, whose mutual vertical displacement depends on the elementary load (Figures 2, 5).

$$dP = q(y)\cdot dy \tag{20}$$

equal to (see (12) and (18))

$$dv_g = dv_{g1} + dv_{g2} = -\frac{2 \cdot a^2}{3 \cdot \pi} \cdot \left(\frac{1-\mu_1^2}{E_1} + \frac{1-\mu_2^2}{E_2} \right) \cdot \frac{q(y) \cdot dy}{(t-y)^2}. \quad (21)$$

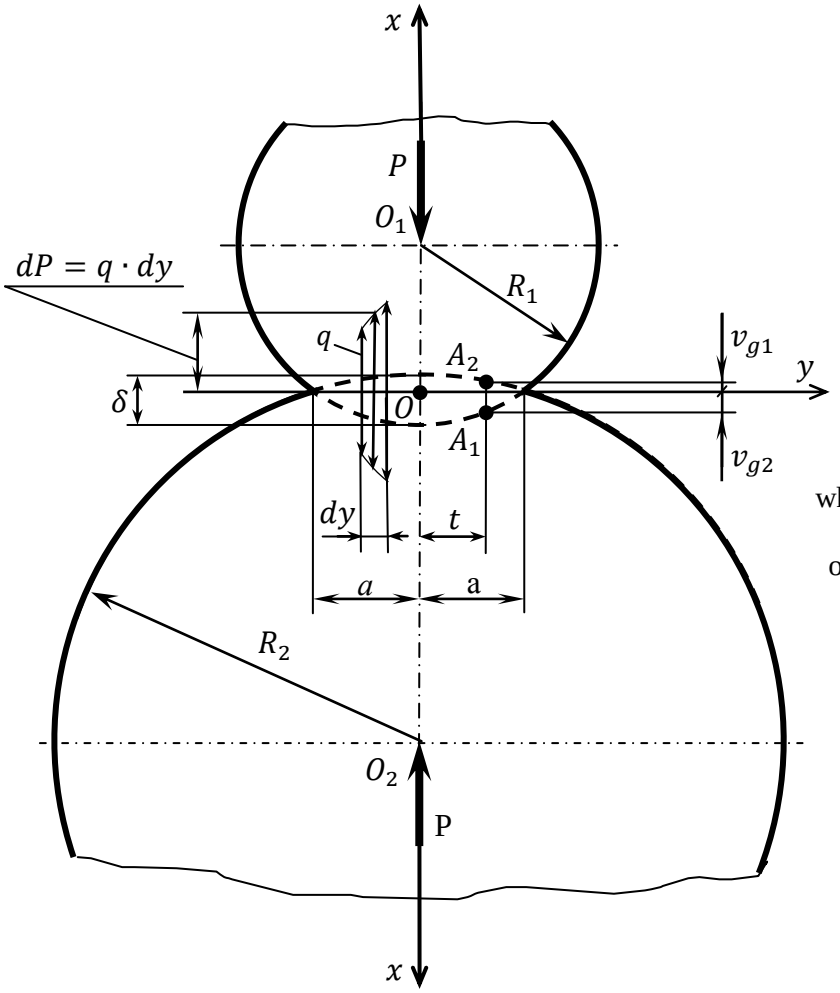

$$v_g = v_{g1} + v_{g2} = \delta - \frac{1}{2}\left(\frac{1}{R_2} \pm \frac{1}{R_1} \right) t^2,$$

where is the sign "-" for the model of cylinder pressure on a concave cylindrical surface (Figures 1b, 2b)

Fig*ure*.5. Basic scheme of contact interaction of cylinders (Fig*ure* 1a) to the interpretation of the integral equation (18)

As noted by the authors of [30], in comparison with the absolutely idealized original (12), in which the directions of force P and displacement $v_g > 0$ coincide (Figure 4), in formulas (18), (21) the "minus" sign indicates the opposite effect of the contact pressure $q(y)$ and the kinematic components v_{g1}, v_{g2} within each cylinder (Figures 1, 5).

Analysis of the conducted theoretical studies allows us to draw the following CONCLUSIONS:

1. The impossibility [10, 11, 21] of using the reference dependency (8) [1, 2, 25] for calculation of the convergence δ of cylinders (Figures 1, 3) due to the logarithmic feature noted in well-known fundamental mechanical and mathematical works [10, 14, 21] is confirmed and proved.

2. For the same reason (see point 1), the use of the basic Flaman model [11–16, 21–25, 28] for solving any plane problems of the elasticity theory is proved incorrect (Figure 4), related to the evaluation of contact stiffness [29] of cylindrical parts of load-bearing structures that are in parallel contact.

3. To completely eliminate the considered contradictions, a linear integral equation (18), which makes it possible to determine the reaction pressure function $q(y)$ and its extremum $q_0 = max$; the half-width a of the contact site and the total mutual displacement δ of points O_1, O_2 (Figures 1, 5) is formulated.

References

1 Пономарев С.Д. Расчеты на прочность в машиностроении. — Т. II / С.Д. Пономарев, В.Л. Бидерман и др.; под ред. д-ра техн. наук, проф. С.Д. Пономарева. — М.: Машгиз, 1958. — 975 с.

2 Биргер И.А. Расчет на прочность деталей машин: Справоч./ И.А. Биргер, Б.Ф. Шорр, Г.Б. Иосилевич. — М.: Машиностроение, 1979. — 702 с.

3 Искрицкий Д.Е. Строительная механика элементов машин / Д.Е. Искрицкий. — Л.: Изд-во «Судостроение», 1970. — 448 с.

4 Абдеев Б.М. Математическое моделирование взаимодействия неподвижного гибкого вальца дорожного катка и уплотняемой среды / Б.М. Абдеев, М.В. Дудкин, С.В. Речицкий. Материалы Междунар. симпоз. «Наноматериалы для защиты промышленных и подземных конструкций» и XI Междунар. конф. «Физика твердого тела (ФТТ — XI)», 9–12 июня 2010 г. — Усть-Каменогорск: ВКГТУ, 2010. — С. 81–86.

5 Калужский Я.А. Уплотнение земляного полотна и дорожных одежд / Я.А. Калужский, О.Т. Батраков. — М.: Изд-во «Транспорт», 1970. — 160 с.

6 Лукаш П.А. Основы нелинейной строительной механики / П.А. Лукаш. — М.: Стройиздат, 1978. — 204 с.

7 Жидков А.В. Плоские задачи теории упругости: учеб.-метод. пос. / А.В. Жидков, А.К. Любимов. — Нижний Новгород: Нижегород. гос. ун-т, 2019. — 38 с.

8 Стружанов В.В. Теория упругости: основные положения: учеб. пос. / В.В. Стружанов, Н.В. Бурмашева. — Екатеринбург: Изд-во Урал. ун-та, 2019. — 204 с.

9 Каюмов Р.А. Основы теории упругости и элементы теории пластин и оболочек: учеб. пос. / Р.А. Каюмов. — Казань: Изд-во Казан. гос. архит.-строит. ун-та, 2016. — 111 с.

10 Галин Л.А. Контактные задачи теории упругости и вязкоупругости / Л.А. Галин. — М.: Наука, 1980. — 304 с.

11 Филин А.П. Прикладная механика твердого деформируемого тела. — Т. I / А.П. Филин. — М.: Наука, 1975. — 832 с.

12 Киселев В.А. Плоская задача теории упругости: учеб. пос. для вузов / В.А. Кисилев. — М.: Высш. шк., 1976. — 151 с.

13 Flamant A. Sur la repartition des pressions dans un solide rectangulaire, charge transsversalement. Comptes rendus des sèances de l'Academie des Sciences, 1892, tome 114, 1 Semestre, № 22, pp. 1465–1468.

14 Лурье А.И. Теория упругости / А.И. Лурье. — М.: Наука, 1970. — 940 с.

15 Шарафутдинов Г.З. Некоторые плоские задачи теории упругости: моногр. — М.: Научный мир, 2014. — 464 с.

16 Сапунов В.Т. Задачи прикладной теории упругости: учеб. пос. для вузов. — М.: Изд-во Нац. исслед. ядер. ун-та «Московский инженерно-физический институт», 2011. — 208 с.

17 Тен Ен Со. Решение задач теории упругости с применением *Mathcad* 14.0: учеб. пос./ Ен Со Тен. — Хабаровск: Изд-во Тихоокеан. гос. ун-та, 2010. — 75 с.

18 Boussinesq J. Application des Potentielsa l'Etude l'Equilibre et du Mouvement des Solides Elasticques. Gauthien — Villars, Paris 1885.

19 Биргер И.А. Сопротивление материалов: учеб. пос. / И.А. Биргер, Р.Р. Мавлютов. — М.: Наука, 1986. — 560 с.

20 Рындин Н.И. Краткий курс теории упругости и пластичности / Н.И. Рындин. — Л.: Ленинград. ун-т, 1974. — 136 с.

21 Штаерман И.Я. Контактная задача теории упругости / И.А. Штаерман. — М.; Л.: Гостехиздат, 1949. — 270 с.

22 Тимошенко С.П. Теория упругости / С.П. Тимошенко, Дж. Гудьер; пер. с англ. М.И.Рейтмана, под ред. Г.С.Шапиро. — М.: Наука, 1975. — 576 с.

23 Александров В.М. Аналитические методы в контактных задачах теории упругости: моногр. / В.М. Александров, М.И. Чебаков. — М.: Физматлит, 2004. — 299 с.

24 Жемочкин Б.М. Теория упругости / Б.М. Жемочкин. — М.: Госстройиздат, 1957. — 256 с.

25 Писаренко Г.С. Справочник по сопротивлению материалов / Г.С. Писаренко, А.П. Яковлев, В.В. Матвеев. — Киев: Наукова думка, 1975. — 704 с.

26 Самуль В.И. Основы теории упругости и пластичности / В.И. Самуль. — М.: Высш. шк., 1970. — 288 с.

27 Безухов Н.И. Основы теории упругости, пластичности и ползучести / Н.И. Безухов. — М.: Высш. шк., 1968. — 512 с.

28 Варданян Г.С. Сопротивление материалов с основами теории упругости и пластичности: учеб. / Г.С. Варданян, В.И. Андреев, Н.М. Атаров, А.А. Горшков; под ред. Г.С. Варданяна. — М.: Изд-во Ассоциации строительных вузов (АСВ), 1995. — 568 с.

29 Левина З.М. Контактная жесткость машин / З.М. Левина, Д.Н. Решетов. — М.: Машиностроение, 1971. — 264 с.

30 Абдеев Б.М. Уточненная плоская механико-математическая модель для определения напряжений в основании ленточного фундамента и его упругой осадки / Б.М. Абдеев, Т.Ф. Брим, Г. Муслиманова // Вестн. Перм. нац. исслед. политех. ун-та. Сер. Механика. — 2020. — № 1. — С. 150–164.

31 Цлаф Л.Я. Вариационное исчисление и интегральные уравнения: Справоч. рук. — М.: Наука, 1970. — 192 с.

32 Демидович Б.П. Численные методы анализа / Б.П. Демидович, И.А. Марон, Э.З. Шувалова. — М.: Наука, 1967. — 368 с.

33 Мышкис А.Д. Математика для втузов: Специальные курсы / А.Д. Мышкис. — М.: Наука, 1971. — 632 с.

Т. Брим, Б. Абдеев, Г. Муслиманова, С. Байгереев, Г. Байзакова

Параллель жасаушылармен жанасатын серпімді цилиндрлердің сығылуы туралы матералдардың кедергісі байланыс есебінің жаңа шешімі сұрағына

Серпімді деформацияланатын қатты дененің механиканың классикалық есебінің жазықтағы белгілі логарифмдік ерекшелігіне байланысты біртекті, изотропты және физикалық сызықты материалдан жасалған статикалық сығылған екі параллель цилиндрдің жақындауын анықтауға арналған анықтамалық формуланың қолданылмайтындығы осы жұмыста дәлелденді. Цилиндрдің жартылай жазықтық пен серпімді әсерлесуінің ерекше жағдайында, радиустардың біреуінің ұзындығы шексіз болған жағдайында, жақындаудың шексіздікке тең болатынығы анықталған. Жақындаудың шексіздікке тең болған парадоксалды нәтижесі мақалада зерттеліп отырған процестің физикалық және механикалық мағынасына қарсы келеді, сонымен қатар ығысуларды анықтауда қарапайым радиалды кернеу күйінің Фламан моделінің сәйкессіздігін растайды. Бұл модельге негізделіп, тек параллель жанасатын цилиндрлердегі кернеулерді анықтауға болады, бұл жағдайда орын ауыстыруларды есептеу мүмкін емес. Осы мақаланың авторлары бұрын әзірлеген және математикалық жуықтайтын, үш кернеу құрамдас бөлігі мен цилиндрдің жанасу аймағының енін ескеретін жалпақ Фламан есептеу схемасы негізінде, шешуге негізделген қайшылықтарды жою алгоритмін ұсынған, яғни бірінші текті Фредгольм интегралдық теңдеуі, әрі қарай серпімділік теориясының жаңа іргелі–қолданбалы мәселесі ретінде қарастырылуы мүмкін, жалпы және жергілікті деформацияларды ескере отырып, ол жүк көтергіш құрылымдардың цилиндрлік бөліктерінің жанасу беріктігін және қаттылығын нақты бағалауда үлкен маңызға ие (цилиндрлік роликтер, тісті доңғалақтар, болат біліктермен тығыздалған кездегі жол төсемдері және т.б.).

Кілт сөздер: жылжыту, жақындау, цилиндр, кернеу, күш, жүктеме, сығылу, жанасу қысымы, жартылай жазықтық, біртектілік, изотропия, серпімділік.

Т. Брим, Б. Абдеев, Г. Муслиманова, С. Байгереев, Г. Байзакова

К вопросу нового решения контактной задачи сопротивления материалов о сжатии упругих цилиндров, соприкасающихся с параллельными образующими

Вследствие известной логарифмической особенности в плоской классической задаче механики упругодеформируемого твердого тела доказана неприменимость справочной формулы для определения сближения двух статически сжатых параллельных цилиндров из однородного, изотропного и физически линейного материала. В частном случае упругого взаимодействия цилиндра с полуплоскостью, когда один из радиусов имеет бесконечную длину, установлено, что и сближение становится равным бесконечности. Этот парадоксальный результат противоречит не только физико-механическому смыслу исследуемого процесса, но и подтверждает неадекватность модели Фламана о простом радиальном напряженном состоянии при определении перемещений. Основываясь на этой модели, можно определять только напряжения в параллельно расположенных контактирующих цилиндрах, в то время как расчет перемещений в этом случае не представляется возможным. На основе ранее разработанной и математически аппроксимированной авторами данной статьи плоской расчетной схемы Фламана, учитывающей три компоненты напряжений и размер ширины площадки контакта цилиндров, предложен алгоритм исключения противоречий, базирующийся на решении интегрального уравнения Фредгольма первого рода, что может быть рассмотрено в дальнейшем как новая фундаментально-прикладная задача теории упругости, имеющая большое значение при уточненной оценке контактной прочности и жесткости цилиндрических деталей несущих конструкций с учетом общих и местных деформаций (цилиндрических катков, зубчатых передач, дорожных покрытий при их уплотнении стальными вальцами и т.д.).

Ключевые слова: перемещение, сближение, цилиндр, напряжение, сила, нагрузка, сжатие, контактное давление, полуплоскость, однородность, изотропность, упругость.

References

1 Ponomarev, S.D., Biderman, V.L., Likharev, K.K., Makushin, V.M., Malinin, N.N., & Fedosev, V.I. (1958). Raschety na prochnost v mashinostroenii [Strength Calculations in Mechanical Engineering]. Vol. 2. S.D. Ponomarev (Ed.). Moscow: Mashgiz [in Russian].

2 Birger, I.A., Shorr, B.F., & Iosilevich, G.B. (1979). Raschet na prochnost detalei mashin [Strength Calculation of the Machine Parts: handbook]. Moscow: Mashinostroenie [in Russian].

3 Iskritskii, D.E. (1970). Stroitelnaia mekhanika elementov mashin [Structural Mechanics of Machine Elements]. Leningrad: Sudostroenie [in Russian].

4 Abdeev, B.M., Dudkin, M.V., & Rechitskii, S.V. (2010). Matematicheskoe modelirovanie vzaimodeistviia nepodvizhnogo gibkogo valtsa dorozhnogo katka i uplotniaemoi sredy [Mathematical Modeling of the Interaction of a Stationary Flexible Roller of a Road Roller and a Compacted Medium]. Proceedings from "Nanomaterials for the protection of industrial and underground structures" and "Solid State Physics" (SSP): *Mezhdunarodnyi simpozium – International symposium* and *XI Mezhdunarodnaia konferentsiia (9–12 iiulia 2010 goda) – 11th International Conference*. (pp. 81–86). Ust-Kamenogorsk: Vostochno-Kazakhstanskii tekhnicheskii universitet [in Russian].

5 Kaluzhskii, Ya.A., & Batrakov, O.T. (1970). Uplotnenie zemlianogo polotna i dorozhnykh odezhd [Compaction of the Roadbed and Road Clothing]. Moscow: Transport [in Russian].

6 Lukash, P.A. (1978). Osnovy nelineinoi stroitelnoi mekhaniki [The Foundations of Nonlinear Structural Mechanics]. Moscow: Stroiizdat [in Russian].

7 Zhidkov, A.V., & Liubimov, A.K. (2019). Ploskie zadachi teorii uprugosti: Uchebno-metodicheskoe posobie [Planar Problems of the Theory of Elasticity: An Educational and Methodological Guide]. Nizhnii Novgorod: Nizhegorodskii gosudarstvennyi universitet [in Russian].

8 Struzhanov, V.V., & Burmasheva, N.V. (2019). Teoriia uprugosti: osnovnye polozheniia: Ucheboe posobie [Theory of Elasticity: Basic Provisions: Textbook]. Ministertsvo nauki i vysshego obrazovaniia Rossiiskoi Federatsii, Uralskii federalnyi universitet. — Ekaterinburg: Izdatelstvo Uralskogo universiteta [in Russian].

9 Kaiumov, R.A. (2016). Osnovy teorii uprugosti i elementy teorii plastin i obolochek: Uchebnoe posobie [Fundamentals of the Theory of Elasticity and the Elements of the Theory of Plates and Shells: Textbook]. Kazan: Izdatelstvo Kazanskogo gosudarstvennogo arkhitekturno-stroitelnogo universiteta [in Russian].

10 Galin, L.A. (1980). Kontaktnye zadachi teorii uprugosti i viazkouprugosti [Contact Problems of the Theory of Elasticity and Viscoelasticity]. Moscow: Nauka [in Russian].

11 Filin, A.P. (1975). Prikladnaia mekhanika tverdogo deformiruemogo tela [Applied Mechanics of a Solid Deformable Body]. Moscow: Nauka [in Russian].

12 Kiselev, V.A. (1976). Ploskaia zadacha teorii uprugosti [Planar Problem of the Theory of Elasticity]. Moscow: Vysshaia shkola [in Russian].

13 Flamant, A. (1892). Sur la repartition des pressions dans un solide rectangulaire. charge transsversalement. Comptes rendus des sèances de l'Academie des Sciences. Tome 114. 1 Semestre. №22. pp. 1465-1468.

14 Lure, A.I. (1970). Teoriia uprugosti [Theory of Elasticity]. Moscow: Nauka [in Russian].

15 Sharafutdinov, G.Z. (2014). Nekotorye ploskie zadachi teorii uprugosti [Some Flat Problems of the Theory of Elasticity]. Moscow: Nauchnyi mir [in Russian].

16 Sapunov, V.T. (2011). Zadachi prikladnoi teorii uprugosti [Problems of the Applied Theory of Elasticity]. Moscow: Moskovskii inzhenerno-fizicheskii institut [in Russian].

17 Te, En So (2010). Reshenie zadach teorii uprugosti s primeneniem Mathcad 14.0 [The solution to problems of elasticity theory with the use of Mathcad 14.0]. — Khabarovsk: Tikhookeanskii gosudarstvennyi universitet [in Russian].

18 Boussinesq, J. (1885). Application des Potentielsa l'Etude l'Equilibre et du Mouvement des Solides Elasticques. Gauthien – Villars.

19 Birger, I.A., & Mavliutov, R.R. (1986). Soprotivlenie materialov [Strength of Materials]. Moscow: Nauka [in Russian].

20 Ryndin, N.I. (1974). Kratkii kurs teorii uprugosti i plastichnosti [Short Course of the Theory of Elasticity and Plasticity]. Leningrad: Leningradskii universitet [in Russian].

21 Shtaerman, I.Ya. (1949). Kontaktnaia zadacha teorii uprugosti [Contact Problem of the Theory of Elasticity]. Moscow; Leningrad: Gostekhizdat [in Russian].

22 Timoshenko, S.P., & Guder, Dzh. (1975). Teoriia uprugosti [Theory of Elasticity]. Moscow: Nauka [in Russian].

23 Aleksandrov, V.M., & Chebakov, M.I. (2004). Analiticheskie metody v kontaktnykh zadachakh teorii uprugosti [Analytical Methods in Contact Problems of Elasticity Theory]. Moscow: Fizmatlit [in Russian].

24 Zhemochkin, B.M. (1957). Teoriia uprugosti [Theory of Elasticity]. Moscow: Gosstroiizdat [in Russian].

25 Pisarenko, G.S., Yakovlev, A.P., & Matveev, V.V. (1975). Spravochnik po soprotivleniiu materialov [Handbook on the Strength of Materials]. Kiev: Naukova dumka [in Russian].

26 Samul, V.I. (1970). Osnovy teorii uprugosti i plastichnosti [Fundamentals of the Theory of Elasticity and Plasticity]. Moscow: Vysshaia shkola [in Russian].

27 Bezuhov, N.I. (1968). Osnovy teorii uprugosti, plastichnosti i polzuchesti [Fundamentals of the Theory of Elasticity, Plasticity and Creep]. Moscow: Vysshaia shkola [in Russian].

28 Vardanian, G.S., Andreev, V.I., Atarov, N.M., & Gorshkov, A.A. (1995). Soprotivlenie materialov s osnovami teorii uprugosti i plastichnosti [Strength of Materials with the Basics of the Theory of Elasticity and Plasticity]. G.S. Vardanian (Ed.). Moscow: Izdatelstvo Assotsiatsii stroitelnykh vuzov [in Russian].

29 Levina, Z.M., & Reshetov, D.N. (1971). Kontaktnaia zhestkost mashin [Contact Rigidity of Machines]. Moscow: Mashinostroenie [in Russian].

30 Abdeev, B.M., Brim, T.F., & Muslimanova, G. (2020). Utochnennaia ploskaia mekhaniko-matematicheskaia model dlia opredeleniia napriazhenii v osnovanii lentochnogo fundamenta i ego uprugoi osadki [Refined Plane Mechanical and Mathematical Model for Determining Stresses in the Base of the Strip Foundation and Its Elastic Sediment]. *Vestnik Permskogo natsionalnogo issledovatelskogo politekhnicheskogo universiteta. Seriia Mekhanika – Perm National Research Polytechnic University Bulletin. Mechanics series,* 1, 150–164 [in Russian].

31 Tslaf, L.Ya. (1970). Variatsionnoe ischislenie i integralnye uravneniia [Variational Calculus and Integral Equations]. Moscow: Nauka [in Russian].

32 Demidovich, B.P., Maron, I.A., & Shuvalova, E.Z. (1967). Chislennye metody analiza [Numerical Methods of Analysis]. Moscow: Nauka [in Russian].

33 Myshkis, A.D. (1971). Matematika dlia vtuzov [Mathematics for technical colleges]. Moscow: Nauka [in Russian].

DOI 10.31489/2022PH3/36-42

UDC 620.3

A.A. Markhabayeva*, M.B. Baidilda, Sh.T. Nurbolat,
Zh.K. Kalkozova, R.R. Nemkayeva, Kh.A. Abdullin

Al-Farabi Kazakh National University, Almaty, Kazakhstan
*(*E-mail: Aiko_marx@mail.ru)*

Comparison of electrochemical characteristics of $NiCo_2O_4$ and $NiCo_2S_4$ nanostructures for supercapacitors

This paper presents the results on the synthesis and study of the properties of $NiCo_2O_4$ and $NiCo_2S_4$ nanostructures obtained by hydrothermal synthesis for their use as supercapacitor electrodes. A method is developed for growing a nanostructure from a ternary metal oxide $NiCo_2O_4$ on a nickel substrate. The structural features of the synthesized $NiCo_2O_4$ and $NiCo_2S_4$ nanostructures are studied using X-ray phase analysis. The obtained samples have a cubic modification $NiCo_2O_4$ and $NiCo_2S_4$. The data on the morphology of the synthesized samples obtained by scanning electron microscopy are presented. The samples are in the form of nanoneedles and nanowires grown on a nickel substrate. Methods for the synthesis of $NiCo_2O_4$ nanostructures have been studied, optimal conditions for the growth of nanostructures from $NiCo_2O_4$ have been determined, and a $NiCo_2O_4$ sulfurization method has been developed to obtain a $NiCo_2O_4$ nanostructure. Comparative studies have been carried out on the effects of sulfurization on the electrochemical characteristics of the obtained electrodes. It is found that, despite the fact that $NiCo_2O_4$ oxide nanostructures have a high theoretical capacitance, the replacement of oxygen atoms by sulfur atoms increases the conductivity of the materials and leads to a further increase in the specific capacitance of the end electrodes. The maximum Cs obtained specific capacitance for $NiCo_2S_4$ is 1976 F g^{-1} and while for $NiCo_2O_4$ it is 413 F g^{-1} at a scan rate of 5 mV/s. The results of the dependence of the specific capacitance on the scanning speed during measurements are also presented.

Keywords: supercapacitors, energy storage, metal oxides, electrodes, nanomaterials, $NiCo_2O_4$, $NiCo_2S_4$ and nanostructures.

Introduction

With the growth in electricity consumption, the depletion of natural fossil fuel resources and pollution of the environment due to carbon dioxide emission, there is a growing global need to develop renewable energy sources. However, the production of electrical energy from renewable sources requires reliable and efficient storage systems to meet worldwide demand. In recent decades, there has been significant interest in the development of new technologies to solve energy problems. In this context, significant efforts have been put into the research and development of more efficient energy storage devices and systems. An example of such a device is electrochemical energy storage devices such as batteries and supercapacitors, which are promising due to their high energy density and power. An electrochemical capacitor is a device that stores electrical energy in an electrical double layer that forms at the interface between an electrolytic solution and an electronic conductor [1].

Supercapacitors (SCs), a new type of system for energy storage and conversion, are getting a lot of attention. SC can be divided into two categories: electrical double-layer capacitors and pseudocapacitors that store electrical energy through electrosorption, reduction and oxidation reactions. At present, owing to the high energy density (approaching 180 $W \cdot h \cdot kg^{-1}$), lithium-ion batteries are widely used in consumer domestic electronics. However, because of the slow transport of electrons and ions in these batteries, heat generation and dendrite formation are observed when operating at high power, which can lead to serious safety problems [2, 3].

Due to their high conductivity and capacitance, ternary metal sulfides are widely used for energy storage. Recently, great interest is being attracted by pseudocapacitors based on cobalt-nickel sulfide $NiCo_2S_4$, as they have low cost, high conductivity, good electrochemical activity, and also exhibit several oxide states that provide a high redox potential, originating simultaneously from Ni and Co ions in contrast to individual NiO and Co_3O_4 [4]. They also show an electronic conductivity about 100 times higher than that of $NiCo_2O_4$, although $NiCo_2O_4$ has a much better electronic conductivity than NiO and Co_xO_y [5]. Various nanostructures

based on $NiCo_2S_4$, such as nanotubes, nanospheres, flower morphology, etc., have been synthesized for the production of supercapacitors.

Metal oxides represent an alternative as a promising material for manufacturing supercapacitor electrodes since they have a high specific capacitance and relatively low resistance, which simplifies the design of high energy and high-power supercapacitors [6]. In such materials, the mechanism of charge accumulation can occur both due to redox processes (Faraday reactions) and a double electric layer. Commonly used metal oxides are nickel oxide (NiO), ruthenium dioxide (RuO_2), manganese oxide (MnO_2), iridium oxide (IrO_2), tungsten oxide (WO_3), and cobalt oxide (Co_3O_4). Ternary metal oxides have advantages over single-component metal oxides because of the coexistence of a double metal cation, which allows for rich redox reactions.

In this study, our strategy is to improve electrochemical characteristics of electrodes based on cobalt-nickel oxide by sulfidization for supercapacitor devices. These electrodes demonstrated a high specific capacity for $NiCo_2S_4$ is 1976 F g^{-1} at a scan rate of 5 mV/s compared with $NiCo_2O_4$ (413 F g^{-1}). Characteristics such as the morphology and structure of the material are investigated, and the electrochemical characteristics of the electrodes are demonstrated.

Experimental

For hydrothermal synthesis, the precursors $CoCl_2$ (1.855 g), $NiCl_2$ (0.95 g) and urea (0.72 g) were dissolved in 60 ml of deionized water and stirred with a magnetic stirrer until a transparent homogeneous pink solution was formed. Then the solution was transferred to an autoclave, where a piece of nickel foam was also placed diagonally across the container. The autoclave was hermetically sealed and kept in a furnace at a temperature of 120°C for 6 hours. After cooling to room temperature, the precursor grown on nickel foam was washed with deionized water and dried at 50°C for 4 hours. The resulting $NiCo_2O_4$ product was sulfidized through hydrothermal treatment in an autoclave containing 1.8 g of Na_2S solution. The temperature of the furnace was 180°C, the treatment time lasted 8 hours. After cooling to room temperature, the resultant sample on a nickel substrate was processed in an ultrasonic bath to remove excess powders that did not adhere to the substrate. Then the samples were dried at a temperature of 50°C in air.

Results and Discussion

The phase composition in this work was determined using a MiniFlex Rigaku X-ray diffractometer. The XRD patterns were acquired by scanning in the range of 2θ from 5° to 90° and step size = 0.02°. The X-ray source was an X-ray tube with a copper anode, CuKα radiation at a wavelength of 1.5418 Å, operating parameters of the tube: voltage 40 kV, current 44 mA. Figure 1 illustrates the XRD data of the synthesized $NiCo_2O_4$ and $NiCo_2S_4$ samples. The results show the formation of nickel-cobalt oxide, which is characterized by intense peaks at 2θ angles of 36.7°, 55.5°, 59.1°, and 65.1°, and these reflections can be well identified as (311), (422), (511), and (440) reflections from the $NiCo_2O_4$ phase [7]. In addition, two intense diffraction peaks at 44.7° and 52.1° are indexed by the (111) and (200) diffraction planes of nickel, which correspond to the substrate. Figure 1b shows that after sulfurization, the XRD pattern shows distinct peaks at 31.6°, 38.3°, 50.5°, and 55.3°, which correspond to diffraction on the (311), (400), (511), and (440) planes that can be attributed to a cubic phase of $NiCo_2S_4$ (Fig. 1b). However, individual peaks at 21.69°, 31.4°, 38.26°, 50.3°, and 55.4° correspond to the (101), (110), (003), (113), and (300) diffraction planes characteristic for the Ni_3S_2 phase (PDF no. 24– 0334). This is because the replacement of Ni atoms by Co atoms does not change the crystal structure of Ni_3S_2, except for changing the lattice parameters [8].

Figure 2 demonstrates SEM images of samples obtained using a Quanta 200i 3D scanning electron microscope (FEI Company, USA, 2008). Figure 2a shows typical morphology of three-dimensional (3D) nickel foam with as synthesized samples. It can be seen (Fig. 2b) that $NiCo_2O_4$ nanostructures in the form of nanoneedles uniformly grown on the substrate. Also, the nanoneedles grew at various angles relative to the substrate. This is caused by the high concentration of the precursor, which affected the growth direction of the nanoneedles. The diameter of nanoneedles can reach up to 200 nm (Fig. 2c).

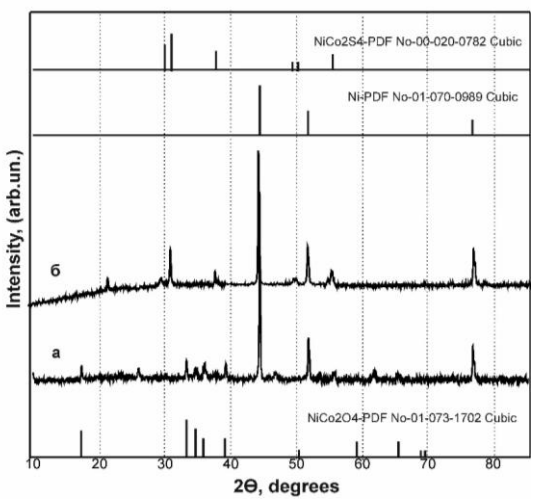

Figure 1. XRD pattern of synthesized samples $NiCo_2O_4$ (a) and $NiCo_2S_4$ (b)

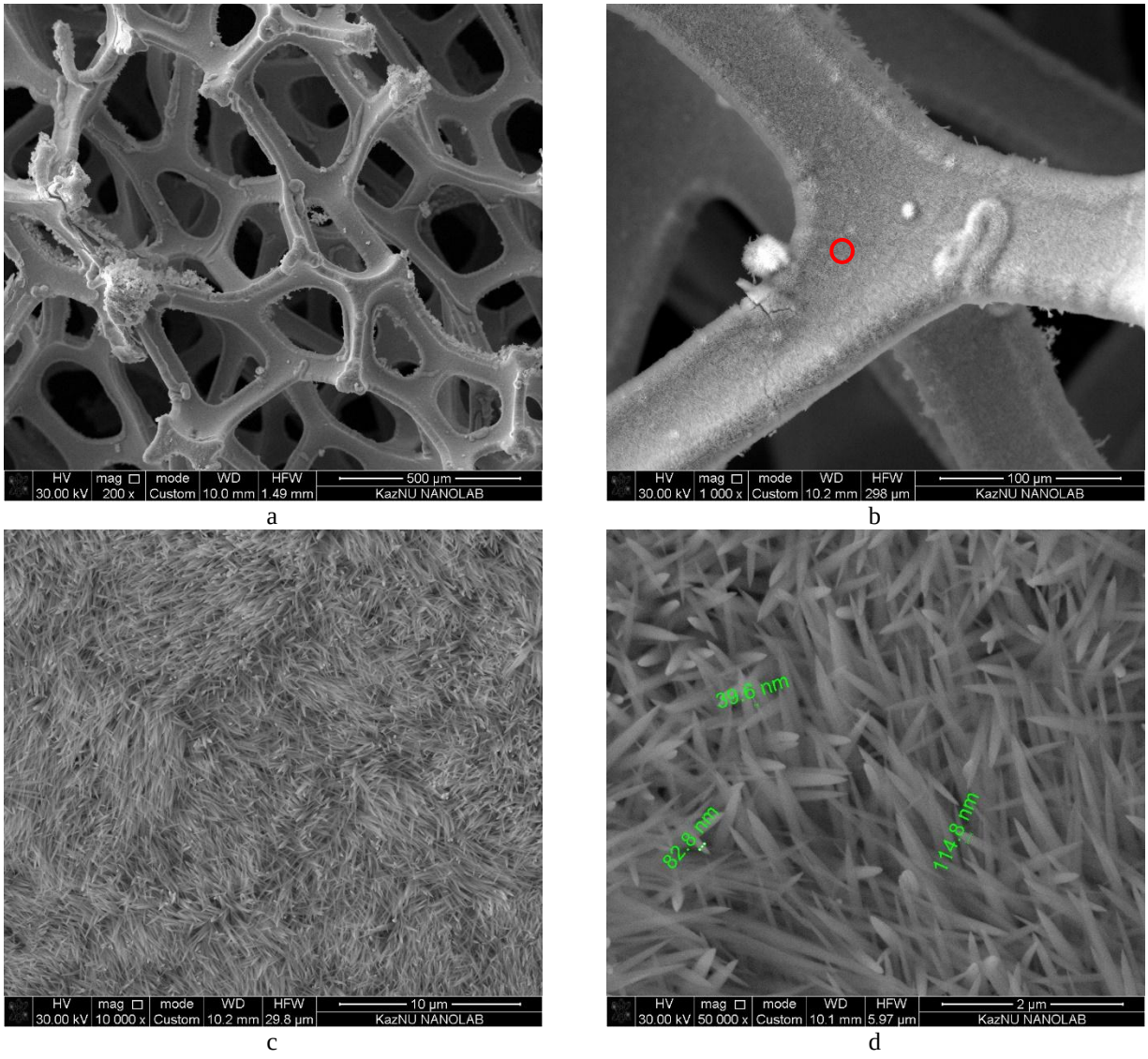

Figure 2. SEM images and morphology of $NiCo_2O_4$ at different magnifications

Figure 3 indicates the surface of the samples after sulfurization, exactly $NiCo_2S_4$ nanostructures. Figure 3a shows morphology with low magnification, so there are no changes compared to Figure 2a. Figure 3b also

has no distinguishing features compared to the samples before sulfurization. However, at high magnification (Figure 3c), there is no initially smooth surface of nanoneedles. Each needle has a nanosized branch, which increases the specific surface of the samples (Fig. 3d).

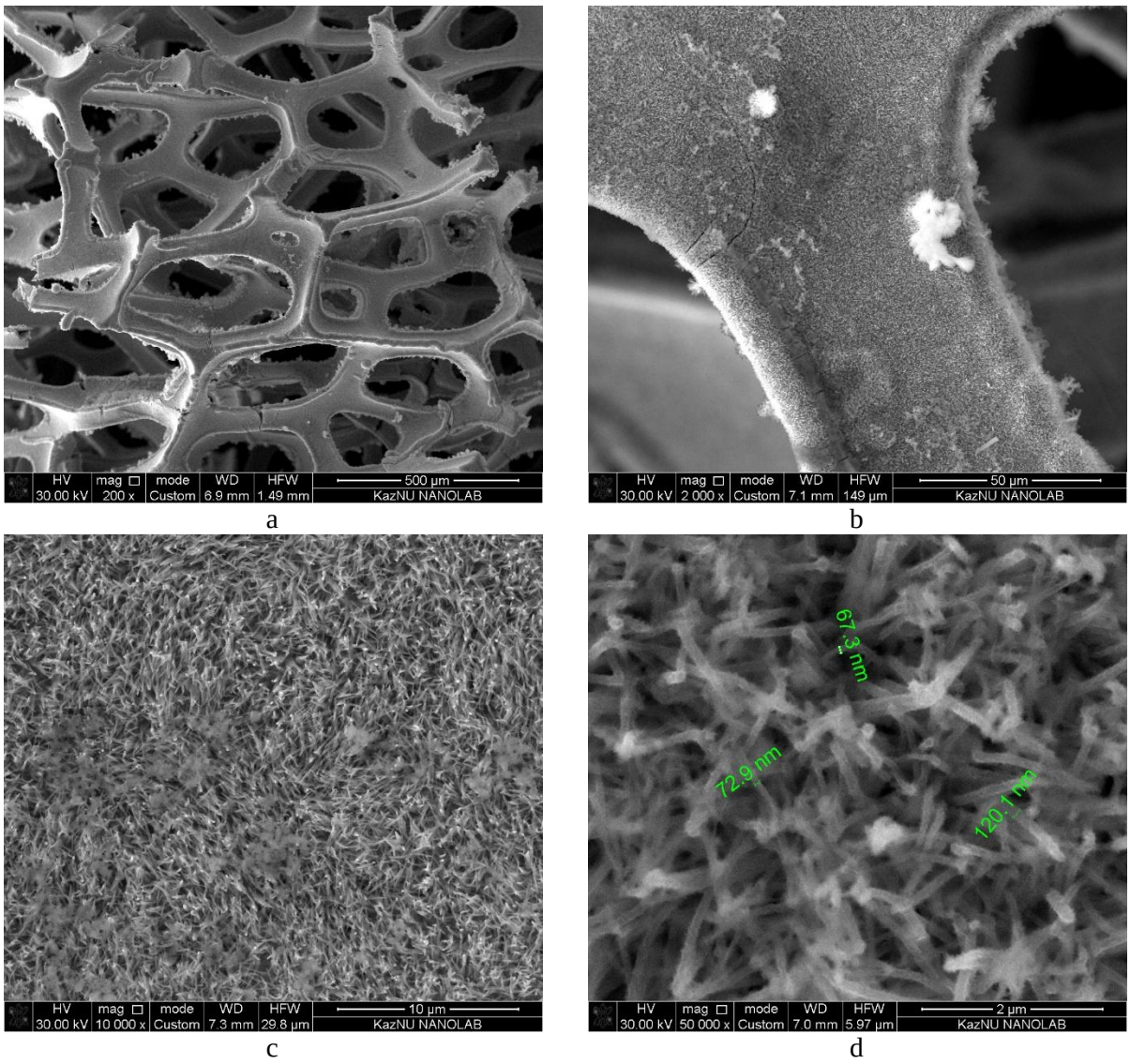

Figure 2. SEM images and morphology of $NiCo_2S_4$ at different magnifications

The electrochemical properties of the synthesized sample were tested by cyclic voltammetry (CV) and galvanostatic charge-discharge (GCD) measurements. All measurements of electrochemical characteristics were carried out using a 3M KOH aqueous electrolyte. In the three-electrode system, the active material in the form in which it was synthesized was used as the working electrode, while a platinum electrode was used as the counter electrode, and silver chloride (Ag/AgCl) electrode was used as the reference electrode. The area of the working electrode is 1×1 cm^2. Before measurement, the samples were pressed under a pressure of 3 MPa.

Figure 4 shows the CV (current-voltage) characteristics of the obtained $NiCo_2O_4$ and $NiCo_2S_4$ samples, measured in a three-electrode system at scan rates of 5, 10, 20, and 50 mV/s and a potential range of -0.2 to 0.5 V. The shape of the CV curves indicates that the capacitive characteristics correspond to a material with a typical pseudocapacitance, the CV characteristic strongly differs from the electric capacitance of a double layer, which demonstrates a CV shape close to rectangular [9]. Two pairs of observed peaks mainly result from the Faraday redox reactions Co(II)↔Co(III) and Ni(II)↔Ni(III) [10]. The mechanism of charge accumulation by $NiCo_2S_4$ in an alkaline electrolyte can be explained by the following reactions [11–12]:

$$CoS + OH^- \leftrightarrow CoSOH + e^- \quad (1)$$

$$CoSOH + OH^- \leftrightarrow CoSO + H_2O + e^- \quad (2)$$

$$NiS + OH^- \leftrightarrow NiSOH + e^- \quad (3)$$

with an increase in the scan rate, the anodic and cathodic peaks shift towards more positive and negative potentials, respectively, due to redox reaction that is determined by dynamics of charge transfer in both samples (Fig. 4a, b) [13].

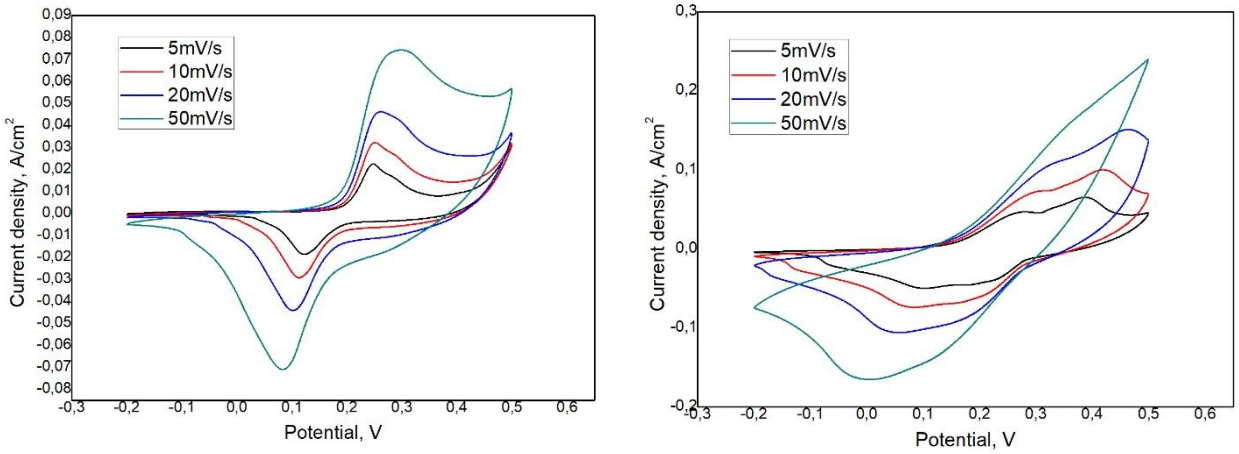

Figure 4. Cyclic voltammetry (CV) curves of $NiCo_2O_4$ (a) and $NiCo_2S_4$ (b) samples measured in a three-electrode system

It is seen from Frigure 5a that $NiCo_2S_4$ sample has a large area under CV curves compared to that of $NiCo_2O_4$. Specific capacitance C_s depicted in Figure 5b was calculated from the CV curves at three-electrode measurements using the following equation (4):

$$C_s = \frac{1}{2m\nu(V_{max}-V_{min})} \oint I(V)dV \quad (4)$$

where C_s – specific capacitance, m – mass of deposited material, ν – scan rate, V_{max}-V_{min} – potential window, I(V) – current, the integration is performed for 1 CV cycle. $NiCo_2S_4$ sample demonstrates high capacitance at all scan rates as opposed to $NiCo_2O_4$ sample. The C_s value considerably increases with decreasing scan rate since at a low scan rate H^+ ions diffuse deep inside the electrode. Maximal C_s value calculated from CV curves equals 1976 $F \cdot g^{-1}$ for $NiCo_2S_4$ and 413 $F \cdot g^{-1}$ for $NiCo_2O_4$.

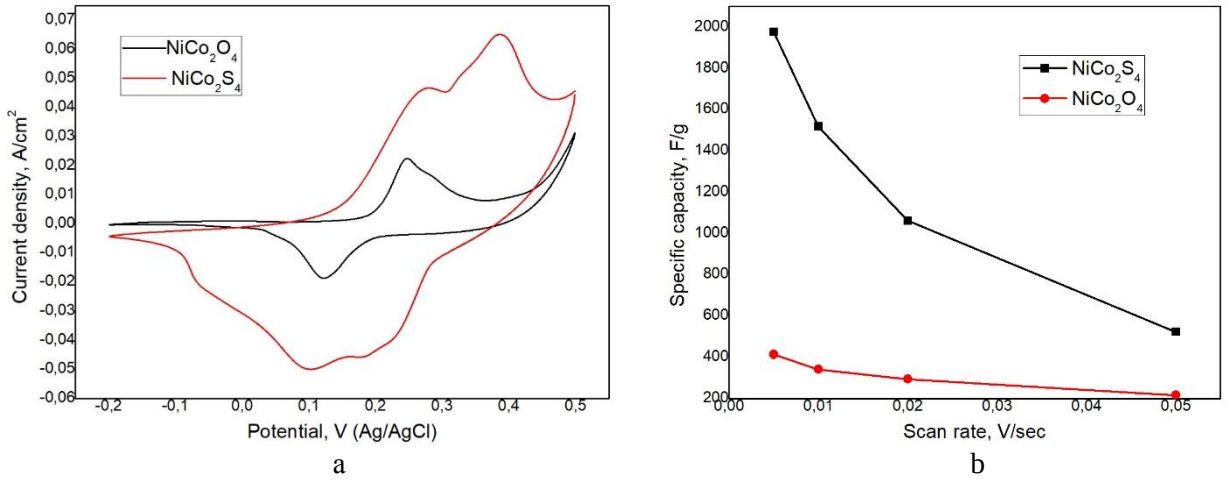

Figure 5. Comparative cyclic voltammetry curves of $NiCo_2O_4$ and $NiCo_2S_4$ samples measured at a scan rate of 5 mV/s (a) and dependence of specific capacitance on scan rate (b)

Conclusions

The paper presents the results of the synthesis of $NiCoO_x$ nanostructures for the development of electrochemical energy storage systems. Methods for the synthesis of $NiCo_2O_4$ nanostructures by the hydrothermal method were worked out, followed by the production of $NiCo_2S_4$ nanostructures by sulfidization. The main characteristics, such as structure, phase composition and morphology were determined, and comparative studies of the electrochemical characteristics of the electrodes were carried out. It is shown that the sulfidization of oxides leads to an increase in the conductivity and specific capacitance of the samples. High capacitance values (1976 $F \cdot g^{-1}$) were obtained, which is the main criterion in the development of energy storage systems. A comparison of the electrochemical properties showed that sulfidization of $NiCo_2O_4$ samples with the formation of the $NiCo_2S_4$ phase increases the electrical conductivity and increases capacitance by several times.

Acknowledgments

This research was funded by Program of the Committee of Science of the Ministry of Education and Science of the Republic of Kazakhstan, Grant No. AP09058501.

References

1 Winter, M., & Brodd, R.J. (2004). What are batteries, fuel cells, and supercapacitors. *Chemical reviews*, *104, 10,* 4245–4270.

2 Yang, Y., Liu, T., Zhang, L., Zhao, S., Zeng, W., Hussain, S., Deng, C., Pan, H., & Peng, X. (2016). Facile synthesis of nickel doped walnut-like MnO2 nanoflowers and their application in supercapacitor. *Journal of Materials Science: Materials in Electronics*, *27,* 6202–6207.

3 Borenstein, A., Hanna, O., Attias, R., Luski, S., Brousse, T., & Aurbach, D. (2017). Carbon-based composite materials for supercapacitor electrodes. *Journal of Materials Chemistry A, 5,* 12653–12672.

4 Cai, X., Shen, X., Ma, L., & Ji, Z. (2015). Facile synthesis of nickel-cobalt sulfide/reduced graphene oxide hybrid with enhanced capacitive performance. *RSC Advances*, *5, 72,* 58777–58783.

5 Xiao, J.W., Zeng, X.W., Chen, W., Xiao, F., & Wang, S. (2013). High electrocatalytic activity of self-standing hollow $NiCo_2S_4$ single crystalline nanorod arrays towards sulfide redox shuttles in quantum dot-sensitized solar cells. *Chemical Communication*, *49,* 11734–11736.

6 Makhanov, K.M., Ermaganbetov, K.T., Chirkova, L.V., Zeinidenov, A.K., & Arinova, E.T. (2018). Receiving and research of thin films of graphite and oxide of aluminium as bases for high capacitance capacitors. *Bulletin of the university of Karaganda-Physics*, 1(89), 32–38.

7 Wang, J., Wang, S., Huang, Z., & Yu, Y. (2014). High-performance $NiCo_2O4@Ni_3S_2$ core/shell mesoporous nanothorn arrays on Ni foam for supercapacitors. *Journal of Materials Chemistry A, 2, 41,* 17595–17601.

8 Mi, L., Wei, W., Huang, S., Cui, S., Zhang, W., Hou, H., & Chen, W. (2015). A nest-like $Ni@Ni_{1.4}Co_{1.6}S_2$ electrode for flexible high-performance rolling supercapacitor device design. *Journal of Materials Chemistry A, 3, 42,* 20973–20982.

9 An, C., Wang, Y., Wang, Y., Liu, G., Li, L., Qiu, F., Xu, Y., Jiao, L., & Yuan, H. (2013). Facile synthesis and superior supercapacitor performances of Ni_2P/rGO nanoparticles. *RSC Advances*, *3, 14,* 4628–4633.

10 Peng, S., Li, L., Li, C., Tan, H., Cai, R., Yu, H., Mhaisalkar, S., Srinivasan, M., Ramakrishna, S., & Yan, Q. (2013). In situ growth of $NiCo_2S_4$ nanosheets on graphene for high-performance supercapacitors. *Chemical communications*, *49, 86,* pp. 10178–10180.

11 Li, W., Zhang, B., Lin, R., Ho-Kimura, S., He, G., Zhou, X., Hu, J., & Parkin, I.P. (2018). A dendritic nickel cobalt sulfide nanostructure for alkaline battery electrodes. *Advanced Functional Materials*, *28, 23,* 1705937.

12 Wei, C., Zhan, N., Tao, J., Pang, S., Zhang, L., Cheng, C., & Zhang, D. (2018). Synthesis of hierarchically porous $NiCo_2S4$ core-shell hollow spheres via self-template route for high performance supercapacitors. *Applied Surface Science, 453,* 288–296.

13 Ouyang, Y., Xia, X., Ye, H., Wang, L., Jiao, X., Lei, W., & Hao, Q. (2018). Three-dimensional hierarchical structure ZnO@C@NiO on carbon cloth for asymmetric supercapacitor with enhanced cycle stability. *ACS applied materials & interfaces*, *10, 4,* 3549–3561.

А.А. Мархабаева, М.Б. Байділда, Ш.Т. Нұрболат,
Ж.К. Калкозова, Р.Р. Немкаева, Х.А. Абдуллин

Суперконденсаторларға арналған $NiCo_2O_4$ және $NiCo_2S_4$ наноқұрылымдардың электрохимиялық қасиеттерін салыстыру

Мақалада суперконденсаторларда электрод ретінде қолданылатын $NiCo_2O_4$ және $NiCo_2S_4$ наноқұрылымдарын гидротермалды әдіспен синтездеу және олардың қасиеттерін зерттеу нәтижелері көрсетілген. Үш оксиді металдан тұратын $NiCo_2O_4$ наноқұрылымдарын никель төсеніште өсіру әдісі оңтайланды. Алынған $NiCo_2O_4$ наноқұрылымдарының құрылымдық ерекшеліктері рентген фазалық

анализбен зерттелген. $NiCo_2O_4$ және $NiCo_2S_4$ нанокұрылымдарының үлгілері кубтық модификацияға ие екендігі анықталды. Алынған үлгілердің беттік морфологиясы сканерлеуші электрондық микроскопия арқылы зерттелінді. Үлгілер никель төсенішінде өскен наноине және нанотармақ пішіндес болып шықты. $NiCo_2O_4$ нанокұрылымдарын синтездеу әдісі және олардың өсуінің оңтайлы шарттары анықталды, сонымен қатар $NiCo_2O_4$ нанокұрылымдарынан күкірттеу әдісі арқылы $NiCo_2S_4$ нанокұрылымдарын алу әдісі тағайындалды. Күкірттеудің электрохимиялық сипаттамаларына әсерін байқау үшін салыстыру жұмыстары жүргізілді. Нәтижесінде, $NiCo_2O_4$ нанокұрылымдарының теориялық меншікті сыйымдылығы үлкен болғанына қарамастан, оттегі атомдарын күкірт атомдарына ауыстыру алынған $NiCo_2S_4$ үлгілердің меншікті сыйымдылығының жоғарлауына әкелетіндігі анықталды. $NiCo_2S_4$ электродтары үшін алынған ең үлкен меншікті сыйымдылық C_s 1976 Ф $г^{-1}$ және $NiCo_2O_4$ электродтары үшін 413 Ф $г^{-1}$ (5 мВ/сек сканерлеу жылдамдығында алынған) болды. Сонымен қатар, сканерлеу жылдамдығына меншікті сыйымдылықтың тәуелділігі берілген.

Кілт сөздер: суперконденсаторлар, энергияны сақтау, металл оксидтері, электродтар, наноматериалдар, $NiCo_2O_4$, $NiCo_2S_4$ және нанокұрылымдар.

А.А. Мархабаева, М.Б. Байділда, Ш.Т. Нұрболат,
Ж.К. Калкозова, Р.Р. Немкаева, Х.А. Абдуллин

Сравнение электрохимических характеристик наноструктуры из $NiCo_2O_4$ и $NiCo_2S_4$ для суперконденсаторов

В статье представлены результаты по синтезу и исследованию свойств наноструктур $NiCo_2O_4$ и $NiCo_2S_4$, полученных методом гидротермального синтеза для применения их в качестве электродов суперконденсаторов. Отработан метод выращивания наноструктуры из тройного оксида металлов $NiCo_2O_4$ на никелевой подложке. Изучены структурные особенности синтезированных наноструктур $NiCo_2O_4$ и $NiCo_2S_4$ с помощью рентгенофазового анализа. Полученные образцы имеют кубическую модификацию $NiCo_2O_4$ и $NiCo_2S_4$. Приведены данные по морфологии синтезированных образцов, полученных методом сканирующей электронной микроскопии. Образцы имеют форму наноиголки и нановетки, выращенные на никелевой подложке. Изучены методы синтеза наноструктур $NiCo_2O_4$ и определены оптимальные условия роста наноструктур из $NiCo_2O_4$, а также отработан метод сульфидизации $NiCo_2O_4$ для получения $NiCo_2S_4$ наноструктуры. Проведены сравнительные исследования по влияниям сульфидизации на электрохимические характеристики полученных электродов. Обнаружено, что, несмотря на то, что оксидные наноструктуры из $NiCo_2O_4$ имеют высокую теоретическую емкость, замена атомов кислорода на атомы серы повышает проводимость материалов и приводит к дальнейшему росту удельной емкости конечных электродов $NiCo_2S_4$. Максимальная C_s, полученная удельная емкость для $NiCo_2S_4$, составляет 1976 Ф $г^{-1}$, и тогда как для $NiCo_2O_4$ она равна 413 Ф $г^{-1}$ при скорости сканирования 5 мВ/с. Также представлены результаты зависимости удельной емкости от скорости сканирования при измерении.

Ключевые слова: суперконденсаторы, хранение энергии, оксиды металлов, электроды, наноматериалы, $NiCo_2O_4$, $NiCo_2S_4$ и наноструктуры.

DOI 10.31489/2022PH3/43-51

UDC: 621.794

Zh.B. Sagdoldina[1], D.R. Baizhan[1,2*], Y. Y. Kambarov[1,3], K. Torebek[1]

[1]*S. Amanzholov East Kazakhstan University, Ust-Kamenogorsk, Kazakhstan*
[2]*Institute of Composite Materials, Kazakhstan*
[3]*Plasma Science LLP, Kazakhstan*
(E-mail: daryn.baizhan@mail.ru)

Obtaining functional-gradient Ti-HA coatings by detonation spraying

Functional-gradient titanium/hydroxyapatite (TiHA) coatings were obtained using detonation spraying technology to improve the structure and mechanical properties. To obtain functional-gradient coatings, pulsed energy sources are best suited, namely, detonation spraying, in which the energy of the explosion of gas mixtures is used as a source of pulsed action. By controlling the modes of detonation spraying, it is possible to vary the temperature and rate of coating deposition; accordingly, it is possible to obtain a certain structural-phase structure of the coatings. The structural-phase state and tribological properties of TiHA detonation coatings were investigated by modern materials science methods: X-ray phase analysis (XRD), scanning electron microscopy (SEM), energy dispersive spectroscopy (EDX-mapping), profilometry and ball-disk wear-resistance test. The results showed that the coatings had a continuously gradient elemental composition across the cross-section of the coatings with no boundary between the elemental layers of the coatings. The amount of Ti gradually decreased and the amount of hydroxyapatite gradually increased in the direction from the substrate to the surface of the coatings, which allows to expand the possibilities of using TiHA-coatings for bone implants. Since the surface layer is composed of HA, the resulting functional-gradient coating demonstrates excellent biocompatibility and the ability to create new bone tissue. The excellent mechanical strength of the functionally graded coatings is ensured by the Ti phase.

Keywords: detonation spraying, functional gradient coatings, microstructure, phase composition, mechanical properties, hydroxyapatite, titanium, wear resistance, roughness.

Introduction

The development and production of biomaterials for bone replacement are one of the highly technological sectors of the economy, but the type and quality of implant materials and manufacturing technology currently available require further improvement. The “bottleneck” is not the medical technology associated with implant placement in the body, it is the engineering and materials science problems of producing an implant, with a specific chemical and phase composition and a specific morphological architecture [1]. One of the most promising solutions to these problems is the various combinations of metallic and non-metallic structures where the components gradually change in the materials. In particular, functional-gradient materials are new materials for both orthopaedic and dental applications. Currently, such materials are used for orthopaedic prostheses because functional-gradient materials can be adapted to reproduce the local properties of the original bone, which helps to minimise the effects of stress protection [2]. In stomatology, functional-gradient materials are used in dental crowns to imitate the connection of enamel and dentin of natural teeth and to avoid peeling and delamination between the layers [3, 4]. Various techniques such as PVD, CVD, and powder metallurgy have been used to produce functional-gradient materials [5–8]. In addition, functional-gradient materials have also been produced by gas-thermal spraying [9, 10]. Among the gas-thermal spraying methods, plasma spray technology has been used to produce various functional-gradient coatings suitable for biomedical applications. These include Ti/HA systems [11], HA/β-TCP [12], and HA/TiO_2 [13]. It is important to emphasise that in the widely used plasma spraying method for the application of coatings a continuous flame or plasma sputtering is used [14, 15]. This can lead to undesirable overheating or melting of the particles and a significant substrate temperature increase, which is a major limitation of this method. Pulsed energy sources like detonation spraying, which uses the energy of an explosion of gas mixtures as a pulse source, are best suited for obtaining functional-gradient coatings [16]. This technology, which operates in pulsed mode, is better for obtaining functional-gradient coatings. On one side, it allows for minimising the above-mentioned negative effects. For another, the particle velocity in the detonation spraying method is much higher than in plasma spraying methods, which positively influences important coating parameters such as adhesion strength.

Functional-gradient materials are peculiar and promising composite materials whose composition/components and/or microstructure gradually change in space according to a given profile or sequence,

along one or more space directions [10, 16–19]. Due to the gradual change in composition and/or microstructure, the physical and mechanical properties change in space according to the specific requirements for the prescribed application, which improves the operational characteristics of the material. Hydroxyapatite and Ti can be combined to create a perfect functional-gradient material. As the surface layer consists of HA, the resulting functional-gradient coating demonstrates excellent biocompatibility and the ability to create new bone. The excellent mechanical strength of the functional-gradient coatings is provided by the Ti phase.

There are no studies in the literature aimed at obtaining functional-gradient coatings using the detonation spraying method. Given the above, the purpose of this work is to obtain composite coatings having a gradient structure by changing the technological parameters of detonation spraying, where the HA ratio is characterized by a smooth change in the chemical composition, structure, and properties over the thickness of the coating.

Experimental

Composite HATi coatings with a thickness of about 60 μm were applied to a Ti6Al4V substrate using a CCDS2000 detonation complex (CCDS-2000, developed by Siberian Protective Coating Technologies LLC, Novosibirsk, Russia), the operation principle of which is described in detail in [20, 21]. Detonation spraying is performed by feeding combustible and oxidizing gases (propane, oxygen) into the channel in a ratio close to stoichiometric. The gas mixture is ignited in the channel by an electric spark. The ignition process is completed by the creation of a detonation wave, in the immediate vicinity of which the powder is injected into the channel by a dispenser device. During detonation combustion of a mixture of gases, propane and oxygen, the powder particles are affected by elevated temperatures, pressures and acceleration. The calculated temperature in the channel reaches 3000 K and the pressure is 5 MPa [22, 23]. At the beginning of the process, the gas powder cloud reaches a velocity of 1500 m/s, and then slightly melted powder particles are moved to the substrate at a velocity of up to 1000 m/s. Figure 1 demonstrates a general view and a schematic diagram of the detonation spraying process.

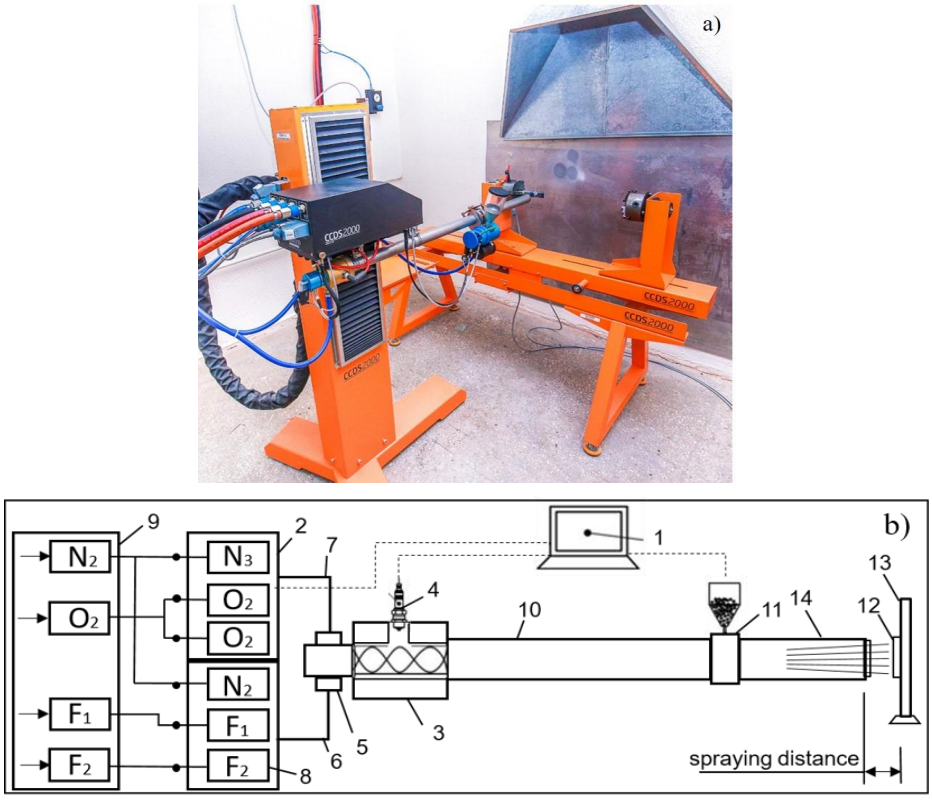

Figure 1. Computerized detonation complex CCDS2000: general view (a) and schematic diagram of the installation (b):
1 - control computer, 2 - gas distributor, 3 - mixing-ignition chamber, 4 - spark plug,
5 - barrel valve, 6 - fuel line, 7 - oxygen line, 8 - gas valves, 9 - gas supply unit, 10 - breech,
11 - powder dispenser, 12 - workpiece; 13 - manipulator, 14 - muzzle of the barrel

Ti6Al4V titanium alloy was used as the substrate material. The sample used to observe the microstructure was a rectangular size of 30 mm × 30mm × 3 mm. Table 1 presents the composition of the Ti6Al4V titanium alloy. The samples were sanded (using SiC paper with a grain size from 100 to 2000). Before coating, the substrates were sandblasted with a grain size of 250–300 microns of aluminium oxide and treated with an ultrasonic bath.

Table 1

Chemical composition of Ti6Al4V alloy (weight percent)

Ti	Al	V	Fe	C	O	N	H
88,5-92,5	5,5-6,5	3,5-4,5	<0,25	<0,08	<0,13	<0,05	<0,012

By characterizing the phase composition of the resulting HA coatings deposited at different spraying parameters, it is possible to determine suitable spraying conditions in DS. Our previous studies showed [24, 25] that by controlling the detonation spraying modes (fuel/oxidizer ratio, spraying distances) it is possible to control the temperature and speed of the coatings, respectively, which significantly influenced the melting and decomposition of HA. Preliminary studies of the microstructure, phase composition and chemical structure of DS HA coatings deposited at different spraying regimes were carried out, and the optimum spraying conditions for depositing composite HA coatings without a thermally decomposed HA phase were determined (Table 2).

Table 2

Spraying conditions

Parameters	Values
Fuel/oxidiser ratio	1,856
Spraying distance, mm	100

Based on this, Ti-HA composite coatings were obtained at different values of the barrel filling volume and different exposure times between shots to study the effect of detonation spraying process parameters on the chemical composition, structure, and properties of the coatings. The volume of the explosive gas mixture of the detonation gun barrel varied from 30% to 60% and the exposure time between shots varied from 0.25 s to 1 s. Table 3 shows the modes of production of Ti-HA-based coatings.

Table 3

Technological parameters for obtaining TiHA coatings

Name of the coatings	Barrel filling volume, %	Time between shots, s	Number of shots
TiHA-1	60	1	15
TiHA-2	45	0,5	15
TiHA-3	30	0,25	15

On this basis, Ti-HA-based coatings were obtained at different barrel filling volumes and different exposure times between shots to obtain coatings having a gradient structure. The HA ratio in these coatings is characterised by a smooth change in chemical composition, structure, and properties over the thickness of the coating (Table 4).

Table 4

Technological parameters for obtaining gradient coating

Name	Layers	Volume of barrel filling, %	Time between shots, s	Number of shots
Gradient	Top layer	30	0,25	5
	Middle layer	45	0,5	5
	Bottom layer	60	1	5

Angular hydroxyapatite (HA) powder (99.95%, produced by Sigma-Aldrich, Steinheim, Germany) with a diameter of 5-25 microns and spherical titanium powder (CL42TI) (made by Concept Laser, Germany) with a diameter of 15-45 microns were used as feedstock. HATi composite powders were obtained by

mechanically mixing HA powder with Ti powder for 0.5 x using a PULVERISETTE 23 planetary ball mill. The mass ratio HA toTi for composite powders HA-Ti was 50:50. The phase composition of the coatings was studied using X-ray diffractometer X'PertPRO (Philips Corporation, Amsterdam, the Netherlands) with Cu-Kα radiation (λ = 1.5405 Å), voltage 40 kV and current 30 mA. The diffractograms were interpreted using HighScore software and measurements were taken in the 2θ range of 20°-90° in 0.02 step and 0.5 s/step counting time. The coating structure was analysed by scanning electron microscopy (SEM) using a MIRA 3 TESCAN microscope. Sliding friction wear was evaluated on a TRB^3 tribometer (Anton Paar Srl, Peseux, Switzerland) using the standard ball-and-disk technique (ASTM G 133-95 and ASTM G99 international standards), where a 6.0 mm diameter ball of SiC coated steel was used as a counterbody, at 6 N load and 15 cm/s linear speed, 5 mm radius of curvature of wear, 200 m friction path. The surface roughness of the coatings was evaluated using a profilometer model 130 (OAO Zavod PROTON, Moscow, Russia).

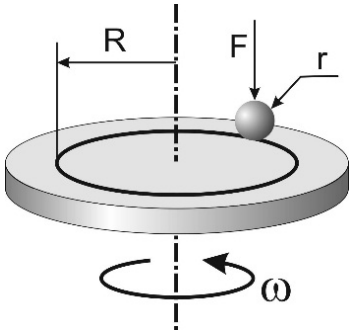

Figure 2. Experiment a schematic of the TRB^3 tribometer.

Results and Discussion

Figure 3 shows the diffractograms of the HATi composite coatings. It can be seen that the HATi composite coatings showed complex phases consisting of HA, Ti, TiO_2. HA, $Ca_3(PO_4)_2$ (TCP), and CaO thermal decomposition phases were not detected in any of the coatings. The peak intensities of HA phase decreased and the peak intensities of Ti and TiO_2 phases increased with increasing detonation spraying barrel filling volume. These results showed that the detonation spraying barrel filling volume is strongly influenced the phase composition. In addition, the diffraction patterns of the HATi composite coatings showed a decrease in the intensity of the Ti diffraction peaks indicating TiO_2 formation [26].

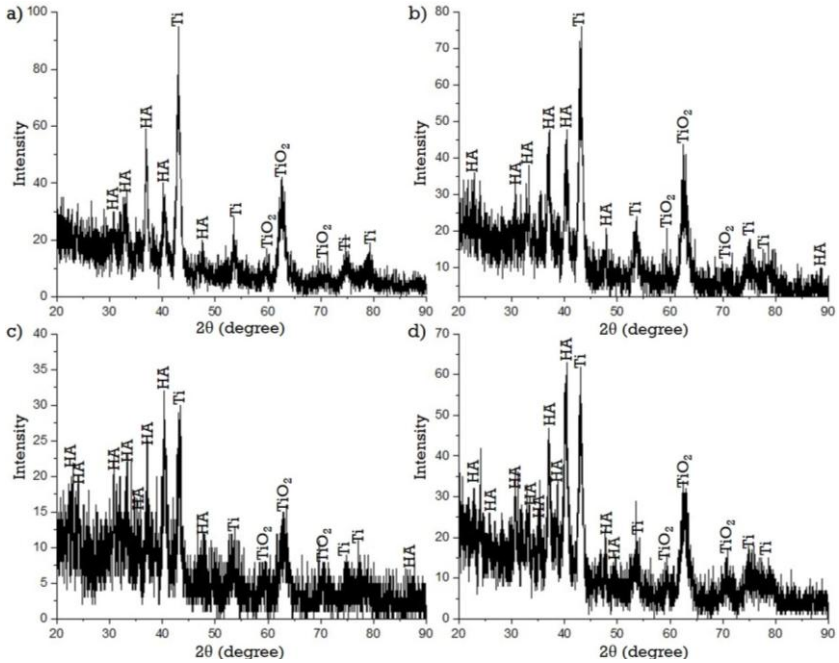

Figure 3. Diffractogram of coating TiHA: a) TiHA-1; b) TiHA-2; c) TiHA-3; d) gradient

Table 5 demonstrates the results of roughness measurements of composite and gradient coatings obtained by the detonation spraying method. The surface of all coatings has heterogeneous structure with pores, typical layered, wavy arrangement of structural components. The surface roughness of the composite coatings was measured using a model 130 profilometer on a 7 mm length segment on the sample surface. It follows from the obtained data that the roughness of composite coatings according to Ra parameter changes from 5.44 to 8.61 μm with change of technological parameters of detonation spraying. Comparison of these dependences allows to conclude that the coatings obtained with increase of detonation spraying barrel filling volume increase the roughness of coatings surface.

Table 5

Roughness measurement results for composite and gradient coatings

Name	Ra (μm)	Rz (μm)	Rt (μm)	Rq (μm)	Rv (μm)
TiHA-1	8,61	51,1	55,9	10,4	28,1
TiHA-2	6,58	44,3	46,6	8,42	27,6
TiHA-3	5,79	39,3	47,9	7,40	23,4
Gradient	5,44	39,9	48,5	6,51	22,6

Figure 4 shows a polished cross-section of the gradient coatings obtained by detonation spraying. The gradient coating consists of plates formed from molten particles during impact, some molten particles and small cracks. The presence of small cracks is beneficial in relieving thermal stresses during cooling. The total thickness of gradient coatings is about 60 μm. No obvious cracks appear at the interface between the coating and the substrate, which means that there is excellent adhesion between the coating and the substrate.

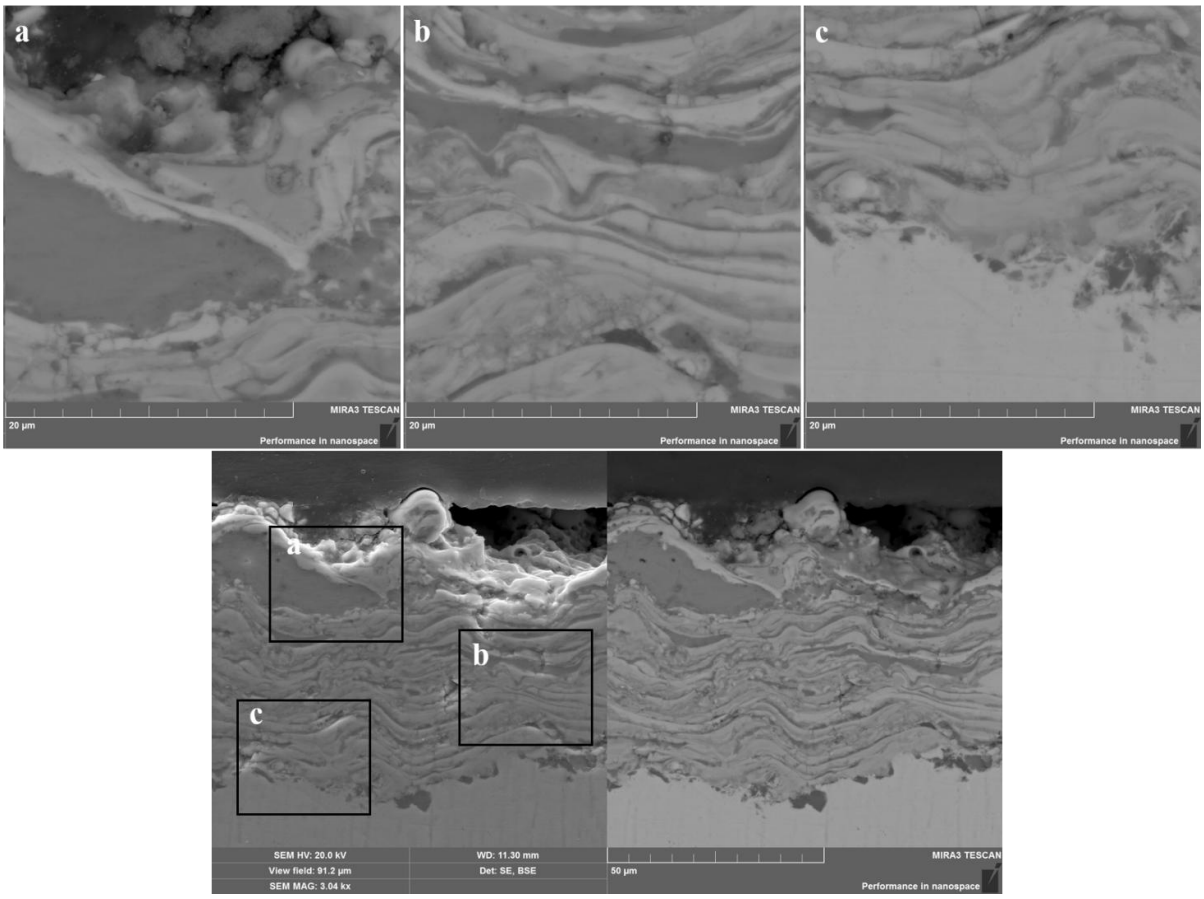

Figure 4. Cross-sectional microstructure of the HATi gradient coating.

EDS scanning light analysis shows that the coatings have a continuous gradient composition across the entire cross section with no distinguishable interface (Fig. 5 a, b, c). The Ca and P concentrations gradually increase from the substrate to the surface and the Ti concentration gradually decreases. The EDS compari-

sons for the gradient coating (Fig. 5 e, f) further confirm that the coating conforms to the expected gradient composition structure.

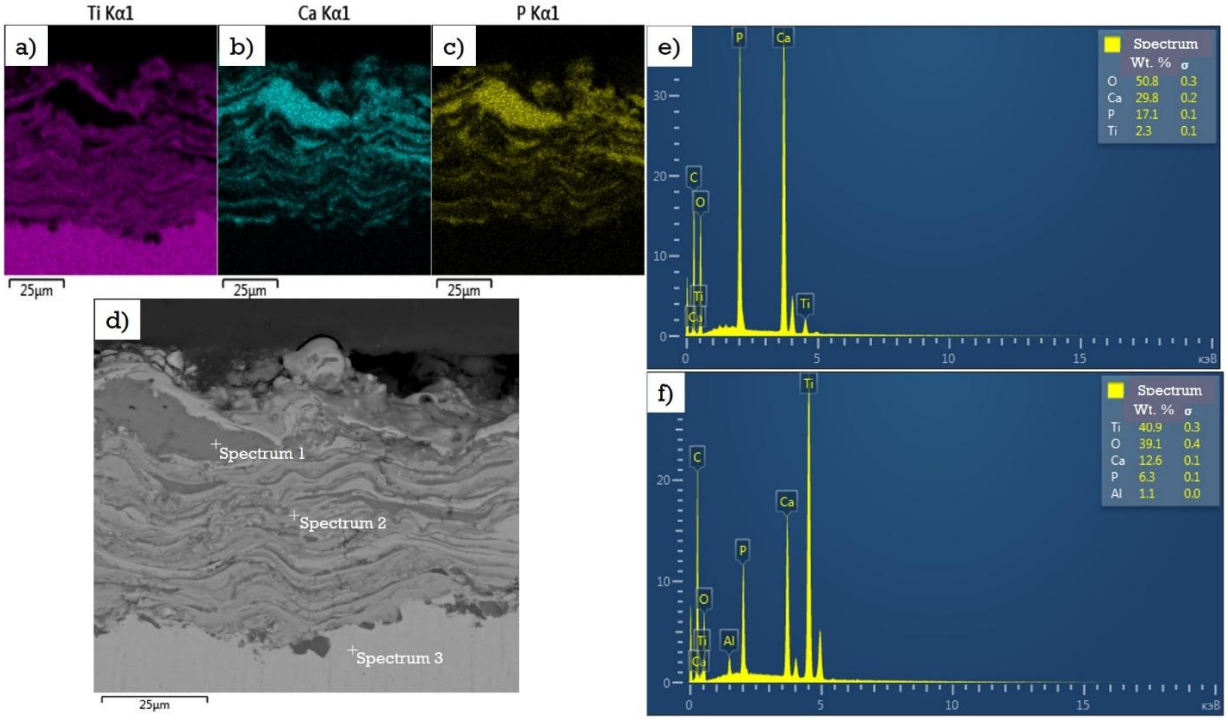

Figure 5. Cross-sectional microstructure and EDS analysis of the TiHA gradient coating.

To determine the wear resistance of the coatings, tribological tests were carried out in the ball-and-disk scheme. Figure 6 represents the friction coefficient of the composite and gradient TiHA coatings. According to the obtained results of tribological test of detonation coatings, TiHA-1 low friction coefficient values of 0.548 are observed, respectively high wear resistance in sliding friction conditions. However, the effect of surface roughness on the initial friction of the coatings is relatively higher compared to other coatings. An increase in barrel filling volume leads to an increase in the coefficient of friction of the coatings.

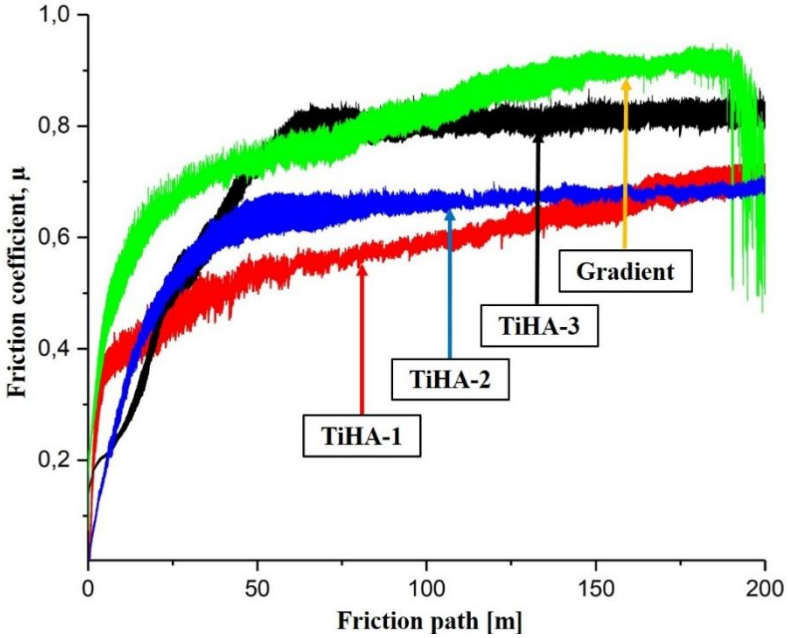

Figure 6. Coefficient of friction of composite and gradient coatings

Conclusions

The functional-gradient TiHA coating was successfully applied to the surface of Ti6Al4V alloy by detonation spraying. To obtain functional-gradient coatings, the following detonation spraying process parameters were varied: detonation barrel filling volume with acetylene-propane gas mixture from 60% to 30% and exposure time between shots from 1 to 0.25 s. A study of the phase composition of the coatings depending on the technological parameters showed that with increasing volume of barrel filling the content of HA phases in the composition of the coatings decreases, and the intensity of the diffraction peaks of Ti and TiO_2 increases. The study of the coatings surface morphology showed that the roughness of the coatings by Ra parameter varies from 5.44 to 8.61 μm with a change in the detonation barrel filling volume from 30% to 60%. The higher surface roughness and porosity of the outer layer of the functional gradient coating is a favourable microstructure for bone growth. We can conclude that the functional-gradient coatings obtained by the detonation spraying method have great potential for use as bioimplantation materials and need further research to reveal its hidden potential.

Acknowledgment

This research was funded by the Science Committee of the Ministry of Education and Science of the Republic of Kazakhstan (Grant No. AP13068485).

References

1 Corpe, R.S., Young, T.R., Steflik, D.E., Whitehead, R.Y., Wilson, M.D., & Jaramillo, C. (2000). Correlative experimental animal and human clinical retrieval evaluations of hydroxyapatite (HA)-coated and non-coated implants in orthopaedics and dentistry. *Journal of Critical Reviews in Biomedical Engineering. Prefac*, 28, 395–398.

2 Sagdoldina, Z., Rakhadilov, B., Skakov, M., & Stepanova, O. (2019). Structural evolution of ceramic coatings by mechanical alloying. *Materials testing*, 61, 304–308.

3 Rakhadilov, B.K., Baizhan, D.R., Sagdoldina, Zh.B., & Torebek, K. (2022). Research of regimes of applying coats by the method of plasma electrolytic oxidation on Ti-6Al-4V. *Bulletin of the university of Karaganda-Physics*, 1, 99–106.

4 Rakhadilov, B.K., Buitkenov, D.B., Sagdoldina, Z.B., Zhurerova, L.G., & Wieleba W. (2020). Preparation of powder coatings on the surface of steel balls by mechanochemical synthesis. *Bulletin of the university of Karaganda-Physics*, 4, 8–13.

5 Mamaeva, A., Kenzhegulov, A. Panichkin, A., Alibekov Z., & Wieleba W. (2022). Magnetron Sputtering Deposition Conditions on the Mechanical and Tribological Properties of Wear-Resistant Titanium Carbonitride Coatings. *Coatings*, 12.

6 Kenzhegulov, A.K., Mamaeva, A.A., Panichkin, A.V., Prosolov, K.A., Bronczyk, A., & Capanidis D. (2020). Investigation of the adhesion properties of calcium-phosphate coating to titanium substrate with regards to the parameters of high-frequency magnetron sputtering. *Acta of bioengineering and biomechanics*. 22, 111–120.

7 Mamaeva, A.A., Kenzhegulov, A.K., Panichkin, A.V., & Shah A. (2020). Obtaining hydroxyapatite coatings by mechanochemical interaction. *Kompleksnoe ispolzovanie mineralnogo syra*, 3, 76–83.

8 Mamaeva, A.A., Kenzhegulov, A.K., & Panichkin, A.V. (2018). Study of the Influence of Thermal Treatment on Hydroxyapatite Coating. *Protection of metals and physical chemistry of surfaces*, 54, 448–452.

9 Ramasamy, P., & Sundharam S. (2021). Microhardness and corrosion resistance of plasma sprayed bioceramic bilayer coated Ti-6Al-4V implants. *Journal of the Australian Ceramic Society*, 57, 605–613.

10 Singh, B., Singh, G., & Sidhu, B. (2019). Investigation of the in vitro corrosion behavior and biocompatibility of niobium (Nb)-reinforced hydroxyapatite (HA) coating on CoCr alloy for medical implants. *Journal of Materials Research*, 34, 1678–1691.

11 Zhao, G., Xia, L., Wen, G., Song, L., Wang, X., & Wu, K. (2012). Microstructure and properties of plasma-sprayed bio-coatings on a low-modulus titanium alloy from milled HA/Ti powders. *Surface and Coatings Technology*, 206, 4711–4719.

12 Yang, S., Man, H.C., Xing, W., & Zheng, X. (2009). Adhesion strength of plasma-sprayed hydroxyapatite coatings on laser gas-nitrided pure titanium. *Surface and Coatings Technology*, 203, 3116–3122.

13 Singh, H., Prakash, C., & Singh, S. (2020). Plasma spray deposition of HA-TiO_2 on β-phase Ti-35Nb-7Ta-5Zr alloy for hip stem: Characterization of bio-mechanical properties, wettability, and wear resistance. *Journal of Bionic Engineering*, 17, 1029–1044.

14 Mamaeva, A., Kenzhegulov, A., Kowalewski, P., & Wieleba, W. (2017). Investigation of hydroxyapatite-titanium composite properties during heat treatment. *Acta of bioengineering and biomechanics*, 19, 161–169.

15 Hannora, A., Mamaeva, A., & Mansurov, Z. (2009). X-ray investigation of Ti-doped hydroxyapatite coating by mechanical alloying. *Surface review and letters*, 16, 781–786.

16 Rakhadilov, B.K., Baizhan, D.R., Sagdoldina, Z.B., Buitkenov, D.B., & Maulet, M. (2020). Phase composition and structure of composite Ti/HA coatings synthesized by detonation spraying. *AIP Conference Proceedings*, 2297, 020022.

17 Erkmen, Z.E. (1999). The effect of heat treatment on the morphology of D-gun sprayed hydroxyapatite coatings. *Journal of Biomedical Materials Research* , 48(6), 861-868.

18 Rakhadilov, B.K., Kenesbekov, A.B., Kowalevski, P., Ocheredko, Y.A., & Sagdoldina, Zh.B. (2020). Development of air-plasma technology for hardening cutting tools by applying wear-resistant coatings. *News of the National Academy of sciences of the Republic of Kazakhstan-series of geology and technical sciences*.3, 54–62.

19 Chen, H., Wang, C., Yang, X., Xiao, Z., Zhu, X., Zhang, K., Fan, Y., & Zhang, X. (2017). Construction of surface HA/TiO_2 coating on porous titanium scaffolds and its preliminary biological evaluation. *Materials Science and Engineering.* 70, 1047–1056.

20 Rakhadilov, B., Buitkenov, D., Idrisheva, Z., Zhamanbayeva, M., Pazylbek, S., & Baizhan, D. (2021). Effect of pulsed-plasma treatment on the structural-phase composition and tribological properties of detonation coatings based on Ti–Si–C. *Coatings*, 11.

21 Rakhadilov, B., Kakimzhanov, D., Baizhan, D., Muslimanova, G., Pazylbek, S., & Zhurerova L. (2021). Comparative Study of Structures and Properties of Detonation Coatings with alpha-Al_2O_3 and gamma-Al_2O_3 Main Phases. *Coatings*, 11.

22 Baizhan, D.R., Rakhadilov, B.K., Zhurerova, L.G., & Torebek, K. (2022). Preparation of bio-ceramic composite coatings on Ti6Al4V titanium alloy by gas-detonation spraying. *Bulletin of the university of Karaganda-Physics*, 1, 89–98.

23 Rakhadilov, B., & Baizhan, D., (2021). Creation of Bioceramic Coatings on the Surface of Ti-6Al-4V Alloy by Plasma Electrolytic Oxidation Followed by Gas Detonation Spraying. *Coatings*, 11.

24 Rakhadilov, B., Maulet, M., Abilev. M., Sagdoldina, Z., & Kozhanova, R. (2021). Structure and tribological properties of Ni-Cr-Al-based gradient coating prepared by detonation spraying. *Coatings*, 11(2), 1-14.

25 Gledhill, H.C., Turner, I.G., & Doyle, C. (1999). Direct morphological comparison of vacuum plasma sprayed and detonation gun sprayed hydroxyapatite coatings for orthopaedic applications. *Biomaterials*, 20, 315–322.

26 Gledhill, H. (2001). In vitro fatigue behaviour of vacuum plasma and detonation gun sprayed hydroxyapatite coatings. *Biomaterials*, 22, 1233–1240.

Ж.Б. Сағдолдина, Д.Р. Байжан, Е.Е. Қамбаров, Қ. Төребек

Детонациялық бүрку әдісімен функционалды-градиентті жабындарды алу

Функционалды градиентті титан / гидроксиапатит (TiHA) жабыны құрылымы мен механикалық қасиеттерін жақсарту үшін детонациялық бүрку технологиясын қолдану арқылы алынды. Функционалды-градиентті жабындарды алу үшін импульсті энергия көздері ең қолайлы, атап айтқанда, газ қоспаларының жарылыс энергиясы импульстік әрекет көзі ретінде пайдаланылатын детонациялық бүрку. Детонациялық бүрку режимдерін басқару арқылы жабынның тұндыру температурасы мен жылдамдығын өзгертуге болады, сәйкесінше жабындардың белгілі құрылымдық-фазалық құрылымын алуға болады. TiHA детонациялық жабындарының құрылымдық-фазалық күйлері мен трибилогиялық қасиеттері заманауи материалтану әдістерімен анықталды: рентгенофазалық талдау (XRD), сканерлеуші электронды микроскопия (SEM), энергодисперсиялық спектроскопия (EDX-карталау), профильометрия және «шар-диск» схемасы бойынша тозуға төзімділігін сынау. Нәтижелер жабындардың элементтік интерфейсінсіз жабындардың көлденең қимасы бойынша үздіксіз градиентті элементтік құрамы бар екенін көрсетті. Ті мөлшері біртіндеп азайды, ал гидроксиапатит мөлшері субстраттан жабын бетіне қарай біртіндеп өсті, бұл сүйек имплантары үшін TiHA жабындарын қолдану мүмкіндігін кеңейтуге мүмкіндік береді. Беткі қабат HA–дан тұратындықтан, алынған функционалды градиент жабыны керемет биожетімділік пен жаңа сүйек тінін жасау қабілетін жақсартады. Функционалды-градиент жабындарының жоғары механикалық беріктігі Ті фазасымен қамтамасыз етіледі.

Кілт сөздер: детонациялық бүрку, функционалды градиентті жабындар, микроқұрылым, фазалық құрамы, механикалық қасиеттері, гидроксиапатит, титан, тозуға төзімділігі, кедір-бұдырлығы.

Ж.Б. Сагдолдина, Д.Р. Байжан, Е.Е. Камбаров, К. Торебек

Получение функционально-градиентных TiHA покрытий методом детонационного напыления

Функционально-градиентные покрытия титан/гидроксиапатит (TiHA) были получены с использованием технологии детонационного напыления с целью улучшения структуры и механических свойств. Для получения функционально-градиентных покрытий лучше всего подходят импульсные источники энергии, а именно детонационное напыление, в котором в качестве источника импульсного действия используют энергию взрыва газовых смесей. Управляя режимами детонационного напыления, можно варьировать температуру и скорость нанесения покрытий, соответственно, можно получить определенное структурно-фазовое строение покрытий. Структурно-фазовое состояние и трибилогические свойства детонационных покрытий TiHA исследованы методами современного материаловедения: рентгенофазного анализа (XRD), сканирующей электронной микроскопии (SEM), энергодисперсионной спектроскопией (EDX-картирование), профилометрии и испытанием на износотойкость по схеме «шар–диск». Результаты показали, что покрытия имели непрерывный градиентный элементный состав по поперечному сечению покрытий без границы раздела элементных слов покрытий. Количество *Ti* постепенно уменьшалось, а

количество гидроксиапатита постепенно увеличивалось по направлению от подложки к поверхности покрытий, что позволяет расширить возможности применения *TiHA* покрытий для костных имплантатов. Поскольку поверхностный слой состоит из *HA*, полученное функционально-градиентное покрытие демонстрирует отличную биосовместимость и способность для создания новой костной ткани. Превосходная механическая прочность функционально-градиентных покрытий обеспечивается фазой *Ti*.

Ключевые слова: детонационное напыление, функциональные градиентные покрытия, микроструктура, фазовый состав, механические свойства, гидроксиапатит, титан, износостойкость, шероховатость.

DOI 10.31489/2022PH3/52-60

UDC 678.742.3(54.03)

Q.N. Berdinazarov*, E.O. Khakberdiev, N.F. Normurodov, N.R. Ashurov

Uzbekistan Academy of Sciences, Institute of Polymer Chemistry and Physics, Tashkent, Uzbekistan
*(*E-mail: qodirberdinazarov@mail.ru)*

Mechanical and thermal degradation properties of Isotactic Polypropylene Composites with Cloisite15A and Cloisite20A

This work studies the influence of maleic anhydride grafted polypropylene (PP-g-MA) content on thermal and mechanical properties of polypropylene (PP) composites with two types of clays, differing modifier density in the interlayer space, Cloisite15A and Cloisite20A. PP/clay composites are melt blended in presence of different content of PP-g-MA from 3, 6, 9, and 12 wt.%. It is found that Cloisite15A with a high density of the modifier promotes the formation of intercalated structures, while Cloisite20A with a low density of the modifier, predominantly exfoliated nanocomposites are formed. In the first case, the structure tends to become intercalated whilst composites with Cloisite20A favor the formation of predominantly exfoliated structures. The formation of the nanocomposite is accompanied by a significant increase in thermal stability (50% weight loss is observed at temperatures of 360°C and 430°C for polypropylene and nanocomposites based on it, respectively). An analysis of the mechanical properties of nanocomposites generally indicates an increase in the elastic modulus by 15-20%, and this effect is more pronounced for exfoliated structures, the yield strength practically does not change and the elongation at break decreases noticeably.

Keywords: polypropylene, clay, composite, polypropylene grafted maleic anhydride, intercalation, exfoliation, oxidation, montmorillonite.

Introduction

Recently conducted researches in polymer science have shown finer dispersed inorganic layered silicates or smectite clays through the organic polymer, increasing its mechanical, thermal, barrier, and fire retardant properties [1–7]. Layered silicates are made up of several hundred thin platelets stacked in orderly particles or tactoids with dimensions of 8–10 μm. Each disk-shaped platelet has a large aspect ratio of approximately 100–1000 and is easily agglomerated due to the interlayer van der Waals forces. Accordingly, clay particles should be homogeneously finer dispersed and exfoliated as individual platelets within the polymer matrices to accomplish the ultimate properties. Moreover, the lower clay content is also essential to achieve the large contact surface area between the polymer matrix and the fillers and to obtain good dispersion by alleviating the clay aggregation [8, 9].

Thermal stability of PP/clay composites was considerably increased as soon as obtained exfoliated structure [10–16]. The authors concluded that the improvement in the thermal properties was correlated with lower oxygen permeability resulting from an increased diffusion path for oxygen as well as volatile decomposition products. PP-g-MA was found the most effective compatibilizer for PP/clay composites in many articles [17–20]. There are a lot of publications that investigate the effect of different clay modification techniques [21, 22].

Phase diagram of polymer – clay mixture, proposed by Ginzburg et al., revealed that increased length and density of grafted chains led to improved miscibility of the clay and the polymer, in its turn, proper miscibility contributes to exfoliated structure in the wide range of clay volume ratio. In the case of short surfactant macromolecules, the polymer is not likely to insert space between the clay layers. This causes immiscible equilibrium morphology for major values of the Flory – Huggins parameter and the clay volume ratio. There is also a limitation to strong interaction between grafted chains and polymer macromolecules [23].

For different surfactant lengths, surfactant coverage and surfactant – matrix enthalpic, Balazs et al. studied morphological behavior of polymer clay composites by employing their model named self-consistent field calculation. According to their model, it turned out that a longer organic modifier provides better intercalation of polymer macromolecules to penetrate the space between clay platelets. But, the density of surfactant should be reasonable because dense coverage makes intercalation and/or exfoliation impossible [24].

Accordingly, in this paper isotactic PP, PP-g-MA, and two types of clays were chosen in obtaining composites. This study aims to explore the properties of PP/clay nanocomposites obtained with different modifier densities between interlayer spaces in the variation of compatibilizer content.

Experimental:

Materials: Isotactic PP (J-170T) with MFI = (2.16 kg, 230ºC) 21 g/10 min was kindly provided by JV Uz-Kor Gas Chemical LLC. PPMA with 2,5 wt.% maleic anhydride content and MFI = (2,16 kg, 230 ºC) >200 g/min was provided by JV UzAuto CEPLA LLC as a gift. Cloisite15A, (spacing d_{001}=2,96 nm, dimethyl dehydrogenated tallow ammonium conc. 1,25 meq/g), Cloisite20A, (spacing d_{001}=2,47 nm, dimethyl dehydrogenated tallow ammonium conc. 0,95 meq/g) Southern Clay Products, Inc., Gonzales, TX.

Preparation: Components melt blended in Brabender Plastograph (Germany). First PP and PPMA were introduced into plastograph after getting molten mass clay was introduced and kept for 8 min 150 rpm to provide better mixing components one another. Next, tensile test samples were prepared by injection-molding machine Mercator 1971 (Poland). The name of samples and their content ratios are given in Table 1.

Table 1

Name of the obtained samples and their contents

Name of samples	PP, %	PP-g-MA, %	Cloisite15A, %	Cloisite20A,%
PP	100	-	-	-
PPMA	-	100	-	-
PP/MA10	90	10	-	-
PP/MA20	80	20	-	-
15A3	94	3	3	-
15A6	91	6	3	-
15A9	88	9	3	-
15A12	85	12	3	-
20A3	94	3	-	3
20A6	91	6	-	3
20A9	88	9	-	3
20A12	85	12	-	3

XRD measurements

XRD measurements were conducted with Rigaku Miniflex 600 (Japan) in the condition of 40 kV voltage, 15 mA current and 0.02° step.

DSC and TGA measurements

Thermal properties of the samples studied by DSC and TGA analysis were conducted simultaneously, in the range from room temperature to 600ºC by Linseis thermal analysis PT1610.

Mechanical analysis

Tensile tests were conducted according to ASTMD 638 in Shimadzu AG-X PLUS (Japan). For measuring tensile module (E), 1 mm/min crosshead speed was chosen until 0,3% deformation, after that crosshead speed increased immediately to 20 mm/min for further exploring yield stress ($\boldsymbol{\sigma}$) and deformation ($\boldsymbol{\varepsilon}$).

MFI measurement

MFI was measured according to ASTMD 1238 using a Zwick extrusion plastometer (Germany) at 230 ºC/2,16 kg.

Results and Discussion

Small angle X-ray diffraction

Small angle X-ray (SAXS) diffraction is identical for characterizing clay dispersion in the polymer matrix [25–27]. The basal spacing of the silicate layer (d001) was calculated with Bragg's law: $n\lambda=2d\sin\theta$. Figures 1 and 2 show the SAXS pattern of obtained samples. The difference between these two organically modified clays is modifier volume and interlayer distance d (which Cloisite15A has greater than Cloisite20A) [28]. Cloisites have two main peaks, the second peak at $2\theta=7{,}2°$ (d001=1,2 nm) corresponding to interlayer distance of pure unmodified montmorillonite (MMT), the first peak occurs in $2\theta=2{,}88°$ in Cloisite15A corresponding to intercalation of MMT as a result of modifier penetration during modification while in Cloisite20A, this peak accounts for in $2\theta=3{,}68°$. SAXS curves in Figures 1 and 2, compare the effect of PP-g-MA content on the intercalation degree of Cloisite15A and Cloisite20A. There was a considerable difference between the dispersion of clay through the PP matrix. While composites with Cloisite15A show an intercalated structure, Cloisite20A achieves exfoliation except for 20A3. In the case of Cloisite15A,

the first peak in 2θ=2,8° shifts towards small angles about 2θ=2,3° corresponding to d=38,25Å, however, 15A9 has slightly smaller angles than others, indicating all samples' intercalation. The second peak also decreased from 2θ=7,2° to 2θ=4,7°. With respect to the intensity of the peaks, the smallest intensity was seen in both main peaks in 15A9. This reduction in the peak intensity can be interpreted as the formation particular amount of exfoliated structure as well as intercalated. When it comes to Cloisite20A, except for composite with 20A3 all had a considerable shift in peaks to lower than 2θ=2° angle, as a result of exfoliation. The reason for exception 20A3 is the lack of compatibilizer to achieve finer dispersion of clay in the polymer matrix. The occurrence of exfoliation in the composites with Cloisite20A can be proved to shift the first peak smaller angle in relation to pure Cloisite20A.

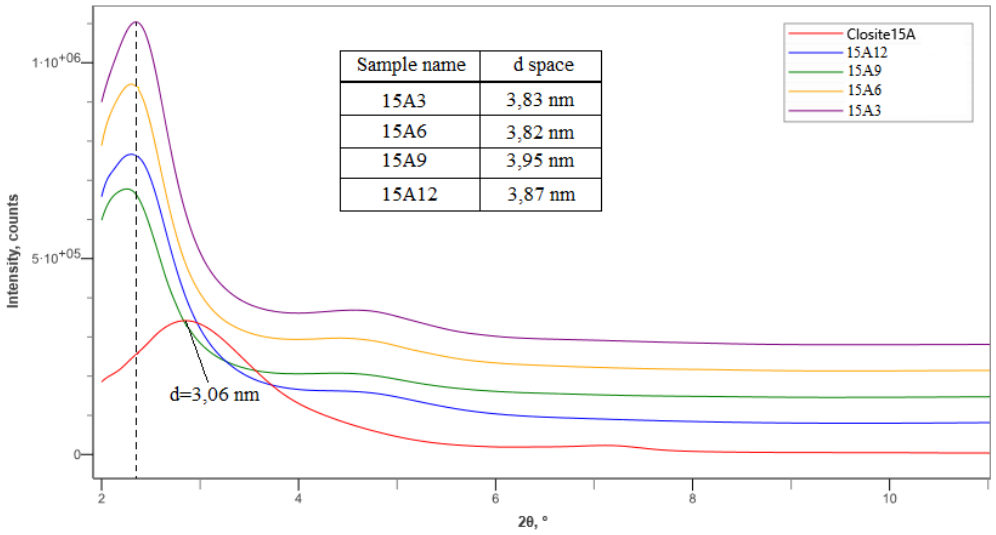

Figure 1. PP and Cloisite15A composites small angle X-ray curves

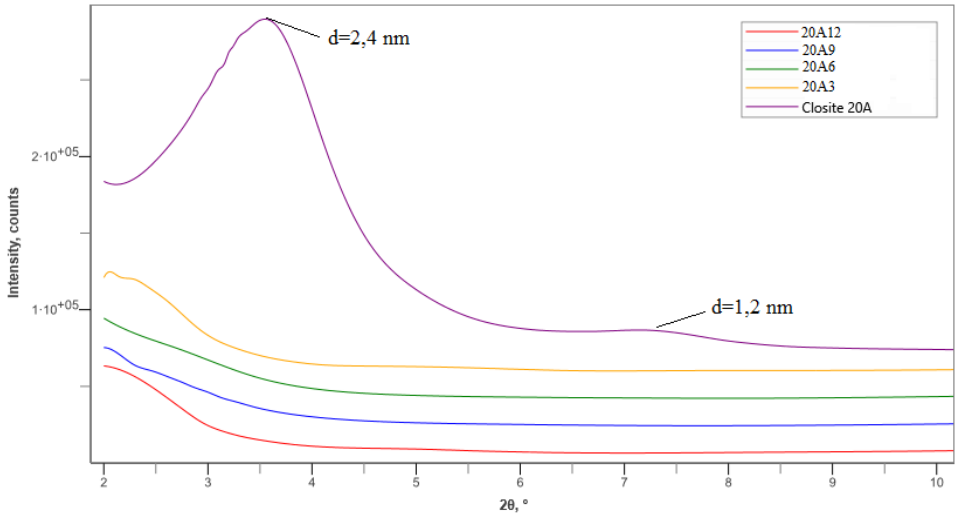

Figure 2. PP and Cloisite20A composites small angle X-ray curves *MFI*

Figure 3 compares MFIs of PP and PP-g-MA blends. PP-g-MA shows more than 200 g/10 min MFI while PP has 21 g/10 min. The presence of 10 wt. % PP-g-MA in PP/PPMA blends MFI accounts for 56 g/10 min and further addition of PP-g-MA increases MFI to 94 g/10 min. This is due to the low molecular weight of PP-g-MA and, as shown in a number of works [14, 15, 23, 24], it is oligomeric functionalized PP that provides favorable conditions for intercalation in the interlayer space and subsequent exfoliation of MMT particles. For PP and clay systems, MFI decreases as soon as the formation of exfoliated and intercalated structures. Our compositions also exhibited such kind of manner (Figure 4). For composites with Cloisite15A, when the ratio of compatibilizer/filler was 1, MFI is 58,6 g/10 min and as compatibilizer content increases MFI decreases to 17,5 g/10 min in the 15A9, however, subsequent addition of PP-g-MA caus-

es slight growth in the 15A12. The initial reduction in MFI is related to the extension of clay particle dimensions as a result of intercalation. When PP-g-MA content reaches saturation point, that is 9 wt.%, additional PP-g-MA causes to increase in MFI. With regard to composites with Cloisite20A, an optimal amount of compatibilizer is 6 wt.% and extra compatibilizer by not taking part in intercalation or exfoliation just leads to the increase in the melt flow. Intercalated centers in the form of physical knots (similar to crosslinking), as PP-g-MA increases, leads to an increase in the viscosity of the composition, for exfoliated structures (uniform distribution of nanoparticles) an extreme viscosity dependence is observed with a minimum at a PP-g-MA content of 6% wt. For these structures, the contribution of low-viscosity PP-g-MA above 6 wt.% becomes noticeable.

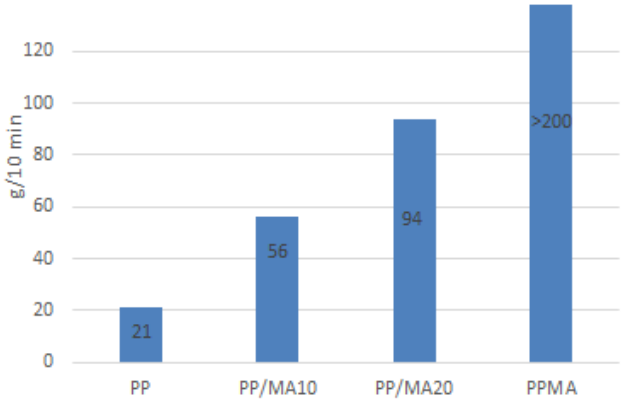

Figure 3. MFI of PP and PP-g-MA blends

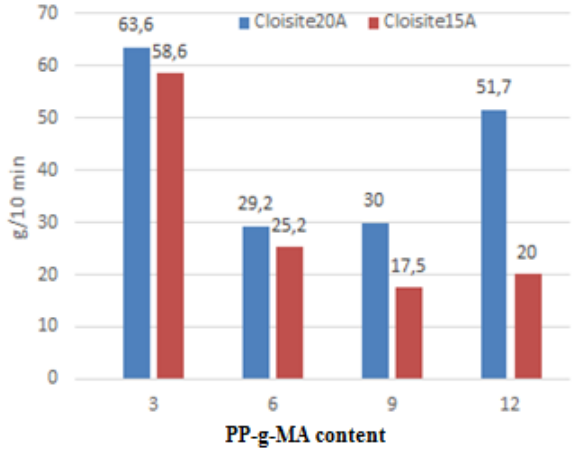

Figure 4. MFI of composites based on Cloisite15A and Cloisite20A.

DSC and TGA measurements

DSC curves for PP and PPMA blends show different oxidation behavior while the melting temperature of the samples is almost the same. Showing a melting point of 158,5°C, PP stands stable until 220°C, and subsequent heating causes intensive oxidation. PP-g-MA with a melting point of 160,6°C, is immediately engaged in oxidation after melting. Their blends indicate thermal behavior corresponding to individual components. As PP-g-MA content increases in the blend, oxidation occurs at relatively lower temperatures (Figure 5). Figure 6 compares DSC curves of composites with Cloisite15A, reflecting differences only in oxidation behavior. In composites with 9 and 12 wt.%, although PPMA leads to oxidation due to intercalation, engaging in oxidation is reduced. DSC curves of composites with Cloisite20A show distinction in both melting point and oxidation (Figure 7). 20A3, intercalated composite, has a melting point of 159,1ºC and gets involved in oxidation intensively after melting. However, when PP-g-MA content is increased by 6 wt.% the composite is stable to oxidation until 188 ºC. Due to the penetration of PP-g-MA molecules into the interlayer space of filler, this exfoliated composite has a lower melting point temperature, which is 157,9 ºC, in this case. Even though there is exfoliation, the subsequent addition of PP-g-MA again causes more sensitive oxidation behavior and increased melting points, in the compositions with 9 and 12 wt.% of Cloisite20A.

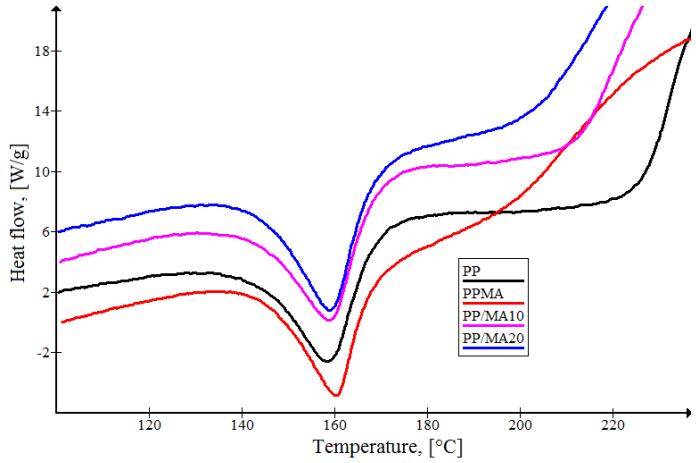

Figure 5. DSC curves of PP and PP-g-MA blends

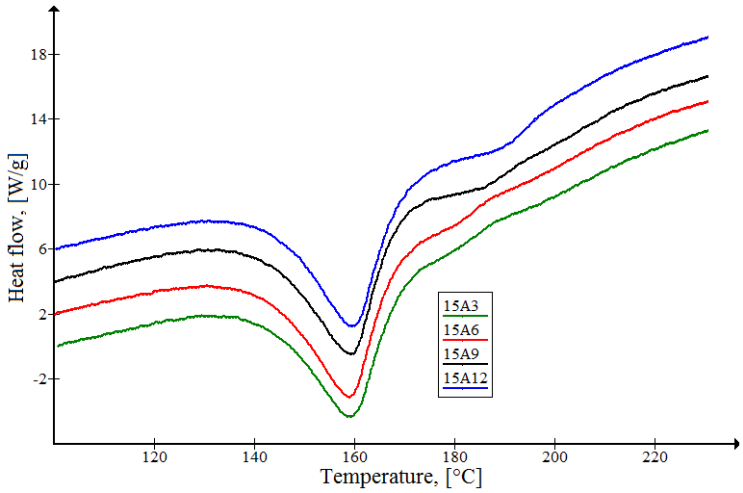

Figure 6. DSC curves of composites with Cloisite15A.

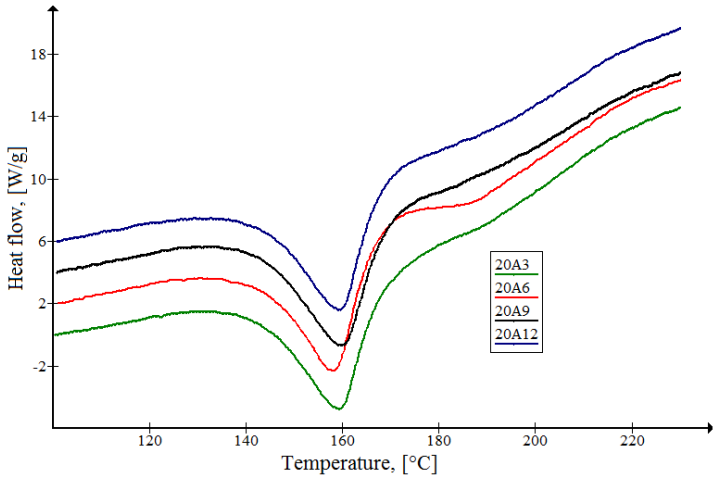

Figure 7. DSC curves of composites with Cloisite20A

Except for DSC, TGA analyses of obtained samples also were conducted, too. In Figure 8, PP starts mass loss at 237ºC (onset temperature of degradation) while in the case of PP-g-MA accounts for 256ºC. Furthermore, after starting degradation, PP engages in degradation more intensively than PP-g-MA. PP and PP-g-MA blends show different degradation mechanisms, as increases PP-g-MA content in the blends degradation curve of the blend tends to become similar to PP-g-MA. However, PP/MA10 and PP/MA20

blends start degradation at lower temperatures relative to PP. The onset temperature of degradation must have been between the degradation temperatures of PP and PP-g-MA according to the rule of polymer additiveness. The reason for this is that PP-g-MA makes PP sensitive toward oxidation, due to its thermal behavior, during melt processing components, according to the DSC curves in Figure 5. PP-g-MA uptakes oxygen during melt processing and then this absorbed oxygen leads to degradation by generating free radicals which cause PP/MA10 and PP/MA20 blends mass loss in relatively earlier temperatures [9]. With regard to TGA analysis of composites obtained with Cloisite15A and Cloisite20A, though PP shows superior thermal stability to oxidation among samples in DSC analysis, thermal degradation properties – mass loss – of PP are inferior to that of PP/clay nanocomposites (Figure 9). In PP/clay nanocomposites, clay acts as an excellent insulating barrier that slows the release of gas from decomposition, so the degradation temperature increases. In general, the presence of clay in the PP tends to the increased thermal stability of the polymer [29].

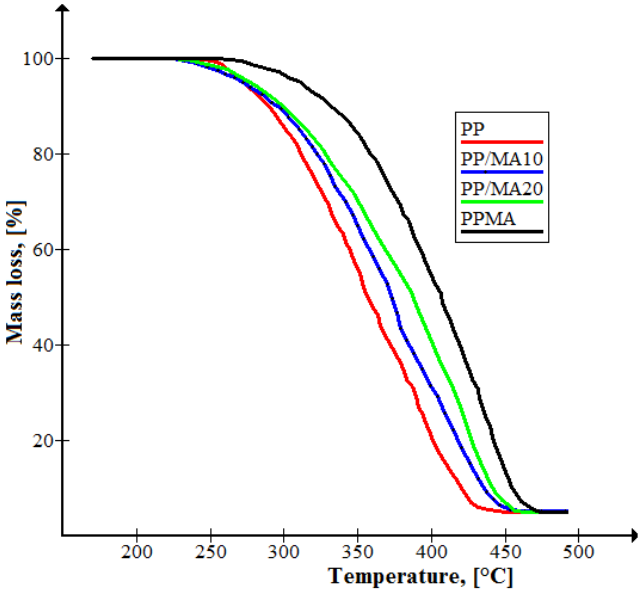

Figure 8. TGA of PP and PPMA blends

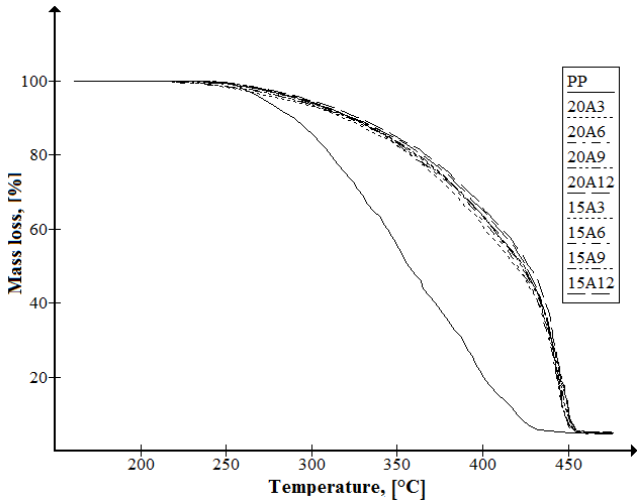

Figure 9. TGA of PP and PP/clay composites

Mechanical measurements

Table 2 presents tensile properties – tensile module (**E**), yield stress (**σ**), and elongation at break (**ε**). The neat PP itself possesses superior mechanical with the best **E** and **σ**, while PPMA has good **ε** which is approximately five times more than neat PP. The addition of PP-g-MA to PP makes PP tougher that **ε** in-

creases and reduces **E** and **σ** PP tends to become more brittle. In the compositions with Cloisite15A, as PP-g-MA increases, unlike PP/PP-g-MA blend, **E** and **σ** also increase; filler content is constant. The reason for this behavior is the development of nano-dispersed clay particles through the matrix as can be seen from SAXS, shifting of the peak in d_{001} to small angles. In the case of composites with Cloisite20A, a saturation of composite with PP-g-MA occurs when PP-g-MA content is 6 wt.% and further addition of compatibilizer leads mechanical properties to diminish by causing oxidation of composite in high temperature.

Table 2

Mechanical properties of obtained PP/clay composites.

Sample names	E, [MPa]	**σ**, [MPa]	**ε**, [%]
PP	922±68	36,2±1,2	845±90
PP/MA10	918±54	36,5±1,2	738±93
PP/MA20	770±7	29,9±0,7	984±150
PPMA	713±61	26,2±1,6	697±52
15A3	946±61	32,8±0,6	18,5±2
15A6	960±52	34,5±1,2	17,8±3,8
15A9	968±49	35,2±0,8	127±18
15A12	1008±41	35,3±1,1	102±29
20A3	1000±51	35,4±0,8	12,7±2
20A6	1087±19	37,6±0,3	52±7
20A9	1002±52	35,9±0,5	17,3±5
20A12	932±51	35,4±0,4	16,8±3

Conclusions

Studies were carried out on the formation of nanocomposites of isotactic polypropylene with modified MMT (Cloisite15A, Cloisite20A), differing modifier densities in the interlayer space. To ensure the diffusion of PP into clays, PP-g-MA (2.5 wt.%) was employed as a compatibilizer, the amount of which is a mixture with PP-g-MA varied within 3, 6, 9, and 12 wt.%. It was found that MMT with a high density of the modifier (Cloisite15A) promotes the formation of intercalated structures, while MMT with a low density of the modifier (Cloisite20A), predominantly exfoliated nanocomposites are formed. In the first case, an increase in the content of PP-g-MA leads to an expansion of the interlayer space (from 30.6 to 39.5 Å). In composites with Cloisite20A, only 3 wt.% content of PP-g-MA shows the formation of mixed intercalated and exfoliated structures, while subsequent increasing compatibilizer content favors the formation of predominantly exfoliated structures. The observed structures are reflected in the viscosity parameter, nanocomposites intercalated with an increase in less viscous PPMA due to limitations associated with the intercalation of macromolecules in the interlayer space and the presence of a specific interaction with the modifier and the clay surface increase markedly (from 65 to 20 g/min), whereas the exfoliation of the structure passes through a minimum in the region between 6 and 9% by weight of PPMA. The formation of the nanocomposite is accompanied by a significant increase in thermal stability (50% weight loss is observed at temperatures of 360°C and 430°C for polypropylene and nanocomposites based on it, respectively). An analysis of the mechanical properties of nanocomposites generally indicates an increase in the elastic modulus by 15–20% (considering the presence of low-modulus PP-g-MA), and this effect is more pronounced for exfoliated structures, the yield strength practically does not change, and the elongation at break decreases significanly. From a practical point of view, heat-resistance properties of intercalated and exfoliated nanocomposites (with a content of 9–12 wt.% and 6 wt.% PP-g-MA, respectively) with enhanced characteristics according to the tensile module and moderate deformability (more than 100%) is interesting.

Acknowledgements

The authors of this work acknowledge JV Uz-Kor Gas Chemical LLC for kindly providing PP grades. For supplying with PP-g-MA JV, UzAuto CEPLA LLC is gratefully acknowledged.

References

1 Gabr, M. H., Okumura, W., Ueda, H., Kuriyama, W., Uzawa, K., & Kimpara, I. (2015). Mechanical and thermal properties of carbon fiber/polypropylene composite filled with nano-clay. *Composites Part B: Engineering, 69*, 94–100. https://doi.org/10.1016/j.compositesb.2014.09.033

2 Dolgov, V.V., Ashurov, N.R., Sheveleva, E.E., & Khakberdiev, E.O. (2013). Strength-strain, barrier, thermal, and fire-resistance properties of nanocomposites based on linear polyethylene with montmorillonite. *Russian Journal of Applied Chemistry, 86*(12), 1885–1896. https://doi.org/10.1134/S1070427213120148

3 Villaluenga, J. P. G., Khayet, M., López-Manchado, M. A., Valentin, J. L., Seoane, B., & Mengual, J. I. (2007). Gas transport properties of polypropylene/clay composite membranes. *European polymer journal, 43*(4), 1132-1143. https://doi.org/10.1016/j.eurpolymj.2007.01.018

4 Kanny, K., Jawahar, P., & Moodley, V. K. (2008). Mechanical and tribological behavior of clay–polypropylene nanocomposites. *Journal of materials science, 43*(22), 7230-7238. https://doi.org/10.1007/s10853-008-2938-x

5 Lee, S. Y., Kang, I. A., Doh, G. H., Kim, W. J., Kim, J. S., Yoon, H. G., & Wu, Q. (2008). Thermal, mechanical and morphological properties of polypropylene/clay/wood flour nanocomposites. *Express Polymer Letters, 2*(2), 78-87. 10.3144/expresspolymlett.2008.11

6 Zhao, C., Qin, H., Gong, F., Feng, M., Zhang, S., & Yang, M. (2005). Mechanical, thermal and flammability properties of polyethylene/clay nanocomposites. *Polymer Degradation and Stability, 87*(1), 183-189. https://doi.org/10.1016/j.polymdegradstab.2004.08.005

7 Kato, M., Usuki, A., Hasegawa, N., Okamoto, H., & Kawasumi, M. (2011). Development and applications of polyolefin–and rubber–clay nanocomposites. *Polymer journal, 43*(7), 583-593. https://doi.org/10.1038/pj.2011.44

8 Hotta, S., & Paul, D. R. (2004). Nanocomposites formed from linear low density polyethylene and organoclays. *Polymer, 45*(22), 7639-7654. https://doi.org/10.1016/j.polymer.2004.08.059

9 Zdiri, K., Elamri, A., & Hamdaoui, M. (2017). Advances in thermal and mechanical behaviors of PP/clay nanocomposites. *Polymer-plastics technology and engineering, 56*(8), 824-840. https://doi.org/10.1080/03602559.2016.1233282

10 Bertini, F., Canetti, M., Audisio, G., Costa, G., & Falqui, L. (2006). Characterization and thermal degradation of polypropylene–montmorillonite nanocomposites. *Polymer degradation and stability, 91*(3), 600-605. https://doi.org/10.1016/j.polymdegradstab.2005.02.027

11 Liu, X., Wu, Q., Berglund, L. A., Lindberg, H., Fan, J., & Qi, Z. (2003). Polyamide 6/clay nanocomposites using a cointercalation organophilic clay via melt compounding. *Journal of applied polymer science, 88*(4), 953-958. https://doi.org/10.1002/app.12031

12 Xie, S., Zhang, S., Wang, F., Liu, H., & Yang, M. (2005). Influence of annealing treatment on the heat distortion temperature of nylon-6/montmorillonite nanocomposites. *Polymer Engineering & Science, 45*(9), 1247-1253. https://doi.org/10.1002/pen.20359

13 Tang, Y., Hu, Y., Song, L., Zong, R., Gui, Z., Chen, Z., & Fan, W. (2003). Preparation and thermal stability of polypropylene/montmorillonite nanocomposites. *Polymer Degradation and Stability, 82*(1), 127-131. https://doi.org/10.1016/S0141-3910(03)00173-3

14 Qin, H., Zhang, S., Zhao, C., Hu, G., & Yang, M. (2005). Flame retardant mechanism of polymer/clay nanocomposites based on polypropylene. *Polymer, 46*(19), 8386-8395. https://doi.org/10.1016/j.polymer.2005.07.019

15 Duvall, J., Sellitti, C., Myers, C., Hiltner, A., & Baer, E. (1994). Interfacial effects produced by crystallization of polypropylene with polypropylene-g-maleic anhydride compatibilitzers. *Journal of applied polymer science, 52*(2), 207-216. https://doi.org/10.1002/app.1994.070520208

16 Lai, S. M., Chen, W. C., & Zhu, X. S. (2009). Melt mixed compatibilized polypropylene/clay nanocomposites: Part 1–The effect of compatibilizers on optical transmittance and mechanical properties. *Composites Part A: Applied Science and Manufacturing, 40*(6-7), 754-765. https://doi.org/10.1016/j.compositesa.2009.03.006

17 Lai, S. M., Chen, W. C., & Zhu, X. S. (2011). Melt mixed compatibilized polypropylene/clay nanocomposites. II. Dispersion vs. thermal properties, optical transmittance, and fracture behaviors. *Journal of composite materials, 45*(25), 2613-2631. https://doi.org/10.1016/j.compositesa.2009.03.006

18 Durmus, A., Woo, M., Kasgöz, A., Macosko, C. W., & Tsapatsis, M. (2007). Intercalated linear low density polyethylene (LLDPE)/clay nanocomposites prepared with oxidized polyethylene as a new type compatibilizer: structural, mechanical and barrier properties. *European Polymer Journal, 43*(9), 3737-3749. https://doi.org/10.1016/j.eurpolymj.2007.06.019

19 Bagheri-Kazemabad, S., Fox, D., Chen, Y., Geever, L. M., Khavandi, A., Bagheri, R., ... & Chen, B. (2012). Morphology, rheology and mechanical properties of polypropylene/ethylene–octene copolymer/clay nanocomposites: Effects of the compatibilizer. *Composites Science and Technology, 72*(14), 1697-1704. https://doi.org/10.1016/j.compscitech.2012.06.007

20 Reichert, P., Nitz, H., Klinke, S., Brandsch, R., Thomann, R., & Mülhaupt, R. (2000). Poly (propylene)/organoclay nanocomposite formation: Influence of compatibilizer functionality and organoclay modification. *Macromolecular Materials and Engineering, 275*(1), 8-17. https://doi.org/10.1002/(SICI)1439-2054(20000201)275:1%3C8::AID-MAME8%3E3.0.CO;2-6

21 Lee, S. S., & Kim, J. (2004). Surface modification of clay and its effect on the intercalation behavior of the polymer/clay nanocomposites. *Journal of Polymer Science Part B: Polymer Physics, 42*(12), 2367-2372. https://doi.org/10.1002/polb.20109

22 Dong, Y., & Bhattacharyya, D. (2010). Dual role of maleated polypropylene in processing and material characterisation of polypropylene/clay nanocomposites. *Materials Science and Engineering: A, 527*(6), 1617-1622. https://doi.org/10.1016/j.msea.2009.10.043

23 Ginzburg, V. V., Singh, C., & Balazs, A. C. (2000). Theoretical phase diagrams of polymer/clay composites: the role of grafted organic modifiers. *Macromolecules, 33*(3), 1089-1099. https://doi.org/10.1021/ma991324e

24 Balazs, A. C., Singh, C., & Zhulina, E. (1998). Modeling the interactions between polymers and clay surfaces through self-consistent field theory. *Macromolecules, 31*(23), 8370-8381. https://doi.org/10.1021/ma980727w

25 Gabr, M. H., Okumura, W., Ueda, H., Kuriyama, W., Uzawa, K., & Kimpara, I. (2015). Mechanical and thermal properties of carbon fiber/polypropylene composite filled with nano-clay. *Composites Part B: Engineering, 69*, 94-100. https://doi.org/10.1016/j.compositesb.2014.09.033

26 Rao, G. R., Srikanth, I., & Reddy, K. L. (2021). Effect of organo-modified montmorillonite nanoclay on mechanical, thermal and ablation behavior of carbon fiber/phenolic resin composites. *Defence Technology*, *17*(3), 812-820. https://doi.org/10.1016/j.dt.2020.05.012

27 Fasihnia, S. H., Peighambardoust, S. H., & Peighambardoust, S. J. (2018). Nanocomposite films containing organoclay nanoparticles as an antimicrobial (active) packaging for potential food application. *Journal of Food Processing and Preservation*, *42*(2), e13488. https://doi.org/10.1111/jfpp.13488

28 Hong, C. H., Lee, Y. B., Bae, J. W., Jho, J. Y., Nam, B. U., & Hwang, T. W. (2005). Molecular weight effect of compatibilizer on mechanical properties in polypropylene/clay nanocomposites. *Journal of Industrial and Engineering Chemistry*, *11*(2), 293-296.

29 Chiu, F. C., Lai, S. M., Chen, J. W., & Chu, P. H. (2004). Combined effects of clay modifications and compatibilizers on the formation and physical properties of melt-mixed polypropylene/clay nanocomposites. *Journal of Polymer Science Part B: Polymer Physics*, *42*(22), 4139-4150. https://doi.org/10.1002/polb.20271

Қ.Н. Бердиназаров, Е.О. Хакбердиев, Н.Ф. Нормуродов Н.Р. Ашуров

Cloisite15A және Cloisite20A изотактикалық полипропилен композиттерінің механикалық және жылулық қасиеттері

Мақалада малеин ангидридімен (PP-g-MA) егілген полипропилен құрамының Cloisite15A және Cloisite20A интерстициалды кеңістіктегі модификатордың тығыздығымен ерекшеленетін саздың екі түрі бар полипропилен (PP) композицияларының термиялық және механикалық қасиеттеріне әсері зерттелген. PP/балшық композиттері 3, 6, 9 және 12 массалық % PP-g-MA әр түрлі құрамның қатысуымен балқытылған. Модификатордың жоғары тығыздығы бар Cloisite15A интеркалирленген құрылымдардың түзілуіне ықпал ететіні, ал модификаторы төмен Cloisite20A негізінен қабыршақтанған нанокомпозиттерді түзетіні анықталды. Бірінші жағдайда құрылым интеркалациялануға бейім, ал Cloisite20A композиттері негізінен қабыршақтанған құрылымдардың пайда болуын қолдайды. Нанокомпозиттің пайда болуы термиялық тұрақтылықтың айтарлықтай жоғарылауымен бірге жүреді (50% салмақ жоғалту полипропилен және оның негізіндегі нанокомпозиттер үшін сәйкесінше 360°C және 430°C температурада байқалады). Нанокомпозиттердің механикалық қасиеттерін талдау, жалпы алғанда, серпімділік модулінің 15–20%-ға артқанын көрсетеді (төмен модульді PPMA болуын ескере отырып) және бұл әсер қабыршақтанған құрылымдар үшін айқынырақ, кернеу кезінде аққыштық шегі іс жүзінде өзгермейді, ал сыну кезінде салыстырмалы ұзару айтарлықтай төмендейді.

Кілт сөздер: полипропилен, саз, композит, малеин ангидридті егілген полипропилен, интеркалация, қабыршақтану, тотығу, монтмориллонит.

К.Н. Бердиназаров, Э.О. Хакбердиев, Н.Ф. Нормуродов Н.Р. Ашуров

Механические и термические свойства изотактических полипропиленовых композитов с Cloisite15A и Cloisite20A

В статье изучено влияние содержания полипропилена, привитого малеиновым ангидридом (PP-g-MA), на термические и механические свойства композиций полипропилена (ПП) с двумя типами глин, различающихся плотностью модификатора в межслоевом пространстве, Cloisite15A и Cloisite20A. Композиты ПП/глина смешивались в расплаве в присутствии различного содержания PP-g-MA от 3, 6, 9 и 12 мас.%. Выявлено, что Cloisite15A с высокой плотностью модификатора способствует образованию интеркалированных структур, тогда как Cloisite20A с низкой плотностью модификатора формируют преимущественно эксфолированные нанокомпозиты. В первом случае структура имеет тенденцию к интеркалированию, в то время как композиты с Cloisite20A способствуют образованию преимущественно эксфолированных структур. Формирование нанокомпозита сопровождается значительным усилением термостабильности (50% потеря веса наблюдается при температурах 360 и 430ºC для полипропилена и нанокомпозитов на его основе, соответственно). Анализ механических свойств нанокомпозитов сведительствует, в целом, об увеличении модуля упругусти на 15–20 % (с учетом присутствия низкомодульного ППМА), причем этот эффект более выражен для эксфоилиированных структур, напряжение при пределе текучести практически не претерпевает изменений, а относительное удилинение при разрушении заметно уменьшается.

Ключевые слова: полипропилен, глина, композит, полипропилен с привитым малеиновым ангидридом, интеркаляция, эксфолиация, окисление, монтмориллонит.

DOI 10.31489/2022PH3/61-67

UDC 621.793

Zh.B. Sagdoldina[1], B.K. Rakhadilov[1,2], D.B. Buitkenov[1,*], L.G. Zhurerova[1], A.B. Kenesbekov[3]

[1]S. Amanzholov East Kazakhstan University, Ust-Kamenogorsk, Kazakhstan
[2]Plasma Science LLP, Kazakhstan
[3]Institute for Composite Materials, Ust-Kamenogorsk, Kazakhstan
*(*E-mail: buitkenovd@mail.ru)*

Improvement of tribological properties of detonation carbosilicide coatings with subsequent pulsed-plasma treatment

This work considers the results of research of mechanical and tribological properties of surface layer of Ti_3SiC_2 coatings after exposure to pulsed-plasma energy flows. Varying of technological parameters of pulsed-plasma treatment is made by changing the distance of pulse exposure. The analysis of the obtained results shows that the pulsed-plasma treatment technology makes it possible to improve the properties of Ti-Si-C based coatings by strengthening the deposited compositions by modifying the structure with an increase in the number of MAX-phases. It is established that the modification of the structural and phase state of the near-surface layers of the carbosilicide coatings leads to a change in their mechanical properties: an increase in the surface microhardness up to 1.8 times, a decrease in the dry friction coefficient by 1.5-2.0 times and an increase in wear resistance by 2.5 times. Based on the XRD analysis, it is established that the improvement of mechanical and tribological properties of Ti_3SiC_2 detonation coatings as a result of pulsed-plasma treatment is associated with phase transformations in the surface layer, in particular with an increase in the Ti_3SiC_2 phase content.

Keywords: detonation spraying, pulsed-plasma modification, tribology, phase, microhardness, wear resistance.

Introduction

The structure and properties of Ti-Si-C-based detonation coatings can be regulated with subsequent heat treatment. The content of Ti_3SiC_2 phases in the coatings can be increased (restored) to some extent depending on the thermal annealing temperature. The results given in papers [1–4] confirm that increasing the volume fraction of Ti_3SiC_2 provides high mechanical and tribological properties of coatings. Thermal stabilization minimizes the residual deformation and residual stresses but has some disadvantages. For example, heat treatment has a considerable time duration and is energy intensive. In addition, there is the need for design and fabrication of accompanying tooling, as well as high capital costs for the purchase and installation of large furnaces [5]. There are also disadvantages associated with the weakening of the substrate material.

Nowadays, methods of surface treatment of products using combined processing technologies are being intensively developed [6, 7]. Surface modification can be performed by various methods, including machining with concentrated energy fluxes. Literature analysis of high-energy density treatment methods used for surface modification of parts shows that they provide multiple increases in the productivity of parts operating in a wide variety of conditions. Among them, of particular interest is the use of pulsed plasma treatment methods [8, 9], which are not inferior, and sometimes even superior, to laser, electron-beam, electric discharge, and other treatment methods. Pulsed plasma treatment is a high-performance surface modification process that is carried out without heating the entire product. It makes it possible to solve the problems of increasing the wear resistance of a particular surface without changing the structural state of the whole product [10]. The advantage is also the possibility of a local impact on the product by pulsed plasma [11].

In this work, the results obtained for the first time on the effect of pulsed plasma treatment (PPT) on the mechanical and tribological properties of Ti-Si-C-based coatings are presented.

Experimental

Detonation spraying was carried out using the CCDS2000 (Computer-Controlled Detonation Spraying) installation developed at the Siberian Branch of the Russian Academy of Sciences, Novosibirsk, Russia. The design and advantages of the barrel of this geometry are described in work [12, 13]. The coatings were obtained at a ratio of O_2/C_2H_2 = 1.856, with explosive mixture volumes of 60% and using nitrogen as a carrier

gas. The coatings were applied at a detonation gun firing rate of 2 rounds per second. The coatings were applied to U9 low-carbon steel substrates at a distance of 200 mm. Before spraying, the substrates were sandblasted for better adhesion of the coatings.

Surface modification of the coatings was carried out by pulsed plasma flow using a plasma generator "Pulse 6" developed by the E.O. Paton Electric Welding Institute at the National Academy of Sciences (NAS) of Ukraine [14, 15]. The detonation coatings were processed under the following conditions: capacitance of capacitors 960 μF, voltage 3,2 kV, inductance 3×10^{-2} mH, electrode W, frequency 1.2 Hz, speed of passage 5 mm/s, electrode recess h=16 mm, number of passes 1. During varying the technological parameters of the pulsed plasma treatment, the distance of the impacts with pulses was changed from 30 to 50 mm.

X'PertPro (Philips Corporation, Nederland) using CuKα radiation was used for X-ray studies of coatings. The shooting was carried out in the following modes: tube voltage U=40 kV; tube current I=20 mA; exposure time 1 s; shooting step 0.02°. The microhardness from the coating's surface was measured using the Metolab-502 testing machine (Metolab, Russia) according to GOST 9450-76. The load on the Vickers pyramid was 200 g. Tribological tests of coatings were carried out on a TRB^3 tribometer (Anton Paar Srl, Peseux, Switzerland) according to the "ball-disc" scheme based on ASTM G-99. An aluminium oxide ball with a diameter of 6 mm was used as a counter body. The samples were tested at a normal load of 10 N, a wear radius of 5 mm, a sliding speed of 2 m/s^{-1} and a total sliding distance of 100 m. The CSEM Micro Scratch Tester (Neuchatel, Switzerland) was used to study the adhesive characteristics of coatings by the "scratching" method. Scratch testing was performed at a maximum load of 30 N; the rate of change of normal loading on the sample was 29.99 N/min, the speed of movement of the indenter was 9.63 mm/min, the length of the scratch was 10 mm, the radius of tip curvature was 100 microns. To obtain reliable results, three scratches were applied to the surface of each coated sample. The roughness (Ra) of the coating surface was measured using a profilometer model 130 (JSC Plant PROTON, Russia). Coatings testing for abrasive wear are carried out on an abrasive-erosion stand by ASTM G65 standards, the principles of which are similar to GOST 23.208-79. In abrasive tests of rubber coatings, a disk with a diameter of 50 mm rotating at a speed of 60 rot/min rubs against a stationary sample. In addition, dry abrasive material is fed to the friction surface. The sample is pressed against the disk with a force of 130 N; electrocorundum powder with sharp-angled particles of 150...190 microns in size is fed to the contact surface. The sample testing procedure consists of 3-5 tests, each of which lasts 15 minutes (600 disk revolutions). After each test, the sample is weighed on an analytical balance. The volume wear is considered, which is determined by dividing the mass loss by the density of the coating material. In erosion tests, a stream of abrasive particles is applied to the surface of the sample at a given angle (30° or 90°) by an air jet. The same sand is used as in abrasive tests. Sand consumption is 1.3g/min, particle velocity is 60m/s, air consumption is 0.12 m^3/min. 8 tests are done, each lasting 5 minutes. Mass loss is recorded; the results are recorded as a mass loss in 5 minutes. Further, as well as abrasive tests, the volume loss is determined in 5 minutes.

Results and Discussion

Figure 1 presents diffractograms of Ti-Si-C system coatings before and after different pulsed plasma treatment distances. The results of the X-ray phase analysis of the coatings show that the phase composition of the coatings before the PPT consists mainly of TiC and a relatively small fraction of Ti_3SiC_2. After PPT, an increase in the intensity of Ti_3SiC_2 peaks is observed as well as the appearance of new reflexes (101, 102, 112, 204, 1110, 0016) of this phase which indicates an increase in the MAX-phase content. The change in phase fraction designates a solid-phase transformation during pulsed plasma activation associated with heating above the melting temperature and cooling of the samples during treatment [16, 17]. The cooling rate of the sample and the crystallization rate of the melt (processed layer) depend on the heat capacity of the base metal (substrate). In diffractograms of coatings, the carbide and oxide phases: WC and TiO_2 are present in small amounts. The samples were treated in an air environment, which caused the formation of oxide phases. Tungsten carbide is formed due to the consumption of the tungsten electrode [18].

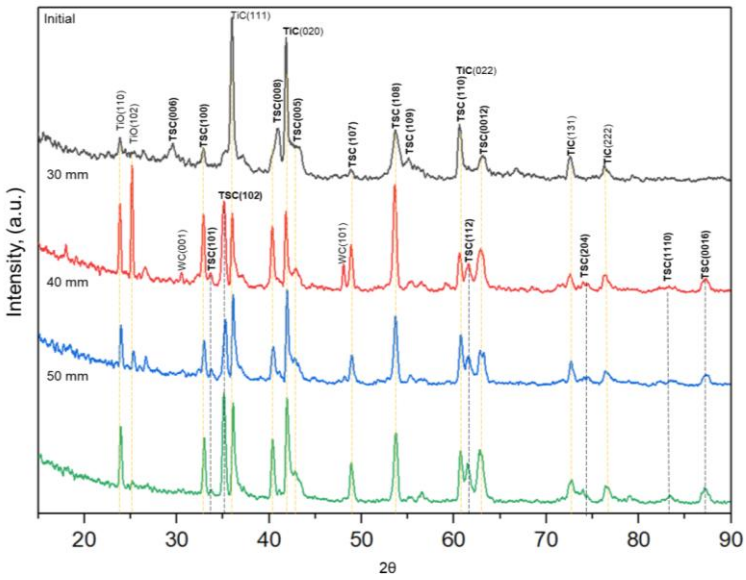

Figure 1. Diffractograms of Ti-Si-C-based detonation coatings before and after PPT

Microhardness of coatings after pulsed plasma treatment increases in comparison with an initial sample in dependence on the distance of treatment (Table 1). The values of microhardness of coatings after PPT application at a distance of 50 mm increased up to ~1785 HV (before PPT ~1000 HV) due to more effective formation of MAX phases.

To assess the resistance of Ti-Si-C coatings to abrasive and erosive wear, tests were carried out on special stands. Comparative studies of the coatings' wear resistance under friction in an abrasive medium showed that after modification by plasma treatment, coatings provide the greatest wear resistance. Table 1 represents the results of testing for abrasive and erosive wear of coatings before and after pulsed plasma treatment depending on the distance from the plasmatron. According to the results of determining the mass losses of the samples after the test, the maximum resistance to all types of wear is provided by the coating treated at a distance of 50 mm.

Table 1

Abrasive and erosive wear of detonation coatings before and after PPT

Coating	Hardness [HV]	Abrasive wear [mg]	Erosive wear [mg]
Ti_3SiC_2	1000	0.87	0.38
PPT (30 mm)	1180	0.65	0.29
PPT (40 mm)	1250	0.59	0.25
PPT (50 mm)	1785	0.52	0.23

An important characteristic of the parts working surfaces is the friction coefficient and wear resistance. Tribological properties are determined by the structural-phase state, strength, and surface chemical properties. Figure 2 demonstrates the curves of wear of coated Ti-Si-C before and after modification by plasma treatment, depending on the distance from the plasmatron. The experiment shows that after the pulsed-plasma treatment of the samples, the friction coefficient μ decreases. If the value of the friction coefficient in the initial Ti-Si-C coatings is 0.65, then after the pulse treatment it decreases depending on the distance H from 0.60up to 0.40. According to the experiments, pulsed plasma treatment leads to an improvement in the tribological properties of Ti-Si-C coatings. A possible reason for the decrease in the friction coefficient is an increase in the content of the Ti_3SiC_2 phase on the surface layer of coatings after pulsed plasma treatment.

The analysis of the surface roughness shows that the value of the arithmetic mean deviation of the initial coating roughness profile was 0.97 mμ (Fig. 2). After pulsed-plasma treatment, this value increased at a distance of 30 mm to 3.75 mμ, at 40 mm to 3.61 mμ and at 50 mm to 3.53 mμ. An increase in the surface roughness compared to the initial sample leads to a decrease in the actual contact area of the interacting bodies, which also causes a decrease in the friction coefficient [19].

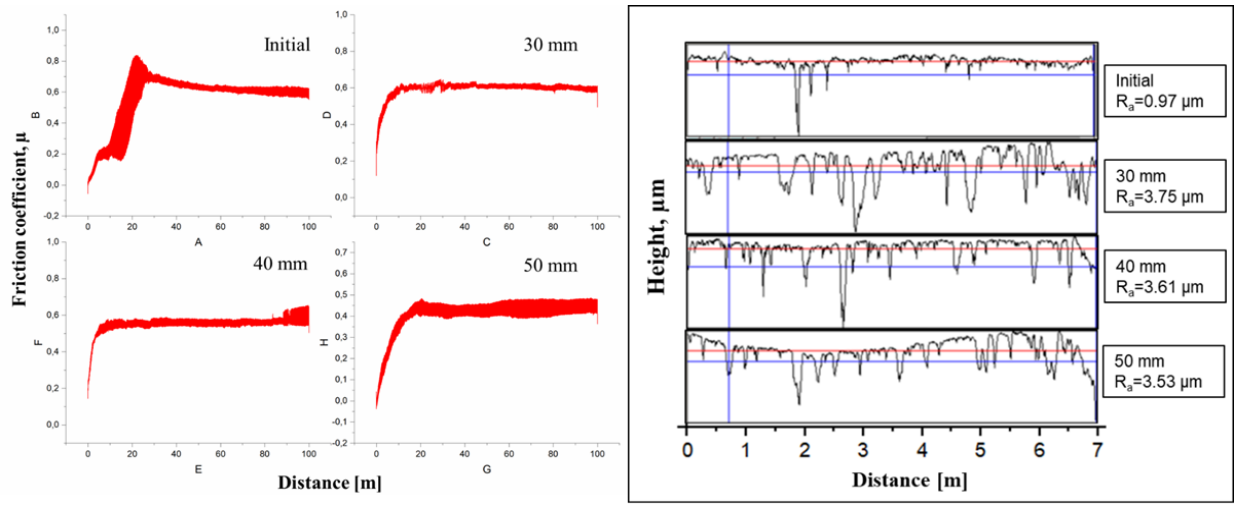

Figure 2. Results of tribological tests of Ti-Si-C coatings before (initial) and after pulsed-plasma treatment

Figure 3 illustrates the results of adhesion and cohesion strength and scratch resistance of Ti-Si-C coatings before and after the PPT. The process of coating failure by indentor scratching can be conventionally divided into three stages. Coatings before PPT at a load in the range of 12.08 N(L_{C1}) show monotonic penetration of the indentor into the coating. At a load of 24,38 N(L_{C2}) the indentor fully sinks into the coating. A sliding diamond indenter to perform a coating with a coefficient of friction of 0.35. As the load is increased by 28.92 N (L_{C3}), the material in front of the indenter is squeezed into knolls and the penetration depth of the indenter increases. Comparative analysis shows that the coatings after PPT erode but do not delaminate when scratched, i.e., they fracture due to the cohesive mechanism of plastic deformation and the formation of fatigue cracks in the coating material. As we can see, there is a monotonic penetration of the indentor into the coating and the first cracks appear (load up to 18.02 N); the coefficient of friction (μ) increases, but the acoustic emission signal remains unchanged. Subsequently, chevron and diagonal cracks appear at increased load, which increases the coefficient of friction to a value of 0.3. Under load up to 18-25 N, the amplitude of the acoustic emission signal increases sharply. Thereafter, with an increase in load reaching 29.88 N, local abrasion of the coating down to the substrate material occurs.

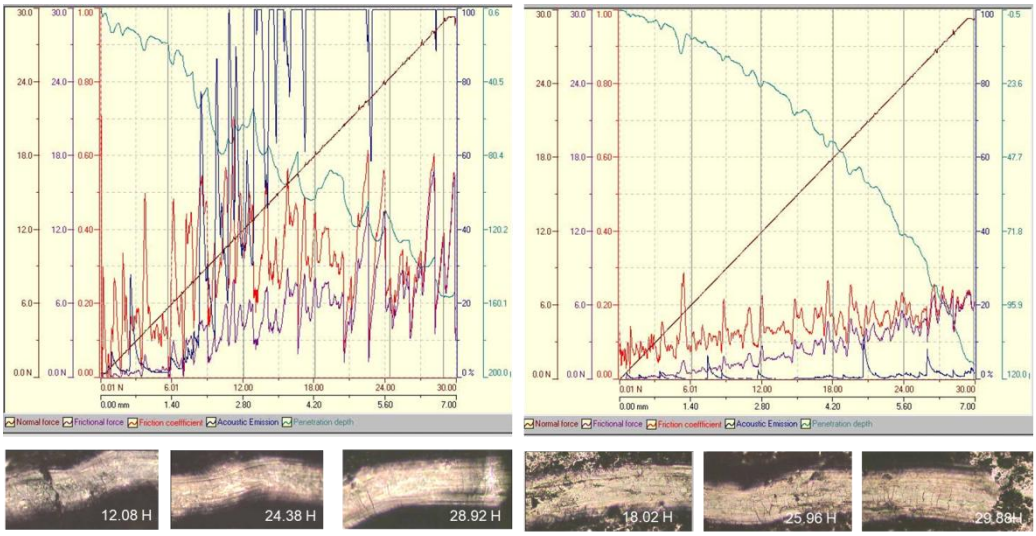

Figure 3. Scratch test results of Ti_3SiC_2 coatings before and after PPT

Conclusions

It is determined that after PPT the intensity of Ti_3SiC_2 peaks increases and new reflexes appear (101, 102, 112, 204, 1110, 0016) which indicates an increase of MAX phase content. Formation of carbide and oxide phases (WC and TiO_2) in small amounts is connected with the evaporation of tungsten electrodes dur-

ing PPT in air environment. It is shown that before PPT the average coefficient of friction of coatings is ~0.60, after treatment the coefficient of friction decreases and is from 0.55 to 0.40 depending on treatment distance. The reason for the friction coefficient reduction may be an increase in microhardness and an increase in the content of MAX phases in the composition of the coatings. After PPT at the distance of 50 mm, the wear resistance of coatings to abrasive and erosive wear increases by 1,5–2,0 times. Thus, when pulsed plasma is treated with detonation coatings based on Ti-Si-C, a modified layer appears on the surface, which, in terms of its mechanical and tribological properties, is superior to the original surface.

Acknowledgment

This research was funded by the Science Committee of the Ministry of Education and Science of the Republic of Kazakhstan (Grant No. AP08857579).

References

1 Rakhadilov B. Structural Features and Tribological Properties of Detonation Gun Sprayed Ti–Si–C Coating / B. Rakhadilov, D. Buitkenov, Z. Sagdoldina, B. Seitov, S. Kurbanbekov, M. Adilkanova // Coatings. — 2021. — Vol. 11. — P. 141.

2 Rakhadilov B.K. Structural-phase and tribo-corrosion properties of composite Ti_3SiC_2/TiC MAX-phase coatings: an experimental approach to strengthening by thermal annealing / B.K. Rakhadilov, O.V. Maksakova, D.B. Buitkenov, M.K. Kylyshkanov, A.D. Pogrebnjak, V.P. Antypenko, Ye.V. Konoplianchenko // Applied Physics A. — 2022. — Vol. 128, No. 2. — P. 1–11.

3 Buitkenov D. Influence of Heat Treatment on the Phase Composition and Microhardness of Coatings Based on Ti_3SiC_2/TiC / D. Buitkenov, B. Rakhadilov, D. Erbolatuly, Zh. Sagdoldina // Key Engineering Materials. — 2020. — Vol. 839. — P. 137–143.

4 Rakhadilov B.K. Preparation of powder coatings on the surface of steel balls by mechanochemical synthesis / B.K. Rakhadilov, D.B. Buitkenov, Z.B. Sagdoldina, L.G. Zhurerova, W. Wieleba // Bulletin of the university of Karaganda-Physics. — 2020. — Vol. 4. — P. 8–13.

5 Погребняк А.Д. Структура и свойства поверхностей материалов и композитных покрытий до и после воздействия концентрированными потоками энергии / А.Д. Погребняк, М.К. Кылышканов, Д.Л. Алонцева. — Усть-Каменогорск: ВКГТУ, 2008. — 296 с.

6 Погребняк А.Д. Импульсно-плазменная модификация свойств поверхности и нанесение покрытий / А.Д. Погребняк, Ю.Н. Тюрин // Успехи физики металлов. — 2003. — Т. 4. — С. 1–66.

7 Оковитый В.А. Исследование и оптимизация технологических параметров лазерной обработки износостойких плазменных покрытий на основе самосмазывающихся материалов / В.А. Оковитый, А.И. Шевцов, О.Г. Девойно // Вестн. Брест. гос. техн. ун-та. Машиностроение. — Брест, 2005. — Т. 4. — № 34. — С. 6–8.

8 Tyurin Yu.N. Pulsed plasma hardening of titanium base alloys / Yu.N. Tyurin, L.I. Adeeva // Automatic Welding. — 1999. — No. 3. — P. 43–47.

9 Pogrebnjak A.D. Modification of surface layer of titanium alloys by pulsed plasma treatment / A.D. Pogrebnjak, S.V. Sokolov, E.A. Bazyl, Yu.N. Tyurin, V.S. Kshnyakin // Physics and Chemistry of materials treatment. — 2001. — No. 4. — P. 49–55.

10 Тюрин Ю.Н. Импульсно-плазменное модифицирование поверхности изделия из сплава WC + 20 %Co / С.Н. Кульков, О.В. Колисниченко, И.М. Дуда // ФИП. — 2009. — Т. 7. — № 3. — С. 262–267.

11 Погребняк А.Д. Модификация свойств материалов и осаждение покрытий с помощью плазменных струй / А.Д. Погребняк, Ю.Н. Тюрин // УФН. — 2005. — № 175. — С. 515–544.

12 Ulianitsky, V.Y. Fabrication of layered ceramic-metal composites by detonation spraying / V.Y. Ulianitsky, A.A.Shtertser, I.S. Batraev, D.K. Rybin // Ceramics International — 2020. — Vol. 46. — P. 27903–27908.

13 Ulianitsky V.Y. Computer-controlled detonation spraying: flexible control of the coating chemistry and microstructure / V.Y. Ulianitsky, D.V. Dudina, A.A. Shtertser, I. Smurov // Metals. — 2019. — Vol. 9. — P. 1244.

14 TyurinYu.N. Pulsed plasma hardening of tools and machine parts / Yu.N. Tyurin, M.L. Zhadkevich, O.V. Kolisnichenko // Trans. Materials in Motor Car Industry. — 2003. — P. 234–238.

15 Tyurin Yu.N. Plasma-detonation technology for modification of the surface layer of metal parts / Yu.N. Tyurin, O.V. Kolisnichenko // The Open Surface Science Journal. — 2009. — Vol. 1. — P. 13–19.

16 Rakhadilov B.K. Influence of pulse plasma treatment on the phase composition and microhardness of detonation coatings based on Ti-Si-C / B.K. Rakhadilov, D.B. Buitkenov, M. Adilkhanova, Zh.B. Sagdoldina, Sh.R. Kurbanbekov // Bulletin of the university of Karaganda-Physics. — 2021. — Vol. 2, No. 102. — P. 33–39.

17 Rakhadilov B. Effect of Pulsed-Plasma Treatment on the Structural-Phase Composition and Tribological Properties of Detonation Coatings Based on Ti–Si–C. Coatings / B. Rakhadilov, D. Buitkenov, Zh. Idrisheva, M. Zhamanbayeva, S. Pazylbek, D. Baizhan // Coatings. — 2021. — Vol. 11. — P. 795.

18 Pogrebnjak A.D. Modification of material properties and coating deposition using plasma jets / A.D. Pogrebnjak, Y.N. Tyurin // Physics. — 2005. — Vol.48. — P. 515–544.

19 Sagdoldina Z. Structural evolution of ceramic coatings by mechanical alloying / Z. Sagdoldina, B. Rakhadilov, M. Skakov, O. Stepanova // Materials testing. — 2019. — Vol. 61. ─ P. 304–308.

Ж.Б. Сағдолдина, Б.К. Рахадилов, Д.Б. Буйткенов, Л.Г. Журерова, А.Б. Кенесбеков

Импульстік–плазмалық өңдеумен детонациялық карбосилицидтік жабындардың трибологиялық қасиеттерін жақсарту

Мақалада импульстік-плазмалық энергия ағындарының әсерінен кейін Ti3SiC2 жабындарының беткі қабатының механикалық-трибологиялық қасиеттерін зерттеу нәтижелері қарастырылған. Импульстік-плазмалық өңдеудің технологиялық параметрлерінің түрленуі импульстердің әсер ету қашықтығының өзгеруіне байланысты жүргізілді. Алынған нәтижелерді талдау импульстік-плазмалық өңдеу технологиясы MAX–фазалар санын ұлғайта отырып, құрылымды түрлендіру жолымен қолданылған композицияларды нығайта отырып, Ti–Si-C жүйесі негізінде жабындардың қасиеттерін жақсартуға мүмкіндік беретінін куәландырады. Карбосилицидті жабындардың беткі қабаттарының құрылымдық-фазалық күйін өзгерту олардың механикалық сипаттамаларының өзгеруіне әкелетіні анықталды: беттің микро қаттылығын 1,8 есеге дейін арттыру, құрғақ үйкеліс коэффициентін 1,5–2,0 есе азайту және тозуға төзімділікті 2,5 есе арттыру. XRD талдау негізінде импульсті плазмалық өңдеу нәтижесінде Ti3SiC2 детонациялық жабындарының механикалық-трибологиялық қасиеттерінің жақсаруы беткі қабаттағы фазалық өзгерістермен, атап айтқанда Ti3SiC2 фазасының ұлғаюымен байланысты екендігі анықталды.

Кілт сөздер: детонациялық тозаңдату, импульсті-плазмалық модификация, трибология, фаза, микроқаттылық, тозуға төзімділік.

Ж.Б. Сагдолдина, Б.К. Рахадилов, Д. Б. Буйткенов, Л.Г. Журерова, А.Б. Кенесбеков

Повышение трибологических свойств детонационных карбосилицидных покрытий с последующей импульсно-плазменной обработкой

В статье рассмотрены результаты исследования механико-трибологических свойств поверхностного слоя покрытий Ti3SiC2 после воздействия импульсно-плазменными потоками энергии. Варьирование технологических параметров импульсно-плазменной обработки производилось за счет изменения дистанции воздействия импульсами. Анализ полученных результатов свидетельствует о том, что технология испульсно-плазменной обработки позволяет улучшать свойства покрытий на основе системы Ti–Si–C, упрочняя нанесенные композиции путем модифицирования структуры с увеличением количества MAX-фаз. Установлено, что модифицирование структурно-фазового состояния приповерхностных слоев карбосилицидных покрытий приводит к изменению их механических характеристик: увеличению микротвердости поверхности до 1,8 раз, уменьшению коэффициента сухого трения в 1,5–2,0 раза и повышению износостойкости на 2,5 раза. На основании XRD-анализа установлено, что улучшение механико-трибологических свойств детонационных покрытий Ti3SiC2 в результате импульсно-плазменной обработки связано с фазовыми превращениями в поверхностном слое, в частности, с увеличением содержания фазы Ti3SiC2.

Ключевые слова: детонационное напыление, импульсно-плазменная модификация, трибология, фаза, микротвердость, износостойкость.

References

1 Rakhadilov, B., Buitkenov, Sagdoldina, Z., Seitov, B., Kurbanbekov, S., & Adilkanova M. (2021). Structural Features and Tribological Properties of Detonation Gun Sprayed Ti–Si–C Coating. *Coatings*, 11, 141.

2 Rakhadilov, B.K., Maksakova, O.V., Buitkenov, D.B., Kylyshkanov, M.K., Pogrebnjak, A.D., Antypenko, V.P., & Konoplianchenko, Ye.V. (2022). Structural-phase and tribo-corrosion properties of composite Ti_3SiC_2/TiC MAX-phase coatings: an experimental approach to strengthening by thermal annealing. *Applied Physics A*, 128, 2, 1–11.

3 Buitkenov, D., Rakhadilov, B., Erbolatuly, D., & Sagdoldina, Zh. (2020). Influence of Heat Treatment on the Phase Composition and Microhardness of Coatings Based on Ti_3SiC_2/TiC. *Key Engineering Materials*, 839, 137–143.

4 Rakhadilov, B.K., Buitkenov, D.B., Sagdoldina, Z.B., Zhurerova, L.G., & Wieleba, W. (2020). Preparation of powder coatings on the surface of steel balls by mechanochemical synthesis. *Bulletin of the university of Karaganda-Physics*, 4, 8–13.

5 Pogrebnjak, A.D., Kylyshkanov, M.K., & Alontseva, D.L. (2008). Struktura i svoistva materialov i kompozitnykh poverkhnostei do i posle vozdeistviia kontsentrirovannymi potokami energii [Structure and properties of materials and composite surfaces before and after exposure to concentrated energy flows]. *Ust-Kamenogorsk: Vostochno-Kazakhstanskii tekhnicheskii universitet*, 296 [in Russian].

6 Pogrebnjak, A.D., & Tyurin, Yu.N. (2003). Impulsno-plazmennaia modifikatsiia svoistv poverkhnosti i nanesenie pokrytii [Pulse-plasma modification of surface properties and coating]. *Uspekhi fiziki metallov*, 4, 1–66 [in Russian].

7 Okovity, V.A., Shevtsov, A.I., & Devoino, O.G. (2005). Issledovanie i optimizatsiia tekhnologicheskikh parametrov lazernoi obrabotki iznosostoikikh plazmennykh pokrytii na osnove samosmazyvaiushchikhsia materialov [Research and optimization of

technological parameters of laser processing of wear-resistant plasma coatings based on self-lubricating materials]. *Vestnik Brestskogo gosudarstvennogo tekhnicheskogo universiteta. Mashinostroenie*, 4(34), 6–8 [in Russian].

8 Tyurin, Yu.N., & Adeeva, L.I. (1999). Pulsed plasma hardening of titanium base alloys. *Automatic Wielding*, 3, 43–47.

9 Pogrebnjak, A.D., Sokolov, S.V., Bazyl, E.A., Tyurin, Yu.N., & Kshnyakin, V.S. (2001). Modification of surface layer of titanium alloys by pulsed plasma treatment. *Physics and Chemistry of materials treatment*, 4, 49–55.

10 Tyurin, Yu.N., Kulkov, C.N., Kolisnichenko, O.B., & Duda, I.M. (2009). Impulsno-plazmennoe modifitsirovanie poverkhnosti izdeliia iz splava WC + 20 %Co [Pulse-plasma modification of the surface of a product made of WC + 20 %Co alloy]. *FIP*, 7, 3, 262–267 [in Russian].

11 Pogrebnjak, A.D., & Tyurin, Yu.N. (2005). Modifikatsia svoistv materialov i osazhdenie pokrytii s pomoshchiu plazmennykh strui [Modification of material properties and coating deposition using plasma jets]. *Uspekhi fizicheskikh nauk — Advances in Physical Sciences*, 175, 515–544 [in Russian].

12 Ulianitsky, V.Y., Shtertser, A.A., Batraev, I.S., & Rybin, D.K. (2020). Fabrication of layered ceramic-metal composites by detonation spraying, *Ceramics International*, 46, 27903–27908.

13 Ulianitsky, V.Y., Dudina, D.V., Shtertser, A.A., & Smurov, I. (2019). Computer-controlled detonation spraying: flexible control of the coating chemistry and microstructure. *Metals*, 9, 1244.

14 Tyurin, Yu.N., Zhadkevich, M.L. & Kolisnichenko O.V. (2003). Pulsed plasma hardening of tools and machine parts. *Trans. Materials in Motor Car Industry*, 234–238.

15 Tyurin, Yu.N., & Kolisnichenko, O.V. (2009). Plasma-detonation technology for modification of the surface layer of metal parts. *The Open Surface Science Journal*, 1, 13–19.

16 Rakhadilov, B.K., Buitkenov, D.B., Adilkhanova, M., Sagdoldina, Zh.B., & Kurbanbekov, Sh.R. (2021). Influence of pulse plasma treatment on the phase composition and microhardness of detonation coatings based on Ti-Si-C. *Bulletin of the university of Karaganda-Physics*, 2(102), 33–39.

17 Rakhadilov, B., Buitkenov, D., Idrisheva, Zh., Zhamanbayeva, M., Pazylbek, S., & Baizhan, D. (2021) Effect of Pulsed-Plasma Treatment on the Structural-Phase Composition and Tribological Properties of Detonation Coatings Based on Ti–Si–C. *Coatings*, 11, 795.

18 Pogrebnjak, A.D., & Tyurin, Y.N. (2005). Modification of material properties and coating deposition using plasma jets. *Physics*, 48, 515–544.

19 Sagdoldina, Z., Rakhadilov, B., Skakov, M., & Stepanova, O. (2019). Structural evolution of ceramic coatings by mechanical alloying. *Materials testing*, 61, 304–308.

DOI 10.31489/2022PH3/68-79

UDC 534.2:539.3

N.A. Ispulov[1], Abdul Qadir[2], A.Zh. Zhumabekov[1],
A.A. Kurmanov[1], K.R. Dosumbekov[1]*

[1]*Toraighyrov University, Pavlodar, Kazakhstan*
[2]*Sukkur Institute of Business Administration, Sindh, Pakistan*
*(*E-mail: kairat_83@inbox.ru)*

On nonclassical boundary conditions for the contact of thin interlayers with different physical and mechanical properties on wave propagation in anisotropic media

Wave processes are intensively studied in various fields of physics: electrodynamics, plasma physics, radiophysics, acoustics, hydrodynamics, etc. Along with the study of electromagnetic and elastic wave processes, the research of patterns of wave propagation of various physical nature in the presence of mutual transformation are of particular relevance. Wave processes in coupled fields reflect the mutual influence of elastic, electromagnetic and thermal fields. The coupling of electromagnetic fields to the deformation field takes place in a medium with piezoelectric, piezomagnetic and magnetostrictive properties. In the paper, based on the matrix method, the propagation of coupled elastic and electromagnetic waves in media with different physical and mechanical properties is studied. The paper proposes a generalization of non-classical contact conditions for studying the effect of thin layers with different physical and mechanical properties on wave processes. A system of differential equations of the 1st order with variable coefficients is constructed, which describe the propagation of electroelastic waves in anisotropic media of a rhombic system of class 222. The conditions for nonrigid contact for a thin layer with piezoelectric properties are derived. The possibility of studying layers with δ-shaped properties (δ is the Dirac function) is proved.

Keywords: Maxwell's equations, anisotropic medium, waves, non-rigid contact, matricant method.

Introduction

Scientific interest in interrelated elastic and electromagnetic wave processes in media with piezoelectric, piezomagnetic, and thermopiezoelectric properties has recently been associated with the prospect of application in various fields of science and technology, such as instrumentation, micro and nanoelectronics, and information technology. It is possible to allocate applications in high-frequency electronics; the use of multiferroic structures in various kinds of logical elements, memory elements and information processing devices; autonomous wireless energy sources; sensors of variable and constant fields; creation of new composite materials [1–4].

In [5–11], a theoretical model was proposed that describes the properties of composite layered composites based on magnetostrictive and piezoelectric materials in the low-frequency range and the region of electromechanical resonance. The theory is presented and the magnetoelectric effect in multilayer composite materials based on ferrite-piezoelectrics for samples of various shapes and in a two-layer magnetostrictive-piezoelectric structure is experimentally investigated. Theoretical research is conducted not only by Russian scientists, but also by representatives of other countries. For example, in the article [12], the magnetoelectric effect is studied in magnetostrictive layers. Various experimental methods for measuring the magnetoelectric effect are considered in [13–15] and an energy source based on magnetostrictive piezoelectric composites has been designed.

Along with the study of electromagnetic and elastic (acoustic) wave processes, studies of the patterns of propagation of waves of various physical natures in the presence of mutual transformation are of particular relevance. Wave processes in coupled fields reflect the mutual influence of elastic, electromagnetic, and thermal fields. The connection of electromagnetic fields with the deformation field takes place in a medium with piezoelectric, piezomagnetic, and magnetostrictive properties.

Studies of new physical phenomena and the creation of devices and devices for solid-state electronics are largely associated with the synthesis of materials with new specified properties, the manufacture of multifunctional composite materials consisting of two or more separate phases [16–20].

Research method

Based on the matricant method [21], we study the propagation of coupled elastic and electromagnetic waves in media with different physical and mechanical properties and the use of these features for practical purposes; as well as the development of a method for determining the averaged physical and mechanical parameters of heterostructures in the presence of coupled fields.

Wave processes in elastic anisotropic media, in anisotropic dielectric media, waves in anisotropic plates, electromagnetic waves in media with a magnetoelectric effect [22–26], waves in liquid crystals [27], wave propagation in thermoelastic media [28–30], related wave processes in media with piezoelectric and piezomagnetic effects [31]. On its basis, a unified description of Rayleigh-type surface waves, Lamb-type waves in elastic, piezoelectric, piezomagnetic media and media with a magnetoelectric effect was obtained [32–34].

Basic Equations and Relations

In this paper, we discuss the possibility of applying the matricant method to the study of wave propagation in multilayer heterostructures.

In the presence of layers that satisfy the condition $\lambda >> l_i$ (λ is the wavelength, l_i is the thickness of the i-th layer), the construction of wave field solutions and their analysis can be significantly simplified. In this case, the influence of thin layers is considered by special (non-classical) boundary conditions.

Considering the influence of thin layers by means of boundary conditions makes it possible to exclude the construction of solutions to the equations of motion in these layers, which naturally significantly reduces the number of calculations and facilitates the analysis of the obtained solutions.

For the first time, the boundary conditions of a non-rigid contact were proposed in the work of Podyapolsky G.S. [35]. The main purpose of their introduction was to consider the contact conditions occupying an intermediate position between hard contact:

$$\vec{W}_i\Big|_{z=0} = \vec{W}_z\Big|_{z=0} \tag{1}$$

and free surface based on the introduction of thin viscoelastic layers. The substantiation of the introduction of nonrigid contact conditions, as well as the derivation of these conditions, had a number of limitations. Disadvantages were discussed in [36]. In this work, the application of the boundary conditions of non-rigid contact received a deeper physical justification and content. In addition, in the same article, a general algorithm for deriving the boundary conditions of a nonrigid contact was proposed, considering the rheological properties of the interlayer and inertial effects following from the corresponding equations of motion. A wide class of models of continuous media and motion was considered. A wide class of models of continuous media was considered and the boundary conditions of nonrigid contact were obtained, which describe the boundary conditions of nonrigid contact, which describe the influence of the corresponding thin layers on wave processes.

A generalization of the original version of the boundary conditions of a nonrigid contact was carried out in [37]. Some applied issues of hard contact are given in [37]. Boundary conditions for non-rigid contact are considered in the monograph by L.A. Molotkov [38].

In the works noted above and in other scientific publications, the application of the boundary conditions of nonrigid contact was limited to various models of solid mechanics media. At the same time, the area of constructive application of the boundary conditions of nonrigid contact is very extensive.

The derivation of boundary non-rigid contact for elastic anisotropic media with various physical and mechanical phenomena is simple and understandable on the basis of the matricant method. In the case of a piezoelectric elastic medium, the equations of motion:

$$\frac{\partial \sigma_{ij}}{\partial x_j} = \frac{\partial^2 U}{\partial x^2} \tag{2}$$

and Maxwell's equations in differential form:

$$
\begin{aligned}
rot\vec{E} &= -\frac{\partial \vec{B}}{\partial t} \\
rot\vec{H} &= -\frac{\partial \vec{D}}{\partial t} \\
div\vec{B} &= 0 \\
div\vec{D} &= 0
\end{aligned}
\tag{3}
$$

connected by defining relations:

$$
\begin{aligned}
\sigma_{ij} &= e_{ijkl}\varepsilon_{kl} - e_{kil}E_k \\
D_i &= e_{ijkl}\varepsilon_{kl} + э_{ik}E_k \\
B_i &= \mu_0\mu_{ij}H_j
\end{aligned}
\tag{4}
$$

where c_{ijkl} – elastic stiffness, ρ – medium density, $\varepsilon_{kl} = \frac{1}{2}(u_{l,k} + u_{k,l})$ – strain tensor, e_{ikl} – piezoelectric constants relating the electric field to mechanical stresses; $э_{ik}$ – components of the permittivity tensor.

Construction of a system of differential equations of the 1st order. Analysis of coefficient matrices

Consider a rhombic system of class 222.

The rhombic system of class 222 is a system with three mutually perpendicular axes, which are double axes of symmetry. Such a system must correspond to two class 2 monoclinic systems: one with a twofold symmetry axis parallel to the Y axis and the other with a twofold symmetry axis parallel to the Z axis. The material constants must be determined by both monoclinic systems. This condition leads to a decrease in the number of constants. The coefficient matrices for the class 222 rhombic system are [39]:

$$
c_{ijkl} = \begin{pmatrix}
c_{11} & c_{12} & c_{13} & 0 & 0 & 0 \\
c_{12} & c_{22} & c_{23} & 0 & 0 & 0 \\
c_{13} & c_{23} & c_{33} & 0 & 0 & 0 \\
0 & 0 & 0 & c_{44} & 0 & 0 \\
0 & 0 & 0 & 0 & c_{55} & 0 \\
0 & 0 & 0 & 0 & 0 & c_{66}
\end{pmatrix}; e_{kij} = \begin{pmatrix}
0 & 0 & 0 \\
0 & 0 & 0 \\
0 & 0 & 0 \\
e_{14} & 0 & 0 \\
0 & e_{25} & 0 \\
0 & 0 & e_{36}
\end{pmatrix}; э_{ij} = \begin{pmatrix}
э_{11} & 0 & 0 \\
0 & э_{22} & 0 \\
0 & 0 & э_{33}
\end{pmatrix}
\tag{5}
$$

Here we have 9 independent coefficients c_{ijkl} , 3 coefficients e_{kij} , and 3 coefficients $э_{ij}$.

In abbreviated matrix notation, relations (4) are written as follows:

$$
\left.
\begin{aligned}
\sigma_p = T_p &= c_{pq}S_q - e_{kp}E_k \\
D_i &= e_{iq}S_{ql} + э_{ik}E_k
\end{aligned}
\right\}
\tag{6}
$$

where *i, k = 1,2,3; p,q=1,2,3,4,5,6*

$$
\begin{aligned}
S_p &= \varepsilon_{ij}, i = j \\
2\varepsilon_{ij} &= S_p, i \neq j
\end{aligned}
$$

We write the constitutive relations (4) in the matrix form:

$$\begin{bmatrix} T_1 \\ T_2 \\ T_3 \\ T_4 \\ T_5 \\ T_6 \end{bmatrix} = \begin{bmatrix} c_{11} & c_{12} & c_{13} & 0 & 0 & 0 \\ c_{12} & c_{22} & c_{23} & 0 & 0 & 0 \\ c_{13} & c_{32} & c_{33} & 0 & 0 & 0 \\ 0 & 0 & 0 & c_{44} & 0 & 0 \\ 0 & 0 & 0 & 0 & c_{55} & 0 \\ 0 & 0 & 0 & 0 & 0 & c_{66} \end{bmatrix} * \begin{bmatrix} S_1 \\ S_2 \\ S_3 \\ S_4 \\ S_5 \\ S_6 \end{bmatrix} - \begin{bmatrix} 0 & 0 & 0 \\ 0 & 0 & 0 \\ 0 & 0 & 0 \\ e_{14} & 0 & 0 \\ 0 & e_{25} & 0 \\ 0 & 0 & e_{36} \end{bmatrix} * \begin{bmatrix} E_1 \\ E_2 \\ E_3 \end{bmatrix} \tag{7}$$

$$\begin{bmatrix} D_1 \\ D_2 \\ D_3 \end{bmatrix} = \begin{bmatrix} 0 & 0 & 0 & e_{14} & 0 & 0 \\ 0 & 0 & 0 & 0 & e_{25} & 0 \\ 0 & 0 & 0 & 0 & 0 & e_{36} \end{bmatrix} * \begin{bmatrix} S_1 \\ S_2 \\ S_3 \\ S_4 \\ S_5 \\ S_6 \end{bmatrix} + \begin{bmatrix} э_{11} & 0 & 0 \\ 0 & э_{22} & 0 \\ 0 & 0 & э_{33} \end{bmatrix} * \begin{bmatrix} E_1 \\ E_2 \\ E_3 \end{bmatrix} \tag{8}$$

where

$$T_1 = \sigma_{11}; T_2 = \sigma_{22}; T_3 = \sigma_{33}; T_4 = \sigma_{23}; T_5 = \sigma_{31}; T_6 = \sigma_{12}; S_1 = \varepsilon_{11} = u_{1,1}; S_2 = \varepsilon_{22} = u_{2,2};$$
$$S_3 = \varepsilon_{33} = u_{3,3}; S_4 = 2\varepsilon_{23} = u_{2,3} + u_{3,2}; S_5 = 2\varepsilon_{31} = u_{3,1} + u_{1,3}; S_6 = 2\varepsilon_{12} = u_{1,2} + u_{2,1}. \tag{9}$$

From relation (7) follow the expressions for the components of the stress tensor:

$$\begin{aligned} \sigma_{xx} &= c_{11}\frac{\partial u_x}{\partial x} + c_{12}\frac{\partial u_y}{\partial y} + c_{13}\frac{\partial u_z}{\partial z} \\ \sigma_{yy} &= c_{12}\frac{\partial u_x}{\partial x} + c_{11}\frac{\partial u_y}{\partial y} + c_{13}\frac{\partial u_z}{\partial z} \\ \sigma_{zz} &= c_{13}\frac{\partial u_x}{\partial x} + c_{13}\frac{\partial u_y}{\partial y} + c_{33}\frac{\partial u_z}{\partial z} \\ \sigma_{yz} &= c_{44}\frac{\partial u_y}{\partial z} + c_{44}\frac{\partial u_z}{\partial y} - e_{14}E_x \\ \sigma_{xz} &= c_{44}\frac{\partial u_z}{\partial x} + c_{44}\frac{\partial u_x}{\partial z} - e_{14}E_y \\ \sigma_{xy} &= c_{66}\frac{\partial u_x}{\partial y} + c_{66}\frac{\partial u_y}{\partial x} - e_{36}E_z \end{aligned} \tag{10}$$

From relation (8) follow the components of electric induction:

$$\begin{aligned} D_x &= e_{14}\frac{\partial u_y}{\partial z} + e_{14}\frac{\partial u_z}{\partial y} + э_{11}E_x \\ D_y &= e_{14}\frac{\partial u_z}{\partial x} + e_{14}\frac{\partial u_x}{\partial z} + э_{11}E_y \\ D_z &= e_{36}\frac{\partial u_x}{\partial y} + e_{36}\frac{\partial u_y}{\partial x} + э_{33}E_z \end{aligned} \tag{11}$$

Given that

$$\frac{\partial f}{\partial z} = \frac{df}{dz}, \frac{\partial f}{\partial x} = -ik_x f, \frac{\partial f}{\partial y} = -ik_y f, \frac{\partial f}{\partial t} = -i\omega f \tag{12}$$

Fulfilling conditions (12), the expressions for the voltage components and electric induction (10) and (11) will take the form:

$$\begin{aligned}
\sigma_{xx} &= -ik_x c_{11} u_x - ik_y c_{12} u_y + c_{13}\frac{\partial u_z}{\partial z} \\
\sigma_{yy} &= -ik_x c_{12} u_x - ik_y c_{11} u_y + c_{13}\frac{\partial u_z}{\partial z} \\
\sigma_{zz} &= -ik_x c_{13} u_x - ik_y c_{13} u_y + c_{13}\frac{\partial u_z}{\partial z} \\
\sigma_{yz} &= c_{44}\frac{\partial u_y}{\partial z} - ik_y c_{44} u_z - e_{14} E_x \\
\sigma_{xz} &= -ik_x c_{44} u_z + c_{44}\frac{\partial u_x}{\partial z} - e_{14} E_y \\
\sigma_{xy} &= -ik_y c_{66} u_x - ik_x c_{66} u_y - e_{36} E_z \\
D_x &= e_{14}\frac{\partial u_y}{\partial z} - ik_y e_{14} u_z + э_{11} E_x \\
D_y &= -ik_x e_{14} u_z + e_{14}\frac{\partial u_x}{\partial z} + э_{11} E_y \\
D_z &= -ik_y e_{36} u_x - ik_x e_{36} u_y + э_{33} E_z
\end{aligned} \tag{13}$$

Since the inhomogeneity is assumed along the z axis, it is necessary to extract the derivatives with respect to z.

Equations of motion (2), considering conditions (12), we rewrite in the following form:

$$\begin{aligned}
-ik_x\sigma_{xx} - ik_y\sigma_{xy} + \frac{\partial\sigma_{xz}}{\partial z} &= -\rho\omega^2 u_x \\
-ik_x\sigma_{xy} - ik_y\sigma_{yy} + \frac{\partial\sigma_{yz}}{\partial z} &= -\rho\omega^2 u_y \\
-ik_x\sigma_{xz} - ik_y\sigma_{yz} + \frac{\partial\sigma_{zz}}{\partial z} &= -\rho\omega^2 u_z
\end{aligned} \tag{14}$$

Electromagnetic fields in anisotropic media in the absence of charges and currents are described by the first pair of Maxwell's equations (3). These equations in component-wise form are written as follows:

$$\begin{aligned}
\frac{\partial E_z}{\partial y} - \frac{\partial E_y}{\partial z} &= -i\omega\mu_0\mu H_x \\
\frac{\partial E_x}{\partial z} - \frac{\partial E_z}{\partial x} &= -i\omega\mu_0\mu H_y \\
\frac{\partial E_y}{\partial x} - \frac{\partial E_x}{\partial y} &= -i\omega\mu_0\mu H_z \\
\frac{\partial H_z}{\partial y} - \frac{\partial H_y}{\partial z} &= i\omega D_x \\
\frac{\partial H_x}{\partial z} - \frac{\partial H_z}{\partial x} &= i\omega D_y \\
\frac{\partial H_y}{\partial x} - \frac{\partial H_x}{\partial y} &= i\omega D_z
\end{aligned} \tag{15}$$

Considering the initial provisions stated above, the representation of wave fields is considered in the form:

$$\vec{F} = \vec{F}(\omega, z)e^{i\omega t \pm ik_x x \pm ik_y y} \tag{16}$$

Using the representation of solutions for vectors $\vec{E}$ and $\vec{H}$ in the form (16), we obtain:

$$\begin{aligned} \vec{E}(\omega, \vec{r}) &= \vec{E}(\omega, z)e^{i(\omega t - k_x x - k_y y)} \\ \vec{H}(\omega, \vec{r}) &= \vec{H}(\omega, z)e^{i(\omega t - k_x x - k_y y)} \end{aligned} \tag{17}$$

and substituting relations (13) and (17) into (15), as well as excluding the components that are not included in the boundary conditions, we obtain a system of ten first-order differential equations relating the components of stresses , strains and electric and magnetic fields:

$$\frac{dU_z}{dz} = \frac{1}{c_{33}}\sigma_{zz} + \left(\frac{ik_x c_{13}}{c_{33}}\right)U_x + \left(\frac{ik_y c_{13}}{c_{33}}\right)U_y;$$

$$\frac{d\sigma_{zz}}{dz} = -\rho\omega^2 U_z + ik_x\sigma_{xz} + ik_y\sigma_{yz};$$

$$\frac{dU_x}{dz} = \frac{1}{c_{55}}\sigma_{xz} + ik_x U_z + \frac{e_{25}}{c_{55}}E_y;$$

$$\frac{d\sigma_{xz}}{dz} = \frac{ik_x c_{13}}{c_{33}}\sigma_{zz} + (-\rho\omega^2 + k_x^2 c_{11} - \frac{k_x^2 c_{13}^2}{c_{33}} + k_y^2 c_{66} + \frac{k_y^2 e_{36}^2}{э_{33}})U_x + (k_x k_y c_{12} - \frac{k_x k_y c_{13} c_{23}}{c_{33}} + k_x k_y c_{66} +$$
$$+ \frac{k_x k_y e_{36}^2}{э_{33}})U_y - \frac{ik_y^2 e_{36}}{\omega э_{33}}H_x + \frac{ik_x k_y e_{36}}{\omega э_{33}}H_y;$$

$$\frac{dU_y}{dz} = \frac{1}{c_{44}}\sigma_{yz} + ik_y U_z + \frac{e_{14}}{c_{44}}E_x;$$

$$\frac{d\sigma_{yz}}{dz} = \frac{ik_y c_{13}}{c_{33}}\sigma_{zz} + (-\rho\omega^2 + k_x^2 c_{66} + k_y^2 c_{22} - \frac{k_и^2 c_{23}^2}{c_{33}} + \frac{k_x^2 e_{36}^2}{э_{33}})U_y + (k_x k_y c_{66} + \frac{k_x k_y e_{36}^2}{э_{33}} + k_x k_y c_{12} -$$
$$- \frac{k_x k_y c_{13} c_{23}}{c_{33}})U_x + \frac{ik_x^2 e_{36}^2}{\omega э_{33}}H_y - \frac{ik_x k_y e_{36}}{\omega э_{33}}H_x;$$

$$\frac{dE_y}{dz} = \frac{ik_x k_y}{\omega э_{33}}H_y + (-\frac{ik_y^2}{\omega э_{33}} + i\omega\mu\mu_0)H_x + \frac{k_y^2 e_{36}}{э_{33}}U_x + \frac{k_x k_y e_{36}}{э_{33}}U_y;$$

$$\frac{dE_x}{dz} = -\frac{ik_x k_y}{\omega э_{33}}H_x + (\frac{ik_x^2}{\omega э_{33}} - i\omega\mu\mu_0)H_y + \frac{k_x k_y e_{36}}{э_{33}}U_x + \frac{k_x^2 e_{36}}{э_{33}}U_y;$$

$$\frac{dH_x}{dz} = \frac{i\omega e_{25}}{c_{55}}\sigma_{xz} + (i\omega\frac{e_{25}^2}{c_{55}} + i\omega э_{22} - \frac{ik_x^2}{\omega\mu\mu_0})E_y + \frac{ik_x k_y}{\omega\mu\mu_0}E_x;$$

$$\frac{dH_y}{dz} = -\frac{i\omega e_{14}}{c_{44}}\sigma_{yz} + (-i\omega\frac{e_{14}^2}{c_{44}} - i\omega э_{11} + \frac{ik_y^2}{\omega\mu\mu_0})E_x - \frac{ik_x k_y}{\omega\mu\mu_0}E_y.$$

This system of differential equations in matrix form has the form:

$$\frac{d\vec{W}}{dz} = B\vec{W}; \vec{W} = (U_z, \sigma_{zz}, U_x, \sigma_{xz}, U_y, \sigma_{yz}, E_y, H_x, H_y E_x) \tag{18}$$

where u_i, σ_{iz} – displacement vector and stress tensor components; E_y, H_x, H_y, E_x – components of electric and magnetic fields; k_x, k_y – respectively x and y are the components of the wave vector; $\hat{B} = \hat{B}\left[c_{ijkl}(z), e_{kij}(z), э_{ij}(z), k_x, k_y\right]$ – matrix of coefficients, the elements of this matrix contain the parameters of the medium in which the electroelastic waves propagate.

The matrix $\hat{B}$ in the case of propagation of electroelastic waves along the Z axis has the following structure:

$$\hat{B} = \begin{pmatrix} 0 & b_{12} & 0 & 0 & 0 & 0 & 0 & 0 & 0 & 0 \\ b_{21} & 0 & 0 & 0 & 0 & 0 & 0 & 0 & 0 & 0 \\ 0 & 0 & 0 & b_{34} & b_{35} & 0 & 0 & 0 & 0 & 0 \\ 0 & 0 & b_{21} & 0 & 0 & 0 & 0 & 0 & 0 & 0 \\ 0 & 0 & 0 & 0 & 0 & b_{56} & 0 & 0 & 0 & 0 \\ 0 & 0 & 0 & i\omega b_{35} & b_{65} & 0 & 0 & 0 & 0 & 0 \\ 0 & 0 & 0 & 0 & 0 & 0 & 0 & b_{78} & 0 & b_{710} \\ 0 & 0 & 0 & 0 & 0 & 0 & b_{21} & 0 & 0 & 0 \\ 0 & 0 & 0 & 0 & 0 & 0 & 0 & -i\omega b_{710} & 0 & b_{910} \\ 0 & 0 & 0 & 0 & 0 & 0 & 0 & 0 & -b_{56} & 0 \end{pmatrix} \vec{u} = \begin{pmatrix} U_z \\ \sigma_{zz} \\ U_x \\ \sigma_{xz} \\ E_y \\ H_x \\ U_y \\ \sigma_{yz} \\ H_y \\ E_x \end{pmatrix} \tag{19}$$

Based on the structure of the matrix of coefficients, it follows that in this case in the piezocrystal there is not one, but several types of waves, the interaction between which is determined by the coefficients $b_{35} = \frac{e_{25}}{c_{55}}$ and $b_{710} = \frac{e_{14}}{c_{44}}$. These coefficients reflect the relationship between the piezoelectric moduli and the elastic constants of the medium in which the waves propagate. An elastic longitudinal wave, described by the coefficients b_{12} and b_{21} propagates independently of other types of waves. The coefficient b_{35} determines the interaction between the elastic transverse x-polarization wave and the electromagnetic TE-wave, and the coefficient b_{710} determines the interaction between the elastic transverse wave of the y-polarization and the electromagnetic TM-wave.

The coefficients that determine the relationship between different types of waves provide a constant transition of the energy of elastic waves into the energy of electromagnetic waves and vice versa.

Boundary conditions for non-rigid contact

If in an elastic dielectric medium there is a thin layer of thickness h and $\lambda >> h$ (λ is the wavelength, h is the inhomogeneity period), then the system of equations (18) can be represented in the finite difference form:

$$\frac{d\vec{W}}{dz} \cong \frac{\Delta\vec{W}}{h} = B\vec{W}; \Delta\vec{W} = \vec{W}_2 - \vec{W}_1 \tag{20}$$

From (20) it immediately follows:

$$\vec{W}_2 = [E + Bh]\vec{W}_1. \tag{21}$$

Writing (21) in the form:

$$\vec{W}_2 = G\vec{W}_1; G = E + Bh; \tag{22}$$

we obtain the boundary conditions describing the effect of a thin layer with piezoelectric properties.

The condition λ >>h makes it possible to exclude the construction of a wave field inside a thin layer, in view of the quasi-static nature of the loaded state. Boundary conditions (22) are the desired conditions for non-rigid contact. For h →, from (22) the hard contact condition (1) follows. The influence of the physical and mechanical properties of a thin layer is taken into account by the elements of matrix *B*. Similarly to condition (8), the influences of other thin layers can be taken into account. As follows from (21), for this it is necessary and sufficient to know the matrix *B* (19) or the system of equations (18).

If in the domain $z \in [0, H]$ the left boundary of the thin layer is at $z = z_1$, then the layer matrix has the form:

$$T(0, H) = T_2 G T_1; \tag{23}$$

T_1 – layer matrix $[0; z_1]$, T_2 – layer matrix $[z_1, H]$.

If there are N thin layers inside some layer, the matrix of the total layer is written as:

$$T = T_{N+1} G_N T_N G_{N-1} ... T_2 G_1 T_1. \tag{24}$$

At present, the matricant method has been developed and equations of the type (18) have been obtained for piezoelectric and piezomagnetic media, considering the magnetoelectric effect, elastic, thermoelastic, liquid crystal media. Based on the boundary conditions in the system (18) for these media, it is possible to design various artificial heterostructures by introducing thin layers with different physical and mechanical properties.

An important aspect of the application of boundary conditions of the type (22) is considering the influence of deformation and distortion of crystalline media in contact with different lattice periods, as well as the study of contact distortions and their influence on physical and mechanical parameters.

One of the design features of the matricant method is the possibility, within the framework of this method, to investigate the δ - shaped properties of the medium. These properties simulate the case of a significant difference between the properties of a thin layer and the properties of the environment. Mathematically, this is written as follows:

$$\lim_{h \to 0} Bh = G; \lim_{h \to 0} b_{ij} h = g_{ij}$$

Conclusions

In this article, based on the analytical method of the matricant, the regularities of the propagation of electro-elastic waves in piezo crystals of the rhombic syngony of class 222 are studied. The complete system of Maxwell's equations and equations of motion are obtained and solved. A generalization of non-classical contact conditions for studying the effect of thin interlayers with different physical and mechanical properties on wave processes is given. The derivation of these conditions for a thin layer with piezoelectric properties is given. The possibility of studying layers with δ - shaped properties (- Dirac function) is proved.

Acknowledgments

This research was funded by the Science Committee of the Ministry of Education and Science of the Republic of Kazakhstan (Grant No. AP08856290).

References

1 Martin L.W. Multiferroic and magnetoelectricheterostructures / L.W. Martin, R. Ramesh // ActaMateriale. — 2012.

2 Dai X. Energy harvesting from mechanical vibrations using multiple magnetostrictive/piezoelectric composite transducers / X. Dai, Y. Wen, P. Li, J. Yang, M. Li // Sensors and Actuators: A Physica. — 2010.

3 Mateu L. Review of Energy Harvesting Techniques and Applications for Microelectronics / L. Mateu, F. Moll // the Proceedings of the SPIE Microtechnologies for the New Millenium, — 2005. — P. 359–373.

4 Li P. A magnetoelectric energy harvester and management circuit for wireless sensor network / P. Li, Y. Wen, P. Liu, X. Li, C. Jia // Sensors and Actuators: A Physica. — 2010. — Vol. 157. — P. 100–106.

5 Бичурин М.И. Магнитоэлектрические композиционные материалы на основе феррит-пьезоэлектриков / М.И. Бичурин, В.М. Петров, Д.А. Филиппов, Г. Сринивасан, В.М. Лалетин // Перспективные материалы. — 2004. — № 6. — С. 5–12.

6 Филиппов Д.А. Теория магнитоэлектрического эффекта в гибридных феррит-пьезоэлектрических композиционных материалах /Д.А. Филиппов // Письма в ЖТФ. — 2004. — Т. 30. — Вып. 9. — С. 6–11.

7 Филиппов Д.А. Гигантский магнитоэлектрический эффект в композиционных материалах в области электромеханического резонанса / Д.А. Филиппов, М.И. Бичурин, В.М. Петров, В.М. Лалетин, Н.Н. Поддубная, Г. Сринивасан // Письма в ЖТФ. — 2004. — Т. 30. — Вып. 1. — С. 15–20.

8 Филиппов Д.А. Резонансное усиление магнитоэлектрического эффекта в композиционных феррит-пьезоэлектрических материалах / Д.А. Филиппов, М.И. Бичурин, В.М. Петров, В.М. Лалетин, Г. Сринивасан // Физика твердого тела. — 2004. — Т. 46. — Вып. 9. — С. 1621–1627.

9 Филиппов Д.А. Теория магнитоэлектрического эффекта в гетерогенных структурах на основе ферромагнетик–пьезоэлектрик / Д.А. Филиппов // Физика твердого тела. — 2005. — Т. 47. — Вып. 6. — С. 1082–1084.

10 Филиппов Д.А. Магнитоэлектрический эффект в двухслойной магнитострикционно-пьезоэлектрической структуре / Д.А. Филиппов, В.М. Лалетин, Т.А. Галичян // Физика твердого тела. — 2013. — Т. 55. — Вып. 9. — С. 1728–1733.

11 Filippov D.A. Theory of magnetoelectric effect in a bilayer magnetostrictive-piezoelectric structure / D.A. Filippov, T.A. Galichyan // Russian Physics Journal. — 2013. — Vol. 56, No. 6. — P. 686–692.

12 Ding Jian-Ming. Influence of the stress on magnetoelectric effect in magnetostrictive-PZ bilayers / Jian-Ming Ding, Chong-Gui Zhong, Qing Jiang // Front. Phys. China. — 2007. — 3(3). P. 312–317.

13 Rivera J.-P. A short review of the magnetoelectric effect and related experimental techniques on single phase (multi-) ferroics / J.-P. Rivera // Eur. Phys. J. B. 2009. — Vol. 71. — P. 299–313.

14 Bedekar V. Magnetoelectric gradiometer / V. Bedekar, R.A. Islam, H. Kim, M.I. Bichurin, S.N. Ivanov, Y.J. Pukinski, S. Priya // Eur. Phys. J. B. — 2009. — Vol. 71. — P. 387–392.

15 Naifar S. Response analysis of a nonlinear magnetoelectric energy harvester under harmonic excitation / S. Naifar, S. Bradai, C. Viehweger, O. Kanoun // Eur. Phys. J. Special Topics. — 2015. — 224. — P. 2897–2907.

16 Кристенсен Р. Введение в механику композитов / Р. Кристенсен. — М.: Мир, 1982. — 333 с.

17 Van Suchtelen J. Product properties: A New Application of Composite Materials / J. Van Suchtelen // Philips Res. Rep., 1972. — Vol. 27. — P. 28–37.

18 Van Suchtelen J. Nonstructural Application of Composite Materials / J. Van Suchtelen // Ann. Chem. Fr., 1980. — Vol. 5. — P. 139–145.

19 Ryu J. Magnetoelectric Effcct in Composites of Magnetostrictive ad Piezoelectric Materials / J. Ryu, S. Priya, K. Uchino, H.E. Kim // *J. Of Electroceramics.* — 2002. — Vol. 8. — P. 107–119.

20 Филиппов Д.А. Резонансное усиление магнитоэлектрического эффекта в композиционных феррит-пьезоэлектрических материалах / Д.А. Филиппов, М.И. Бичурин, В.М. Петров, В.М. Лалетин, Г. Сринивасан // Физика твердого тела. — 2004. — Т.46. — Вып. 9. — С. 1621–1627.

21 Тлеукенов С.К. Метод матрицанта / С.К. Тлеукенов. — Павлодар, Павлодар. гос. ун-т, 2004. — С. 172.

22 Tleukenov S.K. The equation of dispersion of electromagnetic waves in a layer with magnetoelectric effect / S.K. Tleukenov, A.B. Bobeev, D.S. Sabitova // Proceedings of the school-seminar “Waves-2016”. Physics and application of microwaves. Electrodynamics, 2016. — Vol.6. — P. 75–77.

23 Tleukenov S.K. On a unified description of surface waves and Lemb-type waves / S.K. Tleukenov, M.K. Zhukenov // Materials of the III international scientific-practical conference “Mathematical modeling of mechanical systems and physical processes”. — Almaty, 2016. — pp. 174, 175.

24 Тлеукенов С.К. О едином описании поверхностных волн и волн лэмбовского типа / С.К. Тлеукенов // Тр. школы-семинара «Волны–2016». Акустика неоднородных сред. — 2016. — Т.8. — С. 54–56.

25 Tleukenov S.K. Method of matricant. Unified description of wave processes in media with the mutual transformation of elastic and electromagnetic fields. Indicatrices of the wave vectors of elastic and electromagnetic waves in piezomagnetic medium of rhombic symmetry / S.K. Tleukenov, D.S. Sabitova, A.B. Bobeev // 3rd World Congress on Materials Science and Engineering, Barcelona, Spain, 2016. — P. 84, 85.

26 Kurmanov A.A. Propagation Of Electromagnetic Waves In Stationary Anisotropic Media / A.A. Kurmanov, N.A. Ispulov, A. Qadir, A.Zh. Zhumabekov, Sh.N. Sarymova, K.R. Dossumbekov // Physica Scripta, 2021. — 96. — 085505. DOI: 10.1088/1402–4896/abfe87.

27 Dossumbekov K.R. Propagation of electromagnetic waves in cholesteric liquid crystals / K.R. Dossumbekov, N.A. Ispulov, A.A. Kurmanov, A.Zh. Zhumabekov // Russian Physics Journal. — 2021. — Vol. 64, No. 8. — p. 1391–1399.

28 Ispulov N.A. Reflection of thermoelastic wave on the interface of isotropic half-space and tetragonal syngony anisotropic medium of classes 4, 4/m with thermomechanical effect / N.A. Ispulov, A. Qadir, M.A. Shah, A.K. Seythanova, T.G. Kissikov, E. Arinov // CHINESE PHYSICS B. — 2016. — 038102. DOI: 10.1088/1674–1056/25/3/038102.

29 Ispulov N.A. The Propagation of Thermoelastic Waves in Anisotropic Media of Orthorhombic, Hexagonal, and Tetragonal Syngonies / N.A. Ispulov, A. Qadir, M.K. Zhukenov, E. Arinov // Advances In Mathematical Physics. — 2017. — 4898467. DOI: 10.1155/2017/4898467.

30 Ispulov N.A. The Analytical Form of the Dispersion Equation of Elastic Waves in Periodically Inhomogeneous Medium of Different Classes of Crystals / N.A. Ispulov, A. Qadir, M.K. Zhukenov, T.S. Dossanov, T.G. Kissikov // Advances In Mathematical Physics. — 2017. — 5236898. DOI: 10.1155/2017/5236898.

31 Tleukenov S.K. A method for the analytical description of coupled-field waves in various anisotropic media / S.K. Tleukenov // ActaMechanica. — 2014. — Vol. 225, Iss. 12. — pp. 3535–3547.

32 Tleukenov S.K. Lamb waves in elastic layers with rhombic symmetry / S.K. Tleukenov, A.B. Aitbaev // AcousticalPhysics. – – 2015. — Vol. 61, Iss. 2. — pp. 144–147.

33 Tleukenov S. Matrix method for obtaining Rayleigh wave equations for anisotropic media with hexagonal syngony / S. Tleukenov, L.A. Yeltinova // Bulletin of the Russian Academy of Sciences Physics. — 2013.

34 Tleukenov S.K. An analytical solution of the reflection and refraction problems for coupled waves in elastic and piezoelectric media / S.K. Tleukenova, N.K. Zhakiyev, L.A. Yeltinova // Ultrasonics Symposium (IUS). — 2013. — P. 1025–1028.

35 Подъяпольский Г.С. Отражение и преломление на границе двух сред в случае нежесткого контакта / Г.С. Подъяпольский // Изв. АН СССР. — Сер. Географ. — 1963. — № 4. — С. 525–531.

36 Тлеукенов С.К. Об условиях контакта упругих сред с тонкой прослойкой / С.К. Тлеукенов // В кн. Математические вопросы теории распространения волн // Зап. науч. семин. ЛОМИ им. В.А. Стеклова АН СССР. — Т. 173. — 1988. — С. 163–166.

37 Тлеукенов С.К. О поглощении энергии и разрыве смещений на границах с нежесткими контактами / С.К. Тлеукенов // В кн. Математические вопросы теории распространения волн // Зап. научн. семин. ЛОМИ им. В.А. Стеклова АН СССР. — Т. 128. — 1983. — С. 166–171.

38 Молотков Л.А. Матричный метод в теории распространения волн в слоистых упругих и жидких средах /Л.А. Молотков. — Л.: Наука, 1984. — 201 с.

39 Nowacki J.P. 2D Electro-elastic fields in a piezoelectric layer-substrate structure / J.P. Nowacki, V.I. Alshits, A. Radowicz // Int. J. Eng.Sci. — 2002. — 40. — 2057–2076.

Н.А. Испулов, Абдул Кадыр, А.Ж. Жумабеков, А.А. Курманов, Қ.Р. Досумбеков

Анизотропты ортада толқындардың таралуы кезінде физика-механикалық қасиеттері әртүрлі жұқа қабаттардың классикалық емес шекаралық байланыс шарттары туралы

Толқындық процестер физиканың әртүрлі салаларында қарқынды зерттеледі: электродинамика, плазма физикасы, радиофизика, акустика, гидродинамика және т.б. Электромагниттік және серпімді толқындық процестерді зерттеумен қатар, өзара трансформация болған кезде әртүрлі физикалық сипаттағы толқындардың таралу заңдылықтарын зерттеу ерекше өзекті болып табылады. Байланысқан өрістердегі толқындық процестер серпімді, электромагниттік және жылу өрістерінің өзара әсерін көрсетеді. Электромагниттік өрістердің деформация өрісімен байланысы пьезоэлектрлік, пьезомагниттік және магнитострикциялық қасиеттері бар ортада жүреді. Мақалада матрицалық әдіс негізінде физика-механикалық қасиеттері әртүрлі орталарда байланысқан серпімді және электромагниттік толқындардың таралуы зерттелген. Авторлар толқын процестеріне физика-механикалық қасиеттері әртүрлі жұқа қабаттардың әсерін зерттеу үшін классикалық емес байланыс жағдайларын жалпылауды ұсынған. 222 класындағы ромбтық жүйенің анизотропты орталарында электрлік серпімді толқындардың таралуын сипаттайтын айнымалы коэффициенттері бар 1-ші ретті дифференциалдық теңдеулер жүйесі құрылды. Пьезоэлектрлік қасиеттері бар жұқа қабат үшін қатты емес байланыс жағдайларының нәтижесі келтірілген. δ — тәрізді қасиеттері бар қабаттарды зерттеу мүмкіндігі дәлелденді (δ — Дирак функциясы).

Кілт сөздер: Максвелл теңдеулері, анизотропты орта, толқындар, қатты емес байланыс, матрицант әдісі.

Н.А. Испулов, Абдул Кадыр, А.Ж. Жумабеков, А.А. Курманов, К.Р. Досумбеков

О неклассических граничных условиях контакта тонких прослоек с различными физико-механическими свойствами при распространении волн в анизотропных средах

Волновые процессы интенсивно изучены в различных областях физики: электродинамике, физике плазмы, радиофизике, акустике, гидродинамике и т.д. Наряду с изучением электромагнитных и упругих волновых процессов особую актуальность приобретают исследования закономерностей распространения волн различной физической природы при наличии взаимной трансформации. Волновые процессы в связанных полях отражают взаимовлияние упругих, электромагнитных и тепловых полей. Связанность электромагнитных полей с полем деформаций имеет место в среде с пьезоэлектрическими, пьезомагнитными и магнитострикционными свойствами. В статье, на основе матричного метода, исследовано распространение связанных упругих и электромагнитных волн в средах с различными физико-механическими свойствами. Авторами предложено обобщение неклассических условий контакта для исследования влияния тонких прослоек с различными физико-механическими свойствами на волновые процессы. Построена система дифференциальных уравнений 1-го порядка с переменными коэффициентами, описывающими распространение электроупругих волн в анизотропных средах ромбической системы класса 222. Приведен вывод условий нежесткого контакта для тонкого слоя с пьезоэлектрическими свойствами. Доказана возможность исследования слоев с -образными свойствами (δ-функция Дирака).

Ключевые слова: уравнения Максвелла, анизотропная среда, волны, нежесткий контакт, метод матриканта.

References

1 Martin L.W., & Ramesh, R. (2012). Multiferroic and magnetoelectricheterostructures. *ActaMateriale*.

2 Dai, X., Wen, Y., Li, P., Yang, J., & Li, M. (2010). Energy harvesting from mechanical vibrations using multiple magnetostrictive/piezoelectric composite transducers. *Sensors and Actuators: A Physica.*

3 Mateu, L., & Moll, F. (2005). Review of Energy Harvesting Techniques and Applications for Microelectronics. *Proceedings of the SPIE Microtechnologies for the New Millenium*, 359–373.

4 Li, P., Wen, Y., Liu, P., Li, X., & Jia, C. (2010). A magnetoelectric energy harvester and management circuit for wireless sensor network. *Sensors and Actuators: A Physica*, 157, 100–106.

5 Bichurin, M.I., Petrov, V.M., Filippov, D.A., Srinivasan, G., & Laletin, V.M. (2004). Magnitoelektricheskie kompozitsionnye materialy na osnove ferrit-pezoelektrikov [Magnetoelectric composite materials based on ferrite-piezoelectrics] *Perspektivnye materialy, 6*, 5–12 [in Russian].

6 Filippov, D.A. (2004). Teoriia magnitoelektricheskogo effekta v gibridnykh ferrit-pezoelektricheskikh kompozitsionnykh materialakh [Theory of the magnetoelectric effect in hybrid ferrite-piezoelectric composite materials]. *Pisma v Zhurnal tekhnicheskoi fiziki — Applied Physics Letters*, 30, 9, 6–11 [in Russian].

7 Filippov, D.A., Bichurin, M.I., Petrov, V.M., Laletin, V.M., Poddubnaia, N.N., & Srinivasan, G. (2004). Gigantskii magnitoelektricheskii effekt v kompozitsionnykh materialakh v oblasti elektromekhanicheskogo rezonansa [Giant magnetoelectric effect in composite materials in the field of electromechanical resonance]. *Pisma v Zhurnal tekhnicheskoi fiziki — Applied Physics Letters*, 30, 1, 15–20 [in Russian].

8 Filippov, D.A., Bichurin, M.I., Petrov, V.M., Laletin, V.M., & Srinivasan, G. (2004). Rezonansnoe usilenie magnitoelektricheskogo effekta v kompozitsionnykh ferrit-pezoelektricheskikh materialakh [Resonance amplification of the magnetoelectric effect in composite ferrite-piezoelectric materials]. *Fizika tverdogo tela – Physics of the Solid State*, 46, 9, 1621–1627 [in Russian].

9 Filippov, D.A. (2005). Teoriia magnitoelektricheskogo effekta v geterogennykh strukturakh na osnove ferromagnetik–pezoelektrik [Theory of the magnetoelectric effect in heterogeneous structures based on a ferromagnet-piezoelectric]. *Fizika tverdogo tela – Physics of the Solid State*, 47, 6, 1082–1084 [in Russian].

10 Filippov, D.A., Laletin, V.M., & Galichyan, T.A. (2013). Magnitoelektricheskii effekt v dvukhsloinoi magnitostriktsionno-pezoelektricheskoi strukture [Magnetoelectric effect in a two-layer magnetostrictive-piezoelectric structure]. *Fizika tverdogo tela – Physics of the Solid State*, 55, 9, 1728–1733 [in Russian].

11 Filippov, D.A., & Galichyan, T.A. (2013). Theory of magnetoelectric effect in a bilayer magnetostrictive-piezoelectric structure. *Russian Physics Journal*, 56, 6, 686–692.

12 Ding Jian-Ming, Zhong Chong-Gui, & Jiang Qing (2007). Influence of the stress on magnetoelectric effect in magnetostrictive-PZ bilayers. *Front. Phys. China.* 3(3): 312 – 317.

13 Rivera, J.-P. (2009). A short review of the magnetoelectric effect and related experimental techniques on single phase (multi) ferroics. *Eur. Phys. J. B*, 71, 299–313.

14 Bedekar, V., Islam, R.A., Kim, H., Bichurin, M.I., Ivanov, S.N., Pukinski, Y.J, & Priya, S. (2009). *Eur. Phys. J. B.*, 71, 387–392.

15 Naifar, S., Bradai, S., Viehweger, C., & Kanoun, O. (2015). Response analysis of a nonlinear magnetoelectric energy harvester under harmonic excitation. *Eur. Phys. J. Special Topics*, 224, 2897–2907.

16 Kristensen, R. (1982). *Vvedenie v mekhaniku kompozitov [Introduction to the mechanics of composites]*. Moscow: Mir, 333 [in Russian].

17 Van Suchtelen, J. (1972). Product properties: A New Application of Composite Materials. *Philips Res. Rep.*, 27, 28–37.

18 Van Suchtelen, J. (1980). Nonstructural Application of Composite Materials. *Ann. Chem. Fr.*, 5, 139–145.

19 Ryu, J., Priya, S., Uchino, K., & Kim, H.E. (2002). Magnetoelectric Effcct in Composites of Magnetostrictive ad Piezoelectric Materials. *J. Of Electroceramics*, 8, 107–119.

20 Filippov, D.A., Bichurin, M.I., Petrov, V.M., Laletin, V.M., & Srinivasan, G. (2004). Rezonansnoe usilenie magnitoelektricheskogo effekta v kompozitsionnykh ferrit-pezoelektricheskikh materialakh [Resonance amplification of the magnetoelectric effect in composite ferrite-piezoelectric materials]. *Fizika tverdogo tela — Physics of the Solid State, 46, 9*, 1621–1627 [in Russian].

21 Tleukenov, S.K. (2004). *Metod matritsanta [Matrix method]*. Pavlodar: Pavlodarskii gosudarstvennyi universitet [in Russian].

22 Tleukenov, S.K., Bobeev, A.B., & Sabitova, D.S. (2016). The equation of dispersion of electromagnetic waves in a layer with magnetoelectric effect. *Proceedings of the school-seminar "Waves-2016". Physics and application of microwaves. Electrodynamics*, 6, 75–77.

23 Tleukenov, S.K., & Zhukenov, M.K. (2016). On a unified description of surface waves and Lemb-type waves. *Materials of the III international scientific-practical conference "Mathematical modeling of mechanical systems and physical processes".*

24 Tleukenov, S.K. (2016). O yedinom opisanii poverkhnostnykh voln i voln lembovskogo tipa [On a unified description of surface waves and waves of the Lamb type]. *Trudy shkoly-seminara «Volny–2016». Akustika neodnorodnykh sred — Proceedings of the School Seminar "Waves-2016". Acoustics of Inhomogeneous Media*, 8, 54–56 [in Russian].

25 Tleukenov, S.K., Sabitova, D.S., & Bobeev, A.B. (2016). Method of matricant. Unified description of wave processes in media with the mutual transformation of elastic and electromagnetic fields. Indicatrices of the wave vectors of elastic and electromag-

netic waves in piezomagnetic medium of rhombic symmetry. *3rd World Congress on Materials Science and Engineering, Barcelona, Spain*, 84–85.

26 Kurmanov, A.A., Ispulov, N.A., Qadir, A., Zhumabekov, A.Zh., Sarymova, Sh.N., & Dossumbekov, K.R. (2021). Propagation Of Electromagnetic Waves In Stationary Anisotropic Media. *Physica Scripta, 96, 085505*.

27 Dossumbekov, K.R., Ispulov, N.A., Kurmanov, A.A., & Zhumabekov, A.Zh. (2021). Propagation of electromagnetic waves in cholesteric liquid crystals. *Russian Physics Journal*, 64, 8, 1391–1399.

28 Ispulov, N.A. Qadir, A., Shah, M.A., Seythanova, A.K., Kissikov, T.G., & Arinov, E. (2016). Reflection of thermoelastic wave on the interface of isotropic half-space and tetragonal syngony anisotropic medium of classes 4, 4/m with thermomechanical effect. *CHINESE PHYSICS B, 038102*.

29 Ispulov, N.A. Qadir, A., Zhukenov, M.K., & Arinov, E. (2017). The Propagation of Thermoelastic Waves in Anisotropic Media of Orthorhombic, Hexagonal, and Tetragonal Syngonies. *Advances In Mathematical Physics, 4898467*.

30 Ispulov, N.A. Qadir, A., Zhukenov, M.K., Dossanov, T.S. & Kissikov, T.G. (2017). The Analytical Form of the Dispersion Equation of Elastic Waves in Periodically Inhomogeneous Medium of Different Classes of Crystals. *Advances In Mathematical Physics*.

31 Tleukenov, S.K. (2014). A method for the analytical description of coupled-field waves in various anisotropic media. *ActaMechanica*, 225, 12, 3535–3547.

32 Tleukenov, S.K., & Aitbaev, A.B. (2015). Lamb waves in elastic layers with rhombic symmetry. *AcousticalPhysics*, 61, 2, 144–147.

33 Tleukenov, S., & Yeltinova, L.A. (2013). Matrix method for obtaining Rayleigh wave equations for anisotropic media with hexagonal syngony. *Bulletin of the Russian Academy of Sciences. Physics*.

34 Tleukenov, S.K., Zhakiyev, N.K., & Yeltinova, L.A. (2013). An analytical solution of the reflection and refraction problems for coupled waves in elastic and piezoelectric media. *Ultrasonics Symposium (IUS). IEEE International*.

35 Podieiapolskii, G.S. (1963). Otrazhenie i prelomlenie na granitse dvukh sred v sluchae nezhestkogo kontakta [Reflection and refraction at the boundary of two media in the case of nonrigid contact]. *Izvestiia Akademii nauk SSSR. Seriia Geograficheskaia — News of the Academy of Sciences of USSR. Geography series*, 4, 525–531 [in Russian].

36 Tleukenov, S.K. (1988). Ob usloviiakh kontakta uprugikh sred s tonkoi prosloikoi [On the conditions of contact of elastic media with a thin layer]. In book Mathematical problems in the theory of wave propagation // *Zapiski nauchnykh seminarov LOMI im. V.A. Steklova AN SSSR – Journal of Mathematical Sciences of Steklov Mathematical Institute of the Russian Academy of Sciences*, Vol. 173, 163–166 [in Russian].

37 Tleukenov, S.K. (1983). O pogloshchenii energii i razryve smeshchenii na granitsakh s nezhestkimi kontaktami [On energy absorption and discontinuity of displacements at boundaries with nonrigid contacts]. In book Mathematical problems in the theory of wave propagation // *Zapiski nauchnykh seminarov LOMI im. V.A. Steklova AN SSSR – Journal of Mathematical Sciences of Steklov Mathematical Institute of the Russian Academy of Sciences*, Vol. 128, 166–171 [in Russian].

38 Molotkov, L.A. (1984). *Matrichnyi metod v teorii rasprostraneniia voln v sloistykh uprugikh i zhidkikh sredakh [Matrix Method in the Theory of Wave Propagation in Layered Elastic and Liquid Media]*. Leningrad: Nauka, 201 [in Russian].

39 Nowacki, J.P., Alshits, V.I., & Radowicz, A. (2002). 2D Electro-elastic fields in a piezoelectric layer-substrate structure. *Int. J. Eng.Sci.*, 40, 2057–2076.

DOI 10.31489/2022PH3/80-89

UDC 66.088

A.B. Kengesbekov[1,2], Zh.B. Sagdoldina[1*], D.B. Buitkenov[1],
I.A. Ocheredko[1], S.A. Abdulina[3], K. Torebek[1]

[1]S. Amanzholov East Kazakhstan University, Ust-Kamenogorsk, Kazakhstan
[2]Institute of Composite Materials, Ust-Kamenogorsk, Kazakhstan
[3]D. Serikbayev East Kazakhstan Technical University, Ust-Kamenogorsk, Kazakhstan
*(*E-mail: sagdoldina@mail.ru)*

Investigation of the characteristics of an indirect plasma torch

The main task of creating plasma technologies is to improve the operation parameters of its main element - the plasma torch, which is achieved by designing and constructing its main nodes. The paper analyzes the principles of designing a plasma torch and investigates the characteristics of an arc discharge plasma torch. The possibilities of increasing the thermal stability of the anode structure are considered; the speed and trajectory of powder particles are studied; the axial introduction of the powder through the cathode and the thermal stability of the cathode are studied. Using the finite element method, the effect of the anode shape on the service life of the plasma torch is studied by estimating the heat release power under the condition above the melting temperature of copper (anode). The optimal anode geometry for effective cooling of the unit with radial inlet and outlet of the coolant is determined. The influence of the thermal load on the cathode part of the plasma torch is studied, the thermophysical characteristics of the cathode on the operational characteristics of the plasma torch during the thermal load are taken. The dynamics of the particle by axial injection of the powder through the cathode is calculated, and the dynamics of the heating of the powder particle is determined. The output of the carrier gas is stabilized by a swirler and has great dynamics and is located in the high-temperature part of the arc. The trajectory of the movement of a powder particle in the nozzle area is calculated, which corresponds to the average value of the velocity ≈450-500 m/s. It is found that an increase in the cathode diameter from 3 to 5 mm reduces the thermal load by 50%.

Keywords: plasma treatment, plasma torch, axial powder injection, aerodynamics of particle motion, thermophysical characteristics, 3D model.

Introduction

Plasma technologies occupy a worthy place in a wide range of processes that have great innovative potential but require continuous modernization and constant scientific and technical research [1]. The main task of creating plasma technologies is to improve the operating parameters of its main element - the plasma torch, which is achieved by designing and constructing its main components [2, 3]. The principles of designing a plasma torch are primarily related to the tasks of improving its functional characteristics: productivity, quality, and reliability. However, information about the functioning of the plasma torch as a whole, the design of its elements, gas-dynamic, thermophysical and electrodynamic characteristics is difficult to access [4–6].

When designing plasma torches, it is necessary, first of all, to rely on the system principle and examine the interaction of all subsystems that ensure their operation. However, among the subsystems of the plasma torch, the main functional role is played by the nozzle assembly, the design of which requires considering gas-dynamic, electrical and thermal factors of arc formation. At present, the application of methods obtained by semi-empirical methods of criterion-parametric relationships for the same type of plasma torches requires adjustments that take into account new design solutions [7]. The low thermal stability of the plasma torch units and, as a result, their short service life is an urgent problem that increases the cost of plasma technologies. Low heat resistance of the nodes also reduces the technological potential of the plasma torch, based on its purpose - the melting of refractory materials. The purpose of this work is to optimize and study the technological process of arc plasmatron. Accordingly, the following tasks are solved in this research: to increase the thermal stability of the anode design; to research the thermal stability of the cathode; to study the aerodynamics and dynamics of particles in a plasmatron with a gas swirler.

1. Research the influence of the geometry of the plasma torch anode on its performance characteristics

An urgent problem is to increase the resource of the working units of the plasma torch – the anode and cathode, which experience extreme thermal loads from the effects of low-temperature plasma of about 7000–15000 °C. The low thermal stability of the plasma torch nodes and, as a result, their short service life is an urgent problem that increases the cost of plasma technologies [8]. Figure 1 illustrates the general view of the plasmatron. The modified plasmatron has a cooled anode (1) (copper) and a cathode (2) (the cathode is inserted into a cooled cathode holder (3) interconnected through a ceramic interelectrode insert (4) [9].

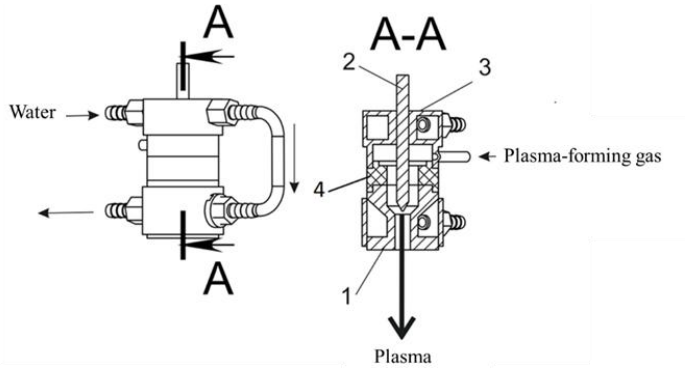

Figure 1. Plasmatron for spraying powder materials: 1 – anode, 2 – cathode, 3 – cooled cathode holder, 4 – ceramic interelectrode insert

On the program SolidWorks using the finite element method, the effect of the anode shape on the service life of the plasma torch was investigated by estimating the heat release power under the condition above the melting temperature of copper (anode). The boundary conditions for the cooled liquid in all studies for the anode are the same: water temperature 21 °C; pressure 5 atm. Figure 2 represents the geometry of the standard plasmatron anode.

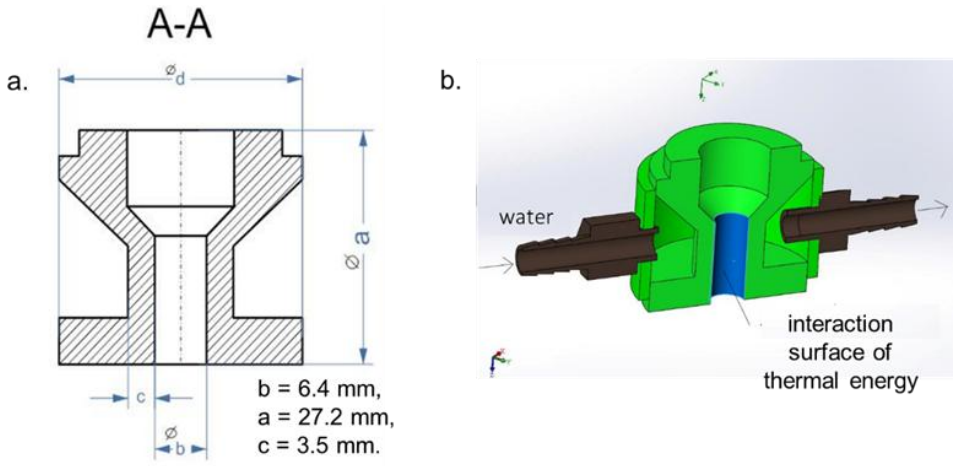

Figure 2. Anode of the plasmatron: a) scheme of the anode; b) 3D anode assembly

Figure 3 shows the graph of thermal conductivity of copper. The heat release power is a variable value. Table 1 presents the initial data on the heat load and the calculation results. The variable controlled parameter is the value – c and d, the dimensions a and b are related to the parameters of plasma formation. To avoid an increase in the dimensions of the plasmatron, dimension d had a fixed value. Going through the geometrical parameters, it is necessary to determine the maximum thermal stability of the anode depending on the geometrical parameters at the same coolant flow rate for all variants.

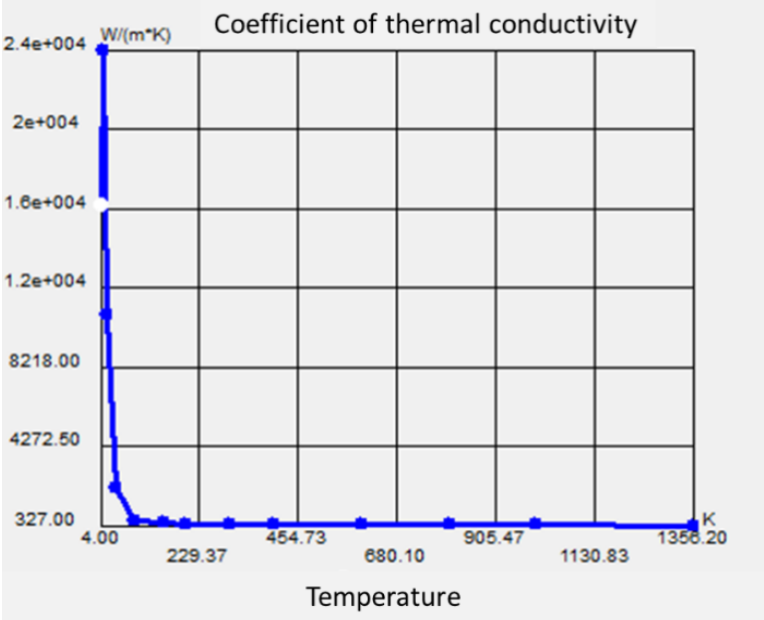

Figure 3. Graph of the thermal conductivity of copper

Table 1

Initial data on heat load and calculation results

Superheat above melting point	Design point 1	Design point 2	Design point 3	Design point 4	Design point 5
Heat dissipation capacity [W]	5000	8750	12500	16250	20000
Overheating above the melting point [℃]	-738.214219	-509.755152	-255.8967	4.706168475	260.2031197

The calculated point 4 is located near the region of the anode melting temperature. The temperature of 4.7°C above the melting point of copper, at 16250 W, is taken as a benchmark against which the results are compared when changing the anode geometry (Figure 4).

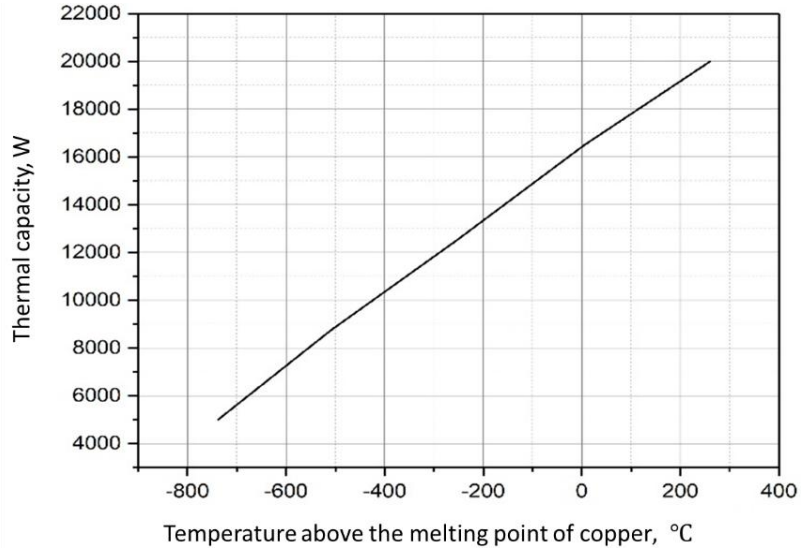

Figure 4. Overheating of the anode above the melting point of copper

Figure 5 shows different anode designs that have vertical and horizontal plates. According to a similar scheme, calculations are made for the design of the anode with a vertical plate (Figure 5a). The temperature exceeding the melting point by 4.7 °C corresponds to a thermal power of 16402 W, which is a gain of 152 W and corresponds to 1%. Further studies of this anode shape seem unpromising and the following option is investigated (Figure 5b). Calculations show that an overheating temperature of 4.7 °C corresponds to power of 16020 W, which amounted to a gain of 2770 W and corresponds to a 17% increase in the thermal resistance of the anode.

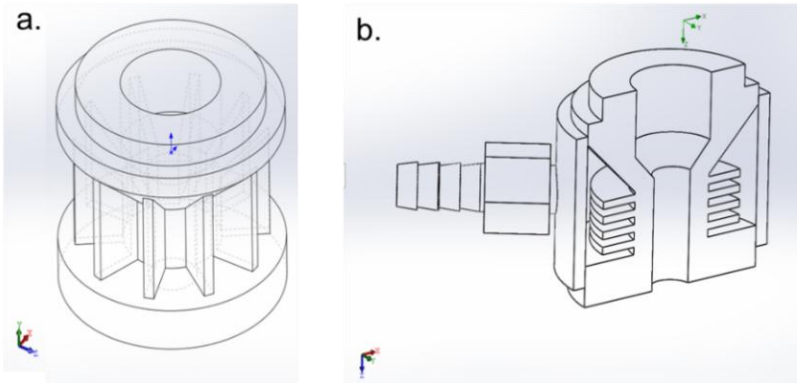

Figure 5. Anode design: a) with vertical plates; b) with horizontal plates

Figure 6 demonstrates the thermal load of 19000 W and the maximum anode temperature of 903 °C (on the temperature distribution field). We can conclude that considering the safety factor of 5%, the reliable operation of the anode will make it possible to utilize 18050 W of thermal energy without thermal destruction. As noted above, this is 17% more efficient compared to the non-optimized anode geometry (Figure 2).

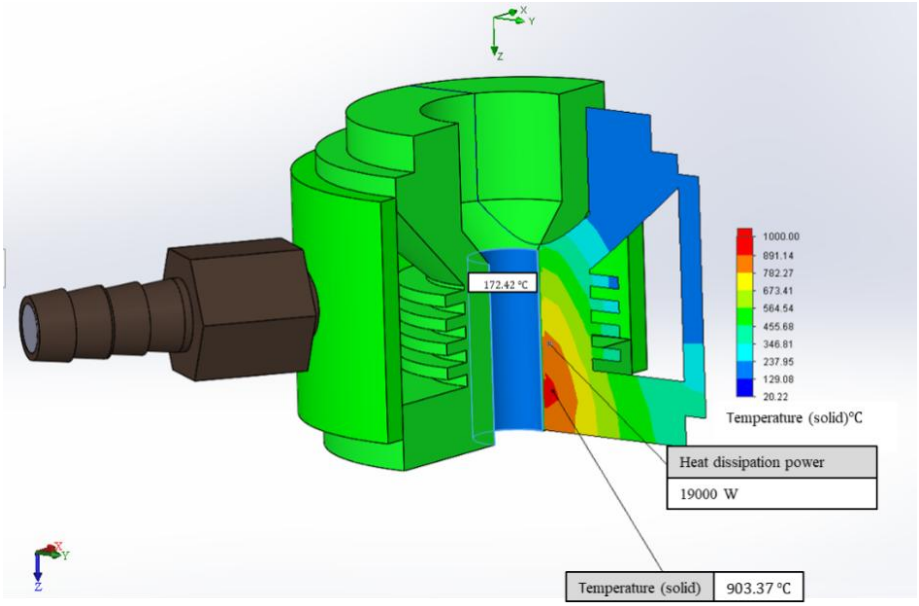

Figure 6. Anode thermal diagram

2. Research the influence of the geometry of the plasma torch anode on its performance characteristics

The cathode is the most thermally loaded part of the plasmatron; it is made of refractory tungsten with a high melting point, but low thermal conductivity relative to the copper anode. Regarding the fact that during the formation of an arc, electrons move in the direction from the anode to the cathode and, when entering the

cathode spot, cause additional heating of the cathode, the correct choice of the cathode geometry and factors affecting cooling is the number one task to ensure the continuous operation of the plasmatron. To study this problem, a 3D model of the plasma torch was created (Figure 7) and the factors affecting the operating temperature of the plasma torch were investigated.

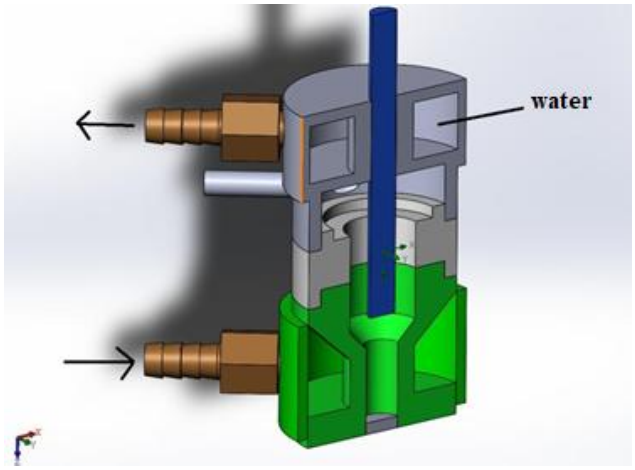

Figure 7. 3D model of the plasmatron

Figure 8 shows the dependence of the cathode temperature (at a thermal power on the cathode spot of 1 kW) on the gas pressure and cathode radius. It can be seen that with an increase in pressure from 3 to 8 atm. the temperature at the cathode drops by 550 °C (Figure 8a). The temperature dependence on the cathode size showed that an increase in the cathode radius leads to a decrease in the cathode temperature. According to Fourier's law, the rate of heat transfer through a material is proportional to the area through which heat flows (through the cathode) [10].

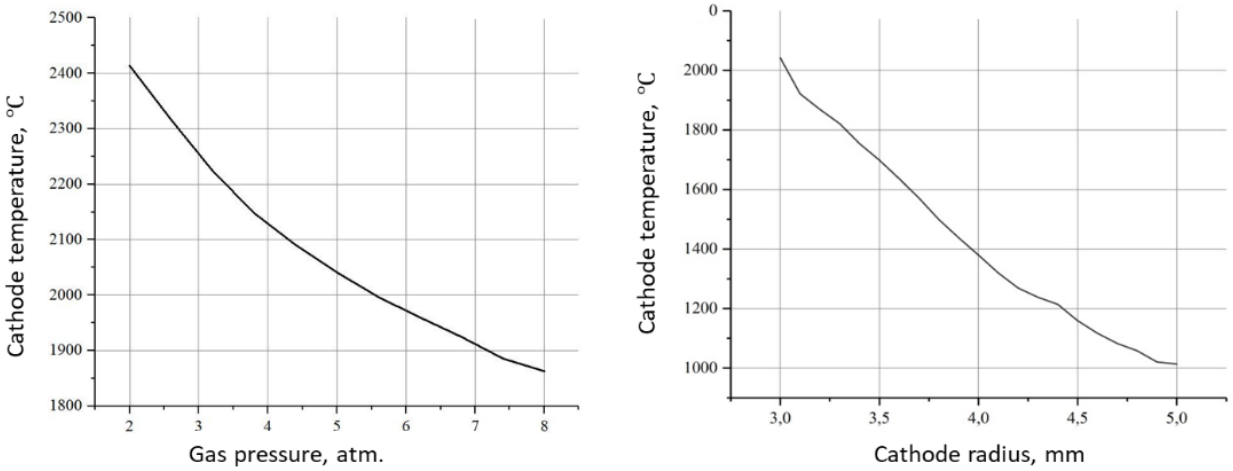

Figure 8. Dependence of the cathode temperature on gas pressure (a) and cathode radius (b)

Figure 9 shows the thermophysical characteristics (thermal conductivity, specific heat, and resistivity) of a cathode with a cooling system according to Figure 7. The plasmatron cooling system ensures the long-term operation of the cathode at a constant thermal load (Figure 10).

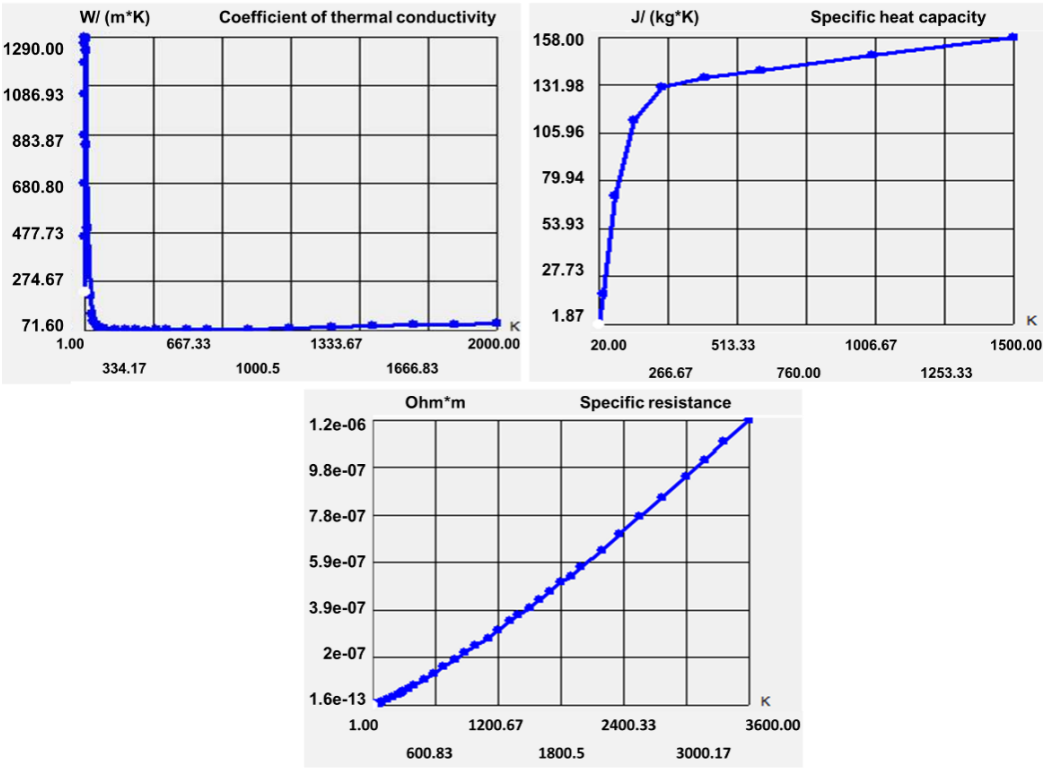

Figure 10. Thermal characteristics of the cathode

Thus, the influence of thermal load on the cathode part of the plasma torch was studied; the thermophysical characteristics of the cathode on the operational characteristics of the plasma torch during the thermal load were taken. The most significant factor affecting the reliability of the cathode is its diameter. Increasing the cathode diameter from 3 mm to 5 mm reduced the maximum temperature of the plasma torch by 50%. The second factor of influence is the pressure of the working gas. Increasing the working gas pressure by 1 atm gives a decrease in temperature by 120 °C. However, an increase in operating pressure can lead to arc failure, which leads to the need to increase the voltage and, consequently, the power of the plasma torch power source.

3. Study of the aerodynamics of particles in a plasma torch with a gas swirler

Using the finite element analysis method, the operation of a plasma torch with a gas swirler with the introduction of powder simultaneously with the working gas is studied. Figure 11a shows the gas flow trajectories and the velocity distribution gradient at an operating pressure of 5 atm. The parametric dependence of the average gas velocity on the working gas pressure at 1-8 atm is studied (Figure 11b). It can be seen that to ensure sufficient gas dynamics, it is necessary to operate the plasma torch in the pressure range of 3–5 atm.

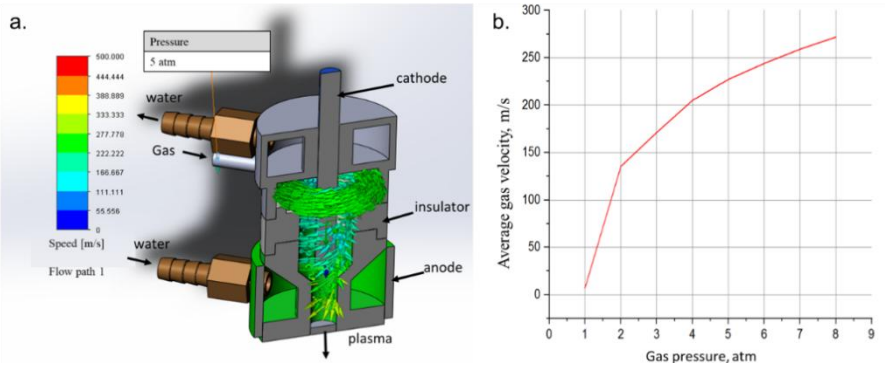

Figure 11. Results of aerodynamic modeling of the carrier gas: a) velocity distribution gradient; b) dependence of the average gas velocity on the operating gas pressure

Then the dynamics and trajectories of the movement of powder particles are studied when it is introduced into the swirler channel. The study is carried out without conditions of sticking and erosion. Titanium nitrite fraction 5 μm is chosen as the powder (conditional powder consumption 0.005 kg/s). The trajectory of the movement of a powder particle to the nozzle area is calculated, which corresponds to an average velocity of ≈220 m/s, as shown in Figure 12b. The length of the particle path in the plasma torch is up to 500 mm, in the plasma zone (nozzle area) about 150 mm.

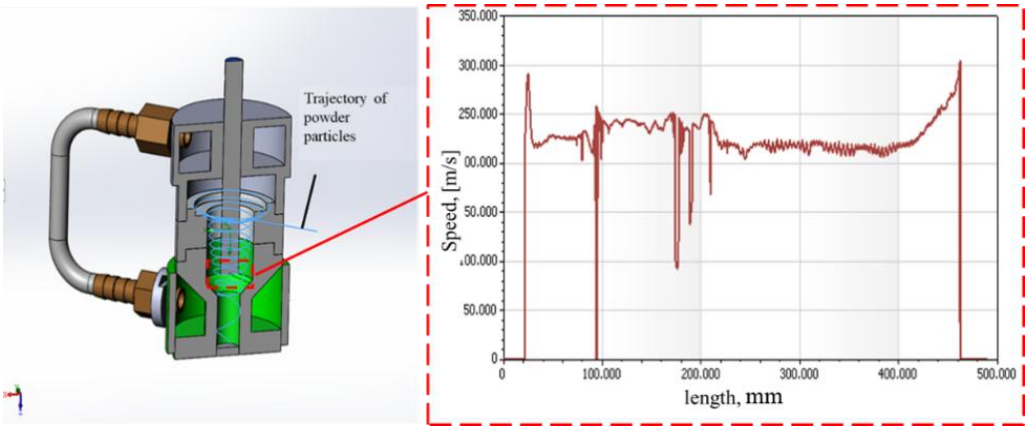

Figure 12. The results of the study of the speed of powder particles: a) the trajectory of the powder particle; b) the speed of movement of a particle of titanium nitride in the plasma torch

A scheme with axial injection of powder through the cathode is investigated (Figure 13). The aerodynamics of this scheme is calculated, the pressure of the working gas in the swirler is 5 atm, and in the cathode axis is 5 atm. The carrier gas outlet is stabilized by the swirler and has high dynamics; it is located in the high-temperature part of the arc (Figure 13b). The flow rate of the transporting gas in the anode area is 445–500 m/s.

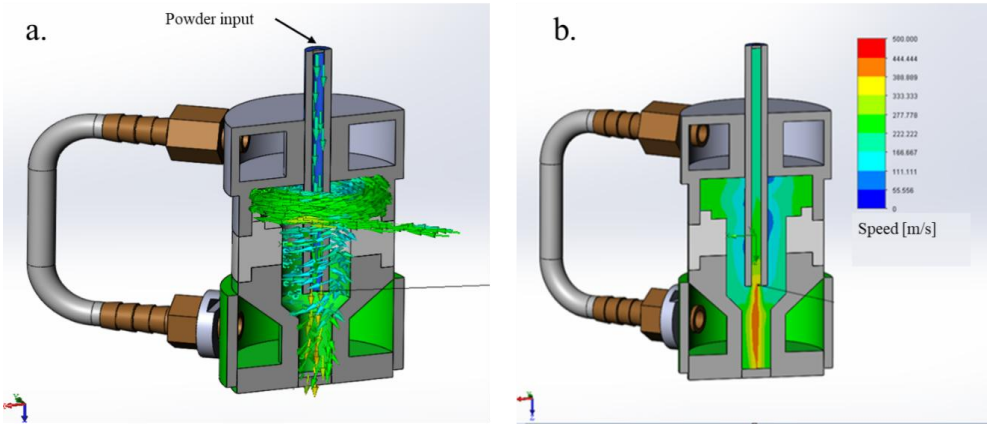

Figure 13. 3D model with axial injection of powder through the cathode (a) and the flow rate (b) of the transporting gas in the plasma torch

Figure 14 shows the velocity gradient and trajectory of the powder particles as the powder is axially injected through the cathode. The study is carried out without conditions of sticking and erosion. Titanium nitride with a fraction of 5 μm was chosen as the powder, at a material consumption of 0.005 kg/s. The trajectory of the movement of a powder particle to the nozzle area is calculated, which corresponds to an average velocity of ≈450-500 m/s.

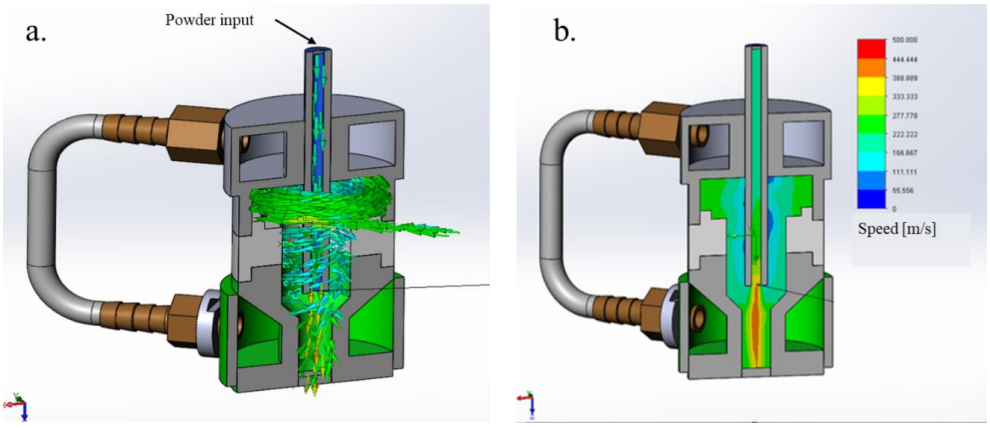

Figure 14. Velocity gradient of powder particles in the plasma torch

The particle dynamics along the motion trajectory is calculated (Figure 15a) and the particle heating dynamics is determined (Figure 15b). A domain in the form of a plasma arc with a temperature of 6000 °C is installed in the plasma torch. It can be seen from the diagrams that the particles move in the axis of the arc and the path length is equal to the length of the arc.

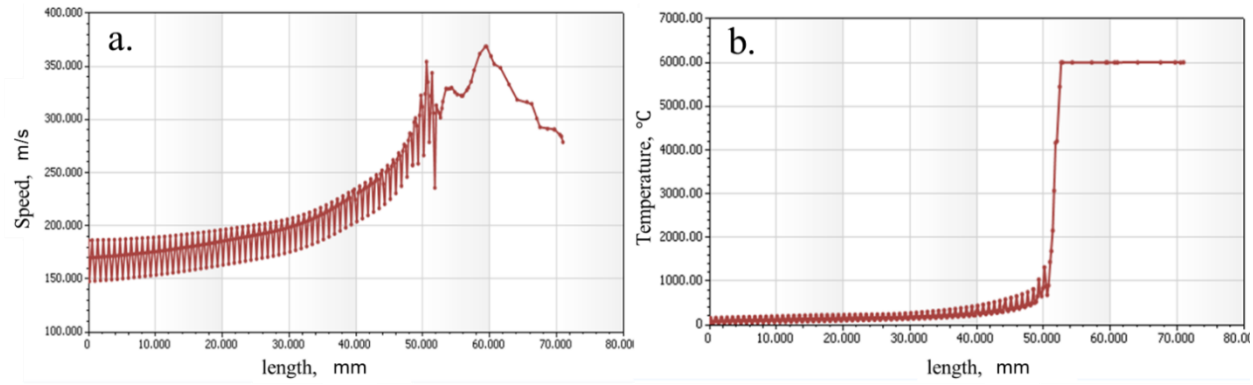

Figure 15. Particle dynamics along the motion trajectory (a) and particle heating dynamics (b)

Conclusions

Analyzing the experimental results obtained in the work, we draw the following conclusions:

– The optimal anode geometry for efficient cooling of the unit with radial inlet and outlet of the coolant was determined. The optimized anode design is 17% more efficient than the standard plasma torch anode geometry. This will increase the anode resource, operating currents, and expand the technological potential of the plasma torch;

– It was found that an increase in the cathode diameter from 3 to 5 mm reduces the thermal load by 50%. An increase in the working pressure of the gas by 1 atm gives a decrease in temperature by 120 °C. However, an increase in operating pressure can lead to arc breakdown, which leads to the need to increase the voltage and, consequently, the power of the plasma torch power source;

– The scheme with powder injection along the cathode axis makes it possible to effectively use the efficiency of the plasma torch and ensures an uninterrupted plasma treatment process.

Acknowledgment

This research was funded by the Science Committee of the Ministry of Education and Science of the Republic of Kazakhstan (Grant No. AP08857800).

References

1 Rakhadilov B. Hydrogen and deuterium storage in tungsten when irradiation with Plasma beam / B. Rakhadilov, A. Kenesbekov, M. Skakov, A. Miniyzov// In METAL 2018-27th International Conference on Metallurgy and Materials, Conference Proceedings. — P. 1216–1221.

2 Chen Xi. Three-dimensional flow and heat transfer in thermal plasma systems / Xi. Chen, H. Li. // Surface and Coatings Technology. — 2003. — Vol. 171. — P. 124–133.

3 Gawne D.T. Modelling of plasma–particle two-phase flow using statistical techniques / D.T. Gawne, B. Liu, Y. Bao, T. Zhang // Surface and Coatings Technology. — 2005. — Vol. 191. — P. 242–254.

4 Ramachandran K. 3D modeling of plasma–particle interactions in a plasma jet under dense loading conditions / K. Ramachandran, N. Kikukawa, H. Nishiyama // Thin Solid Films. — 2003. — Vol. 435. — P. 298–306.

5 Trelles J.P. Multiscale finite element modeling of arc dynamics in a DC plasma torch / J.P. Trelles, P. Emil, H. Joachim // Plasma chemistry and plasma processing. — 2006. — Vol. 26.6. — P. 557–575.

6 Park J. Two-dimensional numerical modeling of direct-current electric arcs in nonequilibrium. / J. Park, J. Heberlein, E. Pfender, G. Candler, C.H. Chang // Plasma Chemistry and Plasma Processing. — 2008. — Vol. 28.2. — P. 213–231.

7 Анахов С.В. Принципы и методы проектирования плазмотронов: моногр. / С.В. Анахов. Екатеринбург: Изд-во Рос. гос. проф.-пед. ун-та, 2018. — 165 с.

8 Kylyshkanov M.K. Processing of industrial waste by plasma-chemical method / M.K. Kylyshkanov, K.A. Shestakov, Z.B. Sagdoldina, B.K. Rakhadilov, A.B. Kengesbekov // Bulletin of the university of Karaganda-Physics. — 2021. — Vol. 3, No. 103. — P. 45–51.

9 Rakhadilov B.K. Development of air-plasma technology for hardening cutting tools by applying wear-resistant coatings / B.K. Rakhadilov, A.B. Kenesbekov, P. Kowalevski, Y.A. Ocheredko, Sagdoldina Zh.B. // News of the National Academy of sciences of the Republic of Kazakhstan-series of geology and technical sciences. — 2020. — Vol. 3.441. — P.54–62.

10 Bird R.B. Transport Phenomena / R.B. Bird, W.E. Stewart, E.N. Lightfoot // Wiley. — 2006. — Vol. 1. ISBN 978-0-470-11539-8.

А.Б. Кеңесбеков, Ж.Б. Сағдолдина, Д.Б. Буйткенов,
И.А. Очередько, С.А. Абдулина, Қ. Төребек

Жанама әсер ететін плазмотрон сипаттамасын зерттеу

Плазмалық технологияларды құрудың негізгі міндеті оның негізгі элементі — плазмотрон жұмысының параметрлерін жақсарту болып табылады, оған оның негізгі түйіндерін жобалау және құрау арқылы қол жеткізіледі. Мақалада плазмотронды жобалау принциптері және доғалық разряд плазматронының сипаттамалары талданған. Анод құрылымының жылу тұрақтылығын арттыру мүмкіндіктері қарастырылған, ұнтақ бөлшектерінің жылдамдығы мен траекториясы зерттелді, катод арқылы ұнтақты осьтік енгізу, катодтың жылу кедергісі зерттелген. Соңғы элементтер әдісімен мыстың (анодтың) балқу температурасынан жоғары болған жағдайда жылу шығару қуатын бағалау бойынша анод формасының плазмотрон жұмысының ресурсына әсері тексерілген. Салқындатқышты радиалды енгізу және шығару кезінде түйінді тиімді салқындату үшін анодтың оңтайлы геометриясы анықталды. Жылу жүктемесінің плазматронның катодты бөлігіне әсері зерттелді, жылу жүктемесі процесінде катодтың жылу-физикалық сипаттамалары плазматронның пайдалану сипаттамаларына алынды. Бөлшектің динамикасы катод арқылы ұнтақты осьтік енгізу арқылы есептеледі және ұнтақ бөлшегінің қыздыру динамикасы анықталады. Тасымалдаушы газдың шығуы турбулентті тұрақтандырады және үлкен динамикаға ие және доғаның жоғары температуралық бөлігінде орналасқан. Ұнтақ бөлшегінің саптама аймағына қозғалысының траекториясы есептеледі, ол жылдамдықтың орташа мәніне сәйкес келеді ≈450-500 м/с. Катод диаметрінің 3-тен 5 мм-ге дейін ұлғаюы жылу жүктемесін 50% төмендететіні анықталды.

Кілт сөздер: плазмалық өңдеу, плазматрон, ұнтақты осьтік енгізу, бөлшектердің қозғалысының аэродинамикасы, термофизикалық сипаттамалары, 3D моделі.

А.Б. Кенесбеков, Ж.Б. Сагдолдина, Д.Б. Буйткенов,
И.А Очередько, С.А. Абдулина, К. Торебек

Исследование характеристики плазмотрона косвенного действия

Основной задачей создания плазменных технологий является улучшение параметров работы основного ее элемента — плазмотрона, что достигается путем проектирования и конструирования его основных узлов. В статье проанализированы принципы проектирования плазмотрона и исследованы характеристики плазматрона дугового разряда. Были рассмотрены возможности увеличения термической стойкости конструкции анода, изучена скорость и траектория частиц порошка, осевым

вводом порошка через катод, исследована термостойкость катода. Методом конечных элементов исследовано влияние формы анода на ресурс работы плазмотрона по оценке мощности тепловыделения при условии выше температуры плавления меди (анода). Определена оптимальная геометрия анода для эффективного охлаждения узла при радиальном вводе и выводе охлаждающей жидкости. Были исследованы влияния термической нагрузки на катодный часть плазмотрона, сняты теплофизические характеристики катода на эксплуатационные характеристики плазмотрона в процессе термической нагрузки. Рассчитана динамика частицы осевым вводом порошка через катод и определена динамика разогрева частицы порошка. Выход транспортирующего газа стабилизирован завихрителем и имеет большую динамику и находится в высокотемпературной части дуги. Вычислена траектория движения частицы порошка в область сопла, который соответствует среднему значению скорости ≈450–500 м/с. Выявлено, что увеличение диаметра катода с 3 до 5 мм снижает термическую нагрузку на 50 %.

Ключевые слова: плазменная обработка, плазмотрон, осевой ввод порошка, аэродинамика движения частиц, теплофизические характеристики, 3D-модель.

References

1 Rakhadilov, B., Kenesbekov, A., Skakov, M., & Miniyzov, A. (2018). Hydrogen and deuterium storage in tungsten when irradiation with Plasma beam. *In METAL 2018-27th International Conference on Metallurgy and Materials, Conference Proceedings,* 1216–1221.

2 Chen, Xi., & Li., H. (2003). Three-dimensional flow and heat transfer in thermal plasma systems. *Surface and Coatings Technology,* 171, 124–133.

3 Gawne, D.T., Liu, B., Bao, Y., & Zhang, T. (2005). Modelling of plasma–particle two-phase flow using statistical techniques. Surface and Coatings Technology, 191, 242–254.

4 Ramachandra, K., Kikukawa, N., & Nishiyama, H. (2003). 3D modeling of plasma–particle interactions in a plasma jet under dense loading conditions. Thin Solid Films, 435, 298–306.

5 Trelles, J.P., Emil, P., & Joachim, H. (2006). Multiscale finite element modeling of arc dynamics in a DC plasma torch. *Plasma chemistry and plasma processing*, 26.6, 557–575.

6 Park, J., Heberlein, J., Pfender, E., Candler, G., & Chang, C.H. (2008). Two-dimensional numerical modeling of direct-current electric arcs in nonequilibrium. *Plasma Chemistry and Plasma Processing,* 28.2, 213–231.

7 Anakhov, S.V. (2018). Printsipy i metody proektirovaniia plazmotronov [Principles and methods of plasma torch design]. *Monography.* Ekaterinburg: Izdatelstvo Rossiiskogo gosudarstvennogo professionalno-pedagogicheskogo universiteta [in Russian].

8 Kylyshkanov, M.K., Shestakov, K.A., Sagdoldina, Z.B., Rakhadilov, B.K., & Kengesbekov, A.B. (2021). Processing of industrial waste by plasma-chemical method. *Bulletin of the university of Karaganda-Physics,* 3(103), 45–51.

9 Rakhadilov, B.K., Kenesbekov, A.B., Kowalevski, P., Ocheredko, Y.A., & Sagdoldina, Zh.B. (2020). Development of air-plasma technology for hardening cutting tools by applying wear-resistant coatings. *News of the National Academy of sciences of the Republic of Kazakhstan-series of geology and technical sciences,* 3(441), 54–62.

10 Bird, R.B. Stewart, W.E., & Lightfoot, E.N. (2006). Transport Phenomena. *Wiley,* 1, ISBN 978-0-470-11539-8.

DOI 10.31489/2022PH3/90-98

UDC 53.047

V.O. Shvidia[1*], S.P. Stepanenko[1], B.I. Kotov[2], A.V. Spirin[3], V.Yu. Kucheruk[4]

Influence of vacuum on diffusion of moisture inside seeds of cereals

[1]National Scientific Centre "Institute for Agricultural Engineering and Electrification", Kyiv, Ukraine,
[2]Institutions of Higher Education "Podilsky State University", Ukraine
[3]Separate structural subdivision "Ladyzhyn vocation college of Vinnytsia National Agrarian University", Ukraine
[4]Vinnytsia National Technical University, Ukraine
*(*E-mail: Shvidia@gmail.com)*

The article solves the problem of thermal injury of seeds of grain crops during drying, which are capillary-porous bodies. It is hypothesized that the use of a vacuum in the drying chamber reduces the risk of thermal stress. In this regard, the article studies the effect of a vacuum inside the drying chamber on the diffusion of moisture inside the seeds. Seeds are complex materials in which moisture has different bonds with dry matter. During the working process, the drying speed in the surface layers and inside the seeds occurs at different speeds. As a result, drying stresses occur, which cause cracks on the surface of the seeds. Based on the solution to the differential diffusion equation with an absorbing screen as a boundary condition, the condition for drying without thermal stresses is found. Experimental verification of theoretical studies is carried out on a specially made experimental setup on the example of corn seeds. The effect of thermal stress on seed viability is determined by laboratory germination. Experimental studies confirm the adequacy of theoretical statements. Thus, when drying the seeds of grain crops, which are capillary-porous bodies, there is a limit value of rarefaction, above which cracks appear on the surface of the seeds due to different drying rates on the surface and inside. For drying seeds of grain crops without thermal stresses, it is necessary to consider not only the heating temperature but also the rarefaction in the drying chamber, which should be close to the limit value.

Keywords: seeds, dilution, vacuum, drying, laboratory germination, exposure.

Introduction

One of the components of the success of obtaining a high yield of cereals is the use of quality seed. Quality sowing material is determined not only by varietal characteristics, but also by homogeneity, content of weed seeds, debris, injured seeds, and moisture.

When drying the seeds, the main attention is paid to the level of injury to the seeds by dryers, and fuel consumption becomes a secondary issue.

In seed production and selection for drying seeds with high humidity, convective drying in a stationary, sedentary and fluidized bed is usually used, which is realized in chamber, conveyor, bunker and mine dryers.

To intensify the moisture transfer in the seeds heating is used, which is provided by air flow with a temperature not exceeding 65 °C. The upper value of the temperature is due to the fact that at a given temperature level there is an intensive removal of moisture, but not yet denatured protein structures of the seed. Mild temperatures have been developed for different crops [1–4], which must be maintained when drying the seeds in different convective dryers to reduce the risk of thermal injury. Since convective drying uses mainly hot air or a mixture of air with combustion products, and the seeds are dried in a layer with a given thickness, when using adapted thermal regimes with minimal mechanical impact, areas of undried seeds are possible. In addition, depending on the type of heat generator used, it is necessary to constantly maintain the required

mode during the drying process, which is not always possible to withstand during the working season due to the human factor. All this is especially important for selecting seed dryers, where each seed counts.

Despite the measures developed to reduce thermal injury to seeds during drying, dried seeds have lower germination, growth strength, and germination friendliness compared to undried seeds. This is explained by the difference in the properties of individual seeds and the nonlinear nature of the thermal conductivity of the seed layer, which leads to overheating or underdrying of individual seeds. To improve the sowing properties of seeds after drying, it is necessary to reduce their thermal injury by limiting or eliminating the influence of the temperature field, as well as increasing the uniformity of drying of seeds. In [5–9], the positive effect of vacuum on the drying process is shown. However, the effect of vacuum on the drying process of crop seeds has been insufficiently explored, which makes this study relevant.

1. Theoretical part

The main parameters that affect the quality of dried seeds are the temperature of the seeds θ and the vacuum in the vacuum drying chamber P. To understand their effects, one needs to know the process of drying seeds. Since we did not consider the diffusion of moisture during drying, but only the evaporation of moisture from the surface layers of the seed, then it is not possible to identify the causes of cracks in the seeds. Therefore, seeds should be considered a heterogeneous material. Any seed consists of an embryo, endosperm, or cotyledon and shell. For most crop seeds, the movement of moisture during drying is as follows (Fig. 1).

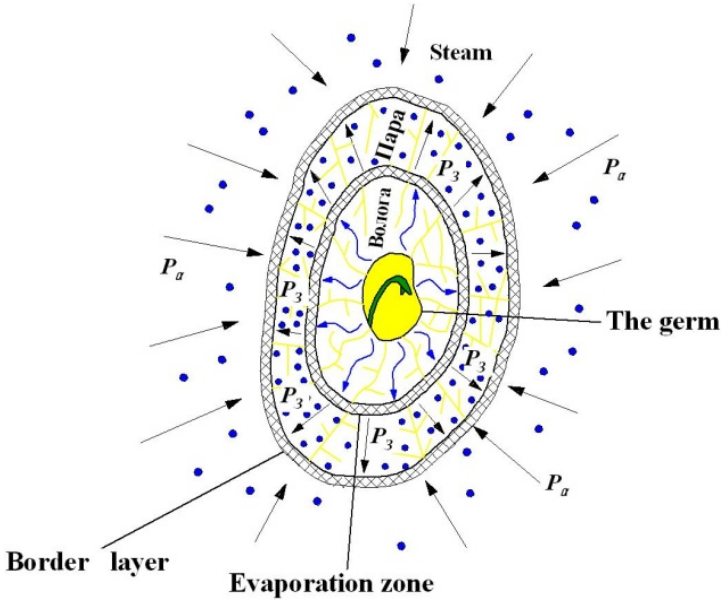

P_Z – partial pressure of water vapor inside the seed; P_α – partial pressure of water vapor inside the drying chamber.

Figure 1. The scheme of removal of moisture during drying of seeds

During vacuum drying, the substance of the seed is heated and part of the moisture located near its shell evaporates. At the same time, a moisture gradient is created, due to which, under the action of diffusion, moisture continuously moves from the inner parts of the seed, where the embryo is located, to the surface on which it evaporates. Water vapor molecules diffuse through the boundary layer and saturate the volume of the vacuum drying chamber. A necessary condition for evaporation is $P_Z > P_\alpha$ (Figure 1). It should be noted that the evaporation of moisture does not occur from the surface, but from the evaporation zone, located in the peripheral part of the seed (Fig. 1). As the moisture evaporates, this area moves deep into the seed.

The heterogeneity of the seed structure is the reason that moisture is removed from different parts in different ways: from the outside - through evaporation, from the inside - due to diffusion. Because of different methods of moisture removal, different parts of the seed are dried at different speeds, which means that the drying of the seeds is uneven. This can be represented by the following scheme (Fig. 2).

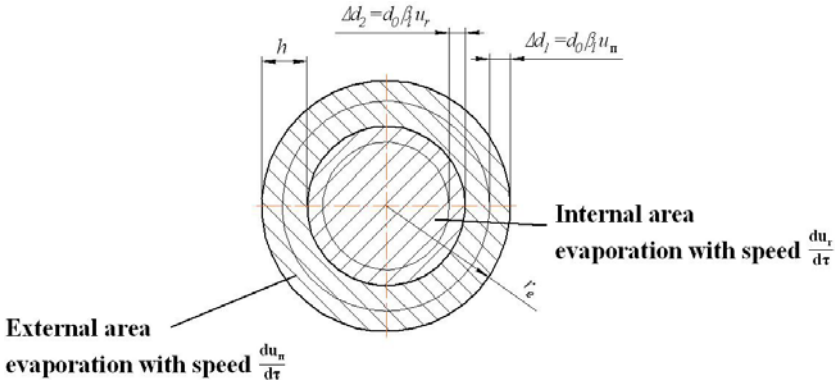

Figure 2. Scheme for determining the drying stresses in the seed

It is divided into two zones: a zone of external evaporation with a thickness of h and a zone of internal evaporation with a thickness of r_e-h. Drying stresses in the seed occur when the difference in deformation of the seed areas $\Delta d_1 - \Delta d_2 > 0$. It is equal to the following value according to Fig. 2:

$$\Delta d_1 - \Delta d_2 = d_0 \cdot \beta_l \cdot (u_п - u_r), \quad (1)$$

where Δd_1, Δd_2– deformations in the outer and inner zone of seed evaporation, respectively, m;

d_0 – the equivalent diameter of a completely dry seed, m;

β_l – coefficient of linear drying;

$u_п$, u_r – humidity in the outer and inner zone of seed evaporation [10–12], respectively, %.

We assume that the deformation occurs in the elastic region, then using the value of deformation (1), the formula for the deformation of spherical shells and the Laplace equation for the sphere [13] we obtain the expression for calculating the drying stresses in the seed:

$$\sigma = \frac{d_0 \cdot \beta_l \cdot E}{r_e \cdot (1-\mu)} \cdot (u_п - u_r), \quad (2)$$

where E – modulus of linear deformation, H/m^2;

μ – Poisson's ratio.

When a certain value of σ exceeds the surface of the seed, cracks appear. Expression (2) shows that the main factor influencing the appearance of cracks is the humidity gradient $(u_п - u_r)$. Therefore, for safe drying it is necessary that the drying rate on the surface was less than or equal to the diffusion rate:

$$\frac{du_п}{d\tau} \leq \frac{du_r}{d\tau}. \quad (3)$$

$\frac{du_п}{d\tau}$ according to [14] is:

$$\frac{du_п}{d\tau} = \frac{A1}{P} \cdot (u_p - u_0) \cdot e^{-\frac{A1}{P} \cdot \tau}, \quad (4)$$

where $A1$ — regime coefficient characterizing the thermophysical properties of seeds, Pa$^{1/2}$/s;

u_p, u_0 — equilibrium and initial seed moisture, respectively,%;

P — vacuum in the drying chamber, Pa.

Drying speed inside the seed $\frac{du_r}{d\tau}$, on the other hand, is described by the differential diffusion equation with an absorbing screen, assuming that moisture is absorbed on the surface of the seed according to the law (4), the diffusion flow is parallel to the equivalent seed radius, and that the rate of moisture diffusion from the center of the equivalent seed ball in all directions and depends only on the distance r) [15–18] (Fig. 3):

$$\frac{\partial u_r}{\partial \tau} = \beta_m \frac{\partial^2 u_r}{\partial r^2}, \quad (5)$$

where β_m – moisture diffusion coefficient, m^2/s;

r – distance from the absorption screen, m.

The center of the equivalent seed ball retains moisture for the longest time ($r = \frac{d_e}{2}$), therefore, comparing the humidity at this point and on the surface of the equivalent sphere, we observe the largest gradient($u_п - u_r$).

To find the gradient ($u_п - u_r$) it is necessary to know the dynamics of humidity change inside the seed u_r. To do this, solve the differential equation (5) under the following boundary conditions:

$$u_r(0,\tau) = u_r(d_e,\tau) = \left(u_0 - u_p\right) \cdot e^{-\frac{A1}{P}\cdot\tau} + u_p \quad (6).$$

Initial conditions:

$$u_r(r,0) = u_0\ . \quad (7)$$

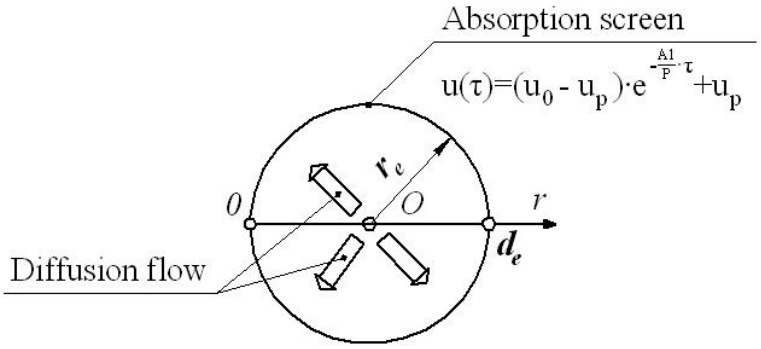

Figure 3. Scheme for determining the differential equation of diffusion inside the seed.

Final condition:

$$u_r(r,\infty) = u_p\ . \quad (8)$$

The differential equation in partial derivatives (5) is a differential equation in partial derivatives of the second order of the parabolic type. They are solved by the Fourier method by introducing an additional function. Then the drying rate inside the seed $\frac{du_r}{d\tau}$ is equal to:

$$\frac{\partial u_r}{\partial \tau} = \frac{A1}{P} \cdot \left(u_p - u_0\right) \cdot e^{-\frac{A1}{P}\cdot\tau} + \left(u_0 - u_p\right) \cdot \mathrm{A1} \cdot \sum_{n=1}^{\infty} \frac{2}{\pi \cdot n} \cdot \left[1 - cos(\pi \cdot n)\right] \cdot \sin(\lambda_n \cdot r) \times,$$

$$\times \frac{\beta_m \cdot \lambda_n^2 \cdot e^{-\beta_m \cdot \lambda_n^2 \cdot \tau} - \frac{A1}{P} e^{-\frac{A1}{P}\cdot\tau}}{\beta_m \cdot \lambda_n^2 \cdot P - A1}, \quad (9)$$

where $\lambda_n = \frac{\pi \cdot n}{d_e}$ — own functions of the boundary value problem.

Equating $\frac{du_п}{d\tau}$ to $\frac{du_r}{d\tau}$ and solving the algebraic equation with respect to P we obtain:

$$P = \frac{A1 \cdot d_e^2}{\beta_m \cdot \pi^2}. \quad (10)$$

The moisture diffusion coefficient β_m depends on the heating temperature of the seeds θ and slightly on the humidity u according to the formula [14]:

$$\beta_m = \beta_m^0 \cdot \left(\frac{\theta}{273+\theta_0}\right)^k, \quad (11)$$

where β_m^0 – moisture diffusion coefficient at seed heating temperature θ_0, m^2/s;

k – empirical coefficient depending on humidity.

Substituting the value (11) in the formula (10) we obtain the minimum value of pressure P for gentle drying of seeds of cereals:

$$P \geq A1 \cdot \frac{d_e^2}{\beta_m^0 \cdot \left(\frac{\theta}{273+\theta_0}\right)^k \cdot \pi^2}. \quad (12)$$

Dependence (12) shows that the value of the pressure inside the drying chamber P is directly proportional to the mode coefficient A1 and inversely proportional to the seed temperature θ. Dependence (12) also

shows that for gentle drying of seeds in the drying chamber the value of pressure must not decrease less than the value of P. With a large value of dilution, damage to the seeds is possible. To verify the validity of this statement, it is necessary to conduct experimental research.

2. Experimental part

2.1 Methods of experiments

To conduct experiment, we use a drum dryer, inside the drying chamber of which it is possible to create a vacuum of up to 2 kPa (Fig. 4).

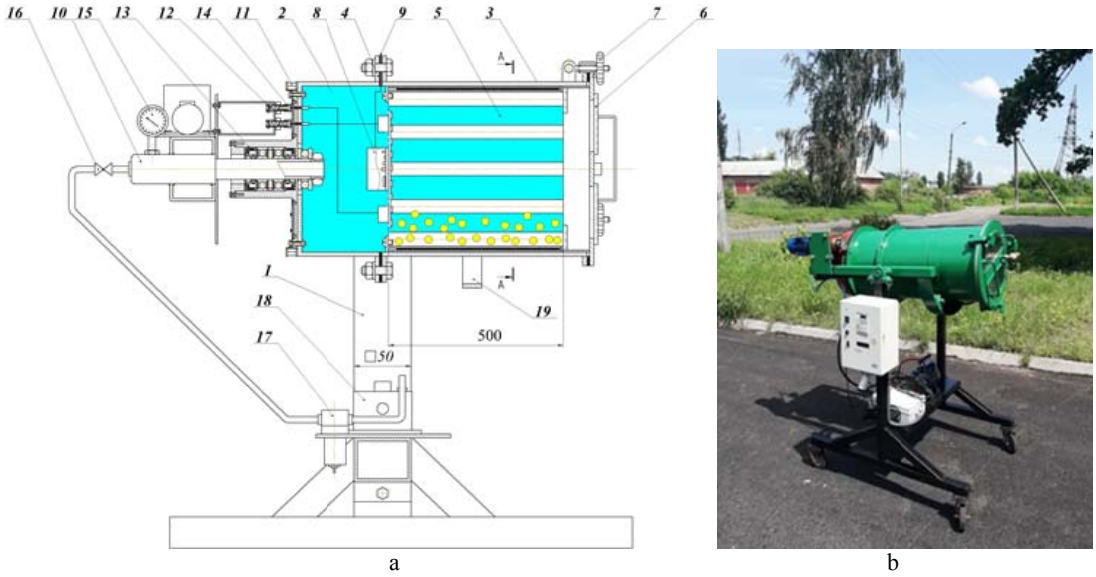

a b

Figure 4. Structural scheme of the drum dryer (a) and its general view (b):

1 – rack; 2 – technological chamber; 3 – drying chamber; 4 – flanges; 5 – heating cylinder with blades; 6 – cover; 7 – clamping mechanism; 8 – transmitter of signals from sensors; 9 – Bluetooth antenna; 10 – hollow axis; 11 – chain crown; 12 – sliding contacts; 13 – drive flange; 14 – cap; 15 – vacuum gauge; 16 – valve of the vacuum pump; 17 – capacitor; 18 – vacuum pump; 19 – arc with support rollers

The vacuum inside the drying chamber (3) is created by the vacuum pump (18). When the required vacuum is reached, the readings are removed from the vacuum gauge (15), close the valve 16 and turn off the vacuum pump (18). The seeds are loaded into the drying chamber (3) by opening the cover (6). A capacitive humidity sensor and a digital temperature sensor DS18b20 are connected to the walls of the heating cylinder with blades (5). During the drying process, the drying chamber (3) rotates around a hollow axis (10). Seed heating in the drying chamber (3) took place through the cylindrical surface of the heating cylinder with blades (5), on the outer cylindrical surface of which through the insulator is wound nichrome wire. The temperature seeds were adjusted by changing the electric power supplied to the heater of the heating cylinder with blades (5). When the humidity reaches the heater is turned off, then open the vacuum valve on the cover (6), after reaching atmospheric pressure in the drying chamber (3) by means of a clamping mechanism (7) open the cover (6) and pour dried seeds (3).

To verify the validity of condition (12), a sample of corn weighing 715 g with an equivalent diameter of 7 mm, with an initial humidity of 24% and a temperature of 15 ºC was used. The drying exposure was determined as the time during which the corn seeds reach a moisture content of 13%. In the experiments, the temperature was changed from 25 ºC to 37 ºC in steps of 3 ºC. For each step, the drying exposure and the change in laboratory germination after drying at a dilution of 45 kPa, 60 kPa, and 75 kPa were determined. Owing to laboratory germination the level of seed injury after drying was identified.

The change in laboratory germination after drying was defined as the difference between the laboratory germination of the sample before drying and the laboratory germination after drying. Laboratory germination of maize samples was determined according to DSTU 4138-2002 [19]. Based on the calculations of the dependence (12) for the sample of corn, the limit value of the vacuum in the drying chamber is 52.4 kPa. This dependence was tested by a series of experiments at a dilution of 45 kPa and 60 kPa. At the same time, a vis-

ual inspection of corn seeds for cracks was performed with a magnifying glass. Also, the vacuum in the drying chamber changed from 42 kPa to 60 kPa in increments of 2 kPa, while calculating the percentage of seeds with cracks to the total number of seeds received for drying.

3. Results and Discussion

Figure 5 demonstates the result of visual inspection of corn seeds after vacuum drying at a vacuum of 45 kPa and 60 kPa at a temperature of 30 ºC.

a b

Figure 5. Appearance of maize seed at a vacuum of 60 kPa (a) and a vacuum of 45 kPa (b)

This review confirmed the validity of condition (12). Due to the significant difference in the drying rate inside the seed and in the surface layers, drying stresses occur, which result in cracks on the surface of the seed, which reduces the sowing quality. Therefore, when choosing the mode of drying the seeds must take into account condition (12).

Figure 6 shows a number of seeds with cracks as a percentage of the vacuum inside the drying chamber.

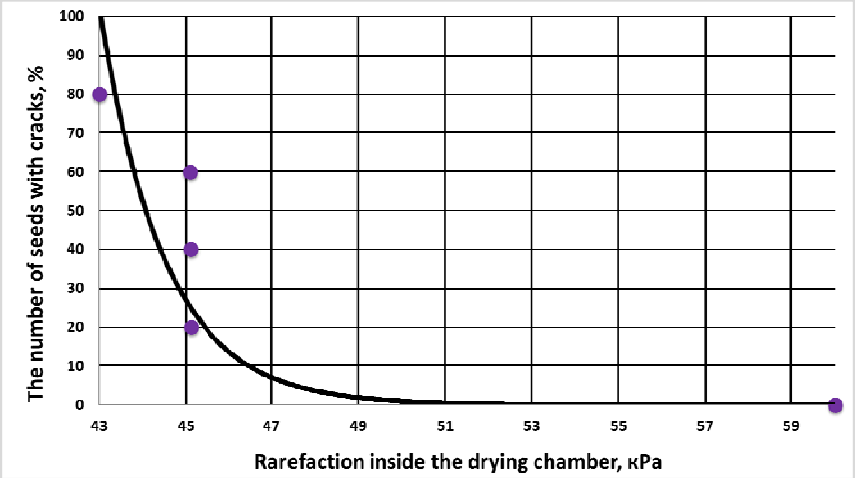

Figure 6. A number of seeds with cracks

It can be seen from Figure 6 that the percentage of cracks increases exponentially when the vacuum decreases above 45 kPa.The fact that cracked seeds begin to appear at different values of vacuum inside the drying chamber (43-51 kPa) is explained by the scattering of the values of the coefficient of diffusion of moisture inside the seeds of corn.

The effect of seed temperature and dilution inside the drying chamber on the change in laboratory germination of corn seeds is presented in Figure 7.

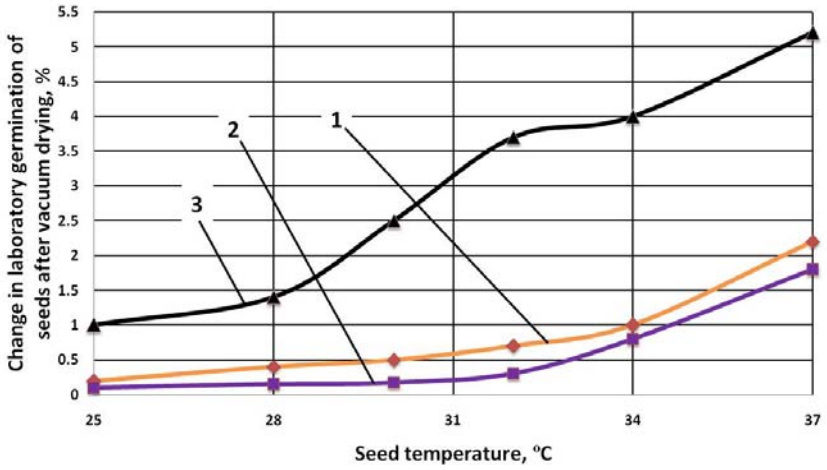

Fig. 7. Graphs of changes in laboratory germination of corn seeds from its heating temperature: 1 - 75 kPa; 2 - 60 kPa; 3 - 45 kPa

According to Figure 7, it is seen that increasing the temperature of the seeds during drying reduces the laboratory germination of seeds. When the value of the vacuum in the drying chamber exceeds the value calculated under condition (12) - graph 3, the laboratory germination decreases sharply. When the vacuum in the drying chamber is reduced to the limit value, the change in the laboratory germination of seeds decreases, this is due to the fact that at a lower value of the vacuum, the part of heat that is spent directly on moisture evaporation increases.

Conclusions

These results show that the thermal stresses in capillary porous bodies, which include in particular the seeds of cereals, significantly depend on the value of the vacuum in the drying chamber. If the critical value of the vacuum is exceeded, cracks appear on the surface of the seeds due to different drying rates on the surface and inside. Therefore, to drying cereal seeds without thermal stresses, it is necessary to consider not only the heating temperature, but also the vacuum in the drying chamber, which must be close to the limit value.

Acnowledgments

This work was performed according to the project 03.01.00.05 F “Develop gentle technological processes for drying agricultural materials”, which is performed at the National Scientific Centre **“**Institute for Agricultural Engineering and Electrification” of the National Agrarian Academy of Sciences of Ukraine.

References

1 Сушка зерна — суть проблемы. Режим доступа: https://agropromex.ru/stati-i-publikaczii/nauchnyie-stati/sushka-zerna-%E2%80%93-sut-problemyi.html

2 Сушка сельскохозяйственных продуктов. Режим доступа: http://agrolib.ru/rastenievodstvo/item/f00/s01/e0001999/index.shtml

3 Мусывов К.М. Технология хранения и переработки продукции растениеводства / К.М. Мусывов, Е.А. Гордеева. – Астана: КазГАУ, 2007. — 367 с.

4 Кирпа М.Я. Травмирование семян: как это предотвратить / М.Я. Кирпа // Пропозиция. — 2017. — № 1. — С. 152–155.

5 Насиковский А.Б. Установка для вакуумной сушки семян рапса / А.Б. Насиковский // Вестн. Винниц. политех. ун-та. — 2007. — № 4. — С. 136–139.

6 Kutovoy V.A. Development of the scientific foundations of energy-efficient thermal vacuum drying equipment / V.A. Kutovoy // Doctor’s thesis. Lviv, 2015. — 42 p.

7 Бурцев С.А. Экспериментальный стенд сушки растительного сырья вакуумно-импульсным методом / С.А. Бурцев, Т.Ф. Фатыхов / Вестн. Казан. технол. ун-та. — 2017. — Т. 20, № 21. — С. 126–128.

8 Гайфуллина Р.Р. Экспериментальная установка для исследования кинетики сушки капиллярно-пористых материалов по вакуумно-импульсной технологии / Р.Р. Гайфуллина, М.С. Курбангалеев, З.И. Зарипов, Д.А. Анашкин // Вестн. Казан. технол. ун-та. — 2011. — № 2. — С. 132–137.

9 Adamchuk V. Experimental study of vacuum drying seeds of grain crops / V. Adamchuk, V. Shvidia // *Mechanization in agriculture & conversing of the resources.* — 2018. — Iss. 2. — Pp. 46–48.

10 Данилов Д.Ю. Повышение эффективности сушки зерна: основные технологические приемы и направления / Д.Ю. Данилов, А.Ю. Рындин // Вестн. НГИЭИ. — 2015. — С. 26–29.

11 Базаров И.П. Термодинамика / И.П. Базаров. — СПб.: Изд-во «Лань», 2010. — 377 с.

12 Эквивалентный диаметр зерна. Технологии и оборудование для изготовления красок, ЛКМ. — 2012. Режим доступа: http://kraska.biz/peremeshivanie-i-apparaty-s-meshalkami/ekvivalentnyj-diametr-zerna/

13 Lecture 5. Режим доступа: https://www.soprotmat.ru/ lectuprugost5.htm

14 Rogovskiy I.L. Experimental researches of modes of drying of seeds of grain crops from high humidity in a low pressure environment / I.L. Rogovskiy, L.L. Titova, V.I. Trochanyak, O.V. Solomka et al. // *INMATEH - Agricultural Engineering*. — 2019. — Vol. 57, No. 1. National institute of research-development for machines and installations designed to agriculture and food industry – INMA Bucharest — 6 Ion Ionescu de la Brad Blvd., sector 1, Bucharest. — P. 141–146.

15 Teschl G. Ordinary Differential Equation sand Dynamical Systems / G. Teschl // Graduate Studies in Mathematics 140. *American Mathematical Society.* — 2012.

16 Drábek P. Elements of partial differential equations (Online ed.) / P. Drábek, G. Holubová // Berlin: de Gruyter. — 2007.

17 Vinogradov A.M. Cohomological Analysis of Partial Differential Equations and Secondary Calculus / A.M. Vinogradov // *American Mathematical Society,* Providence, Rhode Island, USA. — 2001.

18 Roubíček T. Nonlinear Partial Differential Equations with Applications / T. Roubíček // International Series of Numerical Mathematics, 153 (2nd ed.), Basel, Boston, Berlin: Birkhäuser. — 2013.

19 Seeds of agricultural crops. Method of determining quality: DSTU 4138-2002. Kiev, 2003. — 173 p.

В.А. Швидя, С.П. Степаненко, Б.И. Котов, А.В. Спирин, В.Ю. Кучерук

Вакуумның тұқым ішіндегі ылғалдың таралуына әсері

Мақалада капиллярлы-кеуекті денелер болып табылатын дәнді дақылдар тұқымдарын кептіру кезіндегі термиялық зақымдану мәселесі шешілген. Кептіру камерасында вакуумды қолдану термиялық кернеу қаупін азайтады деген болжам бар. Осыған байланысты авторлар кептіру камерасының ішіндегі вакуумның тұқым ішіндегі ылғалдың таралуына әсерін зерттеуді қарастырған. Тұқымдар — бұл ылғалдың құрғақ затпен әртүрлі байланыстары бар күрделі материал. Жұмыс процесін орындау кезінде беткі қабаттардағы және тұқымдардың ішіндегі кептіру жылдамдығы әртүрлі жылдамдықта болады. Нәтижесінде кептіру кернеулері пайда болады, бұл тұқымдардың бетінде жарықтар тудырады. Шектік шарт ретінде жұту экраны бар диффузиялық диффузия теңдеуінің шешімі негізінде термиялық кернеулерсіз кептіру шарты табылады. Теориялық зерттеулерді тәжірибелік тексеру жүгері тұқымының мысалында арнайы жасалған тәжірибелік қондырғыда жүргізілді. Тұқымның өміршеңдігіне термиялық кернеудің әсері зертханалық өну арқылы анықталды. Эксперименттік зерттеулер теориялық тұжырымдардың сәйкестігін растады. Сонымен, капиллярлы-кеуекті дене болып табылатын дәнді дақылдардың тұқымдарын кептіру кезінде сиретудің шекті мәні бар, ол асып кеткен кезде тұқым бетінде және ішінде әр түрлі кептіру жылдамдығына байланысты жарықтар пайда болады. Дәнді дақылдардың тұқымын термиялық кернеусіз кептіру үшін қыздыру температурасын ғана емес, сонымен қатар кептіру камерасындағы сиретуді де ескеру керек, ол шекті мәнге жақын болуы керек.

Кілт сөздер: тұқымдардың термиялық зақымдануы, астық дақылдары, жылу температурасы, капиллярлы-кеуекті денелер.

В.А. Швидя, С.П. Степаненко, Б.И. Котов, А.В. Спирин, В.Ю. Кучерук

Влияние вакуума на диффузию влаги внутри семян

В статье решена проблема термического травмирования семян зерновых культур при сушке, которые являются капиллярно-пористыми телами. Была выдвинута гипотеза о том, что применение вакуума в сушильной камере позволяет снизить риск термических напряжений. В этой связи авторами рассмотрено исследование влияния вакуума внутри сушильной камеры на диффузию влаги внутри семян. Семена являются сложным по структуре материалом, в котором влага имеет разные связи с сухим веществом. При выполнении рабочего процесса скорость сушки в поверхностных слоях и внутри семян происходит с разной скоростью. В результате чего возникают сушильные напряжения, которые вызывают трещины на поверхности семян. На основе решения дифференциального уравнения диффузии с поглотительным экраном в качестве граничного условия найдено условие для сушки без термических напряжений. Экспериментальная проверка теоретических исследований проводилась на специально изготовленной экспериментальной установке на примере семян кукурузы. Воздействие термических напряжений на жизнеспособность семян определяли из-за лабораторной всхожести. Экспериментальные исследования подтвердили адекватность теоретических утверждений. Таким образом, при сушке

семян зерновых культур, являющихся капиллярно-пористым телом, существует предельное значение разрежения, при превышении которого на поверхности семян появляются трещины из-за разной скорости сушки на поверхности и внутри. Для сушки семян зерновых культур без термических напряжений следует учитывать не только температуру нагрева, а также разрежение в сушильной камере, которое должно быть близко к предельному значению.

Ключевые слова: термическое травмирование семян, зерновые культуры, температура нагрева, капиллярно-пористое тело.

References

1 (n.d.). Sushka zerna — sut problemy [Drying grain is the essence of the problem]. Retrieved fromhttps://agropromex.ru/stati-i-publikaczii/nauchnyie-stati/sushka-zerna-%E2%80%93-sut-problemyi.html (Date of access: 14.05.2020) [in Russian].

2 Sushka selskokhoziaistvennykh produktov [Drying of agricultural products]. Retrieved from http://agrolib.ru/rastenievodstvo/item/f00/s01/e0001999/index.shtml (Date of access: 14.05.2020) [in Russian].

3 Musyvov, K.M., & Gordeeva, E.A. (2007). Tekhnologiia khraneniia i pererabotki produktsii rastenievodstva [Technology of storage and processing of crop products]. Astana: Kazakhskaia gosudarstvennaia akademiia upravleniia [in Russian].

4 Kirpa, M.Ya. (2017). Travmirovanie semian: kak eto predotvratit [Injury to seeds: how to prevent it]. *Propozitsiia — Proposition*, 1, 152–155 [in Russian].

5 Nasikovskii, A.B. (2007). Ustanovka dlia vakuumnoi sushki semian rapsa [Installation for vacuum drying of rapeseed]. *Vestnik Vinnitskogo politekhnicheskogo universiteta – Bulletin of Vinnitsa Polytechnic University,* 4, 136–139 [in Russian].

6 Kutovoy, V.A. (2015). Development of the scientific foundations of energy-efficient thermal vacuum drying equipment. *Doctor's thesis.* Lviv, 42 p.

7 Burtsev, S.A., & Fatykhov, T.F. (2017). Eksperimentalnyi stend sushki rastitelnogo syria vakuumno-impulsnym metodom [An experimental stand for drying vegetable raw materials using the vacuum-pulse method]. *Vestnik Kazanskogo tekhnologicheskogo universiteta – Bulletin Kazan Tehmological University,* 20, 21, 126–128 [in Russian].

8 Gaifullina, R.R., Kurbangaleev, M.S., Zaripov, Z.I., & Anashkin, D.A. (2011). Eksperimentalnaia ustanovka dlia issledovaniia kinetiki sushki kapilliarno-poristykh materialov po vakuumno-impulsnoi tekhnologii [Experimental setup for studying the kinetics of drying capillary-porous materials by vacuum-pulse technology]. *Vestnik Kazanskogo tekhnologicheskogo universiteta – Bulletin Kazan Tehmological University,* 2, 132–137 [in Russian].

9 Adamchuk, V.Yu., & Shvidia, V. (2018) Experimental study of vacuum drying seeds of grain crops. *Mechanization in agriculture & conversing of the resources,* 2, 46–48.

10 Danilov, D., & Ryndin, A.Yu. (2015). Povyshenie effektivnosti sushki zerna: osnovnye tekhnologicheskie priemy i napravlenia [Improving the efficiency of grain drying: the main technological methods and directions]. *Bulletin NGIEI,* 26–29 [in Russian].

11 Bazarov, I.P. (2010). Termodinamika [Thermodynamics]. Saint-Petersburg: Lan [in Russian].

12 (2012). Ekvivalentnyi diametr zerna [Equivalent grain diameter]. *Tekhnologii i oborudovanie dlia izgotovleniia krasok, lakokrasochnykh materialov — Technologies and equipment for the manufacture of paints, coatings.* Retrieved from http://kraska.biz/peremeshivanie-i-apparaty-s-meshalkami/ekvivalentnyj-diametr-zerna/ (Date of access: 14.05.2020) [in Russian].

13 Lecture 5. Retrieved from https://www.soprotmat.ru/ lectuprugost5.htm (Date of access: 14.05.2020).

14 Rogovskiy, I.L., Titova, L.L., Trochanyak, V.I., Solomka, O.V. et al. (2019). Experimental researches of modes of drying of seeds of grain crops from high humidity in a low pressure environment. *INMATEH - Agricultural Engineering*. vol. 57, № 1. National institute of research-development for machines and installations designed to agriculture and food industry –INMA Bucharest — 6 Ion Ionescu de la Brad Blvd., sector 1, Bucharest, 141–146.

15 Teschl, G. (2012). Ordinary Differential Equation sand Dynamical Systems. Graduate Studies in Mathematics 140. *American Mathematical Society.* ISBN 978-0-8218-8328-0.

16 Drábek, P., & Holubová, G. (2007). Elements of partial differential equations (Online ed.). Berlin: de Gruyter. ISBN 9783110191240.

17 Vinogradov, A.M. (2001). Cohomological Analysis of Partial Differential Equations and Secondary Calculus. *American Mathematical Society,* Providence, Rhode Island, USA, ISBN 0-8218-2922-X.

18 Roubíček, T. (2013). Nonlinear Partial Differential Equations with Applications (PDF), International Series of Numerical Mathematics, 153 (2nd ed.), Basel, Boston, Berlin: Birkhäuser. https://doi.org/10.1007/978-3-0348-0513-1. ISBN 978-3-0348-0512-4, MR 3014456.

19 (2003). Seeds of agricultural crops. Method of determining quality: DSTU 4138-2002. Kiev, 173 p.

DOI 10.31489/2022PH3/99-107

UDC 539.551

A.Sh. Kazhikenova[1*], D.B. Alibiyev[1], Zh.M. Tentekbayeva[2],
A.S. Smailova[1], R.A. Orazbekova[1], I.S. Kauymbek[1]

[1]Karaganda Buketov University, Kazakhstan;
[2]Karaganda Technical University, Kazakhstan
*(*E-mail: aigul-kazhikenova@mail.ru)*

The use of a cluster-associate pattern for calculation of melt viscosity

The liquid state of the substance is the most complex for theoretical description. Modern ideas about the liquid and its viscosity are reduced to the following: in the structure of the liquid, the spatial arrangement of atoms is not fixed, as in a crystal, and is not in a free state, as in a gas. Therefore, liquid may approach its properties to gas near the boiling point or the solid state near the melting point. Thus, the structure of the liquid is characterized by the short-range order of the bond. The properties of liquid metals are obtained mainly from experimental studies. This article provides mathematical justification for the cluster-associate pattern. The purpose of the study is to show the possibility of applying a semi-empirical model to calculate the viscosity of liquid metals. The proposed model is developed using the concept of chaotized particles, which is based on the Boltzmann distribution. This model is developed based on the association degree of clusters of their crystal-moving particles. For many years, the viscosity of liquid metals has been studied only by experimental methods. The model enables to find melt viscosity values analytically. The calculated viscosity values of some metals are compared to experimental values in this model. It is established that in all cases the obtained values coincide with the experimental values. The correctness of the proposed model is confirmed by the correlation coefficient. The application of the proposed model has been shown previously on some metals. In this work, we also show the applicability of the cluster-associate pattern using the example of beryllium, since it can be correlated with semimetals by many physicochemical properties. The degree of novelty of the scientific results lies in the fact that the obtained high correlation coefficients for the analysed metals indicate their functionality.

Keywords: kinematic viscosity, cluster of crystal-moving particles, metallurgy, boiling point, melting point, melt, correlation coefficient, beryllium.

Introduction

Smelting and casting of metals and alloys are widely used in the national economy. Metallurgical processes in general and in the field of non-ferrous and rare earth metals in particular have been and still remain one of the most important factors affecting the development of the country's economy. In addition to meeting the needs of metallurgical production, liquid metals are used as fluids and heat carriers in heat engineering, nuclear and electronic technology, and other industries contributing to the development of new metallurgical technologies. However, the insufficient use of mathematical methods for calculating and modeling the state of complex polydisperse systems, for example, melts or liquid slags, and their manufacturing application for prediction of flow and industrial processing control significantly hinder the development progress of technologies in metallurgy. The most important direction in solving this problem is the improvement of existing and the creation of new high-efficiency technological schemes and processes for the production of import-substituting and export-oriented products.

The problem of developing theories and methods for modeling the processes of changing the physical properties of metal melts, such as viscosity, melting, ductility is complex and interesting. Therefore, it has been studied thoroughly by researchers all across the world. Despite the existence of numerous methods for studying the processes of measuring the physical properties of metal melts, today there are no single theoretical models for describing the viscosity of liquid metals.

The topological characteristics of the liquid phase are most clearly expressed in simple liquids, to which melts of most pure metals can be attributed, initial information about which appeared indirectly through the research results of the viscosity-temperature dependence, electrical conductivity, and other characteristics. Due to the development of quantum-statistical methods, including computer modeling, there is a certain understanding of the melt structure. However, direct experimental evidence of short-range order existence with non-crystalline coordination in metal melts was obtained using the neutron and X-ray scattering method, which made it possible to identify clusters with different geometries in melts of iron, nickel, and zirconium

in a wide temperature range from a value much higher than the melting point to a deeply supercooled state at a temperature less than the melting point.

Experimental

Earlier, scientists of the Chemical and Metallurgical Institute named after Zh. Abishev put forward the concept of chaotic particles based on the Boltzmann distribution for the study of the chemical properties of melts [1]. According to this concept, in each state of aggregation of matter, crystal-moving, liquid-moving and steam-moving particles are present. Depending on the state of the substance, the proportion of above particles varies. The proportion of three kinds of particles affects melt properties such as meltability, ductility and viscosity. Professors V.P. Malyshev and A.M. Turdukozhayeva (A.M. Mukasheva) proposed three models for calculating viscosity taking into account three types of particles. In particular, considering the proportion of crystal-moving particles, the following formula is proposed

$$\nu(1) = \nu_r T_r / T. \tag{1}$$

If the liquid fluidity, in addition to the inhibitory influence of the crystal-moving particles, is shown by the contributing effect of the liquid-moving particles, then the viscosity equation for the fraction of these particles will take the following form

$$\nu(2) = \frac{\nu_r T_r \left[\exp(-T_m / T_r) - \exp(-T_b / T_r)\right]}{T\left[\exp(-T_m / T) - \exp(-T_b / T)\right]}. \tag{2}$$

Under the influence of all three kinds of particles, the temperature dependence of viscosity will be described by the following formula

$$\nu(3) = \frac{\nu_r T_r}{T} \exp\left(\frac{T_m}{T} - \frac{T_m}{T_r}\right). \tag{3}$$

In these formulas, ν – a kinematic viscosity, T_m – a melting point, T_b – a boiling point, ν_r and T_r – kinematic viscosity and reference point temperature. As a reference point, we can take any reliably established observed point. Nevertheless, for more accurate calculations, it is advisable to choose a reference point near the melting point.

Kinematic viscosities for 28 metals were calculated from these formulas. However, not all formulas showed consistency of calculated data with experimental [1]. After the calculations, it became necessary to choose the most adequate model for a particular metal. Thus, the calculation procedure was complicated. Therefore, it became necessary to create a single model for calculating the viscosity of liquid metals. As a single model for calculating the kinematic viscosity of melts, we developed a semi-empirical model of viscosity [2, 3]

$$\nu(4) = \nu_r (T_r / T)^a. \tag{4}$$

In work [2], a formula was given by which the degree of cluster association is calculated. Obtained values of clusters association degree of analysed metals were tested for range uniformity on the Nalimov criterion according to the following equations:

$$r_{\substack{\max \\ \min}} = \frac{\left|\bar{x} - x_{\substack{\max \\ \min}}\right|}{S(x)\sqrt{\frac{n-1}{n}}} \le r_{cr},$$

$$S(x) = \sqrt{\frac{\sum (x_i - \bar{x})^2}{n-1}},$$

where $x_{\substack{\max \\ \min}}$ – the minimax value of the range, $\bar{X}$ – the average value, $S(x)$ – the mean-root-square error, and n – the volume of the range. Normative table values of Nalimov criterion for 5% of significance level are approximated with accuracy up to 5% to equation [4]

$$r_{cr} = 1{,}483 f^{0{,}187},$$

where $f = n - 2$ – the number of degrees of freedom of Nalimov criterion.

In this work, we will justify the proposed model using any melting energy barrier (RT_m) and melting heat (ΔH_m).

The use of quantum-chemical models of viscosity, as well as models based on activation energy of the process of transferring particles from one virtual cluster to another, will provide a reliable mathematical description of the temperature dependence of viscosity only for a narrow temperature range.

To extend a similar possibility is provided by the concept of chaotic particles, based on the application of the Boltzmann distribution to a single mapping of three aggregate states of the substance, taking into account the proportions of sub-barrier and over-barrier particles with respect to melting and boiling heats. In this case, the viscosity is compared with the proportion of sub-barrier melting heat particles called crystal-moving, which results in the following model

$$\eta = \eta_r (T_r / T)^{a_\eta}, \tag{5}$$

where η – a dynamic viscosity; T – an absolute temperature; η_r and T_r – the coordinates of reference point, experimental or theoretically found; a_η – clusters association degree of crystal-moving particles.

During the processing of experimental data on η_i and T_i according to converse equation (5)

$$a_i = \frac{\ln(\eta_i / \eta_r)}{\ln(T_r / T_i)}$$

it was found that this degree naturally decreases with increasing temperature, moreover the most adequate description will be obtained when the form of dependence is constant (5) relative to a_η, since the dynamics of association splitting is similar to that of the clusters splitting themselves in accordance with the concept of chaotic particles:

$$a_\eta = a_i (T_i / T)^b, \tag{6}$$

where b, for a given range a_i, T_i is a constant value that makes sense of the attenuation degree of the cluster association. In view of $a_i > 0$, the expression (6) guarantees the impossibility of obtaining absurd negative values of the clusters association degree and an asymptotic approximation $a_\eta \to 0$ with a distant extrapolation $T \to \infty$. The degree of attenuation of cluster association (b) is found by using an additional reference point a_j, T_j as

$$b = \frac{\ln(a_j / a_i)}{\ln(T_i / T_j)} \tag{7}$$

by enumerating and averaging all options i, j or by selecting the most reliable points a_i, T_i and a_j, T_j.

Thus, to build an adequate temperature dependence of viscosity based on the Boltzmann distribution and the concept of chaotic particles, only three experimental points are enough: η_r, T_r; a_i, T_i; a_j, T_j. In the most general form, this dependence, taking into account the formulae (5)-(7), will be expressed as

$$\eta = \eta_r (T_r / T)^{\frac{\ln(\eta_i / \eta_r)}{\ln(T_r / T_i)} \left(\frac{T_i}{T}\right)^{\ln \frac{\ln(\eta_j / \eta_r) \ln(T_r / T_i)}{\ln(T_r / T_j) \ln(\eta_i / \eta_r)}}}.$$

With the use of specific values of three reference points, this expression is simplified, reducing to the following view

$$\eta = \eta_r (T_r / T)^{a_i (T_i / T)^b}.$$

Selection of reference points from the experimental data array is advisable for η_r, T_r – at the beginning of temperature dependence, for a_i, T_i – in the middle and for a_j, T_j – at the end of it.

It is of interest to consider justification for derivation of temperature dependence of kinematic viscosity with independent consideration of another individual characteristic of the substance, that is, to consider the melting heat ΔH_m as an energy barrier.

Considering the melting heat as an energy barrier, the fraction of crystalline particles will be expressed

$$P_{crm} = 1 - \exp\left(-\frac{\Delta H_m}{RT}\right).$$

The range of the relative change in kinematic viscosity from ν_m at a melting point T_m to $\nu = 0$ at a infinitely high temperature, where the liquid can exist in the supercritical range of temperature and pressure in an indistinguishable state with the gas, will be as follows:

$$1 \geq \frac{\nu}{\nu_m} \geq 0. \tag{8}$$

The fraction of crystal-moving particles according to the formula with account of the melting heat in the same temperature range varies within the limits

$$1 - \exp\left(-\frac{\Delta H}{RT_m}\right) \geq 1 - \exp\left(-\frac{\Delta H}{RT}\right) \geq 0. \tag{9}$$

Using algebraic transformations, the obtained inequality leads to the form

$$\exp\left(-\frac{\Delta H}{RT_m}\right) \leq \exp\left(-\frac{\Delta H}{RT}\right) \leq 1.$$

After logarithmation we have

$$\frac{\Delta H}{RT_m} \geq \frac{\Delta H}{RT} \geq 0.$$

From where the original inequality (9) will take the following form

$$1 \geq \frac{T_m}{T} \geq 0,$$

that fully coincides with limits of relative changes of kinematic viscosity (8).

Thus, regardless of the choice of substance individual characteristic as an energy barrier, we come to the same equation of the basic formula (1).

Therefore, without changing the limits of changes in kinematic viscosity, it is possible to raise to any power the part $\frac{T_m}{T}$, that is,

$$1 \geq \left(\frac{T_m}{T}\right)^a \geq 0.$$

Therefore, based on the concept of chaotic particles, an additional justification is obtained for derivation of the basic model of kinematic viscosity with independent consideration of another individual characteristic of the substance. It has been shown that the normalization of the equation for the fraction of crystalline particles by melting heat or any other energy characteristic leads to the same model of viscosity (4), which justifies its base value.

Results and Discussion

In works [2, 3], we showed the possibility of applying model (4) to calculation of viscosity of liquid metals. We made calculations for many liquid metals. It was found that the proposed model most accurately describes the dependence of viscosity on temperature. This pattern was revealed in the process of comparing

experimental data [5, 6] and data calculated for model (4). As a result, we believe that this model can be used to calculate viscosity without conducting an experiment.

Let us consider the application of model (4) on beryllium, which can be correlated with semimetals according to physicochemical properties.

There are no data on kinematic viscosity of **beryllium** in work [5] and in reference book [6]. In reference book [6], melting points T_m = 1560 K and boiling point T_b = 2723 K are indicated.

The work [5] gives the formula for the dynamic viscosity of beryllium

$$\eta = 10^{-2} T^{0,2} \text{ , g/(sm·s)}$$

where $T = T_m + \Delta T$.

After analyzing this formula, the author [1] revealed a sharp increase in viscosity with temperature rise. Therefore, the author [1] proposes the following formula for calculating dynamic viscosity

$$\eta = 10^{-2} \Delta T^{-0,2} \text{ , g/(sm·s)} \qquad (10)$$

here ΔT – the degree of superheat of the melt over the crystallization point of pure beryllium, which is equal to 1556 K. The kinematic viscosity of beryllium was estimated according to available data for the area 1560-1670 K through a leveled relationship (10). Point T_r = 1570 K and $\nu_r = 3{,}494 \cdot 10^{-7}$ m^2/s is taken as a reference point. Previously, in the work [1], it was found that the model (3) has an advantage in describing the relationship between viscosity and temperature. However, the results of the calculated viscosity values for four models [2], which are listed in Table 1 and shown in Figure 1, prove the most adequate description of this relationship with the help of the model (4).

Table 1

Comparison of data [1] with models calculated (1-4) on values of kinematic viscosity of beryllium, $\nu \cdot 10^7$, m^2/s

T	$\rho^*_{[6]}$, kg/m^3	$\eta^*_{[1]}$, mPa·s	ν(leveled relationship) $10^7 \cdot \nu = \eta^*/\rho^*$, m^2/s	ν(1)	ν(2)	ν(3)	a	ν(4)
T_m =1556	(1689,5)	(0,758)	-	3,52	3,52	3,54	-	3,71
1570	1688,4	0,590	3,494	3,49	3,49	3,49	-	3,49
1590	1686,1	0,494	2,930	3,45	3,44	3,41	13,91	3,10
1610	1683,8	0,450	2,674	3,41	3,38	3,32	10,63	2,75
1630	1681,5	0,423	2,514	3,37	3,33	3,24	8,78	2,45
1650	1679,2	0,403	2,4	3,32	3,28	3,17	7,56	2,18
1670	1676,9	0,388	2,313	3,28	3,23	3,10	6,68	1,94
R			-	< 0	< 0	0,51	-	0,84

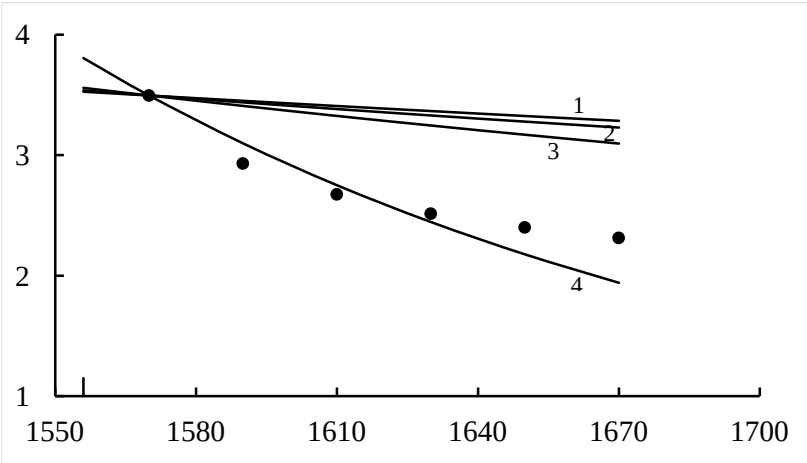

ν – kinematic viscosity, T – temperature.
Points - data [1], 1 – on model (1),
2 – on model (2), 3 – on model (3), 4 – on model (4)

Figure 1. Dependence of kinematic viscosity of beryllium on temperature

The correlation coefficients for models (4) and (3) are equal to 0.84 and 0.51, respectively. Here there is a great difference in the values of correlation coefficients: for model (4), the value is higher. Therefore, the generalized model (4) is reasonable for describing the temperature dependence of viscosity.

The average value of $\bar{a}$ = 9,51 indicates that beryllium has a great tendency to associate clusters of metal atoms. This is because a higher ionization potential makes beryllium less electropositive, and all its compounds, at least partially, have covalent bonds. The tendency of beryllium to form a stronger metal bond due to the transition to the electron conduction zone is reflected in the strength of associates in metal melts, the destruction of which with an increase in temperature requires additional exposure to liquid- and vapor-moving particles.

The homogeneity of the obtained range for a according to Nalimov criterion is observed: $S(x)$ = 2,870; $r_{\min}^{\max}$ = 1,102 < r_{cr} = 1,821.

In this temperature range, considering the degree of cluster association, model (4) with reference point near the melting point can be used as a generalized model of melt viscosity T_r = 1570 K

$$\nu = (0{,}864 \cdot 10^{24} / T^{9{,}51}) \pm 0{,}2,\ \text{m}^2/\text{s}.$$

The activation energy is $E_a = 85231$ J/mol, and for the proposed model, the activation energy is $E_a^{/} = 128017$ J/mol.

However, as it is shown in Figure 1, the processing of experimental data should be carried out for two areas: 1560-1610 K (low temperature) and 1630-1670 K (high temperature). For each of areas clusters association degrees $\bar{a}$ = 12,27 and $\bar{a}$ = 3,62 respectively were calculated.

Taking into account the obtained clusters association degrees for each of the areas, the temperature dependence of melt viscosity can be expressed by the equations:
for low-temperature area

$$\nu = (5{,}69 \cdot 10^{32} / T^{12{,}27}) \pm 7{,}52 \cdot 10^{-9},\ \text{m}^2/\text{s}, \quad (11)$$

for high-temperature area

$$\nu = (1{,}08 \cdot 10^{5} / T^{3{,}62}) \pm 2{,}69 \cdot 10^{-10},\ \text{m}^2/\text{s}. \quad (12)$$

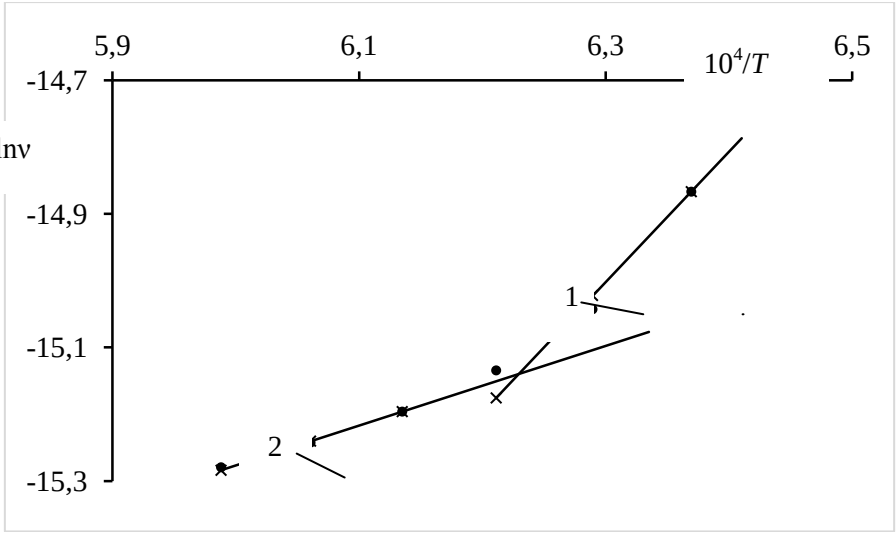

ν – kinematic viscosity, T – temperature.
Points - experimental data, crosses - for models (11) and (12), straight lines - according to the equation $\ln\nu = \ln A' + E_a^{/}/(RT)$ for low-temperature and high-temperature areas

Figure 2. Logarithm dependence of beryllium kinematic viscosity on reciprocal temperature

The homogeneity of the obtained range for *a* according to Nalimov criterion in each area is observed: for low-temperature area $S(x)$ = 2,316; $r_{\min}^{\max}$ = 1,001< r_{cr} = 1,483, for high-temperature area $S(x)$ = 0,260; $r_{\min}^{\max}$ = 0,978< r_{cr} = 1,483.

Activation energy for each of areas is $E_a^{/} = 162181$ J/mol and $E_a^{/} = 49670$ J/mol respectively. The transition temperature from one area to another is 1605 K. The correlation coefficients for each area are equal to each other and $R_1 = R_2$ = 0,999.

This model was tested on 28 metals. In all cases, the viscosity values calculated from the proposed model were closest to the experimental data. Also, according to the proposed model, slag viscosity of the synthetic mixture of the system CaO-SiO_2-Al_2O_3-MgO-Cr_2O_3, obtained by members of the Chemical and Metallurgical Institute named after Zh. Abishev, laboratory of ferroalloys and restorative processes was calculated.

Conclusions

During the research, it was established that the given justification of the cluster-associate pattern makes it possible to judge its veracity and possibility of application for calculation of kinematic viscosity of melts from a mathematical point of view. The veracity of the results is also supported by the coincidence of some results obtained independently from other researchers with data available in the world literature [5–9]. We also assume that this model will allow conducting physical and chemical justification of chemical and metallurgical processes more reliably and will provide more reasonable requirements for their production technology. With the help of the proposed model, it is possible to calculate melt viscosity values at different temperature values, up to the highest values without conducting high-cost experiments. The model also provides prerequisites for calculation of viscosity of multicomponent systems.

References

1 Турдукожаева А.М. Применение распределения Больцмана и информационной энтропии Шеннона к анализу твердого, жидкого и газообразного состояний вещества (на примере металлов): автореф. дис. ... д-ра техн. наук: 05.16.08 — «Теория металлургичеких процессов» / А.М. Турдукожаева. — Караганда, 2008. — 32 с.

2 Kazhikenova A.Sh. Efficiency of applying cluster-associated model of viscosity of liquid metals / A.Sh. Kazhikenova, D.B. Alibiyev, E.S. Ibrayeva // Bulletin of the Karaganda University. Chemistry Series. — 2017. — № 4(88). — P. 58–64.

3 Kazhikenova A.Sh. Application of cluster-associative model for calculation of kinematic viscosity of metal melts / A.Sh. Kazhikenova, D.B. Alibiyev, A.B. Seitimbetova, A.S. Smailova // Bulletin of the Karaganda University. Chemistry Series. — 2020. — № 2(98). — P. 68–76.

4 Малышев В.П. Вязкость, текучесть и плотность веществ как мера их хаотизации / В.П. Малышев, Н.С. Бектурганов, А.М. Турдукожаева. — М.: Научный мир, 2012. — 288 с.

5 Шпильрайн Э.Э. Исследование вязкости жидких металлов / Э.Э. Шпильрайн, В.А. Фомин, С.Н. Сковородько, Г.Ф. Сокол. — М.: Наука, 1983. — 247 с.

6 Свойства элементов: справоч. изд.: [В 2 кн.]. — Кн. 1 / под ред. М. Е. Дрица. — 3-е изд., перераб. и доп. — М.: Изд. дом «Руда и Металлы», 2003. — 448 с.

7 Shaltakov S.N. Mathematical model of high-temperature melt flow with account for short-range order nature / S.N. Shaltakov, S.Sh. Kazhkenova, B.R. Nussupbekov, D.Zh. Karabekova, A.K. Khasennov, M. Stoev // Bulletin of the university of Karaganda-Physics. — 2019. — No. 2(94). — P. 22–28.

8 Frank H. Eine Schwingtiegelapparatur zur Bestimmung der Viskosität von Flüssigkeiten bei hohen Temperaturen / H. Frank, W. Manfred // Z. Metallk. — 1991. — № 12 (82). — P. 913–916.

9 Vargaftik N.B. Viscosity and thermal conductivity of alkali metal vapors at temperatures up to 2000 K / N.B. Vargaftik, Yu.K. Vinogradov, V.I. Dolgov, V.G. Dris, I.F. Stepanenko, Yu.K. Yakimovich, V.S. Yargin // Int. J. Thermophys. — 1991. — № 1(12). — P. 85–103.

А.Ш. Кажикенова, Д.Б. Әлібиев, Ж.М. Тентекбаева,
А.С. Смаилова, Р.А. Оразбекова, И.С. Қауымбек

Балқымалардың тұтқырлығын есептеу үшін кластерлік-ассоциативті модельді қолдану

Белгілі болғандай, заттың сұйық күйін теориялық тұрғыдан сипаттау өте қиын. Сұйықтық пен оның тұтқырлығы туралы қазіргі заманауи ұғымдар мынаған саяды: сұйықтық құрылымында атомдардың кеңістіктік орналасуы кристалдағыдай бекітілмеген және газдағыдай еркін күйде емес. Сондықтан сұйықтық өзінің қасиеттері бойынша қайнау температурасына жақын газға немесе балқу температурасына жақын қатты денеге жақындауы мүмкін. Осылайша, сұйықтықтың құрылымы жақын байланыс тәртібімен сипатталады. Сұйық металдардың қасиеттері негізінен эксперименттік зерттеулерден алынады. Мақалада кластерлік-ассоциативті модельдің математикалық тұрғыдан негіздемесі келтірілген. Зерттеудің мақсаты — сұйық металдардың тұтқырлығын есептеу үшін жартылай эмпирикалық модельді қолдану мүмкіндігін көрсету. Ұсынылған модель Больцманның таратылуына негізделген ретсіз бөлшектер тұжырымдамасын қолдана отырып жасалған. Бұл модель ассоцирленген кластердің дәрежесін ескере отырып жасалған. Көптеген жылдар бойы сұйық металдардың тұтқырлығы тек эксперименттік әдіспен зерттелді. Ұсынылған модель балқымалардың тұтқырлық мәндерін аналитикалық түрде табуға мүмкіндік береді. Осы модель бойынша кейбір металдардың есептелген тұтқырлық мәндері эксперименттік мәндермен салыстырылды. Барлық жағдайларда алынған мәндердің эксперименталды мәндермен сәйкестігі анықталды. Ұсынылған модельдің дұрыстығы корреляция коэффициентімен расталады. Ұсынылған модельді қолдану бұрын кейбір металдарда көрсетілген. Сонымен қатар авторлар бериллий мысалында кластерлік-ассоциативті модельдің қолданылуын көрсеткен, өйткені оны көптеген физика-химиялық қасиеттері бойынша жарты металдармен байланыстыруға болады. Ғылыми нәтижелердің жаңашылдық дәрежесі ұсынылған модельдің негіздемесі оның сенімділігін дәлелдейді және зерттелген металдар үшін алынған жоғары корреляция коэффициенттері оның функционалдығын көрсетеді.

Кілт сөздер: кинематикалық тұтқырлық, ретсізделген бөлшектер, ассоцирленген кластердің дәрежесі, кластерлі-ассоциативті моделі, сұйық металдар, кристаллқозғалысты бөлшектер, тұтқырлықтың температураға тәуелдігі, бериллий.

А.Ш. Кажикенова, Д.Б. Әлібиев, Ж.М. Тентекбаева,
А.С. Смаилова, Р.А. Оразбекова, И.С. Қауымбек

Применение кластерно-ассоциатной модели для расчета вязкости расплавов

Как известно, жидкое состояние вещества является наиболее сложным для теоретического описания. Современные представления о жидкости и ее вязкости сводятся к следующему: в структуре жидкости пространственное расположение атомов не закреплено, как в кристалле, они не находятся в свободном состоянии, как в газе. Поэтому жидкость по своим свойствам может приближаться к газу вблизи температуры кипения или к твердому телу вблизи температуры плавления. Тем самым структуре жидкости характерен ближний порядок связи. Свойства жидких металлов получены в основном из экспериментальных исследований. В статье приведено обоснование кластерно-ассоциатной модели с математической точки зрения. Цель исследования — показать возможность применения полуэмпирической модели для расчета вязкости жидких металлов. Предлагаемая модель разработана с помощью концепции хаотизированных частиц, в основе которой лежит распределение Больцмана. Данная модель разработана с учетом степени ассоциации кластеров их кристаллоподвижных частиц. Многие годы вязкость жидких металлов исследовалась только экспериментальным методом. Предлагаемая модель позволяет аналитически найти значения вязкости расплавов. Рассчитанные значения вязкости некоторых металлов по данной модели были сравнены с экспериментальными значениями, во всех случаях было выявлено их совпадение. Корректность предлагаемой модели подтверждается коэффициентом корреляции. Применение такой модели было показано ранее на некоторых металлах. Кроме того, авторами статьи показана применимость кластерно-ассоциатной модели на примере бериллия, так как его по многим физико-химическим свойствам можно соотнести к полуметаллам. Степень новизны научных результатов состоит в том, что полученные высокие коэффициенты корреляции для исследованных металлов указывают на ее функциональность.

Ключевые слова: кинематическая вязкость, кластер из кристаллоподвижных частиц, степень ассоциации, температура кипения, температура плавления, расплав, коэффициент корреляции, бериллий.

References

1 Turdukozhayeva, A.M. (2008). Primenenie raspredeleniia Boltsmana i informatsionnoi entropii Shennona k analizu tverdogo, zhidkogo i gazoobraznogo sostoianii veshchestva (na primere metallov) [Application of the Boltzmann distribution and Shannon information entropy to the analysis of solid, liquid and gaseous states of matter (on the example of the metals)]. *Extended abstract of Doctor's thesis.* Karaganda [in Russian].

2 Kazhikenova, A.Sh., Alibiyev, D.B., & Ibrayeva, E.S. (2017). Efficiency of applying cluster-associated model of viscosity of liquid metals. *Bulletin of the Karaganda University, Chemistry Series, 4(88),* 58–64.

3 Kazhikenova, A.Sh., Alibiyev, D.B., Seitimbetova, A.B., & Smailova, A.S. (2020). Application of cluster-associate model for calculation of kinematic viscosity of metal melts. *Bulletin of the Karaganda University, Chemistry Series, 2(98),*68–76.

4 Malyshev, V.P., Abdrakhmanov, B.T., & Turdukozhayeva, A.M. (2012). *Viazkost, tekuchest i plotnost veshhestv kak mera ikh khaotizatsii [Viscosity, fluidity and density of substances as a measure of their chaotization]*. Moscow: Nauchnyi mir [in Russian].

5 Schpilrain, E.E., Fomin, V.A., Skovorodko, S.H., & Sokol, G.F. (1983). *Issledovanie viazkosti zhidkikh metallov [Viscosity study of liquid metals]*. Moscow: Nauka [in Russian].

6 Drits, M.E. (Ed.). (2003). *Svoistva elementov [The properties of the elements]*. (Books 1-2). Moscow: Izdatelskii dom «Ruda i metally» [in Russian].

7 Shaltakov, S.N., Kazhikenova, S.Sh., Nussupbekov, B.R., Karabekova, D.Zh., Khasennov, A.K., & Stoev, M. (2019). Mathematical model of high-temperature melt flow with account for short-range order nature. *Bulletin of the university of Karaganda-Physics,* 2(94), 22–28.

8 Frank, H., & Manfred, W. (1991). Eine Schwingtiegelapparatur zur Bestimmung der Viskosität von Flüssigkeiten bei hohen Temperaturen. *Metallk, 12 (82),* 913–916.

9 Vargaftik, N.B., Vinogradov, Yu.K., Dolgov, V.I., Dris, V.G., Stepanenko, I.F., Yakimovich, Yu.K., & Yargin, V.S. (1991). Viscosity and thermal conductivity of alkali metal vapors at temperatures up to 2000 K. *Thermophys, 1(12),* 85–103.

DOI 10.31489/2022PH3/108-114

UDC 533.682

A.R. Bakhtybekova[1,2*], N.K. Tanasheva[1,2], N.N. Shuyushbayeva[3], L.L. Minkov [4], N.K. Botpaev[1]

[1] *Karaganda University of the name of academician E.A. Buketov, Karaganda, Kazakhstan*
[2]*Scientific Center "Alternative Energy", Karaganda, Kazakhstan*
[3] *Sh.Ualikhanov Kokshetau University, Kokshetau, Kazakhstan*
[4] *National Research Tomsk State University, Tomsk, Russia*
*(*E-mail:* asem.alibekova@inbox.ru*)*

Analysis of velocity and pressure vector distribution fields in a three-dimensional plane around a wind power plant

To date, there has been an increase in demand for electric energy obtained from clean renewable energy sources. One of them is wind power. Based on this, the development and research of new types of efficient wind turbines that start working at low wind speeds is an urgent issue. Wind turbines operating based on the Magnus effect have proven their effectiveness. However, the authors of this work, for the first time, to eliminate the problem in the form of an electric drive for the promotion of cylindrical blades added a deflector element to the end of the cylinders. Before creating an experimental setup, it is necessary to numerically investigate the aerodynamics around the wind wheel. For this purpose, numerical simulation of wind wheel aerodynamics has been carried out using the highly efficient Ansys Fluent program. A three-dimensional geometry has been created in Design Modeler. A mathematical model grid with a grid number of 47329 consisting of tetragonal cells is constructed. The Realizable k-ε is chosen as the turbulence model. A thorough analysis of the velocity vector distribution fields for flow and pressure velocities in the three-dimensional plane around the wind wheel at air flow velocities of 5.10 and 15 m/s is carried out.

Keywords: wind power plant, Ansys Fluent, Magnus effect, deflector, mathematical model, numerical simulation.

Introduction

Currently, many problems faced by engineers and researchers in the field of aerodynamics are not amenable to experimental solutions or require huge material and human resources. An alternative solution in this case is the use of numerical research based on computer programs.

Computational fluid dynamics (CFD) is a branch of science that solves the problem of modeling heat and mass transfer in various technical and natural objects. The main task of CFD is the numerical solution to the Navier Stokes equations describing fluid dynamics. These equations constitute a mathematical model of heat and mass transfer [1, 2].

For aerodynamic practice, an important role is played by the data of air flow conditions of cylindrical bodies of various configurations.

The number of papers devoted to CFD in the field of wind energy is growing every year. In [3], the authors performed a high-resolution simulation of the flow around a wind power plant and its blades.

One of the representatives of wind turbines of installations showing their efficiency starting from 2-4 m/s is wind turbines operating based on the Magnus effect. Along with the obvious advantages over traditional blade wind turbines, to increase the performance indicators, it is necessary to improve the shape and parameters of the working power elements - the blades of the installation. The authors of [4] conducted a 3D numerical study of a Magnus-type wind turbine equipped with cylindrical blades with different aspect ratios. The analysis of the influence of various shapes and lengths of blades on the performance of the Magnus wind turbine is carried out.

However, existing wind turbines operating based on the Magnus effect have a disadvantage in the form of an additional source of electric drive for the promotion of cylindrical blades [5]. Accrodingly, we add a deflector to exclude the electric drive, as well as the disruption of the air flow from the ends of the cylinders.

The purpose of this work is to create a mathematical model of a wind turbine with two blades in the form of rotating cylinders with a deflector.

Mathematical model

The simulation was carried out using the Ansys Fluent software package. Structurally, the numerical simulation is shown in Fig. 1.

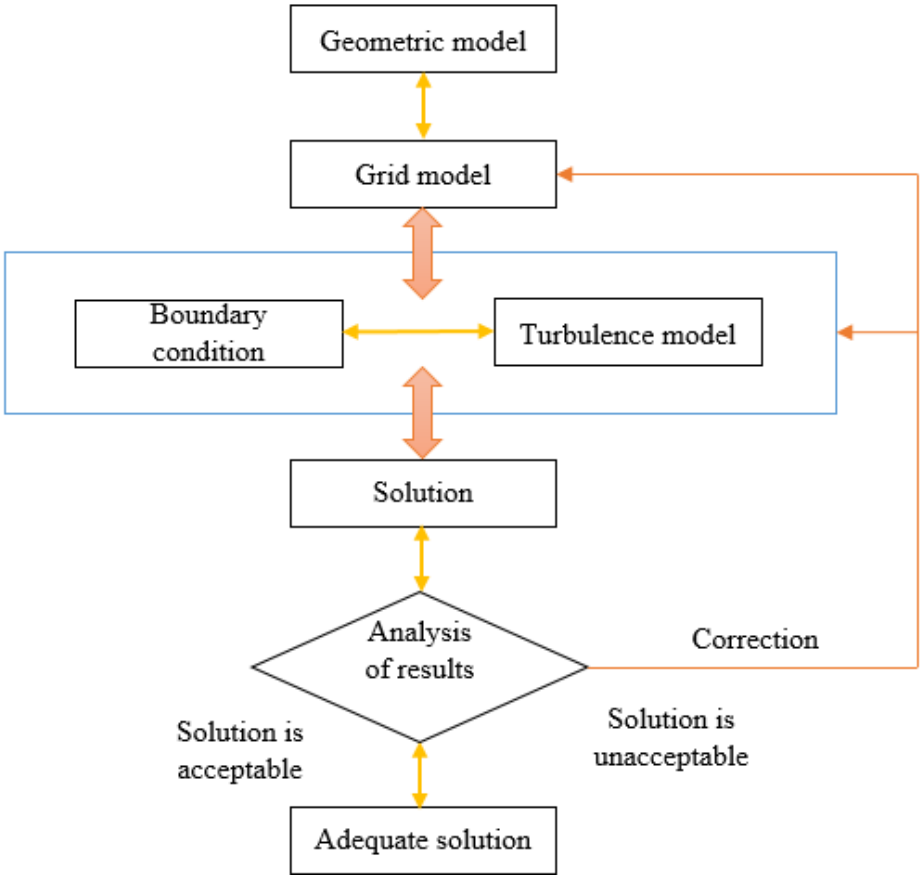

Figure 1. Structure of execution, numerical simulation

The first stage in the numerical simulation process of a wind power plant is the construction of the geometry of a wind power plant using the COMPASS 3D program. A three-dimensional solid-state model of a wind power plant with 2 blades in the form of rotating cylinders with a deflector created using the COMPASS 3D program is shown in Figure 2.

In this case, we consider the flow of air around a wind wheel consisting of two blades in the form of a rotating cylinder with a deflector located in the XY plane at an angle of 180 ° to each other relative to the z-axis of rotation of the wind wheel (Figure 3). The axes of rotation of the cylinders are in the XY plane. The axis of rotation of the wind wheel coincides with the Z axis.

The entire working area was divided into three types of nested subdomains (Fig. 3): subdomains of the 1st type (cylinders), built around the working blades of the wind wheel and rotating at the speed of the working cylinders (1); subdomain of the 2nd type (sphere), built around the wind wheel minus cylindrical subdomains 1-type (2); type 3 subdomain (cube) surrounding type 2 subdomain minus (3).

The radius of the outer cubic subdomain (3) is assumed to be 0.2 m, spherical subdomain (2) has a radius of 0.1 m, cylindrical subdomains (1) have a radius of 0.02 M.

The boundary conditions in the form of the incoming velocity of the incoming air flow are set on the front wall, and the outlet pressure is set on the back wall of the cubic subdomain. The remaining walls are set to the walls of symmetry (Figure 3).

The next step in the process of numerical modeling is to create a computational grid for this task in Ansys Meshing with a minimum set of actions.

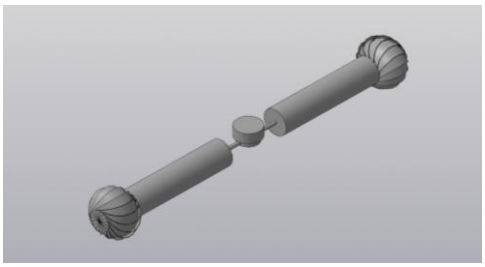

Figure 2. Three-dimensional geometry of a wind power plant with 2 blades created in the COMPASS 3D program

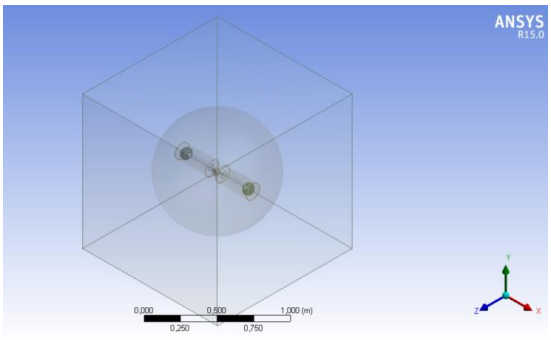

Figure 3. Calculation area

A finite-volume grid constructed in subdomains of type 1, 2, 3 consists of tetragonal cells. Figure 4 represents the grid view in the z=0 plane. The grid is depicted in the XY plane, the cross section of the Z=0 area. The total number of cells is 47329.

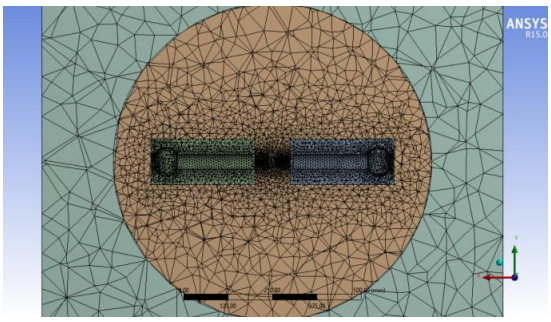

Figure 4. Finite-volume grid

The Realizable k-ε model was chosen as the turbulence model, which gives a general description of turbulence using two transport equations. This model is a widely used model in the field of computational fluid dynamics (CFD) and is used to model average flow characteristics for turbulent flow conditions.

Table 1 presents the boundary conditions specified in the numerical study.

Table 1

List of boundary conditions

Boundary conditions	
At the entrance	
1	2
View	Speed at the entrance
Initial manometric pressure (Pa)	0
Air flow velocity, m/s	3,5,7,10,12,15
Turbulence intensity (%)	5
Coefficient of turbulent viscosity	10
At the exit	
View	Outlet pressure

1	2
Manometric pressure (Pa)	0
Return flow of turbulent intensity (%)	5
Return flow coefficient of turbulent intensity (%)	10
Blade surface	
View	Wall
Shift Condition	No sliding

Results of mathematical modeling of a wind power plant with 2 blades

To calculate aerodynamic characteristics and mathematical modeling, a wind power plant with 2 blades in the form of rotating cylinders with a deflector, created on the basis of the Magnus effect, is considered.

The COUPLED scheme was used to coordinate the pressure field and the velocity field. Time derivatives were resolved with the second order of accuracy. Figure 5 presents the results obtained by numerical investigation of the distribution field of the velocity vectors of the incoming air flow around the wind wheel of a wind turbine with 2 blades at speeds of 5.10 and 15 m/s.

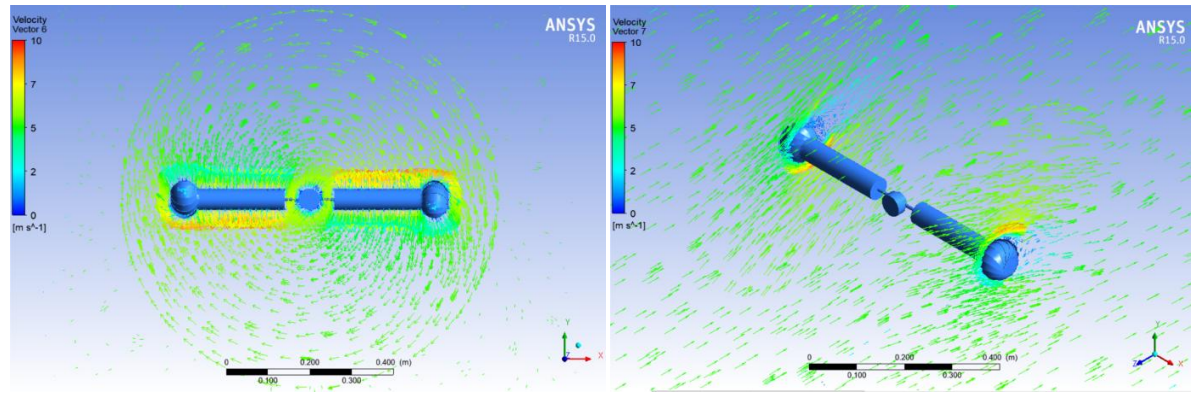

a)

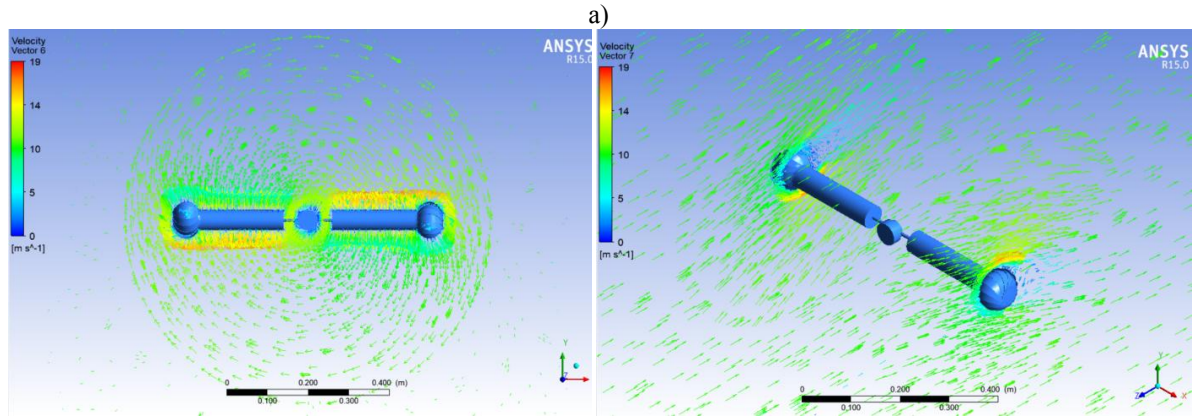

b)

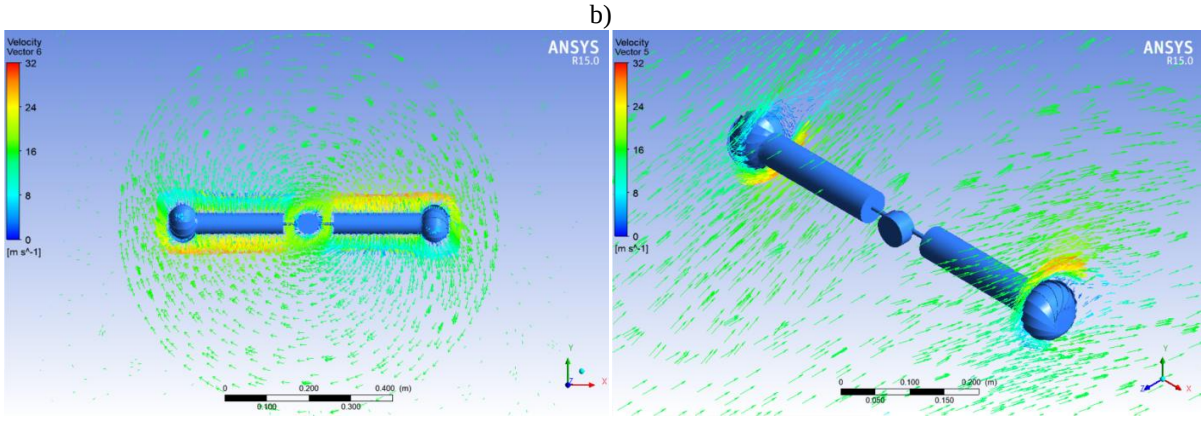

c)

Figure 5. Velocity vector distribution fields in a three-dimensional plane around a wind wheel:
a) at v = 5 m/s; b) at v = 10 m/s; c) at v= 15 m/s.

As can be seen from Figure 5, there is a complex three-dimensional nature of the wind wheel flow. The direction of rotation of the cylinder is set on the x-axis and the wind wheel on the z-axis.

The deformation of the velocity vector distribution field in the three-dimensional plane occurs because of an increase in the air flow velocity on one side of the blade and a decrease in the flow velocity on the other side caused by the rotation of cylinders with deflectors around their axes in the positive direction.

It can be seen that due to the unfavorable pressure gradient, the boundary layer around the surface of the blades separates with an increase in the velocity of the incoming air flow.

It was also found that by adding a deflector to the end part of the cylinder, the aerodynamics around the cylinder improved, the disruption of the airflow from the ends of the cylinders was eliminated.

Figure 6 illustrates the static pressure distributions (pct = p – ratm) in the vicinity of the wind wheel (plane z= 0) obtained for different speeds of the incoming flow (wind).

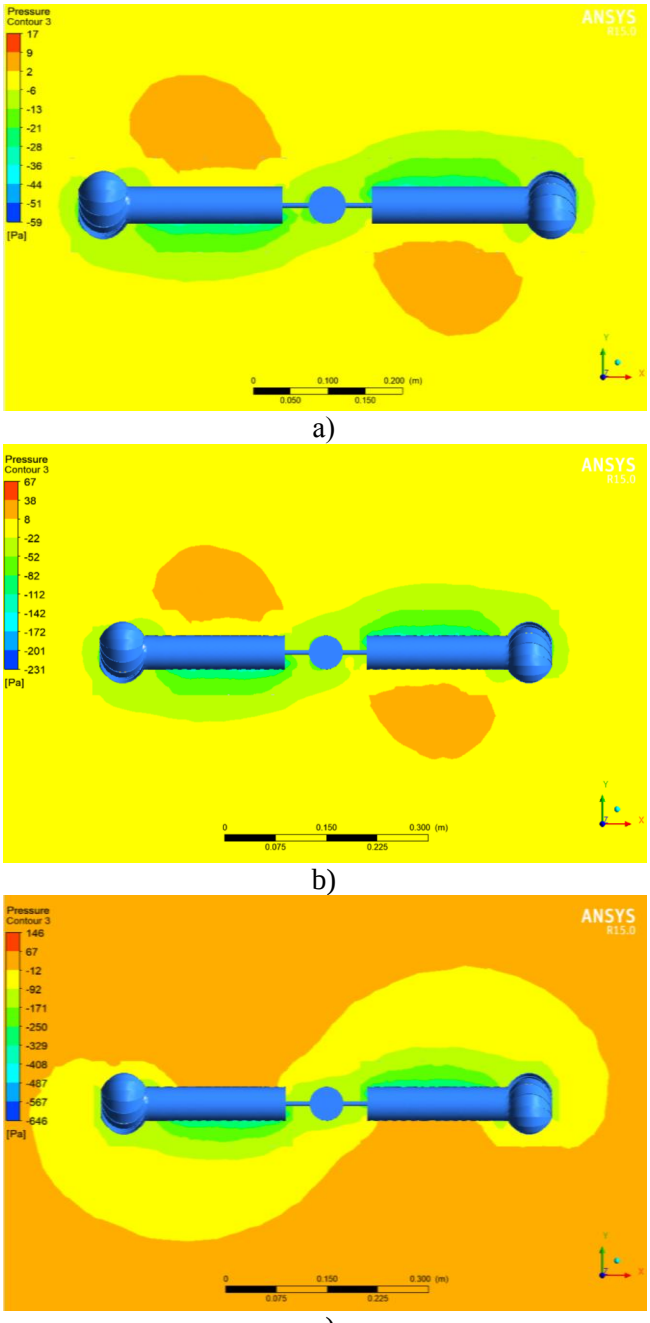

Figure 6. Pressure distribution fields in the three-dimensional plane around the wind wheel:
a) at v = 5 m/s; b) at v = 10 m/s; c) at v= 15 m/s

The rotation of the blades in the conditions of an incoming flow leads to the fact that on one side of the cylinder with a deflector, the air velocity will be greater than on the other side. According to Bernoulli's law, in the area where the flow velocity is higher, the pressure becomes lower. Therefore, on one side of the blade (in the figures shown left side), the pressure is lower than on the other, resulting in a force (lifting) acting on each blade, which is directed perpendicular to the axis of the blade and the direction of the wind. Since all cylinders rotate in the same direction (clockwise) relative to their own axes, the lifting forces will create a moment of forces that causes the wind wheel to rotate clockwise relative to the z axis. The results obtained do not contradict the results of the authors [6, 7].

At an incoming flow velocity of 5 m/s, the static pressure in the vicinity of the rotating wind wheel varies from -59 Pa to 17 Pa. An increase in wind speed leads to an expansion of the range of pressure changes. So for a wind speed of 10 m/s, this range is from – 231 Pa to 67 Pa, for 15 m/s – from -646 Pa to 146 Pa.

Conclusions

The authors found that by adding a deflector to the end zone of the cylinder, the aerodynamics around the cylinder improved, the disruption of the air flow from the ends of the cylinders was eliminated.

In the course of performing a numerical study of aerodynamics around a rotating wind wheel of a wind power plant with 2 blades in the form of rotating cylinders with a deflector:

– a three-dimensional geometry of a wind power plant with 2 blades created in the COMPASS 3D program was created;

– a mathematical model grid with a grid number of 47329 consisting of tetragonal cells was constructed;

– selected as a Realizable k-ε turbulence model, which improved characteristics compared to the standard k-ε model when applied to flows involving boundary layers with strong unfavorable pressure gradients;

– velocity vector distribution fields were obtained for flow velocities of 5.10 and 15 m/s, during which it was determined that due to an unfavorable pressure gradient, the boundary layer around the surface of the blades separates with an increase in the velocity of the incoming air flow;

– pressure distribution fields were obtained in a three-dimensional plane around the wind wheel for flow velocities of 5.10 and 15 m/s, at which it was determined that the rotation of the blades in the conditions of an incoming flow leads to the fact that the air velocity on one side of the cylinder with a deflector will be greater than on the other side.

References

1 Tanasheva, N.K., Bakhtybekova, A.R., Shaimerdenova, G.S., Sakipova, S.E., Shuyushbaeva, N.N. (2022). Modeling Aerodynamic Characteristics of a Wind Energy Installation with Rotating Cylinder Blades on the Basis of the Ansys Suite. *Journal of Engineering Physics and Thermophysics*. https://doi.org/10.1007/s10891-022-02500-3

2 Tanasheva, N.K., Bakhtybekova, A.R., Sakipova, S.E., Minkov, L.L., Shuyushbaeva, N.N., & Kasimov, A.R. (2021). Numerical simulation of the flow around a wind wheel with rotating cylindrical blades. *Eurasian Physical Technical Journal*, 18, 1(35), 51–56. https://up.ksu.kz/phtj/2021_18_1_35/7.pdf

3 Miller, A., Chang, B., Issa, R., & Chen, G. (2013). Review of computer-aided numerical simulation in wind energy. *Renewable and Sustainable Energy Reviews*, 25, 122–134.

4 Sun, X., Zhuang, Y., Cao, Y., & Huang, D. (2012). A three-dimensional numerical study of the Magnus wind turbine with different blade shapes. *Journal of Renewable and Sustainable Energy*, 4, 063139. https://doi.org/10.1063/1.4771885

5 Tanasheva, N.K., Bakhtybekova, A.R., Minkov, L.L, Bolegenova, S.A., Shuyushbaeva, N.N., Tleubergenova, A.Zh., & Toktarbaev, B.A. (2021). Influence of a rough surface on the aerodynamic characteristics of a rotating cylinder. *Bulletin of the university of Karaganda-Physics*, 3(103), 52–59.

6 Wang, M., Avital, E.J., Chunning, Ji X.B., Xu, D., Williams, J.J.R., & Munjiza, A. (2020). Fluid–structure interaction of flexible submerged vegetation stems and kinetic turbine blades. *Computational Particle Mechanics*, 7, 839–848. https://doi.org/10.1007/s40571-019-00304-6

7 Kui, O., Chunlei, L., Sachin, P., & Antony, J. (2009). High-Order Spectral Difference Simulation of Laminar Compressible Flow Over Two Counter-Rotating Cylinders . *27th AIAA Applied Aerodynamics Conference* (22-25 June 2009). San Antonio (Texas). https://doi.org/10.2514/6.2009-3956

А.Р. Бахтыбекова, Н.К. Танашева, Н.Н. Шуюшбаева, Л.Л. Миньков, Н.К. Ботпаев

Жел энергетикалық қондырғысының айналасындағы үш өлшемді жазықтықтағы жылдамдық пен қысым векторларының таралу өрістерін талдау

Бүгінгі таңда таза жаңартылатын энергия көздерінен алынған электр энергиясына сұраныстың өсуі байқалады. Солардың бірі — жел энергетикасы. Осыған сүйене отырып, желдің төмен жылдамдығымен жұмыс істей бастайтын тиімді жел энергетикалық қондырғысының (ЖЭҚ) жаңа түрлерін әзірлеу және зерттеу өзекті мәселе болып табылады. Магнус эффектісі негізінде жұмыс істейтін ЖЭҚ тиімді екенін дәлелдеді, бірақ бұл жұмыстың авторлары электр жетегі түрінде мәселені шешу үшін алғаш рет цилиндр қалақшаларын айналдыру үшін цилиндрлердің соңына дефлектор элементін қосты. Эксперименттік қондырғыны жасамас бұрын жел доңғалағының айналасындағы аэродинамиканы сандық түрде зерттеу қажет. Осы мақсатта Ansys Fluent жоғары тиімді бағдарламасын пайдалана отырып, жел доңғалағының аэродинамикасына сандық модельдеу жүргізілді. Design Modeler-де үш өлшемді геометрия жасалды. Тетрагональды ұяшықтардан тұратын тор саны 47329 болатын математикалық модельдің торы құрастырылды. Турбуленттілік моделі ретінде Realizable k-ε таңдалды. Ауа ағынының жылдамдығы 5, 10 және 15 м/с болатын жел доңғалағының айналасындағы үш өлшемді жазықтықтағы ағын жылдамдығы мен қысымы үшін жылдамдық векторларының таралу өрістеріне мұқият талдау жүргізілді.

Кілт сөздер: жел энергетикалық қондырғы, Ansys Fluent, Магнус эффектісі, дефлектор, математикалық модель, сандық модельдеу.

А.Р. Бахтыбекова, Н.К. Танашева, Н.Н. Шуюшбаева, Л.Л. Миньков, Н.К. Ботпаев

Анализ полей распределения векторов скоростей и давления в трехмерной плоскости вокруг ветроэнергетической установки

К сегодняшнему времени наблюдается рост спроса в электрической энергии, полученной из чистых возобновляемых источников энергии. Одним из них является ветроэнергетика. Исходя из этого, разработка и исследования новых видов эффективных ветроэнергетических установок (ВЭУ), которые начинают работать при малых скоростях ветра, является актуальным вопросом. ВЭУ, работающие на основе эффекта Магнуса, доказали свою эффективность, однако авторами данной работы впервые для устранения проблемы в виде электрического привода для раскрутки цилиндрических лопастей на конец цилиндров добавлен элемент — дефлектор. Перед созданием экспериментальной установки необходимо численным путем исследовать аэродинамику вокруг ветроколеса. С этой целью проведено численное моделирование аэродинамики ветроколеса, используя высокоэффективную программу Ansys Fluent. Создана трехмерная геометрия в Design Modeler. Построена сетка математической модели с числом сетки 47329, состоящей из тетрагональных ячеек. В качестве модели турбулентности выбрана Realizable k-ε. Проведен тщательный анализ полей распределения векторов скоростей для скоростей потока и давления в трехмерной плоскости вокруг ветроколеса при скоростях воздушного набегающего потока 5, 10 и 15 м/с.

Ключевые слова: ветроэнергетическая установка, Ansys Fluent, эффект Магнуса, дефлектор, математическая модель, численное моделирование.

АВТОРЛАР ТУРАЛЫ МӘЛІМЕТТЕР
СВЕДЕНИЯ ОБ АВТОРАХ
INFORMATION ABOUT AUTHORS

Abdeyev B. — Candidate of Technical Sciences, Professor, School of Architecture and Building, D. Serikbayev East Kazakhstan Technical University, 070004, 69, Protozanova str., Ust-Kamenogorsk, Kazakhstan; E-mail: m.abdeeva@mail.ru

Abdul Qadir — PhD, Professor of Physics, Sukkur Institute of Business Administration, Sindh, Pakistan; E-mail: aqadir@iba-suk.edu.pk

Abdulina S.A. — PhD, Associate Professor, Teacher of D. Serikbayev East Kazakhstan Technical University, Ust-Kamenogorsk, Kazakhstan; E-mail: abdulina.saule@mail.ru.

Ablullin Kh.A. — D.Sc. (Physics and Mathematics), Professor, Al-Farabi Kazakh National University, Almaty, Kazakhstan; E-mail: kh.abdullin@gmail.com

Aimukhanov, A.K. — Candidate of Physical and Mathematical Sciences, Associate Professor, Professor of Department of Radiophysics and Electronics, Leading Researcher, Karaganda University of the name of academician E.A. Buketov, Scientific Center for Nanotechnology and Functional Nanomaterials, Karaganda, Kazakhstan.

Alibiyev D.B. — Candidate of Physical and Mathematical Sciences, Karaganda University of the name of academician E.A. Buketov, Karaganda, Universitetskaya street, 28, 100028, Kazakhstan; E-mail: dalibiev@mail.ru

Ashurov N.R. — Doctor of Science (Technical), Professor, Uzbekistan Academy of Sciences, Institute of Polymer Chemistry and Physics, 7$^{«b»}$, str. A.Kadyri, Tashkent, 100128, Uzbekistan; E-mail: nigmat.ashurov@gmail.com

Baidilda M.B. — Master of Engineering Sciences, Al-Farabi Kazakh National University, Almaty, Kazakhstan; E-mail: baidilda.meruyert@gmail.com

Baigereyev S. — PhD, Senior Lecturer, School of Mechanical Engineering, D. Serikbayev East Kazakhstan Technical University, 070004, 69, Protozanova str., Ust-Kamenogorsk, Kazakhstan; E-mail: samat.baigereyev@mail.ru

Baizakova G. — Lecturer, School of Architecture and Building, D. Serikbayev East Kazakhstan Technical University, 070004, 69, Protozanova str., Ust-Kamenogorsk, Kazakhstan, E-mail: gbaizakova@mail.ru

Baizhan, D.R. — Engineer of Research Center "Surface Engineering and Tribology" at S. Amanzholov East Kazakhstan University, Ust-Kamenogorsk, Kazakhstan; E-mail: daryn.baizhan@mail.ru

Bakhtybekova, A.R. — 1st year PhD student, Karaganda University of the name of academician E.A. Buketov, Karaganda, Kazakhstan, E-mail: asem.alibekova@inbox.ru

Berdinazarov Q.N. — PhD student, Uzbekistan Academy of Sciences, Institute of Polymer Chemistry and Physics, 7$^{«b»}$, str. A.Kadyri, Tashkent, 100128, Uzbekistan; E-mail: qodirberdinazarov@mail.ru

Botpaev, N.K. — Laboratory Assistant, Karaganda University of the name of academician E.A. Buketov, Karaganda, Kazakhstan.

Brim T. — Candidate of Technical Sciences, Senior Lecturer, School of Mechanical Engineering, D. Serikbayev East Kazakhstan Technical University, 070004, 69, Protozanova str., Ust-Kamenogorsk, Kazakhstan, E-mail: tbrim@mail.ru

Buitkenov D.B. — Senior Researcher of Research Center "Surface Engineering and Tribology" at S. Amanzholov East Kazakhstan University, Ust-Kamenogorsk, Kazakhstan; E-mail: Buitkenov.d@mail.ru

Dossumbekov K.R. — Master, Senior Lecturer of Computer Science faculty, Toraighyrov University, Pavlodar, Kazakhstan; E-mail: kairat_83@inbox.ru

Ismailov Zh.T. — Professor of Department Radio Physics Electronics, Physical Technical Faculty, Karaganda University of the name of academician E.A. Buketov, Karaganda, Kazakhstan; e-mail: Zhismailov@yandex/kz

Ispulov, N.A. — Candidate of Physical and Mathematical Sciences, Professor of Computer Science faculty, Toraighyrov University, Pavlodar, Kazakhstan; E-mail: nurlybek_79@mail.ru

Kakimzhanov D.N. — Junior Researcher of Scientific Research Center "Surface Engineering and Tribology" at S. Amanzholov East Kazakhstan University, Ust-Kamenogorsk, Kazakhstan; E-mail: dauir_97@mail.ru

Kalkozova Zh.K. — Cand. Sc. (Physics and Mathematics), Senior Teacher, Al-Farabi Kazakh National University, Almaty, Kazakhstan; E-mail: zh.kalkozova@mail.ru

Kambarov Y.Y. — Engineer of of Research Center center "Surface Engineering and Tribology" at S. Amanzholov East Kazakhstan University, Ust-Kamenogorsk, Kazakhstan; E-mail: yedilzhan@gmail.com

Kauymbek I.S. — Senior Teacher, Karaganda University of the name of academician E.A. Buketov, Karaganda, Kazakhstan; E-mail: indira_k79@mai.ru

Kazhikenova A.Sh. — Candidate of Technical Science, Karaganda University of the name of academician E.A. Buketov, Karaganda, Universitetskaya street, 28, 100028, Kazakhstan; E-mail: aigul-kazhikenova@mail.ru

Kengesbekov A.B. — Senior Researcher of Research Center "Surface Engineering and Tribology" at S. Amanzholov East Kazakhstan University, Ust-Kamenogorsk, Kazakhstan; E-mail: Aidar.94.01@mail.ru.

Khakberdiev E.O. — PhD, Uzbekistan Academy of Sciences, Institute of Polymer Chemistry and Physics, 7$^{«b»}$, str. A.Kadyri, Tashkent, 100128, Uzbekistan; E-mail: profhaqberdiyev@gmail.com

Korsakov I.E. — Docent, Department of Inorganic Chemistry, M.V. Lomonosov Moscow State University, Russia; E-mail: i.kors@yandex.ru

Kotov B.I. — Dr. Tech. Sc., Professor, Teacher, State Agrarian and Engineering University in Podilia, 01001, Kyiv, 2 Hospital'na St., Apt 13, Ukraine.

Kucheruk V.Yu. — Doctor of Technical Sciences, Professor, Department of Information Technologies of the Uman National University of Horticulture, Department of Computer Science and Economic Cybernetics of the Vinnytsia National Agrarian University, Kravchik Petro St., 5 Ladyzhyn, Vinnytsia Region, 24321, Ukraine.

Kulbachinskii V.A. — Professor, Department of Low Temperature Physics and Superconductivity, M.V. Lomonosov Moscow State University, Russia; E-mail: kulb@mig.phys.msu.ru

Kupriyanov E.E. — Post graduate student, Department of Low Temperature Physics and Superconductivity, M.V. Lomonosov Moscow State University, Russia; E-mail: ee.kupriyanov@physics.msu.ru

Kurmanov A.A. — Master, Senior Lecturer of Computer Science faculty, Toraighyrov University, Pavlodar, Kazakhstan; E-mail: almaskurmanov@mail.ru

Kytin V.G. — Docent, Department of Low Temperature Physics and Superconductivity, M.V. Lomonosov Moscow State University, Russia; E-mail: kytin@mig.phys.msu.ru

Magazov N.M. — Engineer of Scientific Research Center "Surface Engineering and Tribology" at S. Amanzholov East Kazakhstan University, Ust-Kamenogorsk, Kazakhstan; E-mail: magazovn@mail.ru

Markhabayeva A.A. — PhD, Senior Teacher, Al-Farabi Kazakh National University, Almaty, Kazakhstan; E-mail: aiko_marx@mail.ru

Maulet M. — Junior Researcher of Scientific Research Center "Surface Engineering and Tribology" at S. Amanzholov East Kazakhstan University, Ust-Kamenogorsk, Kazakhstan; E-mail: maulet_meruert@mail.ru.

Minkov L.L. — Doctor of Physical and Mathematical Sciences, Professor, National Research Tomsk State University, Tomsk, Russia.

Muslimanova G. — Candidate of Technical Sciences, Associate Professor, School of Mechanical Engineering, D. Serikbayev East Kazakhstan Technical University, 070004, 69, Protozanova str., Ust-Kamenogorsk, Kazakhstan; E-mail: gmuslimanova@mail.ru

Mussabekova, A.K. — 2nd year PhD student, Karaganda University of the name of academician E.A. Buketov, Karaganda, Kazakhstan; E-mail: assel50193@gmail.com.

Nemkaeva R.R. — Master of Physics, Senior Engineer of "National Nanotechnology Laboratory of Open Type" at Al-Farabi Kazakh National University, Almaty, Kazakhstan; E-mail: quasisensus@mail.ru

Normurodov N.F. — PhD student, Uzbekistan Academy of Sciences, Institute of Polymer Chemistry and Physics, 7«b», str. A. Kadyri, Tashkent, 100128, Uzbekistan; E-mail: nnf7nnf7@gmail.com

Nurbolat Sh.T. — PhD student, Al-Farabi Kazakh National University, Researcher of Institute of Apllied Sciences and Computational Technologies, Almaty, Kazakhstan; E-mail: shyryn0709@gmail.com

Ocheredko I.A. — Junior Researcher, S. Amanzholov East Kazakhstan University, Ust-Kamenogorsk, Kazakhstan; E-mail: egor007kz@mail.ru.

Orazbekova R.A. — Senior Teacher, Karaganda University of the name of academician E.A. Buketov, Karaganda, Kazakhstan.

Rakhadilov B.K. — PhD, Associate Professor, Senior Researcher of Scientific Research Center "Surface Engineering and Tribology" at S. Amanzholov East Kazakhstan University, Director of PlasmaScience LLP, Ust-Kamenogorsk, Kazakhstan; E-mail: rakhadilovb@mail.ru.

Sagdoldina Zh.B. — PhD, Associate Professor, Leading Researcher of Scientific Research Center "Surface Engineering and Tribology" at S. Amanzholov East Kazakhstan University, Ust-Kamenogorsk, Kazakhstan; E-mail: Sagdoldina@mail.ru.

Smailova A.S. — Teacher, Karaganda University of the name of academician E.A. Buketov, Karaganda, Kazakhstan; E-mail: guapa_a@mai.ru

Shuyushbayeva N.N. — PhD, Associate Professor, Sh. Ualikhanov Kokshetau University, Kokshetau, Kazakhstan.

Shvidia V.O. — PhD, Leading Reseracher, Institute of Mechanics and Automatics of Agroindustrial Production of the National Academy of Agrarian Sciences of Ukraine, 03194, Kyiv, Zodchikh, Apt 22/3, Ukraine.

Spirin A.V. — Candidate of Technological Sciences, Associate Professor, Teacher of Separate Structural Subdivision "Ladyzhyn Professional College of Vynnitsia National Agrarian University", Kravchik Petro St., 5 Ladyzhyn, Vinnytsia Region, 24321, Ukraine; E-mail: spirinanatoly16@gmail.com

Stepanenko S.P. — Dr. Tech. Sc., Head of Department of Mechanical and Technological Problems of Harvesting and Post-Harvesting Processing of Grain and Oilseeds, Institute of Mechanics and Automatics of Agroindustrial Production of the National Academy of Agrarian Sciences of Ukraine, 08631, Kyiv region, Fastiv district, Glevakha, 11/1, Vokzalna St., Apt 7, Ukraine.

Tanasheva N.K. — PhD, Associate Professor, Karaganda University of the name of academician E.A. Buketov, Karaganda, Kazakhstan.

Tentekbayeva Zh.M. — Senior Teacher of Foreign Languages Department, MEd, Karaganda Technical University, Karaganda, Nursultan Nazarbayev Avenue, 56, Kazakhstan; E-mail: zhuldyz_83@mail.ru

Torebek K. — Engineer of Research Center "Surface Engineering and Tribology" at S. Amanzholov East Kazakhstan University, Ust-Kamenogorsk, Kazakhstan; E-mail: Kiztore98@mail.ru

Tussupbekova A.K. — PhD, Associate Professor of Department of Radiophysics and Electronics, Karaganda University of the name of academician E.A. Buketov, Karaganda, Kazakhstan.

Zhumabekov A.Zh. — PhD, Senior Lecturer of Computer Science faculty, Toraighyrov University, Pavlodar, Kazakhstan; E-mail: almar89–89@mail.ru

Zhurerova L.G. — PhD, Senior Researcher of Scientific Research Center "Surface Engineering and Tribology" at S. Amanzholov East Kazakhstan University, Ust-Kamenogorsk, Kazakhstan; E-mail: leila_uka@mail.ru